

SURFACE MOTIONS OF THE
BETA CEPHEI STARS

by

Peter Alan

P.A. Stamford, B.Sc.(Hons.), University of Tasmania

A thesis submitted in fulfilment of the requirements

for the degree of

Doctor of Philosophy

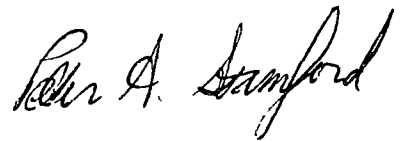
in the

UNIVERSITY OF TASMANIA

HOBART

September, 1980

Except as stated herein, this thesis contains no material which has been accepted for the award of any other degree or diploma in any university. To the best of my knowledge and belief, this thesis contains no copy or paraphrase of material previously published or written by another person, except when due reference is made in the text of the thesis.

A handwritten signature in black ink, reading "Peter A. Stamford". The signature is written in a cursive style with a large, stylized initial 'P'.

Peter A. Stamford

1/9/80

Any part of this thesis may be photocopied.

TABLE OF CONTENTS

| | | |
|-----------|---|-----|
| | ACKNOWLEDGEMENTS | 1. |
| | ABSTRACT | 2. |
| CHAPTER 1 | INTRODUCTION | |
| 1.1 | Observational Characteristics of the β Cephei Stars | 4. |
| 1.2 | Theories of the Excitation Mechanism | 5. |
| 1.3 | Theories of the Oscillation Modes | 7. |
| 1.4 | Surface Motion Diagnostics | 8. |
| 1.5 | The Thesis | 11. |
| CHAPTER 2 | MODELLING THE STELLAR SURFACE | |
| 2.1 | Introduction | 13. |
| 2.2 | The Light Variations | 14. |
| 2.3 | The Line Profile Variations | 22. |
| 2.4 | The Polarization Variations | 23. |
| 2.5 | Accuracy of Numerical Techniques | 26. |
| 2.6 | Analytic Expressions for Light and Velocity Variations | 28. |
| 2.7 | A Baade-Wesselink Method for Nonradial Pulsators | 33. |
| CHAPTER 3 | THE LIGHT VARIATIONS | |
| 3.1 | Introduction | 39. |
| 3.2 | Light, Colour and Radial Velocity Data | 41. |
| 3.3 | Comparison of Pulsation Models with Observational Data | 45. |
| 3.4 | The Pulsation Amplitude Spectra | 57. |
| 3.5 | Conclusion | 64. |

| | | |
|-----------|---|------|
| CHAPTER 4 | POLARIZATION MODELS | |
| 4.1 | Introduction | 66. |
| 4.2 | Solution of the Equations of Radiative Transfer | 67. |
| 4.3 | Nonradial Calculations and Results | 77. |
| 4.4 | Detectability Considerations | 88. |
| 4.5 | Discussion of Individual Stars | 90. |
| 4.6 | Polarization of Multimode Pulsators | 93. |
| 4.7 | Conclusion | 97. |
| CHAPTER 5 | THE LINE PROFILES | |
| 5.1 | Introduction | 98. |
| 5.2 | Nonradial Profile Characteristics | 99. |
| 5.3 | Comparison with Observations of Particular Stars | 108. |
| 5.4 | Radial Velocity Measures | 125. |
| 5.5 | Line Models and the Effect of Atmospheric Structure | 135. |
| 5.6 | Conclusion | 144. |
| CHAPTER 6 | SIMPLE NONLINEAR RADIAL MODELS | |
| 6.1 | Introduction | 146. |
| 6.2 | The Hard-Piston Atmospheric Model | 148. |
| 6.3 | The Linear Adiabatic Solution | 160. |
| 6.4 | Simple Soft-Piston Envelope Models | 162. |
| 6.5 | The Radiative Diffusion Model | 173. |
| 6.6 | Line Doubling Mechanisms for BW Vul | 180. |
| CHAPTER 7 | CONCLUSIONS | 184. |
| | REFERENCES | 187. |

APPENDICES

| | | |
|------|---|------|
| A1 | Cos γ for a Distorted Star | 194. |
| A2 | Plots of the Nonradial Surface Configurations | 197. |
| A3 | The Line-of-Sight Velocity | 198. |
| A4 | Cos ζ for a Distorted Star | 199. |
| A5 | The Nonradial Baade-Wesselink Method and Related Mode Discrimination Methods | 201. |
| A5.1 | <i>Integral Relations</i> | 201. |
| A5.2 | <i>The Nonradial Baade-Wesselink Expression</i> | 203. |
| A5.3 | <i>Amplitude and Phase Techniques</i> | 216. |
| A5.4 | <i>Conclusion</i> | 223. |
| A6 | Nonradial Line Profiles for $l \leq 3$ | 225. |

ACKNOWLEDGEMENTS

I would like to express my sincere gratitude to my supervisor, Dr. Robert Watson, for his encouragement and stimulating advice during the development of the work described in this thesis. I must also thank him for introducing me to the problem of stellar pulsations, for the many invaluable discussions which were essential to the progress of this work, and finally, for his helpful criticisms of the thesis draft.

Dr. Bruce Cogan provided me with models of evolved B star cores which were essential to the work in Chapter 6. I am very grateful for this assistance.

I am also grateful to Dr. Peter Wood for some valuable advice on hydrodynamic modelling, and Dr. Myron Smith for many interesting communications and preprints.

Thanks are also due to the staff of the University Computing Centre for their competent service, and to those people who generously donated computing resources to enable the completion of this work.

Miss Gullinar Gafar must also be commended for her efficiency and patience in typing this thesis.

Finally, I gratefully acknowledge the financial support of an Australian Government Postgraduate Research Award.

ABSTRACT

The nature of the β Cephei surface motions, whether radial or nonradial, has been the subject of considerable controversy. In recent years a number of techniques have been developed for the identification of the pulsation modes operative in variable stars. In this thesis, these mode identification techniques are explored theoretically and applied to some members of the β Cephei group.

The first technique uses the relative amplitudes and phases of the light, colour and radial velocity variations for mode discrimination. It is demonstrated that, for the β Cephei stars, the colour to visual light amplitude ratio is mode discriminating providing the colour index is derived over a sufficiently long wavelength baseline. Of ten β Cephei stars investigated by this method, eight are found to be radial pulsators, while two are probably quadrupole pulsators. However, for the δ Scuti and cepheid variables, it is found that the phase difference between light and colour variations is mode discriminating, whereas the phase difference between light and velocity, and the amplitude ratios, are of no value. These techniques are related to the Baade-Wesselink method as applied to nonradial pulsators. It is shown that the underlying assumption of the Balona and Stobie derivation relating surface brightness to colour is invalid in the general nonradial case. A corrected Baade-Wesselink formula is obtained and the mode identification capabilities of the resulting Baade-Wesselink coefficients are investigated.

A second mode identification method would involve the monitoring of β Cephei stars for variations in linear polarization. Such variations should result from the anisotropic scattering geometry associated with nonradial pulsations. Calculations of the expected polarization variations for nonradial modes up to $l = 3$ are obtained using accurate B-star model atmospheres. It is demonstrated that although

variations in the polarization at visual wavelengths are not likely to be detectable for the β Cephei stars, this technique should be successfully applicable to ultraviolet observations obtained with proposed satellite-borne polarimeters. The polarization variations expected for some of the pulsation models which have been proposed for individual β Cephei stars are then discussed.

The third mode diagnostic considered involves the comparison of observed line profiles with those synthesized theoretically for particular nonradial modes. The line profiles originating from modes with $l \leq 3$ are discussed and an attempt is made to model the line profile variations of 12 Lacertae using two interfering nonradial modes.

From the application of these mode identification methods to a number of β Cephei stars it is inferred that the *singly-periodic* stars are *radial* pulsators. Since BW Vulpeculae is in this category, the radial shock interpretation of its spectral variations demands important consideration. To investigate this hypothesis a hydrodynamic envelope pulsation model was constructed. This model indicates that nonlinear wave propagation of underlying sinusoidal motions into the outer envelope of a large amplitude radial pulsator may indeed generate strong atmospheric shock waves. Observed line doubling and light curve bump phenomena can be understood in terms of this process.

C H A P T E R O N E

INTRODUCTION1.1 OBSERVATIONAL CHARACTERISTICS OF THE β CEPHEI STARS

The β Cephei stars (β Canis Majoris stars) are a group of hot, luminous variable stars pulsating with periods of only a few hours. In 1902 E.B. Frost discovered the radial velocity variability of the prototype star β Cephei. Frost initially ascribed these variations to binary motions. However a very small inclination angle was required by this hypothesis. The inadequacies of the binary interpretation were compounded by the detection by P. Guthnick in 1913 of light variations from this star which did not resemble the light curve of an eclipsing binary system. By 1920, three additional stars, σ Scorpii, β Canis Majoris and 12 Lacertae, were known to display similar behaviour and it became apparent that these stars, all of spectral type B, formed a class of pulsating variables distinct from the classical cepheids.

For many years the β Cephei variables were believed to be the only group of pulsating stars hotter than spectral type A0, however the recent discovery of the 53 Persei variables (Smith, 1977) and the 'ultra-short-period' variables (Jakate, 1979) suggests that this region is prone to widespread stellar instability. Within this region the β Cephei variables occupy an extremely narrow strip, with spectral types B0.5 - B2 and luminosity classes III - IV. The periods of the β Cephei stars range from about 3.5 to 6 hours. These periods are highly stable over many years, in contrast to the 53 Persei variables which can undergo abrupt period changes. The β Cephei stars are known to satisfy a period-colour-luminosity relation with longer periods at earlier spectral types.

Since Meyer (1934) demonstrated the existence of two close periods in the radial velocity variations of β CMa, approximately half of the β Cephei stars have been found to be multiperiodic. For these stars the interference of the different modes produces a modulation of the light and velocity curves. The observed light variations are typically very small. Amplitudes are only a few hundredths of a magnitude. The radial velocity amplitudes are usually in the range of 5 to 50 km s⁻¹. The light and radial velocity variations are nearly sinusoidal in time and are approximately 90° apart in phase. Maxima in light and colour occur near the descent of the radial velocity through the gamma velocity. In comparison with other groups of pulsating stars the ratio of the visual light amplitude to velocity amplitude $\langle \Delta m / 2K \rangle$ is very small.

In 1918 Henroteau discovered that the spectral lines of β CMa exhibit periodic variations in broadening. This phenomenon occurs in the lines of many β Cephei stars, usually near the phase of maximum light. In some cases this extends to the splitting of spectral lines into two components. BW Vul is the most extreme example of this. A further complexity displayed by some β Cephei stars is that the radial velocity curves derived from different elements are found to be slightly out of phase. This phenomenon, known as the 'Van Hoof effect', is presumed to result from differential atmospheric motions.

A considerable expansion of this brief summary of the observational properties of the β Cephei stars can be found in numerous reviews. The most recent of these is the review by Lesh and Aizenman (1978).

1.2 THEORIES OF THE EXCITATION MECHANISM

The β Cephei stars have posed a difficult problem for theorists because no viable excitation mechanism has yet been discovered. Destabilizing mechanisms which have been proposed are described in detail in the excellent reviews of Cox (1976) and Osaki (1978).

The suggested instability mechanisms fall into two categories: those which occur naturally during the course of stellar evolution and those which occur only in particular circumstances peculiar to some early B stars. The high proportion of β Cephei stars within the confines of the observed β Cephei region (Jerzykiewicz and Sterken, 1978; Shobbrook, 1979) suggests that the destabilizing mechanism is probably of the former type. In this category are variants of the envelope ionization mechanism (Underhill, 1966; Stellingwerf, 1978) known to destabilize the cooler variables and the proposal of Schmalberger (1960). Schmalberger had suggested that the instability arises from the structural readjustment of the stellar interior associated with the transfer of energy generation from a core to a shell source. Unfortunately exhaustive analyses of stellar models corresponding to *all* evolutionary states coinciding with the β Cephei strip have been found to be stable to both radial (Davey, 1973) and nonradial (Aizenman, Cox and Lesh, 1975; Osaki, 1976) oscillations.

Of the hypotheses requiring special mechanisms the most prominent have been the μ -mechanism of Stothers and Simon (1969, 1970a), a mechanism resulting from the overstability of the semi-convection zone (Kato, 1966; Shibahashi and Osaki, 1976), and the coupling of a rapidly rotating core to a nonradial mode (Osaki, 1974). The first of these theories is not consistent with the observational data (Plavec, 1971; Watson, 1971a). The last hypothesis appears to be the most promising of the three, but is complex and has not been fully investigated.

At present, the simplest possibility is the suggestion of Stellingwerf (1978) that an opacity mechanism associated with the He^+ ionization edge may be the origin of the β Cephei instability. However the detailed behaviour of the opacity in the region of this opacity feature needs to be determined much more accurately for this mechanism to be properly evaluated.

1.3 THEORIES OF THE OSCILLATION MODES

Allied with the problem of discovering the instability mechanism is the problem of determining the modes in which the β Cephei stars pulsate. The two questions are interrelated since identification of the pulsation modes may well provide a valuable clue to the type of instability mechanism which is responsible. In particular, much effort has been dedicated to deciding whether the pulsations are radial or nonradial.

Historically, the main advocate of the radial hypothesis of β Cephei pulsation has been Van Hoof (1970). He claimed to have observed the fundamental radial mode and its overtones, together with 'difference' oscillations. However the reality of many of the frequency components discovered by Van Hoof in his observational data has been severely questioned (Lesh and Aizenman, 1976). Odgers (1956) interpreted observations of BW Vul in terms of a radial shock model, which envisaged the periodic ejection and return of an atmospheric layer. This theory was extended by Odgers and Kushwaha (1959) and applied to 12 Lac by Leung (1965).

Two nonradial theories have been investigated in detail. The first was proposed by Ledoux (1951) who determined the Lagrangian form of the nonradial surface displacements in the linear approximation. Ledoux also showed that, for a rotating star, a number of close period oscillations at equi-spaced intervals of frequency would be expected. The observational ramifications of Ledoux's theory have been examined in a number of papers, such as those by Christy (1966), Osaki (1971) and Kubiak (1978). The second nonradial model was suggested by Chandrasekhar and Lebovitz (1962). Chandrasekhar and Lebovitz demonstrated that, under certain conditions, a radial and nonradial mode can couple to produce two distinct nonradial modes which, for a rotating star,

are slightly displaced in frequency. This theory has also been investigated by Clement (1965, 1967, 1969) and Hurley, Roberts and Wright (1966). It suffers from the deficiency that it cannot explain stars, such as 12 Lac, which possess more than two distinct periods.

In an alternative approach, Fitch (1967, 1969) has explored the effects of tidal interactions on some β Cephei stars which are members of binary systems. Although this may explain some of the frequency components observed, it is unlikely that all of the multiperiodic β Cephei stars can be satisfactorily explained by a tidal hypothesis.

1.4 SURFACE MOTION DIAGNOSTICS

To discriminate between different proposals for the pulsational modes and consequent surface motions of β Cephei stars, a variety of arguments based on the observational data have been used. These will now be considered in turn.

1. *Pulsational Q-Values*

Considerable restrictions may be placed on the possible pulsation mode by comparing observed values of the pulsation constant $Q = P\sqrt{\rho/\rho_\odot}$ with those determined theoretically from model calculations assuming a particular evolutionary phase. Recent studies by Jones and Shobbrook (1974), Balona and Feast (1975) and Shobbrook (1978) indicate a mean value of $Q \sim 0.027$ day for the β Cephei stars. According to the models of Lesh and Aizenman (1974) this is consistent with pulsation in either the first harmonic radial mode or a nonradial p_1 or p_2 mode.

2. *Frequency Spectra*

The frequency spectrum of the light or radial velocity variations of a pulsating star can reveal the presence of nonradial modes in two ways. The first indication occurs when two modes are present in a frequency ratio which cannot be matched by ratios corresponding to

radial harmonics. Examples of β Cephei stars for which this is true are β CMa, σ Sco, 12 Lac, ν Eri and 16 Lac. Each of these has periods present in a ratio P_{SHORT}/P_{LONG} greater than 0.96, whereas the period ratios of possible radial harmonics are considerably less than this value. This result implies that for each of these stars at least one of the close modes is nonradial.

The second, and more specific, indication of nonradial modes occurs when three or more modes are separated by equal intervals of frequency. Such a result is expected for the rotational splitting of nonradial m -states. This method has been exploited by Jerzykiewicz (1978), who discovered an equi-spaced triplet in the frequency spectrum of 12 Lac.

3. *Spectral Line Profiles*

Ledoux (1951) first showed that the nonradial $l = 2, m = -2$ mode exhibited line broadening variations which were similar to those observed in many β Cephei stars. The line profile characteristics expected from radial and nonradial motions have recently been the subject of a large number of investigations (Smith and McCall, 1978; Campos and Smith, 1980; Smith, 1980a) to the extent that it is now possible to (almost) uniquely identify the pulsation mode providing high quality spectral observations are available.

4. *Light, Colour and Radial Velocity Amplitudes*

Leung (1968) noted that the $\langle 2K/\Delta m \rangle$ value for the β Cephei stars was much larger than the value for other types of variables believed to be radial pulsators. He suggested that this implied nonradial motions for the β Cephei stars. However Watson (1971b) has refuted this argument. Mode identification on the basis of the *amplitudes* of the variations became feasible when Dziembowski (1977) presented

explicit formulae for the light and radial velocity variations of nonradial pulsators. Dziembowski applied this technique to the δ Scuti stars. At the same time Stamford and Watson (1977) numerically modelled the light, colour and velocity amplitudes expected from nonradially pulsating β Cephei stars. Extending these techniques, mode identifications using light, colour and radial velocity amplitudes have been attempted for the β Cephei stars by Stamford and Watson (1978a, 1980a), Balona and Stobie (1979c) and Smith (1980a).

5. *Phase Differences Between Light, Colour and Radial Velocity*

This technique involves the evaluation, using nonadiabatic, nonradial models, of the phase difference between the local flux and radius variations. The theoretical phase shift can be used to predict a phase difference, dependent on the mode order l , between the light and velocity curves or the light and colour curves of the variable. This phase difference can then be compared with the observed value. Dziembowski (1977) has used the former method, and Balona and Stobie (1980) and Kurtz (1979) have used the latter method, to identify modes in δ Scuti stars. The nonradial Baade-Wesselink method, formulated by Dziembowski (1977) and Balona and Stobie (1979a), falls within the general ambit of the phase-difference method. Unfortunately the Wesselink and related phase-difference methods cannot be easily applied to the β Cephei stars since the light curves have similar phases at all wavelengths and the velocity and light curves are close to 90° out of phase for these stars. Under such marginal conditions, the failure of the conventional radial Wesselink method should not be construed to be proof of nonradial oscillations, as Lesh and Aizenman (1978) have remarked.

6. *Polarization Variations*

The detection of polarization variations would provide conclusive proof of the presence of nonradial pulsations. Schafgans and Tinbergen (1979) monitored β Cephei itself for evidence of such variations. Recently Odell (1979) and Stamford and Watson (1980a) have calculated the magnitude of the polarization variations expected from nonradial pulsators.

1.5 THE THESIS

Advances in data acquisition technology and the quality of computing resources are rapidly transforming the mode diagnostic methods just described from rudimentary concepts to powerful experimental methods. This thesis explores theoretically the last four of these methods and, by applying them to a number of β Cephei stars, attempts to infer some conclusions concerning the nature of the β Cephei pulsations.

The structure of the thesis is as follows. Chapter 2 contains a description of a stellar surface model which was used to numerically simulate the observable variations of a pulsating B star. This chapter also contains modifications to the nonradial Baade-Wesselink formula derived by Balona and Stobie (1979a). The results of light, colour and radial velocity calculations are discussed in Chapter 3, where the predicted amplitudes are compared with the observational data obtained from the literature for a number of β Cephei stars. Mode identifications are obtained for ten β Cephei stars in this chapter. The equations of radiative transfer, including the effects of absorption and Thomson electron scattering, are solved for a number of B star atmospheres in Chapter 4. Here the polarization variations expected from a nonradially pulsating atmosphere are discussed and it is shown that only satellite ultraviolet observations are likely to offer the prospect of a positive detection of variable polarization for the

β Cephei stars. In Chapter 5 the line profiles expected for a range of nonradial surface amplitudes and rotational speeds are examined prior to an attempt to model the observed spectral variations of 12 Lac using interfering quadrupole modes. The properties of a radial nonlinear envelope pulsation model are investigated in Chapter 6. This model was designed to explore the role of shock waves in the atmospheres of large amplitude β Cephei variables. Finally, in Chapter 7, a summary of the conclusions reached in this thesis is presented.

Although the investigations described in this thesis have been aimed at understanding the β Cephei pulsations, in some cases the methods are applicable to other types of pulsating variables. They may be relevant, in particular, to identifying the surface motions of the 53 Persei, δ Scuti and ZZ Ceti stars, all of which contain a number of nonradial candidates.

C H A P T E R T W O

MODELLING THE STELLAR SURFACE

2.1 INTRODUCTION

In recent years there has been a considerable resurgence of interest in the Ledoux (1951) proposal of nonradial pulsation for the β Cephei stars. The renaissance of the nonradial hypothesis is associated with technological advances in data acquisition and with increased availability of computing resources to permit better modelling of nonradial variations. This chapter describes the nonradial surface model used to calculate the light, colour, radial velocity and polarization curves and line profile effects seen by a distant observer as a function of time. The model results are then discussed in detail in Chapters 3, 4 and 5 of the thesis.

The complexity of modelling the variations associated with nonradial motions arises from the fact that the local radius, surface velocity, effective temperature, effective gravity and polarization components will vary from point to point over the distorted stellar surface. For this reason it is logical to subdivide the visible hemisphere of the star into a large number of surface elements and to numerically sum over each of these elements to obtain the integrated stellar properties. Such a procedure is the basis of the modelling technique used here and detailed in Sections 2.2, 2.3 and 2.4 in connection with light, line profiles and polarization respectively. This technique was first used in the β Cephei context by Osaki (1971) for a study of line profiles. In Section 2.5 the accuracy of the technique of numerical integration over the stellar surface is examined.

At the time when this work was initiated there were no published models of nonradial light variations. Subsequently, Dziembowski (1977) derived analytic expressions for the light and mean velocity of a

nonradially pulsating star in the linear regime. This formulation is discussed in Section 2.6. The analytic expressions have provided a valuable check on the numerical integration techniques developed and an important insight into some explicit parameter dependencies. However, while the analytic method is useful for light variations and has some relevance to radial velocity calculations, the spectral line profiles and polarization curves have not been obtained analytically. Although lacking the elegance of a formal solution, the numerical method is readily amenable for use in modelling *all* of the observable variations exhibited by nonradial pulsators. This chapter concludes, in Section 2.7, with a formulation of a Baade-Wesselink method for nonradial pulsators which is an extension of ideas developed by Balona and Stobie (1979a) on the basis of Dziembowski's formulae.

2.2 THE LIGHT VARIATIONS

2.2.1 *The Equilibrium Surface*

The equilibrium state of a stellar surface is taken to be defined by the following four parameters: the polar radius (R_p), the stellar mass (M), the polar effective temperature (T_p) and the rotational angular speed (Ω). In the following analysis the changes in the equilibrium surface geometry and temperature due to rotational distortion and gravity darkening are included for completeness. However, as might be expected, these effects were subsequently found to produce negligible changes in the light curve for typical β Cephei rotational velocities, which are considerably less than the break-up velocity.

The rotational shape $R(\theta)$ may be calculated using the constancy of the surface potential (Eddington, 1926),

$$\Phi = \frac{GM}{R} + \frac{1}{2}\Omega^2 R^2 \sin^2 \theta$$

which gives

$$\frac{GM}{R} + \frac{1}{2}\Omega^2 R^2 \sin^2\theta = \frac{GM}{R_p} \quad (2.1)$$

This equation permits the calculation of the equilibrium surface to high accuracy by successive approximation. Rotational disintegration occurs when the equatorial radius (R_e) satisfies

$$\Omega^2 R_e \geq \frac{GM}{R_e^2}$$

i.e.
$$v_e \leq \left(\frac{GM}{R_e}\right)^{\frac{1}{2}}.$$

This corresponds to an equatorial break-up speed of $v_e \sim 500 \text{ km s}^{-1}$ for an early B giant and compares with $v_e \sin i < 100 \text{ km s}^{-1}$ for most of the known β Cephei stars. The effective temperature was assumed to vary over the stellar surface according to

$$T = T_p (g/g_p)^{0.25} \quad (2.2)$$

as prescribed by the Von Zeipel theorem of gravity darkening. The local effective gravity is given by

$$g_{eff} = |\text{grad } \Phi| = \left[\left(\frac{GM}{R^2} - \Omega^2 R \sin^2\theta \right)^2 + (\Omega^2 R \sin\theta \cos\theta)^2 \right]^{\frac{1}{2}}. \quad (2.3)$$

Equations 2.1, 2.2 and 2.3 are sufficient to specify the equilibrium geometric and thermal state of the stellar surface.

2.2.2 Surface Changes

There are three factors which contribute to the light variations of a nonradially pulsating star. These are:

- (1) changes in local temperature and effective gravity due to the expansion and compression of the gas,
- (2) changes in the orientation of the surface elements, which alters their projected area and limb darkening,
- and (3) changes in the size of the apparent disc due to changes in radius.

While in the particular case of radial oscillations only the first and third factors are operative, changes in the shape of the distorted surface of a nonradial pulsator can provide a major source of light variations via the second mechanism. These three factors are discussed in turn in this and the following section.

The change in effective temperature ΔT associated with a change in radius ΔR was calculated by simply assuming a linear relationship of the form $(\Delta T/T) = -B(\Delta R/R)$. For adiabatic changes the value of B can be explicitly obtained for a particular dimensionless frequency $\omega = (\sigma^2 R^3/GM)^{1/2}$ using the linear adiabatic boundary condition of Dziembowski (1971),

$$\frac{\Delta P_{gas}}{P_{gas}} = -[4 + \omega^2 - \frac{\mathcal{L}(\mathcal{L}+1)}{\omega^2}] \frac{\Delta R}{R} . \quad (2.4)$$

This boundary condition has also been used by Buta and Smith (1979).

For short periods and low-order modes this reduces to the usual Stothers and Simon (1970b) boundary condition $\frac{\Delta P_{gas}}{P_{gas}} = -[4 + \omega^2] \frac{\Delta R}{R}$. Thus under adiabatic conditions it follows that

$$B = (1 - \frac{1}{\Gamma_2})[4 + \omega^2 - \frac{\mathcal{L}(\mathcal{L}+1)}{\omega^2}]. \quad (2.5)$$

Assuming a ratio of gas pressure to total pressure of 90%, which is reasonable for the envelope of an early B star, then $\Gamma_2 \sim 1.5$ and B would be expected to lie in the range 4 to 8 based on the observed Q of 0.036 to 0.025. If nonadiabatic effects become significant, then B will depart from these values and a phase shift ψ between $\Delta T/T$ and $-\Delta R/R$ will arise. In this case the temperature variations take the form

$$\frac{\Delta T}{T} = -B \frac{\Delta R}{R} e^{i\psi} . \quad (2.6)$$

Davey (1970) published radial nonadiabatic eigenfunctions for a β Cephei model showing a small phase lag of $\psi \sim 0.07$ radians for the fundamental

oscillation. He obtained a value of $B = 3.31$ for this model, some 25% lower than the adiabatic value with $\Gamma_2 = 1.5$.

The local effective gravity was assumed to scale with local gas pressure as

$$\frac{\Delta g_{eff}}{g} = p_* \frac{\Delta P_{gas}}{P_{gas}},$$

where the coefficient p_* may be estimated from equilibrium model atmospheres. For β Cephei stars $p_* \sim 1.1$. This pressure variation effect takes into account changes in flux resulting from opacity changes, which are in turn generated by the pressure variations accompanying the oscillation. It follows from Equation 2.4 that $\Delta g_{eff}/g$ is related to $\Delta R/R$ by

$$\frac{\Delta g_{eff}}{g} = -p_* \left[4 + \omega^2 - \frac{l(l+1)}{\omega^2} \right] \frac{\Delta R}{R}. \quad (2.7)$$

The effective gravity change produced by this equation is larger, by a factor of $\sim p_*(4+\omega^2)/2 \sim 10$, than the true geometric change in Newtonian gravity, reflecting the comparatively large accelerations imposed on the gas by the pulsational motions. In comparison with the temperature effect, the contribution of the pressure effect to the flux variations is small for the β Cephei stars. However, as will be seen in Section 3.4, it is worth including if accurate observational data is available. Some observational support for an effective gravity variation of the form of Equation 2.7 is provided by Trodahl and Sullivan (1977). They used multicolour observations of the δ Scuti star χ Cae to separate out temperature and effective gravity contributions to the light variations and determined $\Delta \log g_{eff} \sim 0.10$ for this star. Inserting into Equation 2.7 values from their data, one obtains $\Delta \log g_{eff} \sim 0.11$, in accord with the observations. Parsons (1971) has discussed the large effective gravity variations in cepheids

and found that the amplitudes of these variations are consistent with Equation 2.7. Only one determination of effective gravity variations has been published for β Cephei stars. That is the work by Kubiak (1972) on BW Vul. He obtained an effective gravity variation from H_γ equivalent widths after removing the temperature contribution, which was derived from colour indices. Kubiak's observed variation of $\Delta g_{eff}/g \approx \pm 50\%$ is less than the value of $\pm 80\%$ predicted by Equation 2.7. This difference could be due to nonlinear effects since these are very substantial variations. Finally, it is worth noting that if the effective gravity had been defined in terms of changes in the *pressure gradient* rather than changes in the *pressure* then

$$g_{eff} = \frac{\partial P}{\partial m} = \frac{\partial^2 r}{\partial t^2} + g(r) \approx -\sigma^2 \Delta R + g(R) \left(1 - 2 \frac{\Delta R}{R}\right).$$

Hence $\Delta g_{eff}/g = -(\omega^2 + 2)\Delta R/R$, which is not substantially different from Equation 2.7 for the ω^2 values of ~ 18 appropriate to the β Cephei stars.

2.2.3 The Observed Flux

The applicability of static model atmospheres, derived under the assumptions of hydrostatic and radiative equilibrium, to the atmospheres of pulsating stars has been discussed in detail by Ledoux and Walraven (1958) and more recently by Parsons (1971), Kubiak (1972) and Breger (1975). They conclude that when the thermal relaxation time of a stellar atmosphere is short compared with the pulsation period, the atmosphere rapidly adapts to changes in energy flux with little departure from radiative equilibrium. Since the radiative relaxation time for a B star atmosphere is of the order of only a few seconds, it follows that successive states of a pulsating β Cephei atmosphere can be approximated by a sequence of static model atmospheres, each at some appropriate instantaneous effective temperature and effective gravity. Theoretical fluxes were obtained for the pulsating surface model under this assumption.

Monochromatic and filter-convolved fluxes, F_ν , were acquired by interpolation, at the (T_e, g_{eff}) values specified by Equations 2.6 and 2.7, in the model atmosphere tables of Kurucz *et al.* (1974). Since only differential fluxes are required, the absolute accuracy of the model atmospheres is not called into question.

The emitted astrophysical flux per unit area and specific intensity distribution are related by

$$F_\nu = 2 \int_0^1 I_\nu(\mu) \mu d\mu = 2I_\nu(1) \int_0^1 h_\nu(\mu) \mu d\mu$$

where $h_\nu(\mu)$ is the limb darkening function. Values of $h_\nu(\mu)$ can be extracted from tables published by Kurucz (1969). Thus the flux per unit solid angle arriving at the earth from the stellar photosphere is

$$E_\nu = 2 \int_{\substack{\text{visible} \\ \text{surface}}} I_\nu(\mu) \mu dA = \int_{\substack{\text{visible} \\ \text{surface}}} F_\nu h_\nu(\mu) \mu dA / \int_0^1 h_\nu(\mu) \mu d\mu . \quad (2.8)$$

In the case of spherical symmetry the integral reduces to the usual $E_\nu = \pi F_\nu R^2$. However, for a general surface oscillation, the full integral must be considered and attention paid to the fact that $F_\nu(\mu)$ and $h_\nu(\mu)$ are dependent on the instantaneous local surface conditions.

In practice, the surface integral (2.8) is approximated by a sum over a large number of individual elements; typically several thousand. From Equation A1.8 (Appendix 1) it follows that the differential area of such an element having polar angle θ and azimuthal angle ϕ at an instantaneous radius R is

$$dA = \frac{\partial R}{\partial \theta} \times \frac{\partial R}{\partial \phi} d\theta d\phi = R \{ R^2 \sin^2 \theta + \left(\frac{\partial R}{\partial \theta} \right)^2 \sin^2 \theta + \left(\frac{\partial R}{\partial \phi} \right)^2 \}^{\frac{1}{2}} d\theta d\phi . \quad (2.9)$$

The final piece of geometric information required is the instantaneous orientation of the surface element, which is specified by the angle, γ , between the outward surface normal and the line-of-sight of the observer.

In Appendix 1 it is shown that this angle is given by (Equation A1.6)

$$\mu = \cos \gamma = \{R^2 \sin^2 \theta + \left(\frac{\partial R}{\partial \theta}\right)^2 \sin^2 \theta + \left(\frac{\partial R}{\partial \phi}\right)^2\}^{-1/2} \times$$

$$\{R \sin \theta (\cos \theta \cos i + \sin \theta \cos \phi \sin i) + \quad (2.10)$$

$$\frac{\partial R}{\partial \theta} \sin \theta (\sin \theta \cos i - \cos \theta \cos \phi \sin i) + \frac{\partial R}{\partial \phi} \sin \phi \sin i\}$$

where i is the polar angle of inclination of the line-of-sight.

2.2.4 Nonradial Surface Motions

Nonradial surface pulsations can be expressed in terms of spherical harmonic perturbations (Ledoux, 1951; Osaki, 1971) in the form

$$\underline{\xi}(\underline{r}, t) = (\xi_r, \xi_\theta, \xi_\phi) e^{i\sigma t}$$

where the orthogonal Lagrangian displacements are given by

$$\left. \begin{aligned} \xi_r(\theta, \phi) &= a(r) P_{lm}(\cos \theta) e^{im\phi} \\ \xi_\theta(\theta, \phi) &= b(r) \frac{d}{d\theta} P_{lm}(\cos \theta) e^{im\phi} \\ \xi_\phi(\theta, \phi) &= im b(r) \frac{P_{lm}(\cos \theta)}{\sin \theta} e^{im\phi} \end{aligned} \right\} \quad (2.11)$$

Here P_{lm} is the associated Legendre function. For a non-rotating star the oscillation frequency σ is $(2L+1)$ -fold degenerate. Rotation causes this degeneracy to be lifted (Ledoux, 1951). To first order in Ω , the frequency corresponding to a nonradial mode (l, m) is

$$\sigma_{lm} = \sigma_{l0} + m\chi\Omega$$

where σ_{l0} is the frequency without rotation and χ is a constant depending on the mode and stellar structure. The observed frequency will differ from σ_{lm} because of rotation according to

$$\sigma_{obs} = \sigma_{lm} - m\Omega = \sigma_{l0} - m(1-\chi)\Omega. \quad (2.12)$$

The instantaneous radius at time t immediately follows from Equations 2.11 which give

$$R(t) = R_0 + \xi_r e^{i\sigma t}.$$

Substitution of this equation, together with Equations 2.9 and 2.10, into the quadrature (2.8) permits the observed flux originating from the nonradially distorted surface to be calculated as a function of time.

The radial component of the oscillation ξ_r dominates over the azimuthal and polar components, ξ_ϕ and ξ_θ , by a factor $a(R)/b(R) = k^{-1}$. This ratio is related to the pulsation constant Q (Ledoux, 1951) by

$$k = \frac{4\pi G\rho}{3\sigma^2} = \left(\frac{Q}{0.116}\right)^2 = \omega^{-2} \quad (2.13)$$

where $Q = P(\text{days})(\rho/\rho_\odot)^{1/2}$. Empirical values for the pulsation constant have been determined by Lesh and Aizenman (1974), Jones and Shobbrook (1974), Balona and Feast (1975) and Shobbrook (1978). These are in the range 0.025 to 0.037, giving values of k in the range 0.05 to 0.10. Thus, for the β Cephei stars, the radial component would contain most of the pulsation energy.

Each nonradial mode is characterised by two integers. These are the order l and the index m , where $-l \leq m \leq l$, of the associated Legendre function. Modes for which $|m| = l$ are referred to as *sectoral* modes, while those having $m = 0$ are termed *zonal* modes. Otherwise, ($0 < |m| < l$) the mode is known as a *tesseral* mode. Zonal modes correspond to standing waves which are axisymmetric with respect to the rotation axis and hence are also known as *stationary* modes. Modes for which $m > 0$ correspond to waves travelling in the direction opposite to rotation (retrograde), while those having $m < 0$ travel in the same direction as rotation (prograde). All stationary modes have polar antinodes whereas the travelling modes have polar nodes. The mode (l, m) has $l+1-|m|$ antinodes at θ values symmetrically placed about the equatorial plane. Thus modes with even $(l-|m|)$ have an antinode at the equator and exhibit geometric symmetry about the equatorial plane, whereas odd $(l-|m|)$ modes

have a node at the equator and possess equatorial antisymmetry. Pictorial representations of the surface distortions generated by the nonradial modes with $l \leq 3$ are shown in Figures A2.1(a-i) of Appendix 2.

2.3 THE LINE PROFILE VARIATIONS

The method adopted here to generate theoretical line profiles is similar to that initially utilised by Osaki (1971). The technique supposes that the variable line broadening originates solely from the Doppler shift due to the motion of the individual surface elements and disregards the details of atmospheric structure. In Section 5.5 it is shown that this approximation is valid providing hydrodynamic perturbations from uniform gas flow are sufficiently small that the velocity gradient in the absorbing region can be neglected. At atmospheric velocities in excess of the isothermal sound speed, which is typically $\sim 20 \text{ km s}^{-1}$, this assumption fails because shock discontinuities emerge. Under these conditions, profiles must be calculated using the surface solution to the radiative transfer equation taking into account the physical and dynamical structure of the atmosphere. This is done in Sections 5.5 and 6.2 for large amplitude radial pulsators. However, to proceed in the more complex case of nonradial motions, it will be assumed that velocity amplitudes are sufficiently small that these hydrodynamical complications can be disregarded.

The visible hemisphere of the star was partitioned into 2500 elements and for each of these a radial velocity was calculated by projecting onto the line-of-sight the velocity field resulting from pulsation and rotation. In Appendix 3 it is shown that this projected radial velocity is

$$v(\theta, \phi, t) = \{[\dot{\xi}_\phi + (R + \xi_r)\Omega \sin\theta] \sin\phi - [\dot{\xi}_r \sin\theta + \dot{\xi}_\theta \cos\theta] \cos\phi\} \sin i + \{\dot{\xi}_\theta \sin\theta - \dot{\xi}_r \cos\theta\} \cos i \quad (2.14)$$

where the astrophysical convention of negative velocities directed towards the observer is adhered to. It was assumed that each sector contributed an intrinsic line profile of the form $\exp - (\Delta\lambda/\Delta\lambda_0)^2$ where $\Delta\lambda_0 = \lambda_0 v_b/c$. The Doppler broadening velocity v_b is determined by the thermal and microturbulent velocities of the emitting atoms, and a constant value of 8 km s^{-1} was used. The profile generated by each sector was weighted according to its instantaneous projected area and limb darkening. A linear cosine darkening law of the form $I(\mu) = I_0(1 - u + u\mu)$ was assumed. A value of $u = 0.3$ was adopted after a comparison with the limb darkening data tabulated in Kurucz (1969), however the resulting line profiles are very insensitive to the value of u chosen. The line profile seen by a distant observer was formed by summing the profile from each surface element, at the appropriate Doppler displacement, into an array of velocity resolution $\pm \frac{1}{2} \text{ km s}^{-1}$. The effects of variations in intensity of the intrinsic profiles resulting from temperature changes induced by the pulsation were examined, but they were found to exert only a slight influence on the profile shape. Profiles generated by the method described above were calculated allowing for the distortion of the stellar surface due to pulsation and rotation, but, again, they differ only slightly from those predicted assuming spherical geometry. The resultant profiles for particular nonradial modes and their relevance to the spectral observations of the β Cephei stars are discussed in Chapter 5.

2.4 THE POLARIZATION VARIATIONS

2.4.1 *The Origin of the Polarization*

The high temperatures occurring in the atmosphere of an early B star

ensure almost total ionization of hydrogen and first ionization of helium at photospheric depths. The electron number density is therefore comparable to the ion number density and consequently electron scattering provides a major source of radiative opacity. Photons are Thomson scattered by free electrons according to Rayleigh's Law which states that the scattered light is partially plane polarized and that the plane of polarization is at right angles to the plane of scattering. For a scattering angle θ between the incident and scattered radiation, the intensities of the scattered light in directions parallel and perpendicular to the plane of scattering are in the ratio $\cos^2\theta : 1$.

Chandrasekhar (1946) considered the light emergent from a Rayleigh scattering atmosphere and showed that it was polarized. The amount of polarization is highly dependent on the angle between the surface normal and the line-of-sight. This is because as this angle increases, so does the anisotropy of the distribution of scattering angles. Chandrasekhar found that, for a pure scattering atmosphere, the radiation is partially plane polarized with the electric vector perpendicular to the meridian plane (i.e. parallel with the limb). However, a *net* polarization will only be detectable if the star is not spherically symmetric. Departures from spherical symmetry are commonly produced by rapid rotation or the tidal forces of a nearby companion. Alternatively, nonradial pulsations should generate an asymmetric scattering geometry which is capable of producing a net polarization. In this case there should be variations in the amount and orientation of the observed polarization associated with the changes in scattering geometry over the pulsation angle. The attempt of Schafgans and Tinbergen (1979) to detect variable polarization in β Cephei itself, and their request for some theoretical estimate of the expected amplitude of its variations, motivated the work described in Chapter 4. Polarization variations were calculated

by a numerical integration technique which is an extension of that discussed in Section 2.2.

2.4.2 *Calculating the Polarization*

Because both absorption and scattering are important in early B atmospheres, the amount of polarization will differ from that predicted by Chandrasekhar (1946) for a purely scattering atmosphere. The degree of polarization depends in a complex way on the absorption to scattering ratio, on its variation with depth and the wavelength of the radiation considered. In Chapter 4 the radiative transfer equation for the two states of polarization is solved numerically for some particular B star atmospheres. From such a solution the limb darkening ratios $I_l(\mu)/I_l(1)$ and $I_r(\mu)/I_r(1)$ can be determined. Changes in the degree of polarization of each surface element are controlled by the three factors, described in Section 2.2.2, which influence the light variations. An increase in temperature or projected area changes the luminosity of the element and hence alters its contribution to the total polarization. Locally, these two effects act oppositely since (adiabatic) expansion at fixed orientation decreases the temperature but increases the area. A change in orientation of the surface element also produces two opposing effects. An increase in the angle of emergence $\gamma = \arccos(\mu)$ increases the scattering angle and thus the local polarization, but decreases the projected area and its limb-darkened intensity.

To obtain the Stokes parameters of the light from the entire star, the parameters must be transformed from the local (l, r) reference plane (defined relative to the local meridian) into a co-ordinate system fixed to the apparent stellar disc. The observer's reference frame will be denoted by (l_0, r_0) , where l_0 is the projection of the rotation axis onto the plane of the sky. The angle ζ between the observer's axes and the local axes is derived in Appendix 4, where it is shown that

$$\cos \zeta = \{s^2 - [t \sin i + u \cos i]^2\}^{-\frac{1}{2}} \{u \sin i - t \cos i\} \quad (2.15)$$

where

$$s = \{R^2 \sin^2 \theta + \left(\frac{\partial R}{\partial \theta}\right)^2 \sin^2 \theta + \left(\frac{\partial R}{\partial \phi}\right)^2\}^{\frac{1}{2}}$$

$$t = R \sin^2 \theta \cos \phi - \frac{\partial R}{\partial \theta} \sin \theta \cos \theta \cos \phi + \frac{\partial R}{\partial \phi} \sin \phi$$

$$u = R \sin \theta \cos \theta + \frac{\partial R}{\partial \theta} \sin^2 \theta .$$

The Stokes parameters change under rotation from the local to the external frame according to

$$\begin{aligned} I_{l_0, r_0} &= \begin{pmatrix} I_{l_0} \\ I_{r_0} \\ U_{l_0, r_0} \\ V_{l_0, r_0} \end{pmatrix} = L(\zeta) I_{l, r} = \begin{pmatrix} \cos^2 \zeta & \sin^2 \zeta & \frac{1}{2} \sin 2\zeta & 0 \\ \sin^2 \zeta & \cos^2 \zeta & -\frac{1}{2} \sin 2\zeta & 0 \\ -\sin 2\zeta & \sin 2\zeta & \cos 2\zeta & 0 \\ 0 & 0 & 0 & 1 \end{pmatrix} \begin{pmatrix} I_l \\ I_r \\ 0 \\ 0 \end{pmatrix} \\ &= \begin{pmatrix} I_l \cos^2 \zeta + I_r \sin^2 \zeta \\ I_l \sin^2 \zeta + I_r \cos^2 \zeta \\ -I_l \sin 2\zeta + I_r \sin 2\zeta \\ 0 \end{pmatrix} \end{aligned} \quad (2.16)$$

Once the parameters for each surface element have been rotated into the common external reference frame using Equation 2.16, they can then be summed to form the Stokes parameters applicable to the integrated stellar flux. It can be immediately seen that the integrated light will have no component of circular polarization, but, depending on the geometry, may be partially plane polarized. The polarization resulting from nonradial motion is discussed in Chapter 4.

2.5 ACCURACY OF NUMERICAL TECHNIQUES

The number of sectors N into which the observed stellar disc is partitioned is important. While the error associated with approximating the double integral, defined in Equation 2.8, by discrete sums declines in inverse proportion to N , the computer run time increases proportionately.

The best approach is to decide upon some maximum tolerable error δ and choose a minimal N such that the error of the N -sector quadrature is less than δ . The highest quality photometric results obtained from observations of β Cephei stars have typical standard errors of $\sim 10^{-3}$ mag. Hence it is reasonable to require a numerical accuracy of better than 0.1%. For the simple case of a spherically symmetric star, for which an expression for the total flux is trivially derived, the number of sectors required to attain this accuracy was found to be small ($N > 500$). However it is likely that more sectors are required in the case of nonradial motions. Numerical calculations were made for a variety of nonradial test cases with N ranging from 10^2 to 10^5 . These showed that the change in the monochromatic fluxes as a function of N were less than $\delta = 0.1\%$ providing N was greater than 2000. As a result of these tests a value of $N = 2500$ was chosen. Following the publication by Dziembowski (1977) of an explicit expression for the light variations of a nonradial pulsator, it was possible to independently verify the numerical predictions. Comparison of the numerical and analytical results showed good agreement.

As stated in Section 2.3, line profiles were calculated to a velocity resolution of $\pm 0.5 \text{ km s}^{-1}$. Calculations made with N varying from 2500 to 22500 showed that, with the broadening parameters discussed earlier, line profiles were accurate to within 0.5% at any point on the profile for any N in this range. The adopted value of $N = 2500$ is comparable with the number of sectors used by Osaki (1971) but considerably less than the 17424 sectors used recently by Kubiak (1978). A large number of sectors was presumably required by Kubiak for his consideration of the case of an infinitely narrow intrinsic profile originating from each surface element. A broadened intrinsic profile permits a coarser grid to be utilised. As a check on the

numerical method of line profile synthesis, profiles were compared with those published by Osaki (1971). Good agreement resulted. Satisfactory profile comparisons were also made with some models of Smith (1977, private communication).

A limited check on the polarization calculations could be made by examining the recent results of Odell (1979). A calculation of the polarization amplitude for the (2,-2) mode seen at $i = 90^\circ$ was consistent with the value given by Odell for this model if we assumed a pure scattering atmosphere as he did.

2.6 ANALYTIC EXPRESSIONS FOR LIGHT AND VELOCITY VARIATIONS

In an important theoretical paper, Dziembowski (1977) derived analytically an explicit formula for the variations in luminosity and mean velocity of a nonradially pulsating star. Decomposing the flux variations into components resulting from changes in temperature and effective gravity,

$$\text{i.e.} \quad \frac{\Delta F_\lambda}{F_\lambda} = \frac{\partial \log F_\lambda}{\partial \log T} \cdot \frac{\Delta T}{T} + \frac{\partial \log F_\lambda}{\partial \log g} \cdot \frac{\Delta g}{g}$$

and using the assumptions discussed in Section 2.2.2, then Dziembowski's luminosity formula may be readily modified to give the variations in monochromatic or filter-convolved fluxes. This section outlines this modified formula and discusses its consequences.

A star pulsating in the nonradial (l, m) mode will undergo a surface displacement

$$\frac{\Delta R}{R}(\theta, \phi, t) = \epsilon P_{lm}(\cos \theta) \cos(\sigma t + m\phi)$$

in the linear approximation (i.e. $\epsilon \ll 1$). The resulting light curve, as observed at an inclination angle i , is given by

$$\begin{aligned} \Delta m_\lambda(t) = & -1.086[\epsilon P_{lm}(\cos i)] \{ [I_{1\lambda} + I_{2\lambda} - p_* C \frac{\partial \log F_\lambda}{\partial \log g} I_{3\lambda}] \cos(\sigma t) \\ & - \frac{\partial \log F_\lambda}{\partial \log T} B I_{3\lambda} \cos(\sigma t + \psi) \} . \end{aligned} \quad (2.17)$$

The *mean* radial velocity is

$$V_{\text{mean}}(t) = \sigma R [\epsilon P_{lm}(\cos i)] (I_{4\lambda} + k I_{5\lambda}) \sin(\sigma t) . \quad (2.18)$$

Here

$$\left. \begin{aligned} I_{1\lambda} &= \int_0^1 (\mu^2 - 1) \frac{dP_l}{d\mu} \cdot \frac{dh_\lambda}{d\mu} \mu d\mu \\ I_{2\lambda} &= \int_0^1 [2\mu P_l + (\mu^2 - 1) \frac{dP_l}{d\mu}] h_\lambda d\mu \\ I_{3\lambda} &= \int_0^1 P_l h_\lambda \mu d\mu \\ I_{4\lambda} &= \int_0^1 P_l h_\lambda \mu^2 d\mu \\ I_{5\lambda} &= \int_0^1 (1 - \mu^2) \mu \frac{dP_l}{d\mu} h_\lambda d\mu \\ C &= [4 + \omega^2 - l(l+1)\omega^{-2}] \\ \text{and } \omega^2 &= \sigma^2 R^3 / GM = 3\pi / G \rho_\odot Q^2 \end{aligned} \right\} \quad (2.19)$$

$h_\lambda(\mu)$ is the limb darkening function normalized such that

$$\int_0^1 h_\lambda(\mu) \mu d\mu = 1 .$$

Equation 2.17 is similar to that used by Buta and Smith (1979) in an analysis of the light variations of 53 Persei. The wavelength dependent integrals I_1 , I_2 and I_3 represent respectively the surface normal, surface area and effective temperature contributions to the light variations. The integrals I_4 and I_5 are reduction factors which take into account foreshortening, limb darkening and cancellation effects which diminish the mean velocity. An example of the integrals and flux derivatives at a number of wavelengths for a (25000, 3.6) atmosphere is given in Table 2.1.

Equation 2.18 must be used with caution. It gives the mean projected radial velocity, weighted according to limb darkening, and does not take into account the detailed line profile structure.

TABLE 2.1: Nonradial Integrals for $T_e = 25,000$ K

| | Wavelength (Å) | | | | |
|---|----------------|--------|--------|--------|--------|
| | 1000 | 2000 | 3000 | 4000 | 5000 |
| $\frac{\partial \log F_\lambda}{\partial \log T_e}$ | 4.57 | 3.37 | 3.16 | 2.21 | 2.06 |
| $\frac{\partial \log F_\lambda}{\partial \log g}$ | 0.07 | -0.04 | -0.04 | -0.01 | -0.02 |
| I_1 I_2 I_3 | $l = 0$ | | | | |
| | 0 | 0 | 0 | 0 | 0 |
| | 2 | 2 | 2 | 2 | 2 |
| | 1 | 1 | 1 | 1 | 1 |
| | $l = 1$ | | | | |
| | -0.606 | -0.406 | -0.266 | -0.246 | -0.200 |
| | 0.606 | 0.406 | 0.266 | 0.246 | 0.200 |
| | 0.732 | 0.709 | 0.694 | 0.691 | 0.686 |
| | $l = 2$ | | | | |
| | -0.926 | -0.598 | -0.381 | -0.341 | -0.276 |
| | -0.537 | -0.701 | -0.810 | -0.830 | -0.862 |
| | 0.366 | 0.325 | 0.298 | 0.293 | 0.284 |
| | $l = 3$ | | | | |
| | -0.497 | -0.279 | -0.159 | -0.120 | -0.095 |
| | -0.440 | -0.313 | -0.213 | -0.206 | -0.169 |
| | 0.094 | 0.059 | 0.037 | 0.033 | 0.025 |
| | $l = 4$ | | | | |
| | 0.105 | 0.118 | 0.094 | 0.109 | 0.091 |
| | 0.145 | 0.347 | 0.489 | 0.510 | 0.555 |
| | -0.014 | -0.026 | -0.032 | -0.034 | -0.036 |
| | $l = 5$ | | | | |
| | 0.192 | 0.139 | 0.085 | 0.077 | 0.060 |
| | 0.215 | 0.167 | 0.121 | 0.126 | 0.104 |
| | -0.014 | -0.011 | -0.007 | -0.007 | -0.006 |

The mean velocity given by Equation 2.18 will therefore differ from the radial velocity values determined by commonly used radial velocity measures, such as the line core velocity. The extent of these differences is considered in detail in Section 5.4 of this thesis. However, for the present, Equation 2.18 will be used to derive a crude estimate of the velocity amplitude, $2K$.

Equations 2.17 and 2.18 are valuable because they show that:

- (1) the light and mean velocity amplitudes observed at inclination angle i are proportional to $P_{lm}(\cos i)$,
- (2) the $2K_{\text{mean}}/\Delta m$ ratio is independent of amplitude ϵ and aspect, and
- (3) except for some multiplicative factor, the wavelength dependence of the light range is independent of both aspect and the index m of the nonradial mode.

These results were apparent from the numerical work, but only after many calculations. The other advantage of the analytic formulations is that, once the integrals (2.19) have been evaluated for the h_λ appropriate to a chosen stellar model, the light and velocity amplitudes for *any* ϵ , i , m or B can be easily calculated.

The geometric integrals (I_1, I_2) are simply related to the temperature integral (I_3), since

$$I_{1\lambda} + I_{2\lambda} = \int_0^1 \{(\mu^2 - 1) \frac{dP_\lambda}{d\mu} \frac{d}{d\mu} (h_\mu) + 2h_\mu P_\lambda\} d\mu .$$

Integrating the first term by parts, one obtains

$$I_{1\lambda} + I_{2\lambda} = [(\mu^2 - 1) \frac{dP_\lambda}{d\mu} h_\mu]_0^1 - \int_0^1 \frac{d}{d\mu} [(\mu^2 - 1) \frac{dP_\lambda}{d\mu}] h_\mu d\mu + 2 \int_0^1 h_\mu P_\lambda d\mu .$$

The first term is zero. The second term may be simplified using the Legendre equation:

$$(1 - \mu^2) \frac{d^2 P_\lambda}{d\mu^2} - 2\mu \frac{dP_\lambda}{d\mu} + \lambda(\lambda + 1) P_\lambda = 0$$

to give

$$I_{1\lambda} + I_{2\lambda} = [2 - l(l+1)] \int_0^1 P_l(\mu) h_\lambda(\mu) \mu d\mu = (2+l)(1-l) I_{3\lambda} . \quad (2.20)$$

Equation 2.17 may thus be rewritten as

$$\Delta m_\lambda(t) = 1.086 [\epsilon P_{lm}(\cos i)] I_l(\lambda) \{ [(2+l)(l-1) + p_* C \beta_\lambda] \cos(\sigma t) + \alpha_\lambda B \cos(\sigma t + \psi) \} \quad (2.21)$$

$$\left. \begin{array}{l} \text{where} \quad I_l(\lambda) = I_{3\lambda} = \int_0^1 P_l(\mu) h_\lambda(\mu) \mu d\mu \\ \text{and} \quad \alpha_\lambda = \frac{\partial \log F_\lambda}{\partial \log T} , \quad \beta_\lambda = \frac{\partial \log F_\lambda}{\partial \log g} . \end{array} \right\} \quad (2.22)$$

It is also possible to express the remaining integrals (2.19) in terms of $I_l(\lambda)$. This can be done using the recurrence relation

$$(l+1)P_{l+1}(\mu) - (2l+1)\mu P_l(\mu) + lP_{l-1}(\mu) = 0 .$$

$$\left. \begin{array}{l} \text{Thus} \quad I_{4\lambda} = \frac{1}{2l+1} [(l+1)I_{l+1}(\lambda) + lI_{l-1}(\lambda)] \\ \text{and} \quad I_{5\lambda} = \frac{l(l+1)}{2l+1} [I_{l-1}(\lambda) - I_{l+1}(\lambda)] . \end{array} \right\} \quad (2.23)$$

Hence only one integral (2.22) is required for a given equilibrium atmosphere, and the other integrals evaluated by Dziembowski (1977), Buta and Smith (1979) and Balona and Stobie (1979a) are redundant.

One factor which will be shown in Appendix 5 and Chapter 3 to have an important bearing on mode identification for the β Cephei stars is the relative contributions of geometric and temperature effects to the light variations. This ratio is also important for the δ Scuti stars since it determines the phase of the light variations relative to the radial velocity curve, which can be used as a mode identification diagnostic (Dziembowski, 1977). The ratio of geometric and pressure effects (varying as $\cos(\sigma t)$) to temperature effects (varying as $-\cos(\sigma t + \psi)$) is

$$R = \frac{(l+2)(l-1) + p_* C \beta_\lambda}{\alpha_\lambda B} . \quad (2.24)$$

Assuming $\psi \sim 0$, which is the case appropriate to the β Cephei stars, then it is clear that

- (1) for $l = 0$ geometric and temperature effects act oppositely,
- (2) for $l = 1$ geometric effects are absent and only changes in temperature and pressure contribute to the light variations,
- (3) for $l > 1$ geometric and temperature effects are in phase, and
- (4) for large l geometric effects dominate.

2.7 A BAADE-WESSELINK METHOD FOR NONRADIAL PULSATORS

Dziembowski (1977) and Balona and Stobie (1979a) have recently extended the Baade-Wesselink method to the case of nonradially pulsating stars. Balona and Stobie's generalisation is contingent on two assumptions: firstly that the surface brightness ΔS_λ is linearly related to some colour index $\Delta(m_1 - m_2)$, and secondly that the radial velocity variations can be corrected for limb-darkening and projection effects to give the geometric contribution to the light variations. In Section 5.4 it will be shown that the second assumption is only valid when the *centroid* of the line profile is used as the radial velocity indicator, as Balona and Stobie have recommended. In the following subsection it will be shown that the first assumption is invalid for modes more complex than dipole ($l > 1$).

2.7.1 *Relationship Between Surface Brightness and Colour*

Balona and Stobie (1979a) have defined the surface brightness as

$S_\lambda = -2.5 \log F_\lambda$. The observed luminosity per unit area is

$F_\lambda = L_\lambda/A$ where L_λ is the apparent stellar luminosity and A is the projected area of the photosphere. Since the light variation in

magnitudes is $m_V = -1.086 \frac{\Delta L_V}{L_V}$, then $\Delta S_V = -1.086(\Delta L_V/L_V - \Delta A/A)$ in the

linear regime. Balona and Stobie (1979a) have derived an expression for the projected surface area variations which is

$$\frac{\Delta A}{A} = 2(2p_l - q_l) \epsilon P_{lm}(\cos i) \cos(\sigma t). \quad (2.25)$$

The integrals p_l and q_l are defined by Balona and Stobie. It can easily be verified (see Appendix 5) that they satisfy

$$2p_l - q_l = P_l(0) = \begin{cases} (-1)^{l/2} \frac{l!}{2^l (l/2!)^2} & \text{for } l \text{ even} \\ 0 & \text{for } l \text{ odd} \end{cases}. \quad (2.26)$$

The surface brightness variations may then be written, using Equations 2.21 and 2.25, as

$$\Delta S_V = 1.086 \epsilon P_{lm}(\cos i) \{ [(2+l)(l-1) I_{lV} + p_* C \beta_V I_{lV} + 2P_l(0)] \cos(\sigma t) + B \alpha_V I_{lV} \cos(\sigma t + \psi_T) \} \quad (2.27)$$

where α_V, β_V are defined by Equation 2.22 and ψ_T is the phase of $\Delta T/T$ relative to $-\Delta R/R$. This expression is equivalent to that of Balona and Stobie (1979c), since their local flux term, at phase ψ_V relative to the radius variations, is related to the notation used here by

$$f_V \cos(\sigma t + \psi_V) \equiv -B \alpha_V \cos(\sigma t + \psi_T) - p_* C \beta_V \cos(\sigma t).$$

The colour variations are determined by subtracting Equation 2.21 at two different wavelengths, yielding

$$\Delta(B-V) = 1.086 \epsilon P_{lm}(\cos i) \{ [(2+l)(l-1) (I_{lB} - I_{lV}) + p_* C (\beta_B I_{lB} - \beta_V I_{lV})] \cos(\sigma t) + B (\alpha_B I_{lB} - \alpha_V I_{lV}) \cos(\sigma t + \psi_T) \} \quad (2.28)$$

ΔS_V and $\Delta(B-V)$ are in phase providing

$$\frac{[(2+l)(l-1) + p_* C \beta_V] I_{lV} + 2P_l(0)}{\alpha_V B I_{lV}} = \frac{(2+l)(l-1) (I_{lB} - I_{lV}) + p_* C (\beta_B I_{lB} - \beta_V I_{lV})}{B (\alpha_B I_{lB} - \alpha_V I_{lV})} \quad (2.29)$$

excluding the trivial cases $\psi_T = 0^\circ$ or 180° . Equation (2.29) may be rearranged to require that

$$2P_l(0) = \frac{I_{lV}I_{lB}}{\alpha_B I_{lB} - \alpha_V I_{lV}} \{ (2+l)(1-l)(\alpha_B - \alpha_V) + p_* C(\alpha_V \beta_B - \alpha_B \beta_V) \}. \quad (2.30)$$

In general Equation 2.30 does not hold because the coefficients α, β and integrals I_l take predetermined values independently of this constraint. Even for $l = 0$ and 1 , when Equation 2.30 reduces to the simple forms

$$\left. \begin{aligned} 2P_0(0) &= 2 = 2 - p_* C \frac{\alpha_V \beta_B - \alpha_B \beta_V}{\alpha_B - \alpha_V} & (l = 0) \\ 2P_1(0) &= 0 = p_* C \frac{I_{1V}I_{1B}(\alpha_V \beta_B - \alpha_B \beta_V)}{\alpha_B I_{1B} - \alpha_V I_{1V}} & (l = 1), \end{aligned} \right\} \quad (2.31)$$

it is seen that the equality will fail if the influence of pressure effects (through the coefficients β) is significant. The result that gravity effects can cause the surface brightness to become a multi-valued function of colour, so that phases of equal colour are *not* phases of equal surface brightness, has been noted previously (e.g. Breger, 1975; Evans, 1976). When gravity effects are small, or alternatively when a gravity-corrected colour index is utilised, then $\beta_B \sim \beta_V \sim 0$. In this case it can be seen that Equations 2.31 are then satisfied and the Wesselink assumption of a single-valued relation between surface brightness and colour is valid for $l = 0$ and 1 . Neglecting the effective gravity contributions, then Equation 2.30 reduces to

$$2P_l(0) = (2+l)(1-l) \frac{I_{lB}I_{lV}(\alpha_B - \alpha_V)}{\alpha_B I_{lB} - \alpha_V I_{lV}}. \quad (2.32)$$

The important conclusion from this equation is that, although it holds for $l = 0$ and 1 , it fails for $l > 1$ even though the effective gravity changes have been neglected. If the wavelength dependence of I_l is also neglected, then $I_{lB} = I_{lV}$ and Equation 2.32 becomes

$$2P_l(0) = (2+l)(1-l)I_l. \quad (2.33)$$

However this condition (2.33) *still fails* for $l > 1$, despite the

disappearance of the temperature coefficients α . This can be seen from Table 2.2 where the left and right hand sides of Equation 2.33 are tabulated for $l \leq 5$. Thus it is clear that the modified Baade-Wesselink method formulated by Balona and Stobie (1979a) is not strictly valid for $l > 1$. Furthermore, the theoretical estimates of the phase shift between light and colour for nonradial pulsators, which were evaluated assuming $\Delta S_V \propto \Delta(B-V)$ by Balona and Stobie (1979c, 1980) and Kurtz (1980), are also in error for $l > 1$. This point is investigated further in Appendix 5.

2.7.2 A Corrected Nonradial Baade-Wesselink Formulation

The Baade-Wesselink method can be extended to the nonradial case by applying Balona and Stobie's (1979a) method to the explicit form of the colour variations (Equation 2.28). The light and colour variations are

$$\Delta V = 1.086 \epsilon P_{lm}(\cos i) I_{lV} \{ [(2+l)(l-1) + p_* C \beta_V] \cos(\sigma t) + B \alpha_V \cos(\sigma t + \psi_T) \} \quad (2.34)$$

TABLE 2.2: Left and Right Hand Sides of Equation 2.33

| l | $2P_l(0)$ | $(2+l)(1-l)I_l(\text{EDD})$ |
|-----|-----------|-----------------------------|
| 0 | 2 | 2 |
| 1 | 0 | 0 |
| 2 | -1 | -1.300 |
| 3 | 0 | -0.626 |
| 4 | 0.75 | 0.374 |
| 5 | 0 | 0.219 |

$$\text{and } \Delta(B-V) = 1.086 \epsilon P_{lm}(\cos i) \{ [(2+l)(l-1)(I_{lB} - I_{lV}) + p_* C(\beta_B I_{lB} - \beta_V I_{lV})] \cos(\sigma t) \\ + B(\alpha_B I_{lB} - \alpha_V I_{lV}) \cos(\sigma t + \psi_T) \}. \quad (2.35)$$

Solving for $\cos(\sigma t + \psi_T)$ from Equation 2.35 and substituting into Equation 2.34 gives

$$\Delta V = \left(\frac{\alpha_V I_{lV}}{\alpha_B I_{lB} - \alpha_V I_{lV}} \right) \Delta(B-V) + 1.086 \epsilon P_{lm}(\cos i) \cos \sigma t \cdot \frac{I_{lB} I_{lV}}{\alpha_B I_{lB} - \alpha_V I_{lV}} \cdot \\ \{ (2+l)(1-l)(\alpha_V - \alpha_B) - p_* C(\alpha_V \beta_B - \alpha_B \beta_V) \}. \quad (2.36)$$

Integrating the mean velocity curve (2.18) produces

$$\epsilon P_{lm}(\cos i) \cos \sigma t = - \frac{1}{R} \frac{1}{I_4 + k I_5} \int V_{\text{mean}} dt \quad (2.37)$$

Substituting Equation 2.37 into 2.36 yields

$$\Delta V(t) = a_l \Delta(B-V)(t) + b_l \int V_{\text{mean}} dt / R \quad (2.38)$$

where

$$a_l = \frac{\alpha_V I_{lV}}{\alpha_B I_{lB} - \alpha_V I_{lV}}$$

$$\text{and } b_l = \frac{1.086}{I_4 + k I_5} \frac{I_{lB} I_{lV}}{\alpha_B I_{lB} - \alpha_V I_{lV}} [(2+l)(1-l)(\alpha_B - \alpha_V) - p_* C(\alpha_B \beta_V - \alpha_V \beta_B)].$$

This result differs from that of Balona and Stobie (1979a) in that the colour coefficient a_l has been derived explicitly and the geometric coefficient b_l incorporates colour and pressure correction factors. Table 2.3 displays *approximate* values of the coefficients derived from the model atmospheres of Kurucz (1979) at $T_e = 25000K$. The values of a_l and b_l for $l \leq 5$ are tabulated for two colour indices, $\Delta(1500-5000)$ and Stromgren $\Delta(u - y)$. A coefficient b'_l is also tabulated which corresponds to the coefficient b_l with the effective gravity term neglected. The coefficients b_l and b'_l may be compared with the corresponding values derived by Balona and Stobie (1979a), which are also indicated in the table. It can be seen that the principal difference

of the b_l from the Balona and Stobie coefficients is that the values are no longer zero for odd $l > 1$. It is also apparent that effective gravity changes are important for low l but decrease in significance as l increases (as required by Equation 2.24). Finally it is clear that the dependence of the coefficients a_l and b_l on wavelength, and on the uncertain model atmosphere parameters $\alpha_\lambda, \beta_\lambda$ and h_λ , reduce their effectiveness for mode identification. These considerations are elaborated upon in Appendix 5.

TABLE 2.3: Baade-Wesselink Coefficients ($T_e = 25000K$)

| l | $\Delta(1500-5000)$ | | | $\Delta(u - y)$ | | | Balona & Stobie |
|-----|---------------------|-------|--------|-----------------|-------|--------|-----------------------|
| | a_l | b_l | b'_l | a_l | b_l | b'_l | $b_l = 1.086 \beta_l$ |
| 0 | 1.1 | 5.1 | 3.0 | 1.9 | 2.1 | 3.0 | 3.0 |
| 1 | 1.0 | 1.6 | 0 | 1.9 | -1.0 | 0 | 0 |
| 2 | 0.7 | -2.3 | -3.1 | 1.8 | -4.2 | -3.6 | -2.8 |
| 3 | 0.2 | -1.2 | -1.3 | 1.1 | -1.6 | -1.5 | 0 |
| 4 | 12.4 | 140 | 151 | 2.3 | 27 | 26 | 23 |
| 5 | 0.3 | -20 | -21 | 1.4 | -24 | -23 | 0 |

C H A P T E R T H R E E

THE LIGHT VARIATIONS

3.1 INTRODUCTION

In this chapter the observational distinctions that can be made between stars undergoing radial and nonradial oscillations are considered on the basis of existing light and radial velocity information. A number of authors, notably Watson (1971b), Kubiak (1972) and Beeckmans and Burger (1977), have discussed the consistency of their observational data with a radial pulsation hypothesis. However nonradial models have, until recently, been generally neglected in the interpretation of photometric data. Obviously nonradial possibilities cannot be eliminated until the observational properties that distinguish between different modes have been identified. Recent investigations into the problem of mode identification using photometric indices have been undertaken by Stamford and Watson (1977, 1978a, 1980a), Buta and Smith (1979), Smith and Buta (1979), Smith, Africano and Worden (1979) and Balona and Stobie (1979a,c).

The fact that the temperature distribution over the surface of a radially pulsating star is uniform, while for a nonradial pulsator there is a pattern of hot and cool zones, suggests that a distinction might be possible on the basis of the colour variations displayed by the star. In addition, for a nonradial pulsator, regions of the star are expanding towards the observer while simultaneously other regions are contracting inward. It is thus possible to conjecture that nonradial motions might be less efficient in producing radial velocity variations than are radial motions. Leung (1968) noted that the ratio of the visual light amplitude ΔV to the radial velocity amplitude $2K$ was considerably less for the β Cephei stars than for other variable stars commonly presumed to undergo radial oscillations. He suggested that this indicated that the β Cephei stars were nonradial pulsators. However Watson (1971b) argued that the small visual light amplitudes of these stars were simply a consequence

of their higher temperatures, and demonstrated that the ratio of the total change in bolometric flux to the radial surface amplitude was comparable to the value derived for other types of variables. Recent ultraviolet observations of various β Cephei stars by orbiting satellites have confirmed that most of the light variations *are* occurring at wavelengths shorter than the visual. This observation provides an important key to the problem of mode discrimination. For if the light variations are caused primarily by changes in the geometric configuration of the pulsating star, the wavelength dependence of the light amplitude will be fairly small. However, if temperature changes dominate, the amplitude will depend very strongly on the wavelength. Since the ratio of temperature to geometric contributions to the light variation depends on the mode order l (see Equation 2.21), it is plausible that the wavelength dependence of the light amplitude, $\Delta m(\lambda)$ could assist in identifying the pulsation mode. The object of this chapter is to demonstrate that there are indeed considerable differences between $\Delta m(\lambda)$ resulting from different modes which can be exploited for the purpose of mode assignment.

Section 3.2 considers the extensive light, colour and radial velocity data that has been assembled in the literature. The *ranges* of these quantities are assumed to be the relevant values here since variations are approximately sinusoidal except for the extreme cases of BW Vul, σ Sco and 12 Lac. As satellite observations have not yet been obtained for many β Cephei stars, mode identification using visual indices will be attempted in Section 3.3. However the use of satellite ultraviolet data will be shown in Section 3.3 to provide a much more useful mode-typing diagnostic. Finally, in Section 3.4, it will be demonstrated that when there are high quality light amplitudes distributed over a long baseline in wavelength then pulsation modes can be confidently assigned to individual stars.

3.2 LIGHT, COLOUR AND RADIAL VELOCITY DATA

Table 3.1 lists light, colour and radial velocity ranges obtained from published data on well-studied β Cephei stars. $\Delta(U-B)$ colour data are listed since changes in $(B-V)$ are small and poorly determined. This data and the discussion on it follows, with some changes, that of Stamford and Watson (1977). Since it was the intention to compare these data firstly with the predictions of a radially oscillating model, several considerations were borne in mind in selecting data for inclusion in the table. These are discussed here.

Those stars which show only a small variability in the ranges of their light and velocity curves presented no problem. Light and radial velocity data obtained at different times could be used. The stars γ Peg, δ Cet and ξ^1 CMa were considered in this category. The large amplitude variable BW Vul is also singly periodic, showing only small irregular cycle-to-cycle changes. Unfortunately, the situation is complicated in this star by the existence of an apparent long-term increase in $2K$, as discussed by Goldberg, Walker and Odgers (1976), a major part of which is due to improvements in instrumentation. The entry in Table 3.1 came from the recent high-quality observations of these workers.

For stars which do show significant variability in their light and radial velocity curves it is necessary to have sufficient data to be able to average over the variability and list mean ranges in Table 3.1. If there is any hope of a radial model applying to these stars, one might suspect that it applies to the mean ranges. In this case, one would presumably envisage a basically radial pulsation with modulations produced in its light and radial velocity curves by some other effect, such as a nearby companion or an additional mode. The $[\Delta V, \Delta U]$ data used here were selected using the criterion that at least three nights of observations were available and, for stars with a variable light amplitude, that the

TABLE 3.1: Light, colour and radial velocity ranges

| <i>Star</i> | ΔV | $\Delta(U-B)$ | ΔU | $\Delta(1500)$ | 2K | <i>References</i> |
|---------------|----------------------|---------------|------------|----------------|------|---|
| γ Peg | 0.013 | 0.011 | 0.024 | 0.052 | 7 | Sareyan, Le Contel & Valtier (1976), McNamara* (1955), Campos & Smith* (1980), L76# |
| δ Cet | 0.025 | 0.019 | 0.044 | 0.085 | 12.5 | Jerzykiewicz (1970), Watson(1971b), McNamara* (1955), Campos & Smith* (1980), L76# |
| ν Eri | P ₂ 0.070 | | | | 29 | Van Hoof (1961a,b*)† |
| | P ₁ 0.040 | | | | 17 | |
| β CMa | 0.023 | 0.011 | | | | Van Hoof(1963), Watson(1971b), Shobbrook*(1973a), BB# |
| | P ₂ 0.021 | | | 0.036 | 7.5 | |
| | P ₁ 0.004 | | | 0.020 | 11 | |
| ξ^1 CMa | 0.036 | 0.027 | 0.070 | 0.143 | 34 | Watson(1971b), McNamara* (1955), BB#, LW# |
| 15 CMa | 0.016 | | | | 6.5 | Van Hoof(1965), Shobbrook* (1973b) |
| β Cru | 0.019 | 0.0024 | 0.022 | | 5 | Van Hoof(1962), Watson(1971b), Page1*(1956), Milone*(1963) |
| α Vir | 0.014 | 0.0030 | 0.017 | | | Shobbrook, Lomb & Herbison- |
| | 0.029 | | | | 16 | Evans*(1972) |
| τ^1 Lup | 0.030 | | | | 10.5 | Van Hoof, Pretorius & Pikoos (1964), Page1*(1956) |
| σ Sco | P ₂ 0.040 | 0.030 | 0.075 | 0.45 | 110 | Van Hoof(1966), Struve, McNamara & Zebergs*(1955), Campos & Smith* (1980), BB# |
| | P ₁ 0.021 | 0.001 | 0.022 | | 15 | |
| θ Oph | 0.021 | 0.012 | 0.033 | 0.06 | 12 | Watson(1971b), Van Hoof & Blaauw*(1958), L76# |
| λ Sco | 0.025 | 0.010 | 0.037 | 0.08 | 20 | Lomb & Shobbrook*(1975), BB#, L76# |
| BW Vul | 0.19 | 0.15 | 0.34 | 0.66 | 260 | Walker‡(1954), Kubiak‡(1972) Goldberg <i>et al</i> *(1976), L78# |
| β Cep | 0.036 | | | 0.14 | 25 | Gray(1970), Struve <i>et al</i> * §(1953), BB#, HH# |
| 12 Lac | P ₂ 0.078 | | | 0.13 | 37.5 | Sato(1973), Jerzykiewicz(1978) |
| | P ₁ 0.029 | | | | 17.5 | Struve & Zebergs*(1955), BB# |
| 16 Lac | 0.048 | | | 0.10 | 28.5 | Walker*(1952), BB# |
| HR 6684 | 0.026 | | | 0.12 | 18 | Morton & Hansen(1974), Bolton <i>et al</i> * (1975), BB# |
| α Lup | 0.025 | | | 0.07 | 16 | Van Hoof(1964), Breger* (1967), L78# |

Notes to Table 3.1:

*Indicates source of 2K data.

†The P_0 and P_{02} data of Van Hoof are listed. The values are dependent on Van Hoof's procedure for analysis of his data. Not all of the modes assumed to be present by Van Hoof are likely to be real. Struve *et al.* (1952) gave $2K_2 = 49$ cm/s and $2K_1 = 22$ km/s, suggesting substantially larger oscillations than in Van Hoof's analysis. Light and colour data are likely to have been similarly affected. The data for this star are thus particularly uncertain.

‡Amplitudes transformed to $\Delta(U-B)$ and ΔV using filter effective wavelengths.

§Data prior to 1950 give larger 2K values around 35 km/s. Hutchings & Hill (1977) and Campos & Smith (1980) have obtained 2K values of 45 km/s for this star.

#Indicates source of satellite ultraviolet data according to the code:

BB Beeckmans & Burger (1977)

HH Hutchings & Hill (1977)

L76 Lesh (1976)

L78 Lesh (1978)

LW Lesh and Wesselius (1979)

The $\Delta(1500)$ amplitude was found by interpolating in wavelength amongst the satellite ultraviolet amplitudes tabulated in the cited reference.

ΔV and ΔU data be simultaneous. With these conditions, adequate ΔU were obtained for only eight stars: γ Peg, δ Cet, ξ^1 CMa, λ Sco, BW Vul, β Cru, α Vir and σ Sco. The otherwise suitable data of Sato (1973) for 12 Lac were rejected because significant amplitudes were assigned by him to periods which were not subsequently confirmed by the analysis of Jerzykiewicz (1978). More difficulty was encountered in finding simultaneous light and radial velocity data. For the $[\Delta V, 2K]$ data it was assumed that an average ΔV and an average 2K obtained from many non-simultaneous observations would give a $[\Delta V, 2K]$ set approximating that which would be obtained for many simultaneous observations. If the individual ΔV and 2K data points are spread over similar epochs this is reasonable. However, significant uncertainty remains if there is a long-term trend in the ΔV and 2K data and the epochs of observations do not overlap. A case in point is β CMa, as discussed by Shobbrook (1973a). In general, modulation effects on timescales of a few weeks and less should be reasonably well averaged out in the data listed in Table 3.1. Four stars, β CMa, σ Sco, ν Eri and 12 Lac, were sufficiently well observed that data can be presented separately for the two principal periodicities present. These are listed using the (P_1, P_2) notation of Struve (1955). Thus P_2 represents the period associated with the line broadening. The P_1 data should be viewed with caution since it is likely that the interpretation of the data as simply due to interference of two close periods is incorrect in some cases.

Except for BW Vul, sources of light and colour data for Table 3.1 were in the UBV system, or systems, such as that of Watson (1971b), which have effective wavelengths sufficiently similar to make little difference to amplitude data. The only inconvenience was that some observations were in U and B only, and others in U and V only. Where necessary, the conversion $\Delta(U-B) = 0.85\Delta(U-V)$ was performed. This conversion was suggested by theoretical model atmospheres, as discussed by Watson (1971b), and is consistent with the observations of β Cephei stars.

Similarly, in converting an observed ΔB to a ΔV , it was assumed that $\Delta V = \Delta B - 0.15\Delta(U-B)$. If U, B and V data were all available, an average colour range $0.5[\Delta(U-B)+0.85\Delta(U-V)]$ was formed. The ranges listed in Table 3.1 were based either on values given directly by the authors of the references cited, or on averages of data for individual oscillation cycles given in these references. If two references are cited, a weighted average of the results is listed. The $[\Delta V, 2K]$ data are plotted in Figure 3.1. Error bars are shown in this figure (and Figures 3.2 and 3.3) to assist in the data evaluation. Standard deviations are not given in many of the original data sources. In these cases a somewhat subjective assessment of probable errors was made, bearing in mind the uncertainties produced by variable amplitudes.

The data plotted in Figure 3.1 shows clearly the general trend for larger radial velocity ranges with increased light range. This trend is well known and was examined most recently by Leung (1968). A linear fit to observed data suggested that $2K/\Delta V = 480 \pm 120$ s.e. $\text{km s}^{-1} \text{mag}^{-1}$ was applicable to many β Cephei stars, however it is clear from the data plotted here that a unique linear relation is by no means adequate to explain all of the observations. There is a sharp lower cutoff to the plotted data at $2K/\Delta V \sim 300 \text{ km s}^{-1} \text{mag}^{-1}$.

3.3 COMPARISON OF PULSATION MODELS WITH OBSERVATIONAL DATA

3.3.1 *Constraints on B*

Stamford and Watson (1977) compared the data contained in Table 3.1 with theoretical models in the $[\Delta(U-B)/\Delta V, 2K/\Delta V]$ plane. The ratios of the relevant quantities were taken to remove the amplitude and aspect dependence. However this approach suffered from two deficiencies. Firstly the colour baseline needs to be as long as possible to minimise observational and theoretical errors. For this reason a $\Delta(U-V)$ index is slightly preferable to a $\Delta(U-B)$ index, for example. Secondly the

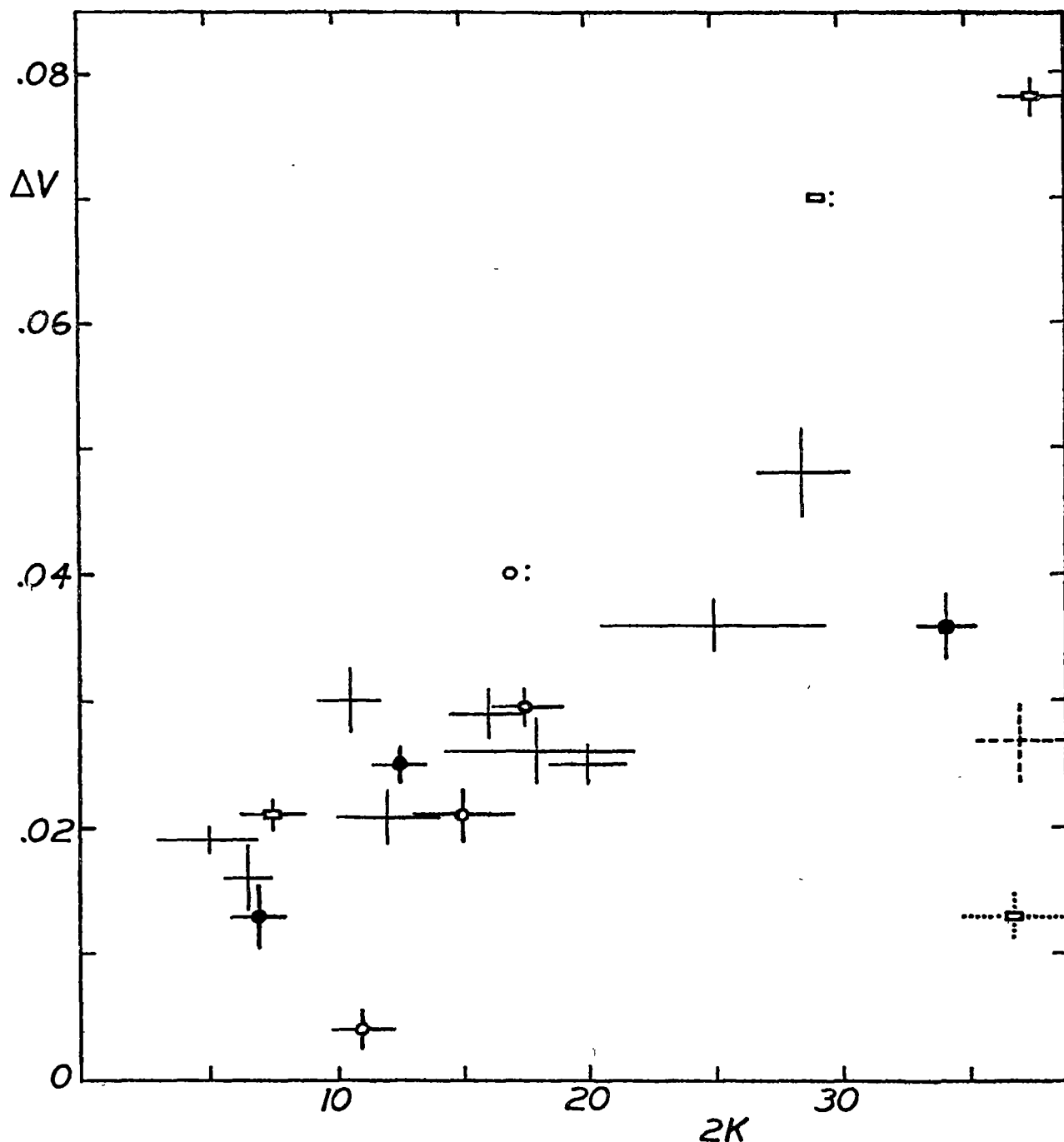


Figure 3.1 Observed light ranges (magnitudes) and radial velocity ranges (km s^{-1}) for the β Cephei stars listed in Table 3.1. Filled circles denote singly periodic objects with small light-range modulation. Objects with significant light-range variability are denoted by unmarked error bars. Those objects for which the data for the two principal periodicities are presented are denoted by open squares (P_2) and open circles (P_1). Colons distinguish the data for ν Eri, which may be substantially in error. Dashed lines indicate the light and velocity data for BW Vul, both of which are reduced by a factor of 7. Dotted lines correspond to the data for σ Sco (P_2) reduced by a factor of 3.

temperature parameter $B = (\Delta T/T)/(\Delta R/R)$ was fixed at the adiabatic value given by Equation 2.5. It is shown later in this section that the data is most consistent with values of B which are somewhat less than the adiabatic estimate, and consequently, in the following improved analysis, B is permitted to vary freely for a given nonradial order l . However some restriction on the possible values which can be attained by B is implied by the observed phase relation between the light and velocity curves for the β Cephei stars. Available data at all wavelengths indicate that maximum light occurs very near to the epoch of zero phase on the descending branch of the velocity curve (i.e. at minimum radius using a radial interpretation). From Equations 2.17 and 2.18 one obtains, in the case where $\psi \sim 0$

$$\left. \begin{aligned} V_{\text{mean}}(t) &\propto (I_4 + kI_5)\sin(\sigma t) \\ \Delta m(t) &\propto I_3[(l^2 + l - 2) + f]\cos(\sigma t) \end{aligned} \right\} (3.1)$$

where the constants of proportionality are positive and $f \sim \alpha B$,
 $\alpha = \frac{\partial \log F_\lambda}{\partial \log T_e}$. The adiabatic phase relationship between temperature and radius variations has been assumed here since the nonadiabatic analysis of Davey (1970) indicates that departures from this are small, as discussed later in this section. Equations 3.1 have the correct relative phase for observations of $V_{\text{mean}}(t)$ and $\Delta m(t)$ providing

$$\text{sign}\{I_4(l) + kI_5(l)\} = \text{sign}\{I_3(l)[l^2 + l - 2 + f]\}$$

which imposes the following loose constraints on B :

$$\left. \begin{aligned} B > 1 \quad (l = 0), \quad B > 0 \quad (l = 1), \quad B > -1.0 \quad (l = 2) \\ B > -2.5 \quad (l = 3), \quad B < -8.7 \quad (l = 4), \quad B > -7.0 \quad (l = 5) \end{aligned} \right\} (3.2)$$

It can be easily shown using the asymptotic expression for I_4 and I_5 given by Dziembowski (1977) that for large even l

$$\text{sign}\{I_4 + kI_5\} = -\text{sign}\{I_3\}.$$

Thus for even $l \geq 4$ we have $B < 1 - l(l+1)/2 < -9$, whereas for $l < \omega^2 \sim 20$ the adiabatic value of $B = (1 - \Gamma_2^{-1})(4 + \omega^2 - l(l+1)/\omega^2) > 0$. Hence the unreasonable values of B required by modes possessing large even l effectively eliminates these modes from contention. Large l odd modes are rejected later using $2K/\Delta V$ considerations.

3.3.2 *Ground-Based Data*

In preference to the $\Delta V/\Delta(U-B)$ ratio used by Stamford and Watson (1977), $\Delta U/\Delta V$ is adopted here as an index of the wavelength dependence of the light amplitude. A comparison of the data with model loci will now be undertaken in the $[2K/\Delta V, \Delta U/\Delta V]$ plane. The $2K/\Delta V$ ratio was formed from Equations 2.17 and 2.18 assuming a constant ratio of radius to period of $R/P = 350 \text{ km s}^{-1}$. This value is consistent with the estimated radii of Lesh and Aizenmann (1974). The observed trend of M_V and P along the β Cephei strip is such that this ratio remains fairly constant. In any case the theoretical $2K$ value is subject to the uncertainties discussed later in Section 3.3.3 and can be regarded as no more than an estimate. The major theoretical uncertainty in the calculation of the light amplitudes is the formation of values of α_U and α_V from the filter-convolved fluxes of Kurucz, Peytremann and Avrett (1974). Slight changes in these values were found to produce quite large changes in the $\Delta U/\Delta V$ ratio. Figure 3.2 shows the data and model loci for varying B in the $[2K/\Delta V, \Delta U/\Delta V]$ plane. The dotted lines bracketing the radial curve indicate the region of uncertainty due to the flux derivatives, but does not take into account the unreliability of the $2K$ -formula. Similar error zones apply to the calculations for the other modes although these are not marked on the figure. The loci are calculated for a $T_e = 25000 \text{ K}$ model atmosphere, but the shift in the model curves due to altering the effective temperature by $\pm 5000 \text{ K}$ lies within the error zones.

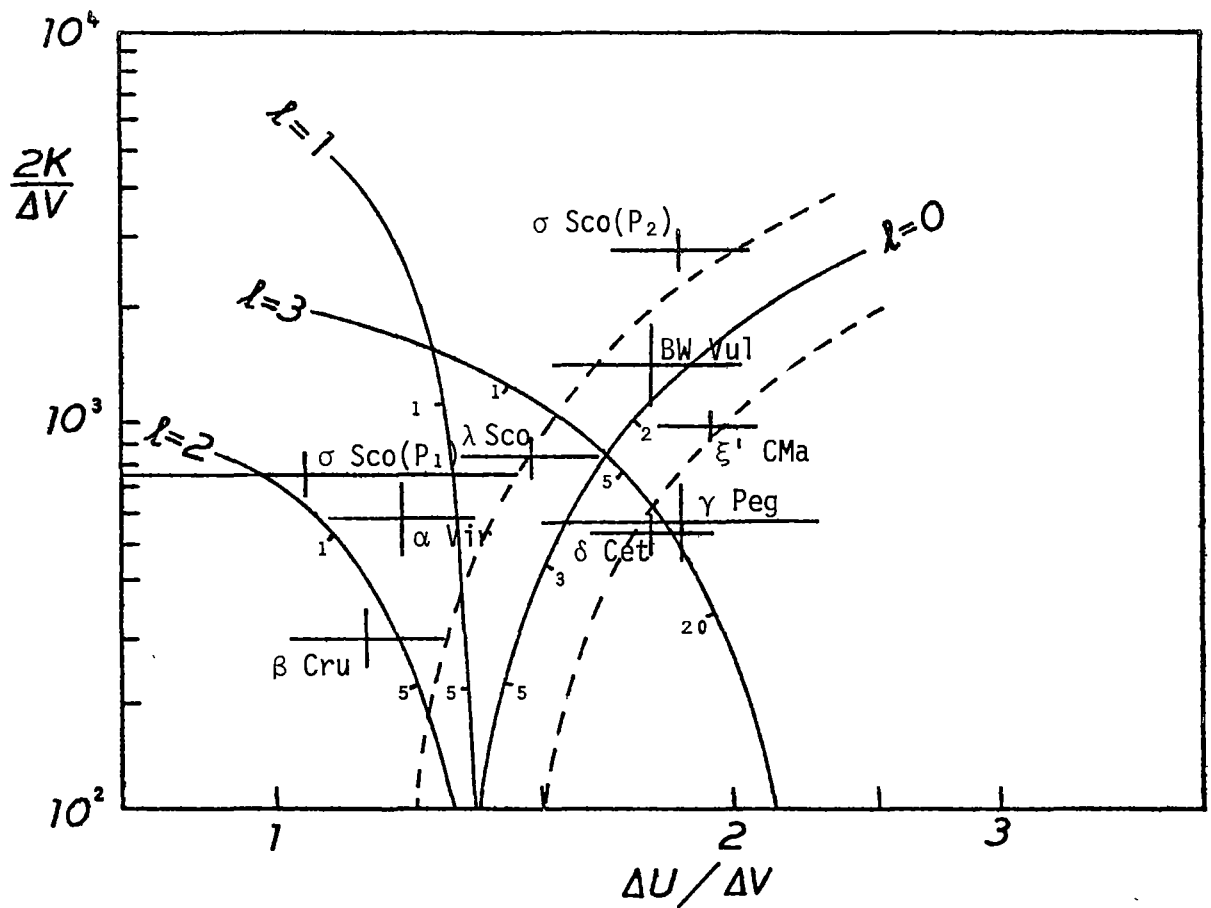


Figure 3.2 Observed data for 8 stars compared with radial and nonradial model loci in the $[2K/\Delta V, \Delta U/\Delta V]$ plane. Each full curve represents the locus of varying B , the ratio of local fractional temperature to radius range, under the assumption that these variations are π out of phase. Some B values are indicated. The dotted lines bracketing the $l = 0$ curve indicate the approximate limits of uncertainty attached to each model curve.

It can be seen immediately from Figure 3.2 that there is a large scatter associated with the data, spread over a magnitude in $2K/\Delta V$ and a factor of two in $\Delta U/\Delta V$. Despite the confused appearance and large observational and theoretical uncertainties, three conclusions emerge from this figure. The first result is that one mode cannot adequately explain all of the data. Data points having large $\Delta U/\Delta V$ and $2K/\Delta V$ ratios, such as σ Sco(P_2), BW Vul and ξ^1 CMa, are most consistent with a radial hypothesis, while data with low $\Delta U/\Delta V$ ratios, such as σ Sco(P_1) and β Cru, are in best accord with a quadrupole oscillation. The central group of data is ambiguously placed with $l = 0, 1$ and 3 modes all possible. The second conclusion is that the $l = 5$ mode (and higher modes) can be rejected on the basis of the $2K/\Delta V$ data. This is because for all B satisfying Condition 3.2 for $l = 5$ it is found that $2K/\Delta V < 120 \text{ km s}^{-1} \text{ mag}^{-1}$, while the observed data is bounded below by $2K/\Delta V \sim 270 \text{ km s}^{-1} \text{ mag}^{-1}$ and the observed mean is $\sim 500 \text{ km s}^{-1} \text{ mag}^{-1}$. Even allowing for generous errors in the calculated $2K$ vis-a-vis the observed $2K$ (as discussed in Section 3.3.3), modes with $l \geq 5$ are clearly unacceptable. The declining $2K/\Delta V$ ratio with l arises from the result, noted by Dziembowski (1977), that even for the most favourable inclination, the projected mean velocity is less than one tenth of the maximum surface velocity when $l \geq 4$. Consequently large surface amplitudes are required to produce very small velocity variations for high order modes. The third result that follows from Figure 3.2 is that values of B are smaller than the adiabatic value by a factor of 2 to 4, irrespective of which mode is present.

Following Stamford and Watson (1977), Balona and Stobie (1979c) have also compared the visual photometric data on a number of β Cephei stars with radial and quadrupole predictions. Their approach was to derive a value of $f_V = \alpha_V B$ from the $2K/\Delta V$ ratio, which was then used to evaluate a $\Delta V/\Delta(U-B)$ ratio. The $\Delta V/\Delta(U-B)$ value was subsequently

compared with the appropriate observed value. This method is unfortunately dogged by the uncertainties of the $2K$ values, described in Sections 3.3.3 and 5.4, particularly for the nonradial oscillations. Notwithstanding this, their conclusions are generally in agreement with the results presented here. In particular, Balona and Stobie obtain values of f_V in the range 4 to 6 for the radial case, implying B values of 2 to 3 which is in agreement with the present results.

3.3.3 *Satellite Ultraviolet Data*

The acquisition of photometric observations in the far ultraviolet by orbiting satellites has considerably increased the wavelength baseline of the light amplitude $\Delta m(\lambda)$. The satellite observations tabulated by Beeckmans and Burger (1977), Hutchings and Hill (1977), Lesh (1976, 1978) and Lesh and Wesselius (1979) contain adequate data for eleven stars over a considerable wavelength range. Eight of these stars (γ Peg, δ Cet, ξ^1 CMa, α Lup, λ Sco, HR 6684, BW Vul, β Cep) are singly periodic and three are multi-periodic (σ Sco, β CMa, 12 Lac). For data on multi-periodic stars to be adequate, sufficient information must exist at each wavelength to enable the light range for a particular mode to be extracted. The data of Beeckmans and Burger (1977) permitted a confident treatment of the line-broadening mode of σ Sco and β CMa and was sufficient to place reasonable error estimates on the satellite ultraviolet range of the line-broadening mode of 12 Lac. The full wavelength dependence of these data is treated in Section 3.4. However here, by analogy with the treatment of the visual data, an index $\Delta(1500)/\Delta(5000)$ can be formed which gives a measure of the slope $\Delta m(\lambda)$. Similarly the light and velocity data can be compared with the theoretical predictions for each mode in the $[2K/\Delta V, \Delta(1500)/\Delta(5000)]$ plane. This is shown in Figures 3.3 a-d for modes $l \leq 3$. Higher order modes need not be considered for the reasons discussed earlier

in Section 3.3.2. The data varies in $\Delta(1500)/\Delta(5000)$ index over a factor of 7 compared with a variation of a factor of 2 in $\Delta U/\Delta V$.

The major theoretical uncertainty in Figures 3.2 and 3.3 is the use of Equation 2.18 for the mean velocity to derive a value for $2K$. This is because Equation 2.18 is independent of rotation which has a considerable influence on the profile shape and hence the conventional measures of radial velocity. The results of calculations performed in Chapter 5.4 indicate that common radial velocity measures would overestimate the mean velocity by a factor of perhaps 2 to 3 for some combinations of rotation and pulsation. Thus the model ordinates are probably underestimates and must be regarded as highly uncertain. The other approximation used in constructing Figures 3.2 and 3.3 was the neglect of a possible nonadiabatic phase shift ψ in the temperature variations. Radial nonadiabatic eigenfunctions for the fundamental mode published by Davey (1970) show a small phase lag of $\psi \sim 0.07$ radians. No equivalent published data of nonradial nonadiabatic phase shifts could be found in the literature, though Buta and Smith (1979) mention $\psi \sim 0.2$ in connection with their discussion of 53 Persei. To test this effect all the loci in Figure 3.3 were recalculated assuming $\psi = 0.2$. The resulting changes were small and do not affect the following comments.

3.3.4 *Individual Modes*

With the above considerations in mind, each mode will now be reviewed in turn.

$l = 0$

Nine of the eleven stars are consistent with a radial mode. The exceptions are 12 Lac(P_2) and β CMa(P_2) whose $\Delta(1500)/\Delta(5000)$ are too small to be explained by radial oscillations. In particular, the data for σ Sco(P_2) can be satisfied only by a radial mode because of its

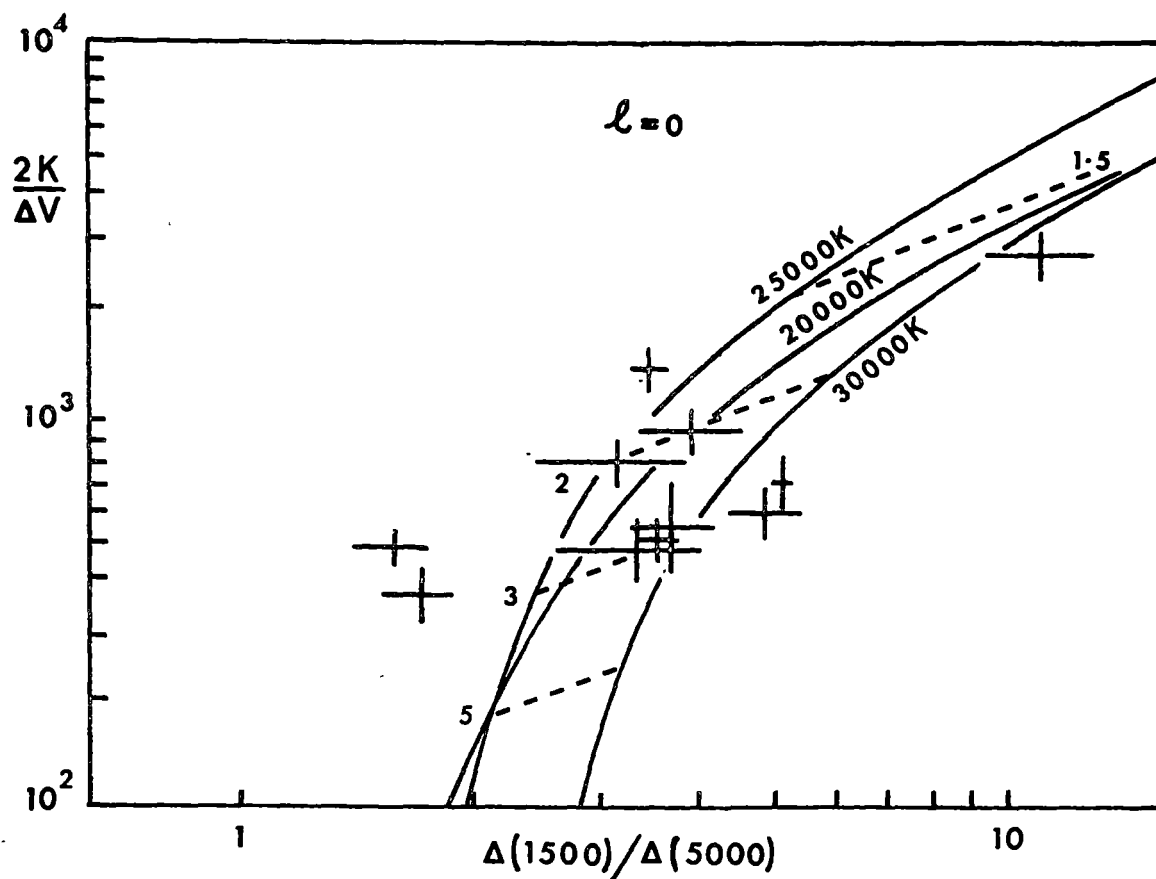


Figure 3.3(a) Observed data and model loci for $l = 0$.

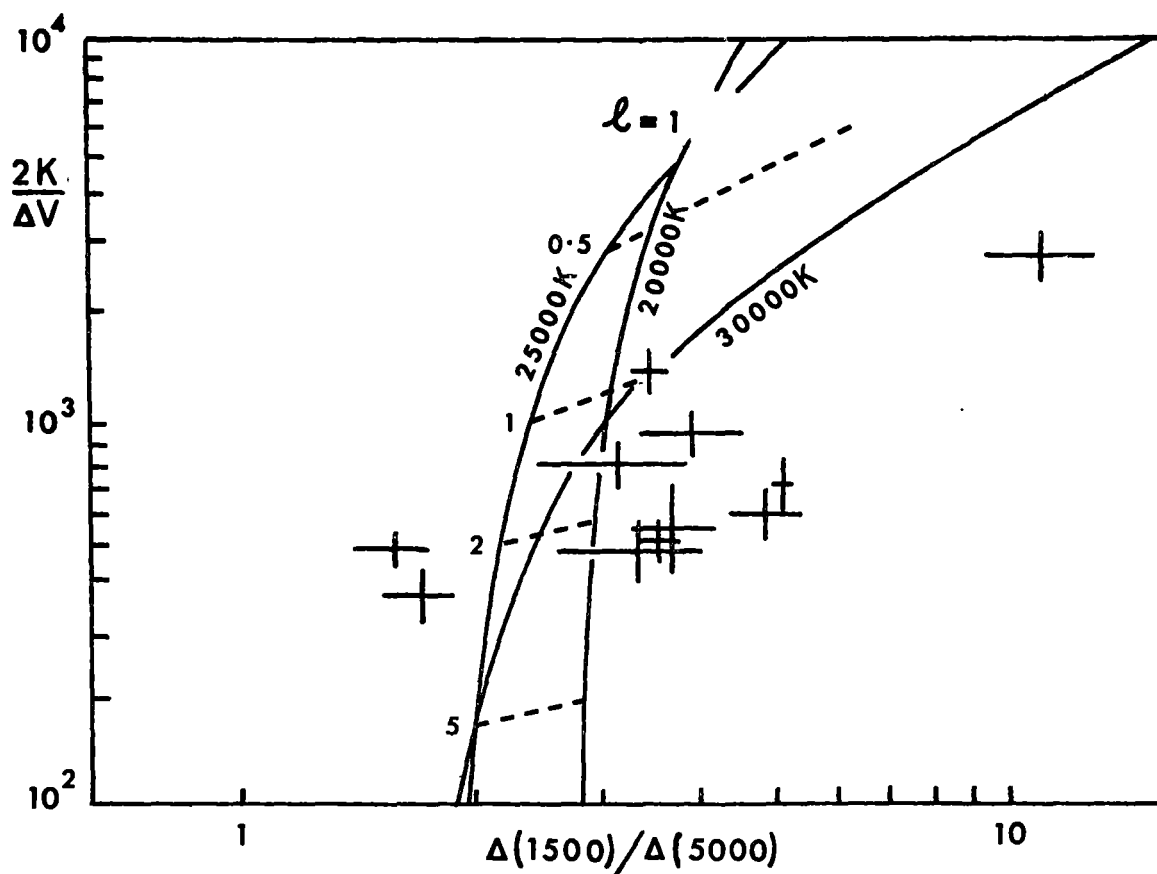


Figure 3.3(b) Observed data and model loci for $l = 1$.

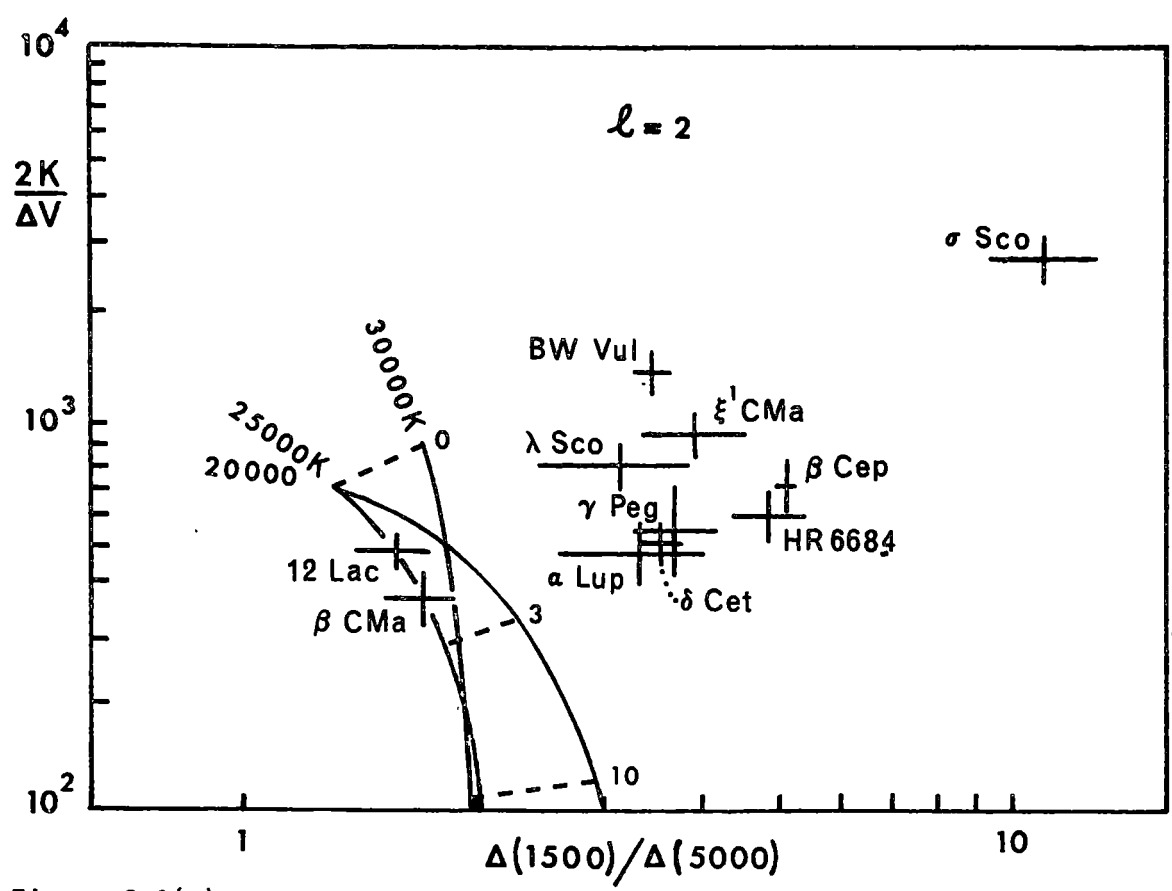


Figure 3.3(c) Observed data and model loci for $l = 2$.

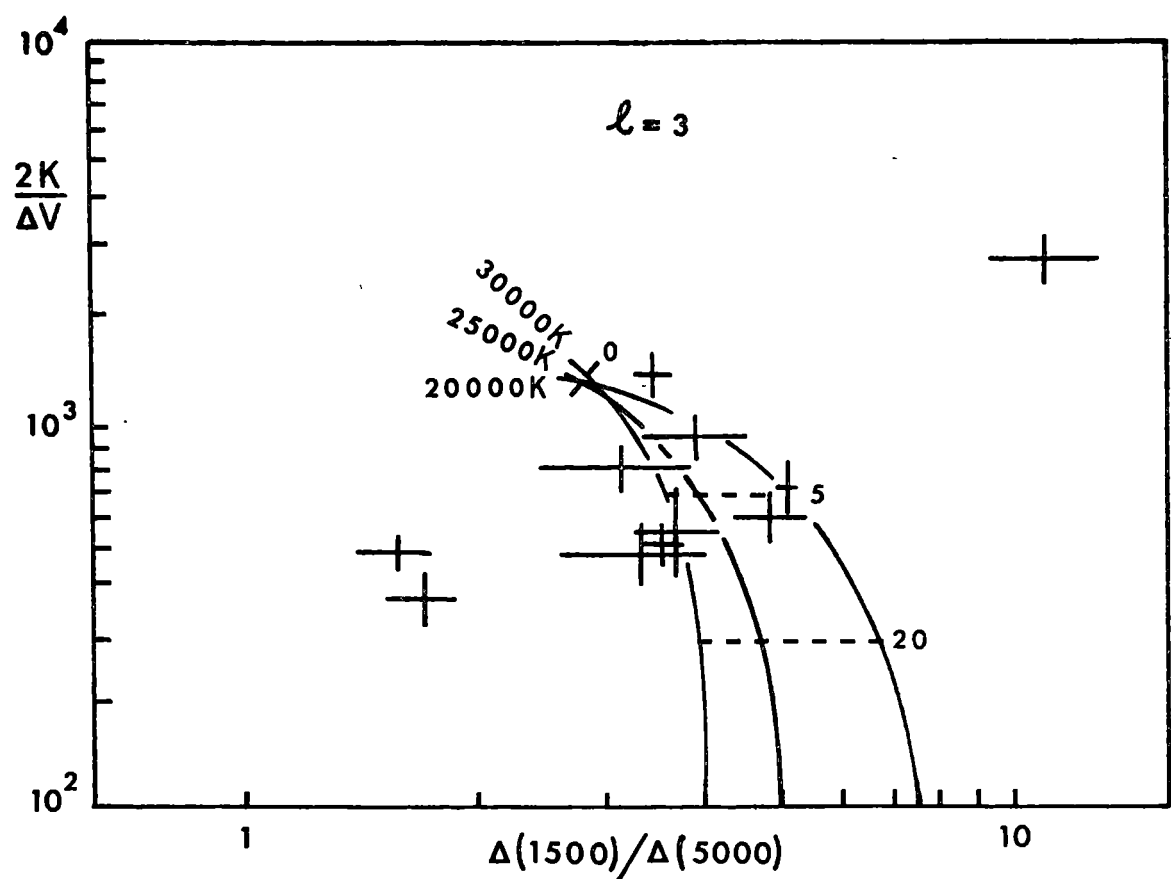


Figure 3.3(d) Observed data and model loci for $l = 3$.

very high $\Delta(1500)/\Delta(5000)$ ratio. Such a steep amplitude spectrum can be achieved only because geometric and temperature contributions oppose for the radial mode. At large values of B , the temperature effect dominates and $\frac{\Delta(1500)}{\Delta(5000)} \rightarrow \frac{\alpha(1500)}{\alpha(5000)}$, where $\alpha(\lambda) = \frac{\partial \log F_\lambda}{\partial \log T_e}$. However as B decreases the cancelling geometric contribution begins to significantly decrease the light amplitude, and this is more severe at longer wavelengths where the temperature effect (i.e. α_λ) is small. From Equation 3.1 it can be seen that, for $l = 0$, $\Delta(5000)$ tends to zero as B decreases to $2/\alpha(5000) \sim 1.5$ and thus $\Delta(1500)/\Delta(5000)$ becomes arbitrarily large. The dependence of the flux on the effective gravity modifies this critical value of B only slightly. For a star executing radial pulsations with a particular value of B , then at wavelengths longer than that for which $\alpha(\lambda) \sim 2/B$ the geometric term will dominate the temperature term. At these wavelengths (somewhere in the infrared) a phase reversal will occur in the light curve, with maximum light at maximum radius. σ Sco is interesting in this context since its light amplitude declines most steeply with wavelength. Some near-infrared observations of this star would therefore be of some value.

B values for the nine radial candidates range from about 2 to 3.

$l = 1$

For this mode there is no contribution to the light variations from changes in geometry and surface orientation. Consequently the dipole mode is most sensitive to the physical assumptions concerning the effective gravity dependence of the flux, as embodied in Equation 2.7. If there were no such contribution, then the flux ratio would take the form $\frac{\Delta(1500)}{\Delta(5000)} = \frac{BI_3(1500)\alpha(1500)}{BI_3(5000)\alpha(5000)}$. Hence the trajectory of varying B would be a vertical line in the $[2K/\Delta V, \Delta(1500)/\Delta(5000)]$ plane. In this case the dipole mode predictions in Figure 3.3 would lie between the central group of data and the data for 12 Lac(P_2) and β CMa(P_2),

but in satisfactory agreement with neither. Assuming the validity of Equation 2.7 then the predicted values of $\Delta(1500)/\Delta(5000)$ for $l = 1$ can be brought into accord with the observational values corresponding to the central data group, but only providing B is in the range $0 < B < 1.5$.

$$\underline{l = 2}$$

The data for 12 Lac(P_2) and β CMa(P_2) are consistent only with this mode. B values of between 1 and 2 are indicated. No other mode can produce a $\Delta(1500)/\Delta(5000)$ value sufficiently small except for $l = 3$ using $B \sim -2$. However, with B of this order, the $l = 3$ mode predicts $2K/\Delta V$ values six times the value of $\sim 400 \text{ km s}^{-1} \text{ mag}^{-1}$ observed for these stars. The model loci corresponding to quadrupole and higher modes curve to the left in Figures 3.2 and 3.3 (i.e. to lower $\Delta(1500)/\Delta(5000)$ with decreasing B) because of the reinforcing geometric and temperature effects.

$$\underline{l = 3}$$

As in the case of the $[2K/\Delta V, \Delta U/\Delta V]$ diagram this mode is consistent with the centrally located group of data. B values in the range 0 to 8 are required by the observations.

3.3.5 *Summary*

Mode identification on the basis of visual colour indices is difficult and unreliable, however the use of satellite ultraviolet data to extend the colour baseline generates a considerable improvement. The $[2K/\Delta V, \Delta(1500)/\Delta(5000)]$ plane provides a useful means of displaying mode properties and comparing them with observations, but it is not a totally reliable means of mode identification for two reasons. Firstly the $2K$ estimates suffer from the limitations described earlier in this section, and in any case the $2K/\Delta V$ value is not a good mode discriminant

for $l \leq 3$. Secondly the $\Delta(1500)/\Delta(5000)$ ratio takes no account of differences in $\Delta m(\lambda)$ over the range 1500 Å to 5000 Å. A more critical test is to require a fit of $\Delta m(\lambda)$ over all of the wavelengths for which data is available. It is by applying this criterion that the ambiguity between the $l = 0$, $l = 1$ and $l = 3$ modes can be resolved.

3.4 THE PULSATION AMPLITUDE SPECTRA

For each of the eleven stars for which extensive satellite ultra-violet data exists the light amplitude $\Delta m(\lambda)$ can be plotted as a function of wavelength to produce a curve unique to that star. This curve is referred to here as the "pulsation amplitude spectrum". The pulsation amplitude spectra have been plotted for a number of stars in Figures 3.4 and 3.5. The wavelength dependence of the theoretical $\log[\Delta m(\lambda)]$ curve depends only on the mode l and parameter B . The surface amplitude parameter ϵ simply introduces a shift in the vertical direction. A least squares fit between the theoretical and observed amplitude spectra was performed for each star in the three parameter space of ϵ , l and B . The theoretical spectrum for each star was calculated at the appropriate effective temperature given by Beeckmans and Burger (1977). Monochromatic calculations were adequate except near the Balmer jump where broadband smoothing was used.

Quadrupole modes can be readily dismissed for nine of eleven cases as the pulsation spectra are sufficiently steep as to eliminate this possibility. All eight singly periodic stars were in this category, together with the line broadening mode of σ Sco. The data for all of these objects are shown in Figure 3.6, normalized in the $\lambda 1550$ Å region. This result had already been foreshadowed by the $\Delta(1500)/\Delta(5000)$ and $\Delta U/\Delta V$ slope indicators. Dipole modes are also inadequate, since for $B > 1$ the slope of the $l = 1$ amplitude spectrum is too shallow for any of the data except λ Sco, while for $B < 1$ the gravity effect becomes significant

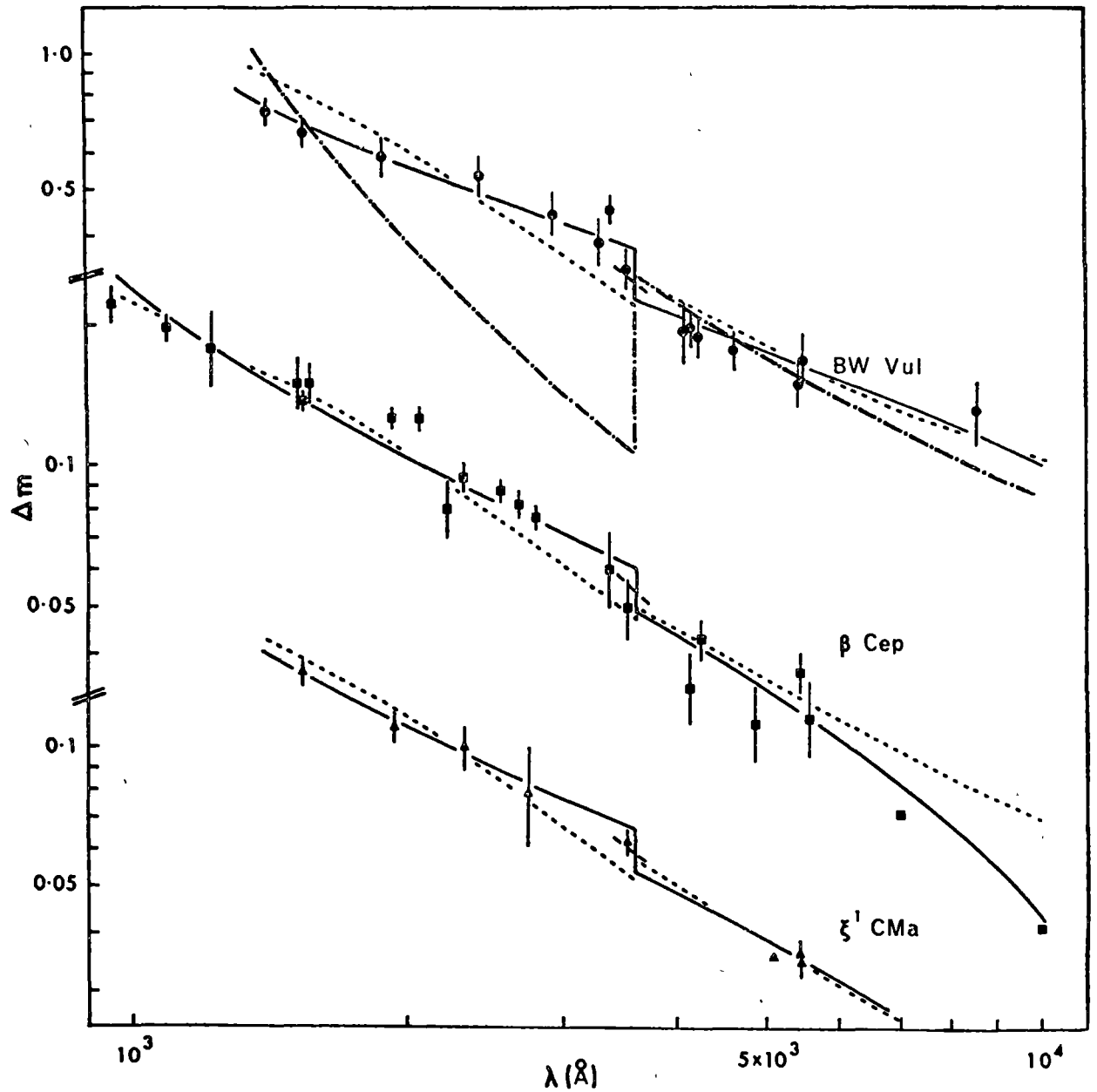


Figure 3.4 Radial and $z = 3$ models least squares fitted to BW Vul, β Cep and ξ^1 CMa. The full line represents the monochromatic radial calculation with a dashed segment to give calculated U band values. The dotted line represents the monochromatic $z = 3$ calculation. Also plotted for BW Vul (dot-dash line) is the monochromatic $z = 1$ calculation having the same $\Delta(1500)/\Delta(5000)$ index as the observed data for that star.

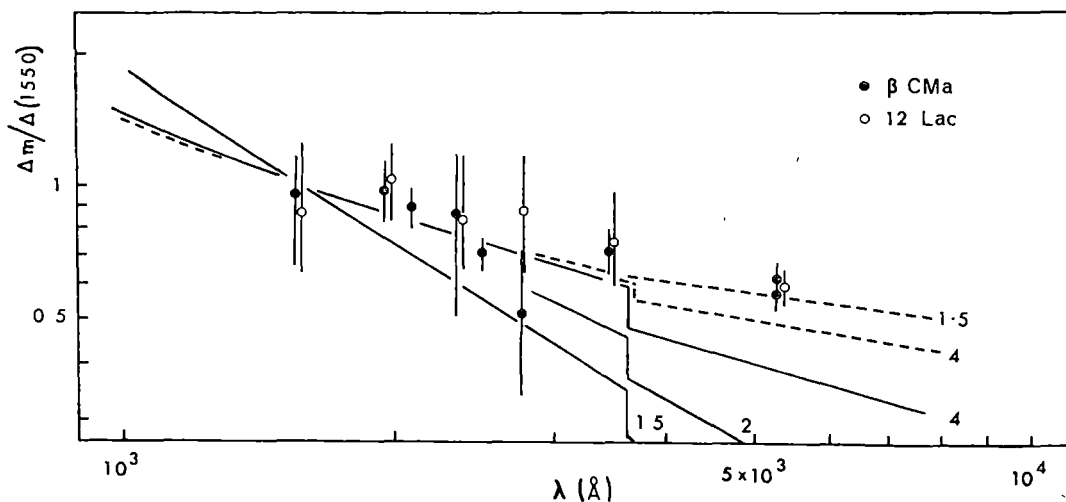


Figure 3.5 Observed broad band data for the line-broadening modes of β CMa and 12 Lac. Models are the same as in Figure 3.6.

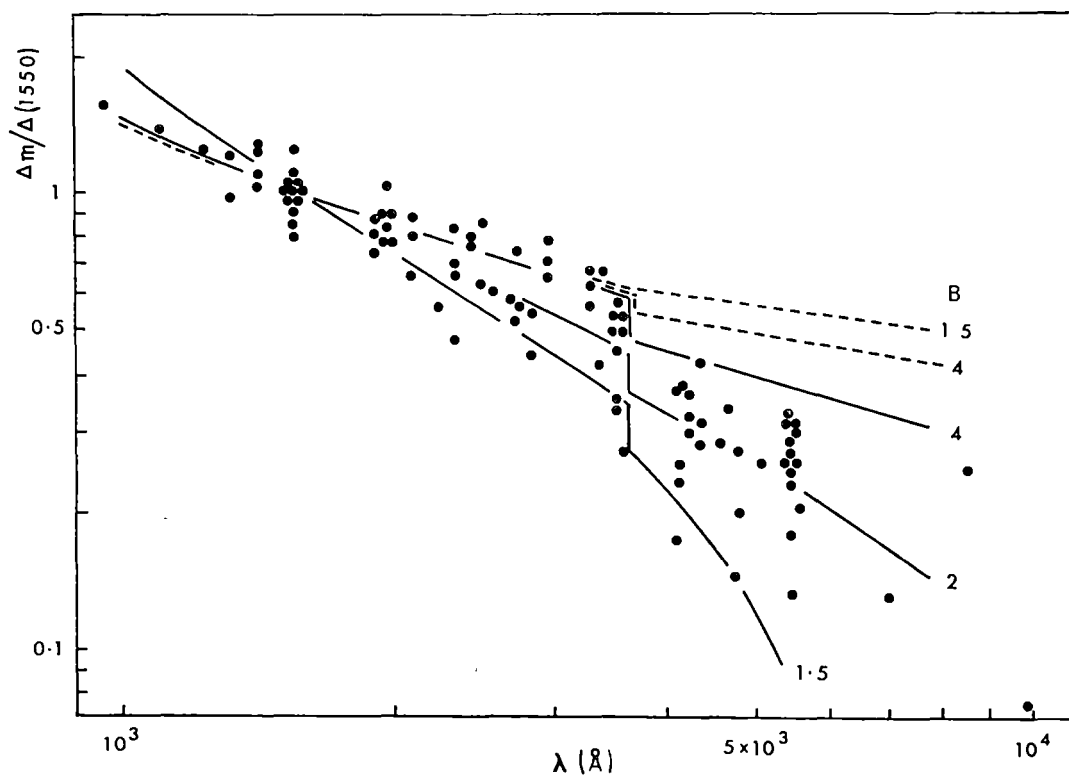


Figure 3.6 Calculated monochromatic light ranges for radial oscillations (full lines) and $l = 2$ oscillations (dashed lines) normalized at $\lambda 1550 \text{ \AA}$. The observed broad band data for all eight singly periodic stars examined, together with the line-broadening σ Sco mode, are superimposed for comparison.

and depresses the amplitude at wavelengths shorter than the Balmer jump. This is illustrated in Figure 3.4 where the data for BW Vul are shown, together with the dipole spectrum having the same $\Delta(1500)/\Delta(5000)$ index. The radial mode gave an excellent fit to the data for these nine stars and the best-fit theoretical spectra are indicated in Figure 3.4. It should be noted that if no attempt had been made in the model calculations to include the effective gravity dependence of F_λ , poorer fits would have resulted. As a further check on this effect, the coefficient p_* in Equation 2.7 was permitted to vary in some trial calculations. Least squares fits were performed in the ϵ , B , p_* parameter space for the stars ξ^1 CMa, HR 6684 and β Cep, whose amplitude spectra are most sensitive to the effective gravity variations (due to their low B). A best-fit value of $p_* \sim 0.9 \pm 0.2$ was obtained.

Deciding between $l = 0$ and $l = 3$ modes for the stars plotted in Figure 3.4 requires more care. The r.m.s. errors of the best-fit $l = 0$ and $l = 3$ curves were roughly comparable despite the use of data at all wavelengths. On average the best-fit $l = 3$ errors were worse by only about 50 percent than the corresponding radial fit errors. However, if the three best observed stars (β Cep, BW Vul and ξ^1 CMa) are examined it becomes clear that the shape of $\Delta m(\lambda)$ does favour the radial model over the $l = 3$ case. This is most noticeable in the slopes near the Balmer jump, as can be seen from Figure 3.4 where the optimal $l = 3$ spectra are shown for these three stars.

The best-fit values of B and $\Delta R/R$ are given in Table 3.2 for the singly periodic stars γ Peg, δ Cet, ξ^1 CMa, α Lup, HR 6684, BW Vul and β Cep and for the line broadening mode of σ Sco. Under the assumption of radial oscillations, radius ranges $\Delta R/R$ can be readily estimated from the radial velocity data. Values found this way are listed in Table 3.2 for comparison with the results of the $\Delta m(\lambda)$ determinations.

TABLE 3.2: Radial Oscillation Parameters

| <i>Star</i> | <i>B</i> | $\frac{\Delta R}{R}\%$ (<i>Photometric</i>) | $\frac{\Delta R}{R}\%$ (<i>Radial Velocity</i>) |
|---------------------------|------------------------------|---|---|
| γ Peg | 2.40(+90, -30%) ¹ | 0.65($\pm 60\%$) ¹ | 0.40 |
| δ Cet | 2.80(+60, -20%) | 0.85(+70, -50%) | 0.70 |
| ξ^1 CMa | 2.05($\pm 5\%$) | 2.45($\pm 10\%$) | 1.70 ³ |
| α Lup | 3.20(+90, -30%) | 0.65($\pm 55\%$) | 0.85 |
| σ Sco ² | 1.60($\pm 15\%$) | 7.20($\pm 35\%$) | 7.0 |
| HR 6684 | 1.90($\pm 20\%$) | 2.20($\pm 40\%$) | 1.15 ⁴ |
| BW Vul | 2.65($\pm 15\%$) | 8.20($\pm 20\%$) | 7.10 ⁵ |
| β Cep | 1.90($\pm 5\%$) | 2.60($\pm 15\%$) | 2.40 |

Notes to Table 3.2:

1. Bracketed values are 2σ confidence limits throughout.
2. Line-broadening mode.
3. Adopted $11 R_{\odot}$, consistent with spectral classification.
4. Radius not given by Lesh and Aizenman (1978), so value of $7 R_{\odot}$ was adopted, consistent with spectral classification.
5. Radial velocity is highly non-sinusoidal so ΔR of Goldberg *et al.* (1976) used.

Unless otherwise indicated, these $\Delta R/R$ (Radial Velocity) entries were obtained by assuming sinusoidal motion with a foreshortening factor of 1.31 and values of P , $2K$ and R given by Lesh and Aizenman (1978).

The agreement between the photometric and radial velocity determinations of $\Delta R/R$ is satisfactory, as can be seen from Figure 3.7. This supports the results of Section 3.3 which demonstrated the consistency of a radial model with the $2K/\Delta V$ data for these stars.

Campos and Smith (1980) have obtained high dispersion Reticon spectra of γ Peg, β Cep and δ Cet which can be explained only by the presence of a single radial pulsation in each case. Their spectroscopic observations of σ Sco indicate that the P_2 mode is also radial. The conclusions of Campos and Smith for these four stars, derived by an entirely independent method, strongly support the radial identifications determined here from the pulsation amplitude spectra.

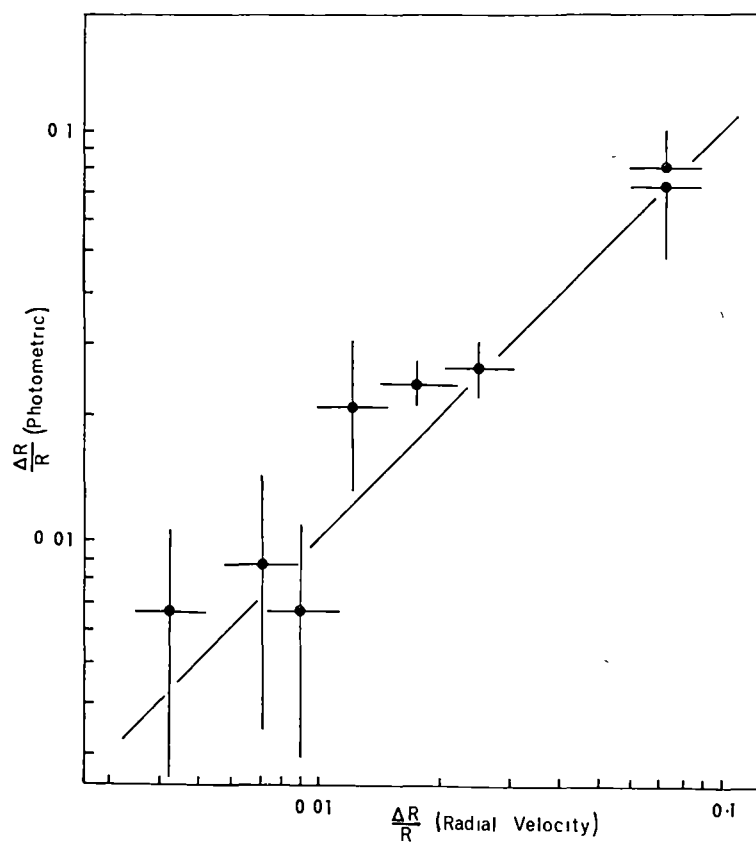


Figure 3.7 Comparison of estimates of the range of surface motion using the data of Table 3.2. Nominal $\pm 20\%$ confidence limits are shown on $\Delta R/R$ (Radial Velocity) values.

Because of the large scatter of the data for λ Sco, a reliable value of B could not be estimated for this star. The slope of its pulsation amplitude spectrum is consistent only with $l = 0$, $B > 4$ or $l = 1$, $B \sim 1$. λ Sco is the only star for which the dipole mode is feasible. However because of the choice of the $l = 0$ mode for the other eight stars it must be considered that the $l = 1$ possibility is unlikely.

In both of the remaining cases for which good satellite ultraviolet data is available, the line-broadening modes of β CMa and 12 Lac, there is only a weak dependence of light amplitude on wavelength which is compatible solely with quadrupole oscillations. A comparison of the data for these two stars with radial and quadrupole amplitude spectra is shown in Figure 3.5. Precise values of B remain difficult to gauge because of the large data scatter and the insensitivity of the slope of the quadrupole spectrum to changes in B . As noted in Section 3.3, values in the range 1 to 2 are implied.

A note of caution must be expressed in the case of the multiperiodic stars, since the observational data has been extracted under the assumption that only two modes are present. In some cases there is evidence for more than two modes. However, in β CMa and 12 Lac, the P_2 modes are dominant photometrically and most of the uncertainty is attached to any other modes present. Jerzykiewicz (1978) has in fact shown that six component frequencies are present in the data of 12 Lac, three of which form an equidistant triplet. One of the triplet frequencies corresponds to the line-broadening mode P_2 . Since the frequency triplet can be most readily understood in terms of the rotational splitting of three nonradial m states, the implication is that the triplet of modes, including the P_2 mode, are all nonradial.

Stamford and Watson (1977) and Smith (1980a) have contended on the basis of detailed line profile arguments that the P_2 mode in 12 Lac is

quadrupole. In particular the accurate multimode solutions to the high quality Reticon observations of Smith strongly indicate that the triplet frequencies in this star correspond to the stationary and prograde ($m = 0, -1, -2$) quadrupole oscillations and that the P_1 mode is radial. It is also worth noting that, using the velocity ranges of 80 km s^{-1} and 26 km s^{-1} given by Smith for the (2,0) and (0,0) modes respectively, together with the corresponding light amplitudes of 0.082 mag and 0.026 mag obtained by Jerzykiewicz (1978) and a radius of $8.5 R_\odot$ (Lesh *et al.*, 1978), the light amplitude equation may be solved for B to yield values of 2.00 and 1.98. These values are consistent with the rough estimates obtained from the slope of the pulsation amplitude spectrum. Thus these independent arguments give support to the photometric identification here as well as for the radial cases previously discussed.

3.5 CONCLUSION

Mode identification can be undertaken for the β Cephei stars by utilising the pulsation amplitude spectrum, but satellite and preferably infrared data need to be available for this technique to be reliable. All of the singly periodic stars considered were consistent with radial oscillations and all other modes (with the possible exception of $l = 3$) can be rejected for these stars. Of particular interest is the fact that σ Sco and BW Vul are in this class. Since line-splitting is observed for both of these objects, this suggests that a radial line-splitting mechanism is operative in at least some members of the β Cephei class. A radial shock scenario is an important possibility in this context and such models are considered in Chapter 6 of this thesis. The data is consistent with the presence of quadrupole modes in β CMa and 12 Lac. The UBV data on β Cru and α Vir suggest that these will fall in this category once suitable satellite data become available. B values are considerably less than the adiabatic values. This suggests that either

nonadiabatic effects are important or that the pressure boundary condition is inadequate.

C H A P T E R F O U R

POLARIZATION MODELS

4.1 INTRODUCTION

This chapter investigates a possible mode-typing test which has received much less attention than the techniques discussed in Chapter 3 and Chapter 5. The test involves the accurate monitoring of the light emitted by a hot pulsating star to detect any variations in the degree of polarization, P and polarization angle, θ . The observation of variable photospheric polarization would provide a conclusive demonstration of the presence of nonradial oscillations. In this chapter the nature of the variations in P and θ over the polarization cycle are determined for a number of nonradial modes. Most importantly, the threshold at which these variations will become detectable is established.

Some isolated polarization measurements of β Cephei variables have been reported by Serkowski (1968, 1970) and Serkowski and Robertson (1969). These measurements suggested any polarization changes must be small. Schaefgans and Tinbergen (1979) have monitored β Cephei itself for two complete periods and detected no variations in P or θ , though an order of magnitude improvement could be gained over their limits with better observing conditions. Line profile evidence of Campos and Smith (1980) and the pulsation amplitude spectrum analysed by Stamford and Watson (1978a) strongly argue for a radial pulsation in the star β Cephei, so a null result for this particular object may be reasonable. From calculations of rotationally distorted stars, such as those of Haisch and Cassinelli (1976), it is to be expected that effects of nonradial pulsation will be small. The important question is, at what level does such a null result become significant in discriminating against nonradial suggestions like that of Kubiak (1978)? This question, coupled with the strong evidence for nonradial effects in other objects,

led us to pursue Schafgans and Tinbergen's request for predictions of expected polarization variations. Similar work has been independently undertaken by Odell (1979). This work goes beyond that of Odell in a number of ways and makes it clear that visual polarization monitoring is unlikely to be useful.

The reasons why changes in polarization are to be expected from nonradial pulsators were briefly discussed in Section 2.4. The large contribution of electron scattering to the total opacity in early B star atmospheres ensures that the light will be *locally* polarized. However the extent of this polarization depends on the scattering to absorption ratio and the way that this quantity varies with optical depth. In Section 4.2 the equations of radiative transfer are solved, yielding the degree of polarization for realistic β Cephei atmospheres. These results are applied in Section 4.3, where the polarization variations for $1 \leq 3$ are presented. Subsequently the detectability of these variations is considered (Section 4.4) and some particular stars are examined in this context (Section 4.5). The polarization models are generalised to the case of multimode pulsators in Section 4.6 and predictions are made for 12 Lac using this method. The results and discussion here are being presented in papers by Stamford and Watson (1980 a & b).

4.2 SOLUTION OF THE EQUATIONS OF RADIATIVE TRANSFER

Polarization calculations by Chandrasekhar (1946) for a pure-scattering atmosphere were extended by Code (1950) to include absorption effects. Harrington (1969) pointed out that the addition of some absorption to a scattering atmosphere can lead to polarization effects which may exceed the pure-scattering predictions at wavelengths where large source function gradients occur. This matter was also taken up by Collins (1970). The limb darkening parallel and perpendicular to the

limb has been calculated here for four accurate model atmospheres applicable to hot variable stars using the technique outlined by Harrington (1969).

4.2.1 The Method of Solution

The method used involves the solution of coupled integral equations for the source functions of the two states of polarization. It is assumed that the scattering is according to Rayleigh's Law and that the absorption and re-emission of radiation is consistent with local thermodynamic equilibrium. Then the equations of radiative transfer for a semi-infinite plane-parallel atmosphere are (Code, 1950):

$$\begin{aligned} \mu \frac{dI_{L,v}}{d\tau_v} &= I_{L,v} - \frac{3}{4}(1-\lambda_v) \{ 2(J_{L,v} - K_{L,v}) + \mu^2(3K_{L,v} - 2J_{L,v} + J_{r,v}) \} - \frac{1}{2}\lambda_v B_v \\ \text{and} \quad \mu \frac{dI_{r,v}}{d\tau_v} &= I_{r,v} - \frac{3}{4}(1-\lambda_v) \{ J_{r,v} + K_{L,v} \} - \frac{1}{2}\lambda_v B_v \end{aligned} \quad (4.1)$$

where $I_{L,v}$ and $I_{r,v}$ are the monochromatic intensities in the states of polarization with electric vector respectively parallel and perpendicular to the meridian plane. Here

$$\lambda_v = \frac{\kappa_v}{\kappa_v + \sigma_v} \quad ; \quad J_v = \frac{1}{2} \int_{-1}^1 I_v d\mu \quad ; \quad K_v = \frac{1}{2} \int_{-1}^1 I_v \mu^2 d\mu .$$

λ_v is the ratio of absorption to total opacity. Summing and subtracting Equations 4.1, and suppressing the frequency dependence from the notation gives

$$\begin{aligned} \mu \frac{dI}{d\tau} &= I - (1-\lambda) \{ (J_L + J_r) + \frac{3}{4}(\frac{1}{3} - \mu^2)(2J_L - 3K_L - J_r) \} - \lambda B \\ &= I - \{ s + (\frac{1}{3} - \mu^2)p \} \\ \text{and} \quad \mu \frac{dQ}{d\tau} &= Q - \frac{3}{4}(1-\lambda)(2J_L - 3K_L - J_r)(1-\mu^2) \\ &= Q - (1-\mu^2)p \end{aligned} \quad (4.2)$$

where the auxiliary functions s and p are defined according to

$$s(\tau) = (1-\lambda)(J_L + J_r) + \lambda B$$

and

$$p(\tau) = \frac{3}{4}(1-\lambda)(2J_L - 3K_L - J_r) .$$

The Stokes parameters of the emergent radiation can be obtained from the solution to Equations 4.2. These are

$$\left. \begin{aligned} I(\mu) &= \int_0^\infty \{s(\tau) + (\frac{1}{3} - \mu^2)p(\tau)\} e^{-\tau/\mu} \frac{d\tau}{\mu} \\ \text{and} \quad Q(\mu) &= \int_0^\infty \{(1-\mu^2)p(\tau)\} e^{-\tau/\mu} \frac{d\tau}{\mu} \end{aligned} \right\} (4.3)$$

The source functions for each state of polarization can be expressed in terms of s and p as follows:

$$S_L(\tau) = \frac{1}{2}s(\tau) + (\frac{2}{3} - \mu^2)p(\tau)$$

and

$$S_r(\tau) = \frac{1}{2}s(\tau) - \frac{1}{3}p(\tau).$$

Substituting the source functions into the Schwarzschild solutions for J and K (viz. $J(\tau) = \frac{1}{2} \int_0^\infty S(t) E_1 |\tau-t| dt$, $K(\tau) = \frac{1}{2} \int_0^\infty S(t) E_3 |\tau-t| dt$) one obtains the pair of integral equations

$$\left. \begin{aligned} s(\tau) &= (1-\lambda) \left\{ \frac{1}{2} \int_0^\infty s(t) E_1 |\tau-t| dt + \int_0^\infty p(t) \left[\frac{1}{6} E_1 |\tau-t| - \frac{1}{2} E_3 |\tau-t| \right] dt \right\} + \lambda B \\ \text{and} \quad p(\tau) &= \frac{3}{8}(1-\lambda) \left\{ \int_0^\infty s(t) \left[\frac{1}{2} E_1 |\tau-t| - \frac{3}{2} E_3 |\tau-t| \right] dt \right. \\ &\quad \left. + \int_0^\infty p(t) \left[\frac{5}{3} E_1 |\tau-t| - 4 E_3 |\tau-t| + 3 E_5 |\tau-t| \right] dt \right\} \end{aligned} \right\} (4.4)$$

where $E_n(x) = \int_1^\infty e^{-xt} t^{-n} dt$.

Following Harrington (1969), these may be solved using the method developed by Gebbie (1967) for the isotropic scattering case. This method replaces the integrations over s and p by Gaussian quadratures. However, in order to truncate the indefinite integrals at some convenient upper limit, it is necessary to introduce the function $s^* = s - B$. From the definitions of s and p it can be seen that s^* and p both vanish as $\tau \rightarrow \infty$.

Equations 4.4 can then be replaced by the Gaussian sums

$$\begin{aligned}
 s^*(\tau) = (1-\lambda) \{ & \sum_{\substack{n=1 \\ \neq i}}^N [\frac{1}{2}s^*(t_n) + \frac{1}{6}p(t_n)]E_1|\tau-t_n|t_n'w_n \\
 & - \frac{1}{2} \sum_{n=1}^N p(t_n)E_3|\tau-t_n|t_n'w_n + [\frac{1}{2}s^*(\tau) + \frac{1}{6}p(\tau)][h(\tau) - \sum_{\substack{n=1 \\ \neq i}}^N E_1|\tau-t_n|t_n'w_n] \\
 & - B(\tau) - \frac{1}{2}g_1(\tau) \}
 \end{aligned}
 \tag{4.5}$$

and

$$\begin{aligned}
 p(\tau) = \frac{3}{8}(1-\lambda) \{ & \sum_{\substack{n=1 \\ \neq i}}^N [\frac{1}{2}s^*(t_n) + \frac{5}{3}p(t_n)]E_1|\tau-t_n|t_n'w_n \\
 & + \sum_{n=1}^N [-\frac{3}{2}s^*(t_n)E_3|\tau-t_n| + p(t_n)(3E_5|\tau-t_n| - 4E_3|\tau-t_n|)]t_n'w_n \\
 & + [\frac{1}{2}s^*(\tau) + \frac{5}{3}p(\tau)][h(\tau) - \sum_{\substack{n=1 \\ \neq i}}^N E_1|\tau-t_n|t_n'w_n] + \frac{1}{2}g_1(\tau) - \frac{3}{2}g_3(\tau) \}
 \end{aligned}$$

where $h(\tau) = \int_0^\infty E_1|\tau-t|dt = 2 - E_2(\tau)$

and $g_n(\tau) = \int_0^\infty B(t)E_n|\tau-t|dt$.

Here $\tau = t_i$, $t_n' = \frac{d\tau}{dz}(z_n)$, and z_n, w_n are the Gaussian zeros and weights respectively. The function g_n is precalculated for the particular stellar model under consideration. The singularity of E_1 at $t = \tau$ has been removed by adding and subtracting integrals of the form $s^*(\tau) \int_0^\infty E_1|\tau-t|dt$. This is possible because the singularity is logarithmic (Collins, 1970).

With $\tau = t_i$ for $i = 1, 2, \dots, N$, Equations 4.5 are a set of $2N$ linear inhomogeneous equations for the $2N$ unknowns $s^*(t_i), p(t_i)$.

Writing $s_i^* = s^*(t_i)$ and $p_i = p(t_i)$, these equations take the form

$$\left. \begin{aligned}
 s_i^* &= \sum_{n=1}^N K_{in}s_n^* + \sum_{n=1}^N L_{in}p_n + (1-\lambda_i)(\frac{1}{2}g_{1i} - B_i) \\
 \text{and } p_i &= \sum_{n=1}^N M_{in}s_n^* + \sum_{n=1}^N N_{in}p_n + \frac{3}{16}(1-\lambda_i)(g_{1i} - 3g_{3i})
 \end{aligned} \right\} \tag{4.6}$$

where

$$\begin{aligned}
 K_{in} &= \begin{cases} (1-\lambda_i) \left\{ \frac{1}{2} E_1 |t_i - t_n| t_n' w_n \right\} & \text{if } i \neq n \\ (1-\lambda_i) \left\{ \frac{1}{2} h(t_i) - \frac{1}{2} \sum_{\substack{m=1 \\ m \neq i}}^N E_1 |t_i - t_m| t_m' w_m \right\} & \text{if } i = n \end{cases} \\
 L_{in} &= \begin{cases} (1-\lambda_i) \left\{ \frac{1}{6} E_1 |t_i - t_n| - \frac{1}{2} E_3 |t_i - t_n| \right\} t_n' w_n & \text{if } i \neq n \\ (1-\lambda_i) \left\{ \frac{1}{6} h(t_i) - \frac{1}{2} E_3(0) t_i' w_i - \frac{1}{6} \sum_{\substack{m=1 \\ m \neq i}}^N E_1 |t_i - t_m| t_m' w_m \right\} & \text{if } i = n \end{cases} \\
 M_{in} &= \begin{cases} \frac{3}{8} (1-\lambda_i) \left\{ \frac{1}{2} E_1 |t_i - t_n| - \frac{3}{2} E_3 |t_i - t_n| \right\} t_n' w_n & \text{if } i \neq n \\ \frac{3}{8} (1-\lambda_i) \left\{ \frac{1}{2} h(t_i) - \frac{3}{2} E_3(0) t_i' w_i - \frac{1}{2} \sum_{\substack{m=1 \\ m \neq i}}^N E_1 |t_i - t_m| t_m' w_m \right\} & \text{if } i = n \end{cases} \\
 N_{in} &= \begin{cases} \frac{3}{8} (1-\lambda_i) \left\{ \frac{5}{3} E_1 |t_i - t_n| - 4 E_3 |t_i - t_n| + 3 E_5 |t_i - t_n| \right\} t_n' w_n & \text{if } i \neq n \\ \frac{3}{8} (1-\lambda_i) \left\{ \frac{5}{3} h(t_i) + [3 E_5(0) - 4 E_3(0)] t_i' w_i - \frac{5}{3} \sum_{\substack{m=1 \\ m \neq i}}^N E_1 |t_i - t_m| t_m' w_m \right\} & \text{if } i = n. \end{cases}
 \end{aligned}$$

In matrix notation these equations become

$$s^* = K s^* + L p + (1-\lambda) \left(\frac{1}{2} g_1 - B \right)$$

and
$$p = M s^* + N p + \frac{3}{16} (1-\lambda) (g_1 - 3g_3) .$$

Solving for the matrices s^* and p yields

$$\begin{aligned}
 s^* &= [1 - K - L(1-N)^{-1}M]^{-1} \left[(1-\lambda) \left(\frac{1}{2} g_1 - B \right) + \frac{3}{16} L(1-N)^{-1} (1-\lambda) (g_1 - 3g_3) \right] \\
 \text{and } p &= (1-N)^{-1} [M s^* + \frac{3}{16} (1-\lambda) (g_1 - 3g_3)] .
 \end{aligned} \quad (4.7)$$

The matrix solutions for s^* and p contain values of the auxiliary functions at the Gaussian points $\{t_i\}$ and so can be readily inserted into Equation 4.3. These equations can then be easily integrated by Gaussian quadrature to give the intensity and polarization emergent from the stellar atmosphere at a meridian angle $\arccos(\mu)$.

As a numerical check on the formulation described above, the results of some calculations were compared with the data presented in

Table 1 of Harrington (1969). Most of the polarization data could be reproduced within errors of 0.001, although in one segment of one example the differences reached 0.003.

4.2.2 *The Resulting Polarization*

The emergent polarization was calculated for four model atmospheres which were selected as follows. A $(T_e, \log g) = (23000, 3.6)$ model was chosen to represent conditions applying in the centre of the β Cephei instability strip. Models of $(30000, 3.5)$ and $(22500, 4.0)$ were selected as a check on the effects of temperature and gravity variation. A $(16000, 4.0)$ model was chosen for comparison with 53 Per, following Buta and Smith (1979). The structural details of the first model were obtained using our coding of Kurucz (1970) and those of the other three were taken directly from Kurucz (1979). The temperature and density data appropriate to each atmosphere were fed into an ATLAS opacity routine (Kurucz, 1970) which was modified to produce values of $\lambda_v = \kappa_v / (\kappa_v + \sigma_v)$ as a function of optical depth at a number of different wavelengths. The integrals $g_1(B_\lambda, \tau)$ and $g_3(B_\lambda, \tau)$ were calculated by Gaussian quadrature and values of $Q_\lambda(\mu)$ and $I_\lambda(\mu)$ could then be evaluated using Equations 4.7 and 4.3.

The wavelength dependence of the resulting polarization $Q_\lambda(\mu)/I_\lambda(\mu)$ for the $(23000, 3.6)$ model is shown in Figure 4.1. In the visual region the polarization is small but it rises substantially near the peak of the energy distribution in the far ultraviolet. Values exceed the pure-scattering predictions here. This strong dependence of the polarization on wavelength is the results of two factors. The first of these may be understood as follows. At photospheric depths bound-free hydrogen absorption exceeds the opacity due to Thomson electron scattering by over an order of magnitude at almost all wavelengths. However at wavelengths immediately longer than the Lyman

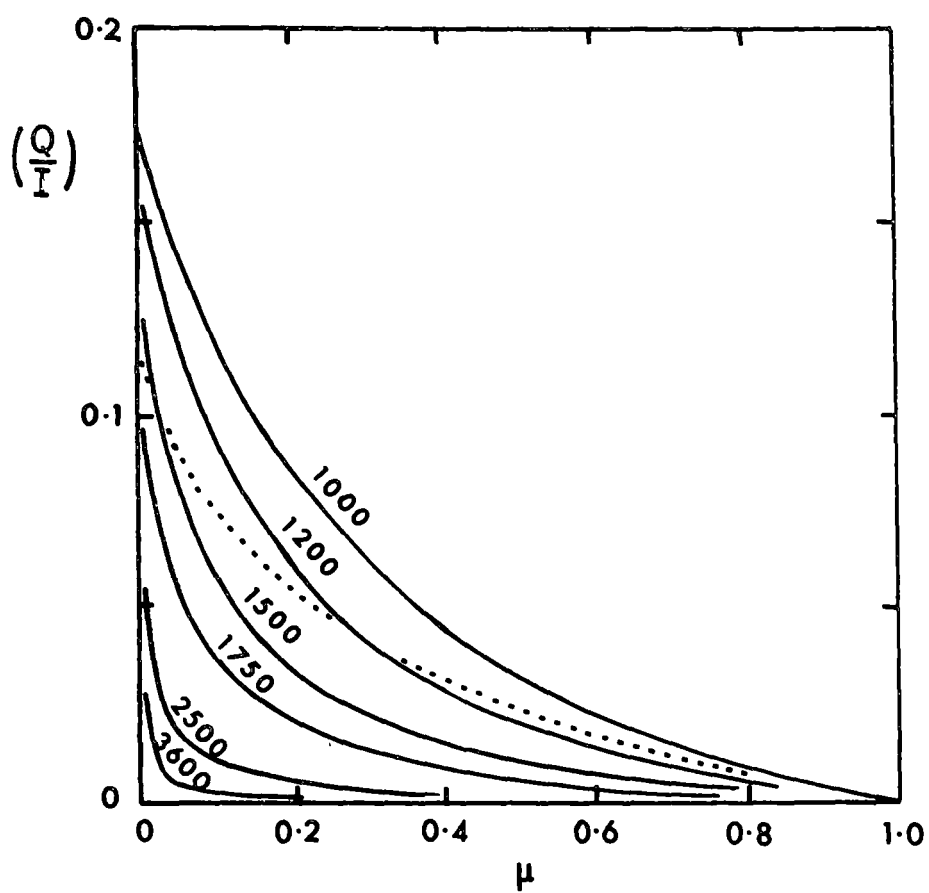


Figure 4.1 The wavelength dependence of polarization in a model atmosphere with $(T_e, \log g) = (23000, 3.6)$. The dotted line represents the result for a pure-scattering atmosphere.

and Balmer edges the absorption falls to a minimum, becoming comparable with electron scattering. In this absorption "window" scattering becomes a major opacity contributor and so the polarization increases accordingly. This can be seen in Figure 4.2a which displays the optical depth $\tau_v(50\%)$ for which $\lambda_v = \frac{1}{2}$ as a function of wavelength for the (23000, 3.6) atmosphere. At wavelengths longer than about 2000 Å the regime of scattering dominance occurs too high in the atmosphere for significant polarization to be produced. This is also shown in Figure 4.2b which illustrates the dependence of λ_v on τ_v at a number of wavelengths for the same atmosphere.

The second factor responsible for the rapid decline of the local polarization with increasing wavelength is the influence of the source function gradient on the anisotropy of the radiation. At shorter wavelengths the gradient of the source function steepens due to the effect of the Planck function exponent ($hc/\lambda kT$). An increase in the anisotropy of the intensity distribution results, favouring radiation flow in the outward normal direction. This generates a scattering geometry which considerably enhances the polarization parallel to the limb. Conversely, at longer wavelengths, the source function gradient declines and the intensity distribution becomes more isotropic. In this case more radiation is flowing tangential to the limb rather than normal to it and the polarization reverses, with Q assuming positive values, as described by Harrington (1970).

As will be obvious in the subsequent discussion, the expected polarization variability in the visual is too small to enable detection, but broadband observations in the region of 1000 Å to 2000 Å offer a brighter prospect. This confirms Odell's (1979) reservations about his use of a pure-scattering model in predicting observable effects in the visual. For the nonradial models a wavelength of 1500 Å was used as an indicator of the effects that can be expected. In Table 4.1

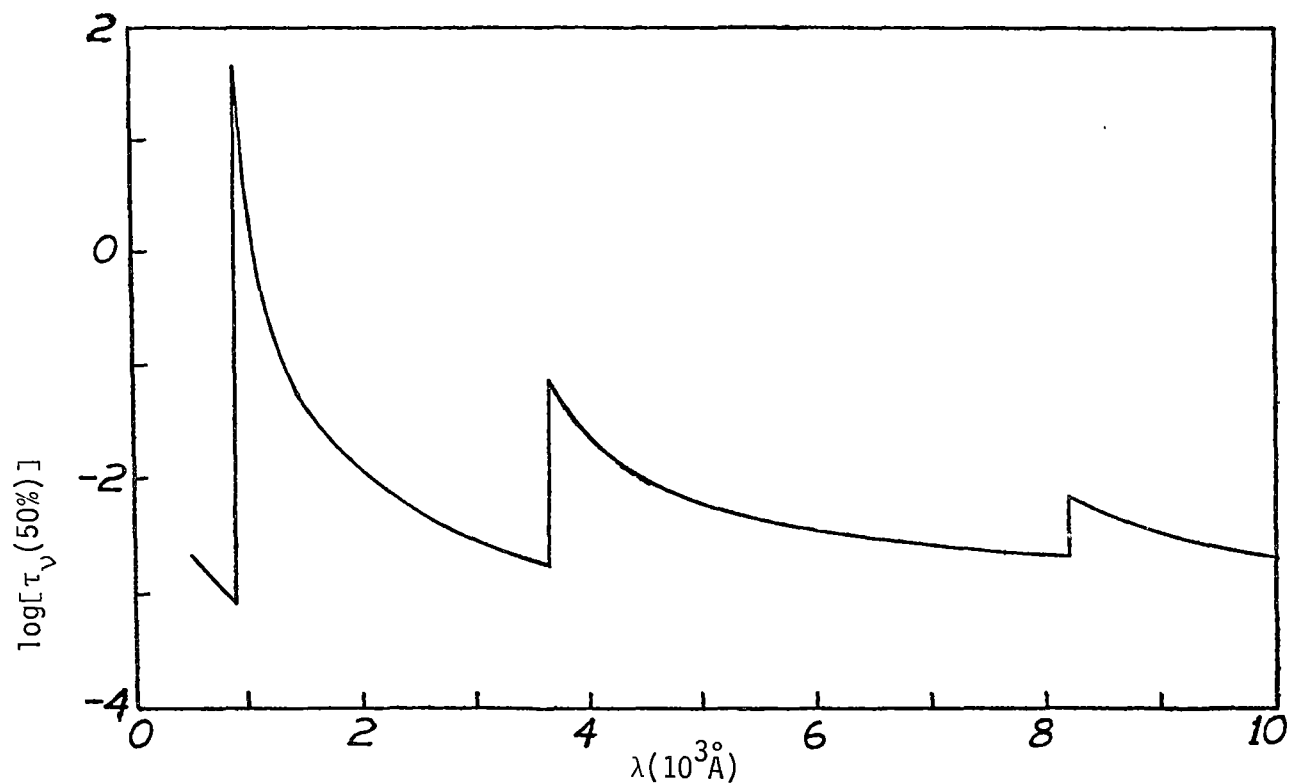


Figure 4.2(a) The optical depth $\tau_v(50\%)$ for which $\kappa_v/(\kappa_v + \sigma_v) = \frac{1}{2}$ as a function of wavelength for the (23000, 3.6) atmosphere.

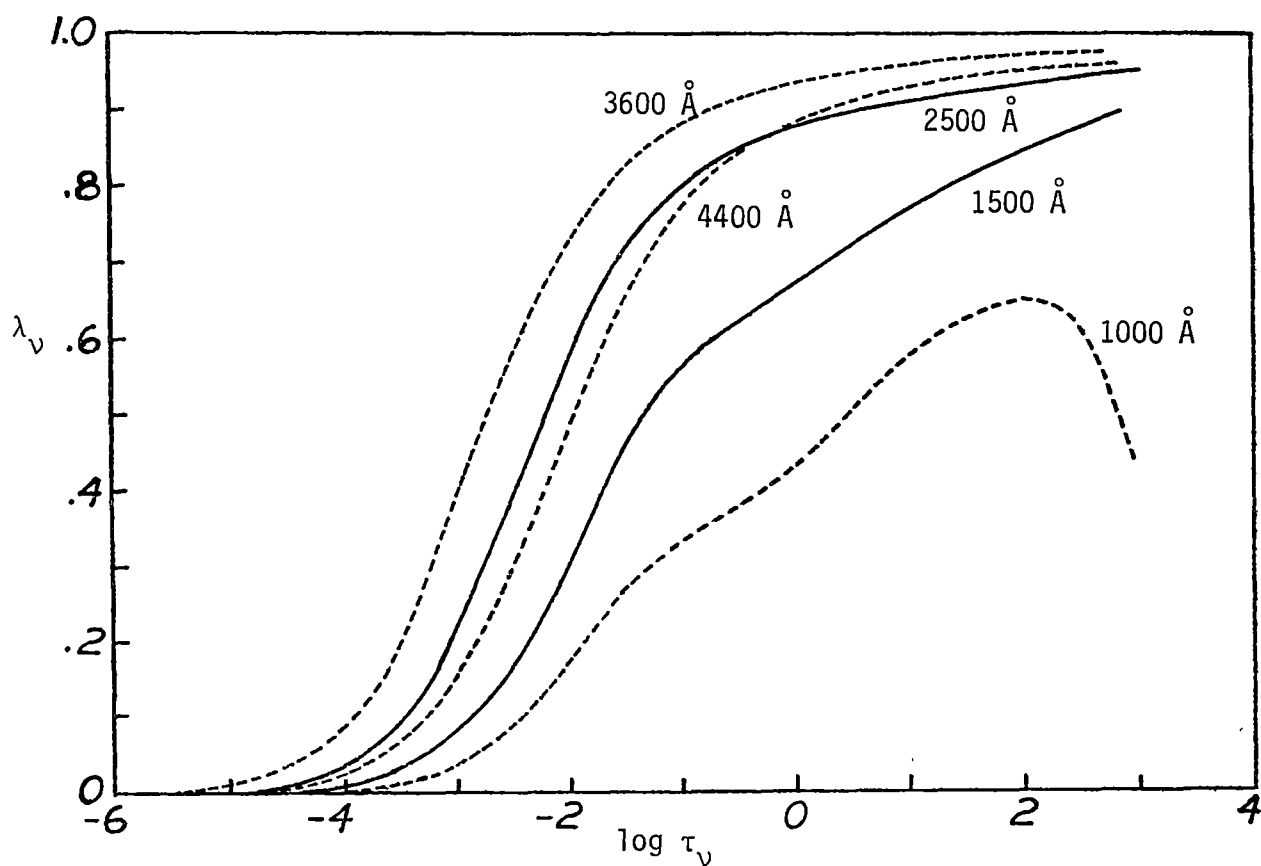


Figure 4.2(b) The dependence of the absorption fraction $\lambda_v = \kappa_v/(\kappa_v + \sigma_v)$ on optical depth τ_v for the (23000, 3.6) atmosphere.

TABLE 4.1: Model atmosphere polarization $Q_{1500}(\mu)/I_{1500}(\mu)$

| $(T_e, \log g)$ | (30000, 3.5) | (23000, 3.6) | (22500, 4.0) | (16000, 4.0) |
|-----------------|--------------|--------------|--------------|--------------|
| μ | | | | |
| 0.00 | -0.098 | -0.133 | -0.131 | -0.169 |
| 0.05 | -0.063 | -0.080 | -0.065 | -0.071 |
| 0.10 | -0.046 | -0.057 | -0.043 | -0.044 |
| 0.20 | -0.027 | -0.033 | -0.023 | -0.022 |
| 0.30 | -0.016 | -0.021 | -0.015 | -0.013 |
| 0.40 | -0.010 | -0.014 | -0.010 | -0.0086 |
| 0.50 | -0.0061 | -0.010 | -0.0064 | -0.0057 |
| 0.60 | -0.0036 | -0.0066 | -0.0042 | -0.0038 |
| 0.80 | -0.0009 | -0.0024 | -0.0015 | -0.0014 |
| 1.00 | 0.0000 | 0.0000 | 0.0000 | 0.0000 |

$Q_{1500}(\mu)/I_{1500}(\mu)$ values are listed for all four atmospheric models. The (23000, 3.6) model must be close to the optimal conditions for producing polarization but the other models are down by less than 40 percent on this one.

4.3 NONRADIAL CALCULATIONS AND RESULTS

4.3.1 *Calculation Techniques*

The calculation of (P, θ) generated by a nonradial surface distortion was done by numerical integration over 1600 surface elements according to the method described in Section 2.4. There are three parameters which control the amplitude of the polarization variations for a given mode and stellar model. These are the range of the radial displacement at a surface antinode having polar angle θ_A , $\Delta R(\theta_A)/R$, the temperature parameter B and the axial inclination angle i . As in Chapter 3, the adiabatic phase relationship between local surface temperature changes and local radius variations was assumed for the short-period low-order modes modelled. Odell (1979) did not attempt to incorporate local temperature effects into his polarization calculations. The following analysis confirms his suspicion that they have a strong influence on polarization amplitude for a given range in surface motion. In integrating over the surface, the degree of polarization $Q(\mu)/I(\mu)$ of the equilibrium atmosphere was assumed to apply locally to the surface elements even though their effective temperature and gravity changed during the pulsation. The data listed in Table 4.1 for the other equilibrium atmospheres indicate that this approximation is adequate in view of the other uncertainties in the model.

The (23000, 3.6) atmosphere was chosen as the one for extensive study and the calculations were performed with a specific B of 4.0.

Calculations at other B values, for selected i , were undertaken to test the sensitivity of the results to this parameter. Changes of B by a factor of two lead to changes in the maximum polarization P_{MAX} , in the same sense, by up to a similar factor. Work was confined to the linear regime of $\Delta R(\theta_A)/R$ dependence.

Calculations were performed for all modes up to $l = 3$. The $l = 1$ modes gave no significant polarization because of the cancelling effects of distortions in opposite hemispheres, as noted in Odell's work. The polarization may be precisely zero for those modes, but the numerical accuracy of our procedure only permits us to claim that any non-zero effect must be about two orders of magnitude down on the effects for the $l = 2, 3$ modes.

A catalogue of all $l = 2, 3$ modes is presented in Figure 4.3(a-g). Data for $-m$ modes is presented, but of course $+m$ values follow from phase inversion of these. For each mode a plot of (P, ϕ) is given for a selected set of i and a specific surface range parameter $\Delta R(\theta_A)/R$ as an example. Here ϕ is the phase of the pulsation. Similarly (θ, ϕ) is given for a selected set of i . Because P scales linearly with $\Delta R(\theta_A)/R$ and is also affected strongly by B , the top panel in each of Figure 4.3 (a-g) is not particularly convenient for a direct comparison with observations. Therefore we have also plotted the maximum P value achieved at a particular i , divided by the light range at 1500 \AA evaluated at the same i . The latter comes from Dziembowski's formula (Equation 2.20). Since both polarization and light range scale linearly with the surface distortion, their ratio is independent of $\Delta R(\theta_A)/R$. Furthermore testing showed that $P_{\text{MAX}}/\Delta(1500)$ is also insensitive to B . It changes by less than 10 percent for a factor of two change in B . The lower panels in Figure 4.3 can then be used as follows. An observed light range $\Delta(1500)$ for a star in or near the β Cephei region, combined with an i suggested in a specific mode

Figure 4.3(a-g) Polarization data for nonradial modes with $l = 2$ and $l = 3$ calculated for a model with $(T_e, \log g, B) = (23000, 3.6, 4)$ at 1500 \AA . Degree and position angle of polarization is given as a function of phase for sample i . The ratio of the maximum polarization to the light range, $\Delta(1500)$, is also given as a function of i . The angular location of modes (N) and antinodes (A) in the surface motion is indicated.

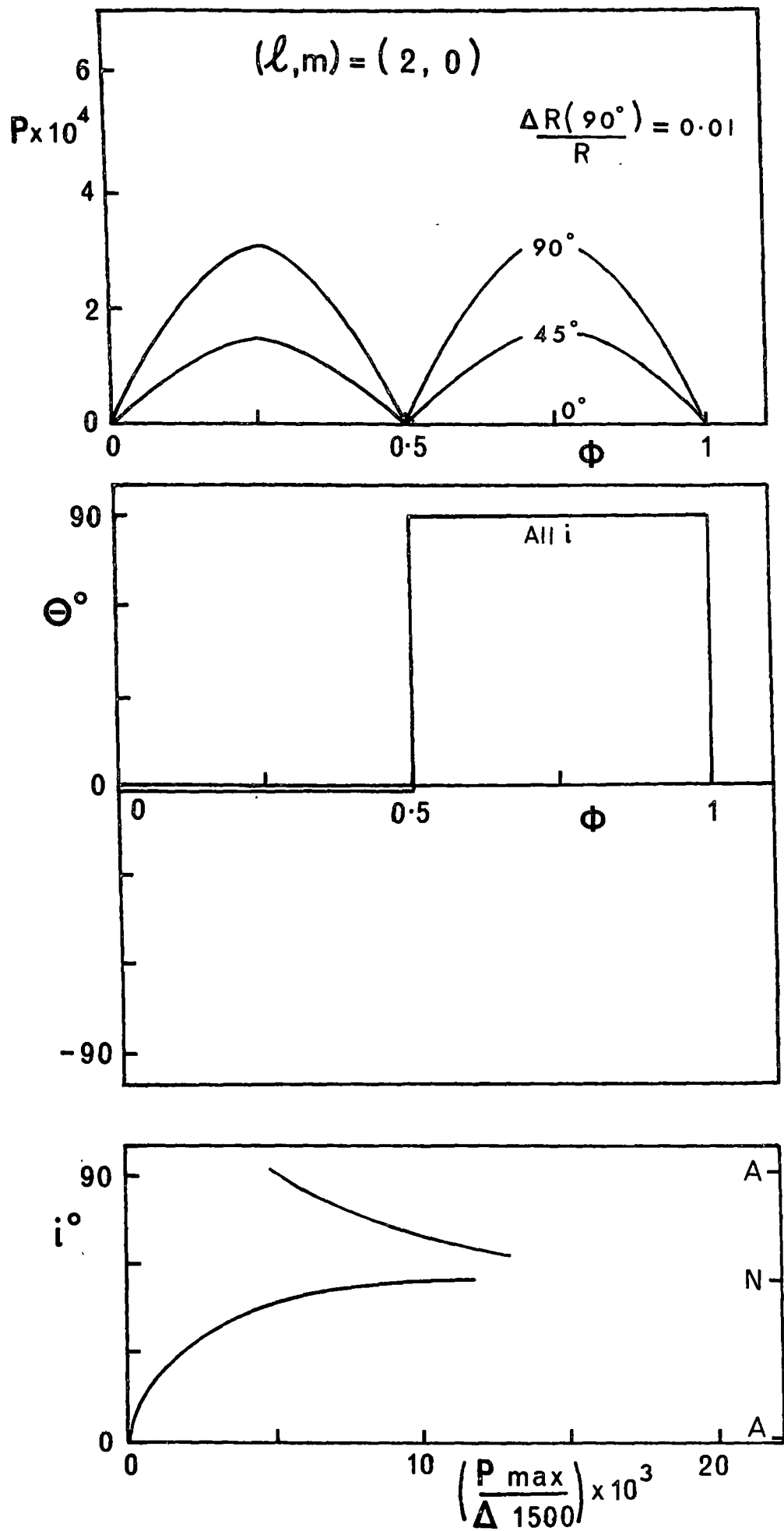


Figure 4.3(a) Polarization curves for the $(2,0)$ mode.

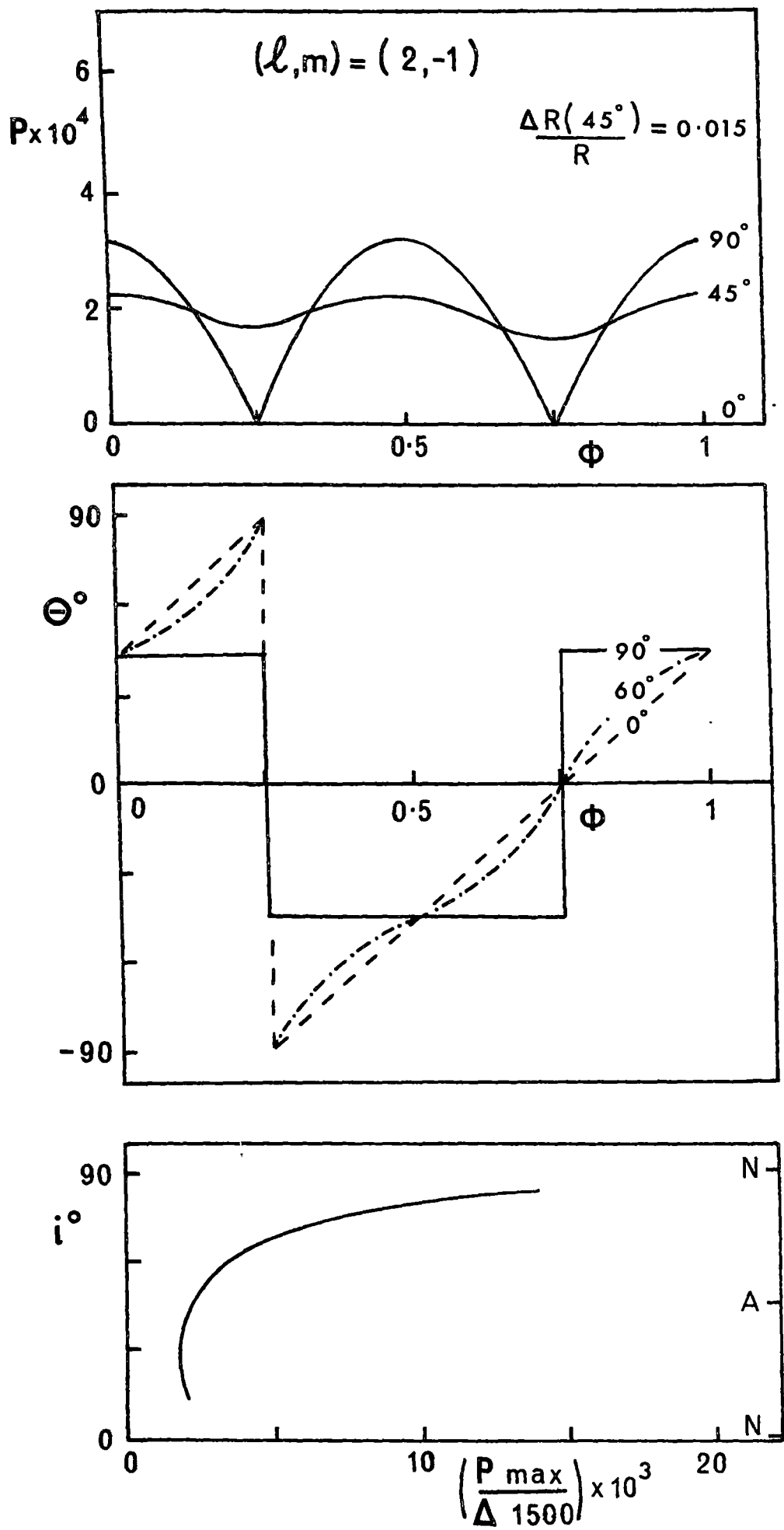


Figure 4.3(b) Polarization curves for the $(2, -1)$ mode.

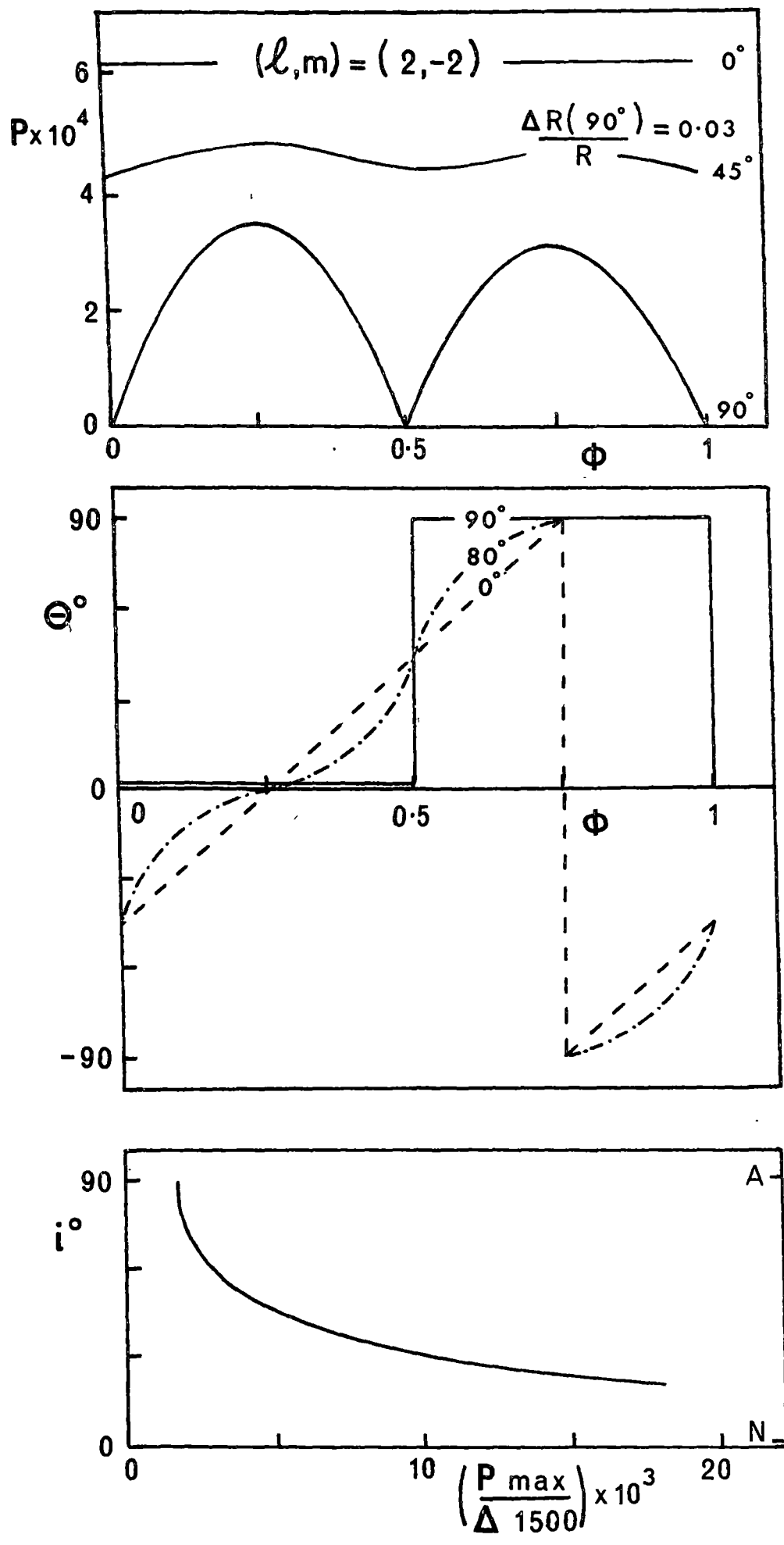


Figure 4.3(c) Polarization curves for the (2,-2) mode.

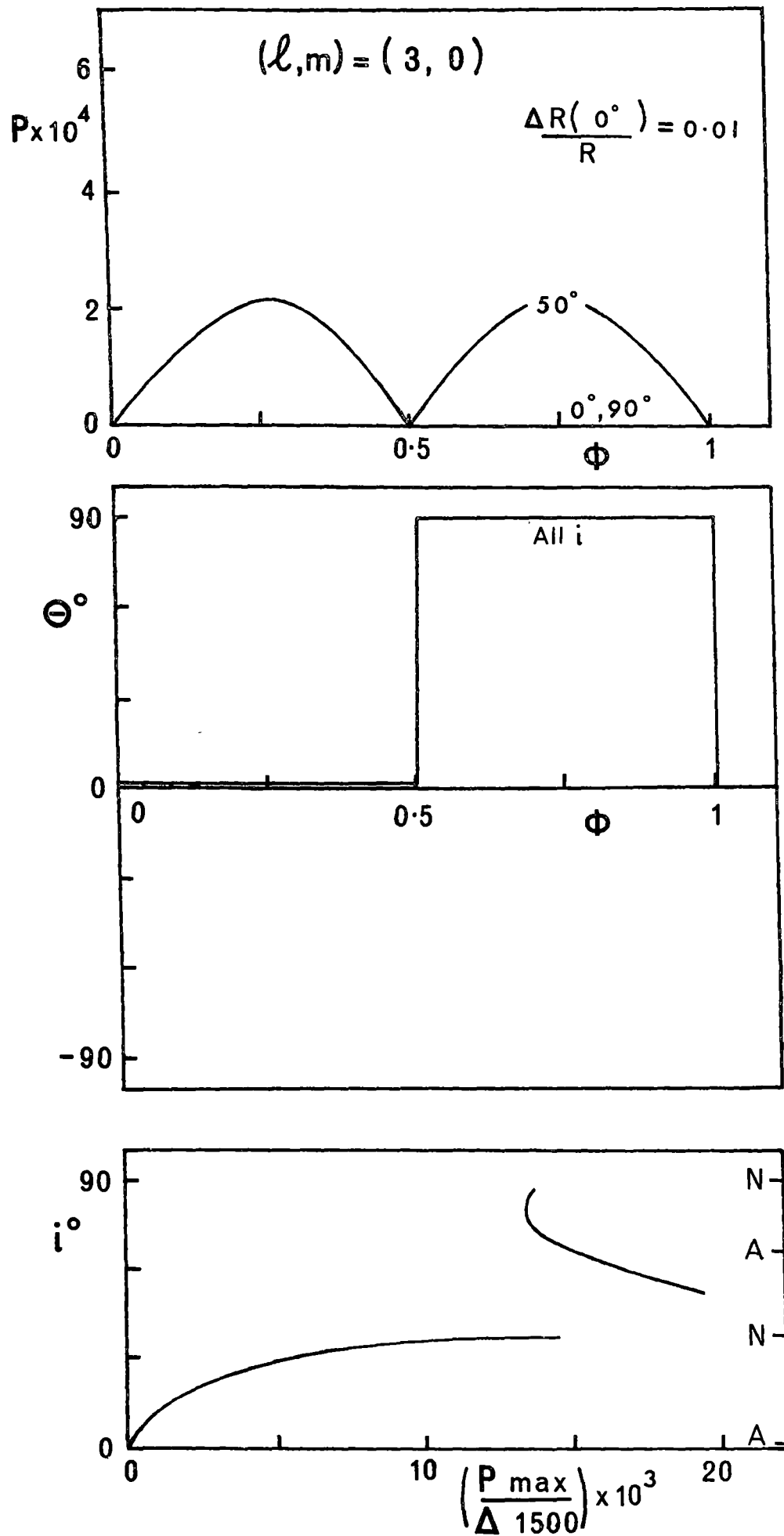


Figure 4.3(d) Polarization curves for the (3,0) mode.

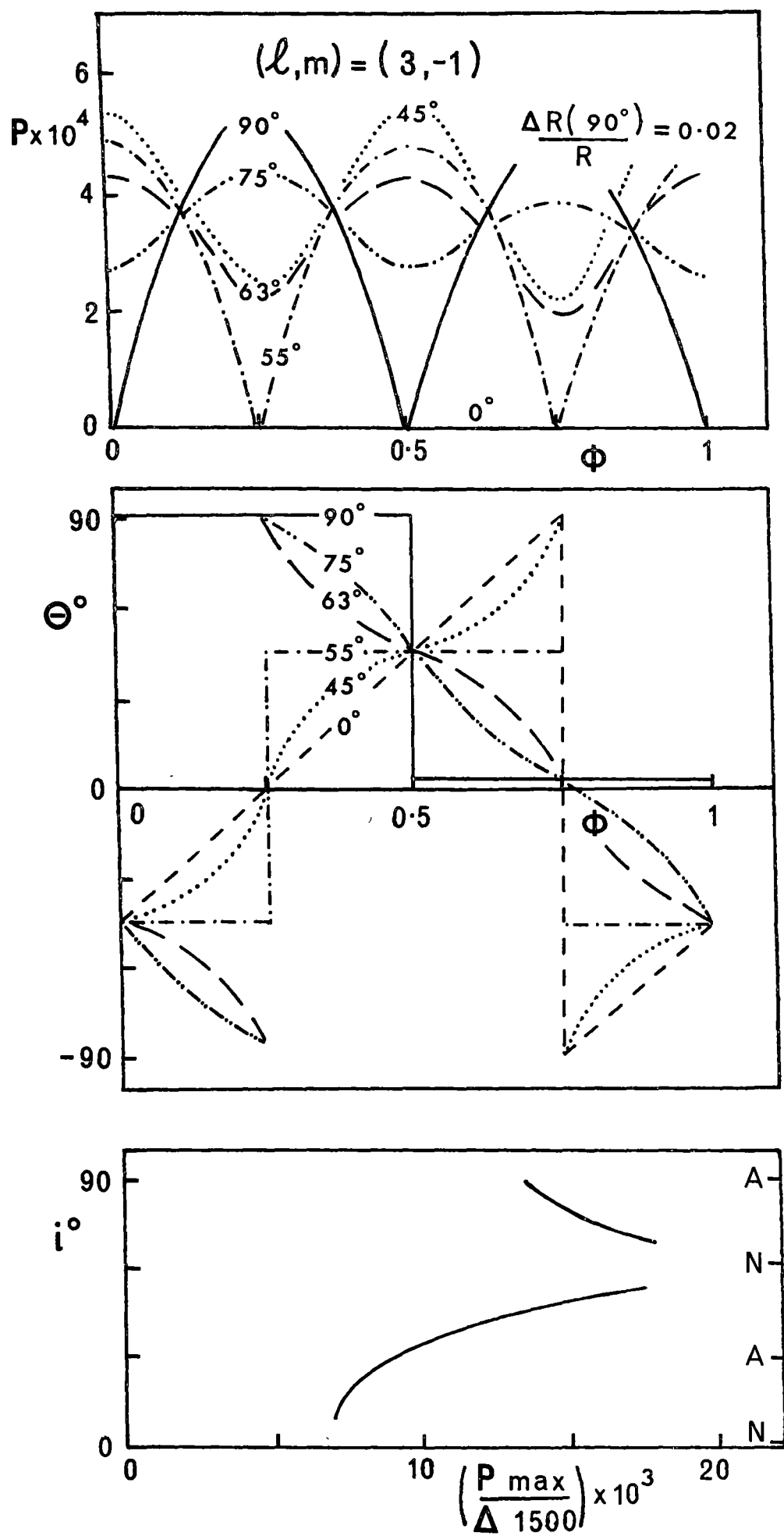


Figure 4.3(e) Polarization curves for the (3,-1) mode.

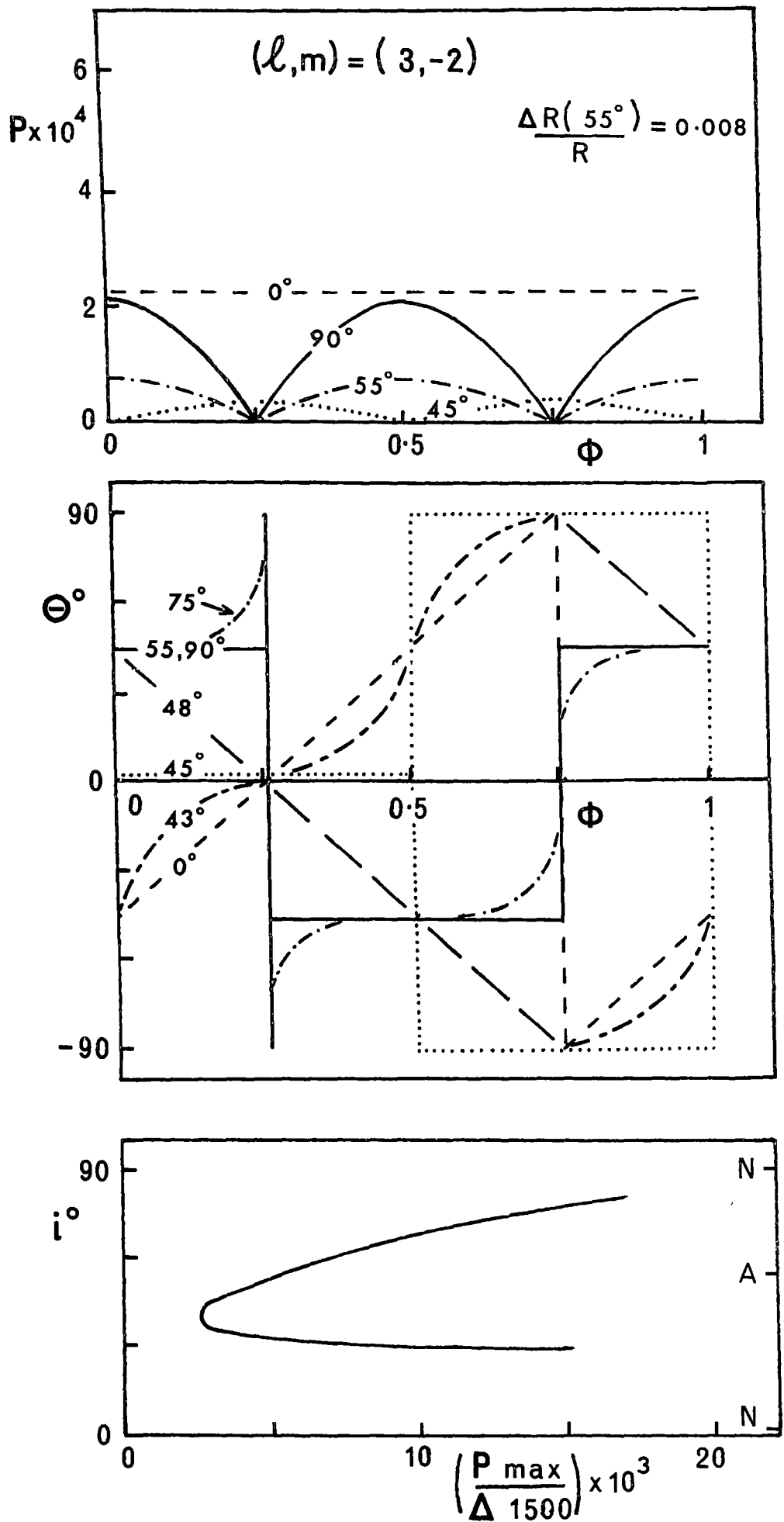


Figure 4.3(f) Polarization curves for the (3,-2) mode.

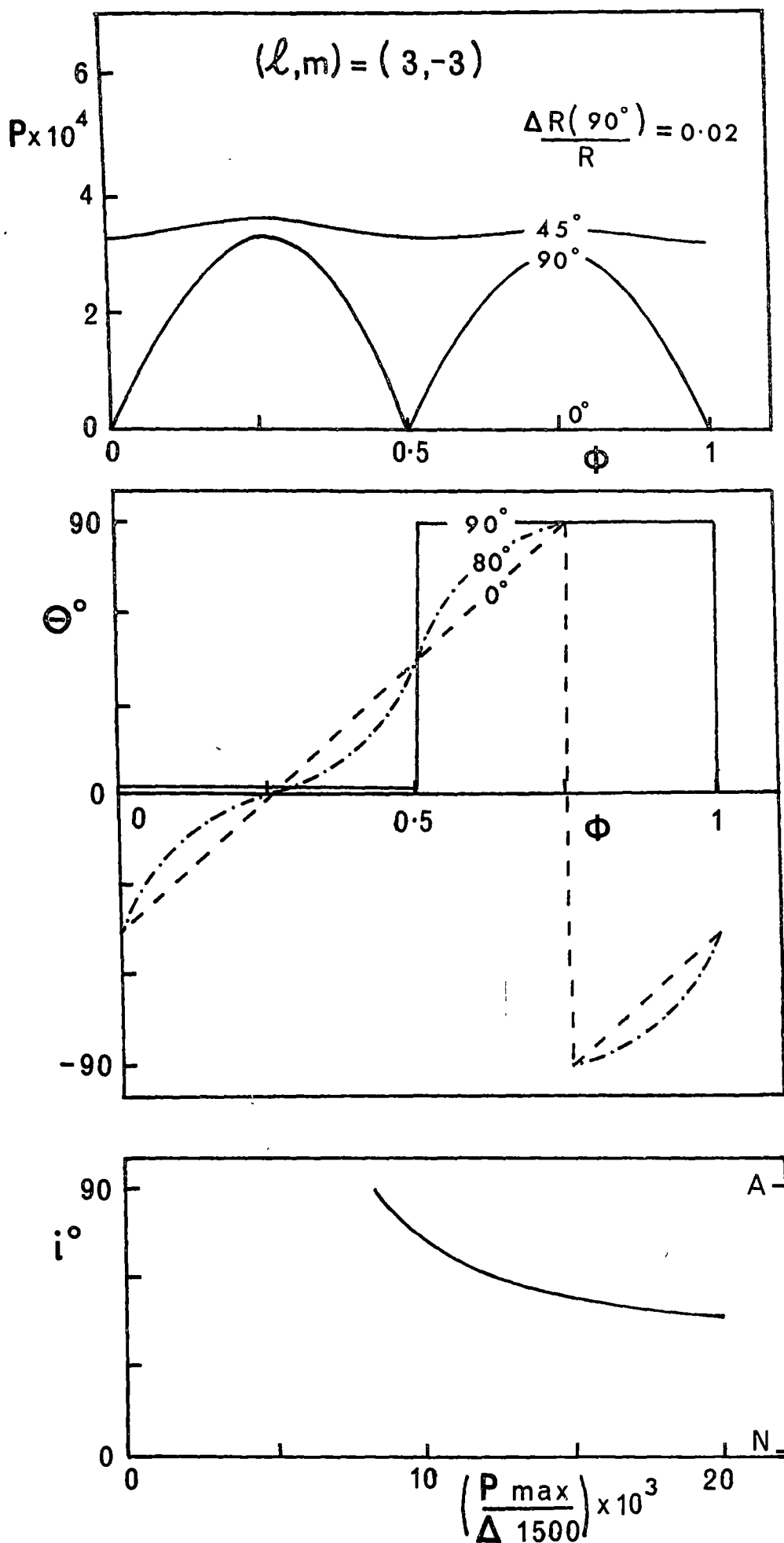


Figure 4.3(g) Polarization curves for the (3, -3) mode.

proposal or from statistical arguments, can be used to predict the value of P_{MAX} . The expected Φ variability of P and θ is then determined from the top and middle panels in Figure 4.3. Tests using the (30000, 3.5) and (22500, 4.0) atmospheres at the same B , imply that Figure 4.3 may be satisfactorily applied to predict P_{MAX} for hot variables anywhere near the β Cephei strip to within about 40 percent accuracy. For a variable with $(T_e, \log g) = (16000, 4.0)$ use of Figure 4.3 gives P_{MAX} too high by a factor of two. Grossly non-adiabatic conditions would naturally require a separate treatment. It is of course possible to use 2K data to predict a P_{MAX} at some proposed i , but this procedure is sensitive to the assumed B value and to any difficulty associated with line profile structure. Figure 3.3 and Figure 4.3 in combination would enable this approach to be executed if necessary.

4.3.2 (P, θ, Φ) Results

The general character of the Φ dependence of all the modes in Figure 4.3 is similar. When a variation in P appears it has two maxima per period, while θ takes on either stepwise or linear changes with time. For the $m = 0$ modes the double maximum P variation and stepwise θ variation is true for all i . For the other modes, the double maximum P variation degenerates to a fairly constant P and a linearly changing θ outside restricted ranges of i . For the (2,0) and (2,-1) modes maximum polarization is seen equator-on, dropping to zero when pole-on. For the (2,-2) mode polarization is seen at all inclinations rising to a maximum when pole-on. The (3,0) mode only gives polarization at intermediate inclinations, with maximum values occurring for $i \sim 50^\circ$. The (3,-1) mode shows complex changes with i . The equator-on double maximum reduces to an approximately constant P for $i \sim 70^\circ$ with the Φ dependence of θ becoming linear at this point. For smaller i another double maximum effect appears, out of phase with the original one. This strengthens to give a stepwise variation in θ for $i \sim 55^\circ$.

and maximum values of P comparable with the equator-on situation. Beyond $i \sim 45^\circ$ polarization drops steadily to zero and θ changes linearly with time, though in the opposite sense to that prevailing for $i \sim 70^\circ$. For the (3,-2) mode polarization effects are seen at both $i = 0^\circ$ and $i = 90^\circ$ but become small for i between 45° and 55° . The θ variation is stepwise for $i = 90^\circ$ and stays close to this until $i \sim 55^\circ$. It then becomes linear by $i \sim 48^\circ$ and returns to a stepwise change by $i \sim 45^\circ$ subsequently going steadily back to a linear change in the opposite sense as the pole-on situation is approached. The complex changes in the θ variation between $i \sim 55^\circ$ and $i \sim 45^\circ$ in this (3,-2) mode should be treated with some reservation. They are occurring for small model P values and hence are sensitive to numerical inaccuracies in our modelling. The (3,-3) mode has maximum polarization seen at large i and this drops to zero when pole-on. The $P_{\text{MAX}}/\Delta(1500)$ graphs in Figure 4.3 show singularities at surface nodes (N), where $\Delta(1500) = 0$. The results are numerically indeterminate if $P = 0$ at the same i .

4.4 DETECTABILITY CONSIDERATIONS

Next the central question of the detectability of the variable polarization is considered. Without a specific satellite-based observing system in mind, this procedure must of necessity be somewhat arbitrary. It was approached as follows. The work of Schafgans and Tinbergen, together with comments by Serkowski (1962), suggests that a constant magnitude $P \sim 3 \times 10^{-4}$ would, with optimal conditions over a 4-hour monitoring time, which is typical for β Cephei stars, enable the positive detection of an accompanying θ variation, either stepwise or linear. Therefore $P_{\text{MAX}} = 3 \times 10^{-4}$ was taken as an approximate detectability threshold even if P drops to zero twice during the period. Fourier techniques could naturally improve the detectability at the

expense of much observing time. Although the $P_{MAX} = 3 \times 10^{-4}$ criterion comes from ground-based experience, it is assumed to give a rough guide to the satellite situation since lack of atmospheric scintillation may partially make up for a smaller aperture in an orbiting polarimeter.

In Table 4.2 the detectability of the polarization in the $l = 2$ and 3 modes is summarized. The data listed there are the minimum values of $\Delta(1500)$ which would ensure that $P_{MAX} \geq 3 \times 10^{-4}$ for all $i > 45^\circ$. This table may then be used, in a statistical sense, to discuss detectability. For the β Cephei stars, observed $\Delta(1500)$ values are large enough in almost all cases to permit detection of modes such as $l = 3, m = 0, \pm 1, \pm 3$ if they are present. However, only a few larger amplitude members have the $\Delta(1500) > 0.17$ necessary for detection of the much discussed $(l, m) = (2, \pm 2)$ modes. The minimum visual light ranges required for detection of the 1500 \AA polarization are less than the $\Delta(1500)$ values in Table 4.2 by a factor of about two for the $l = 2$ modes and by a factor of about four for the $l = 3$ modes. This can be seen from Figure 3.3.

Calculations of P for the $l = 2, 3$ modes at 4400 \AA using the standard (23000, 3.6) atmosphere showed that P_{MAX} values are down by a factor of *fifteen* on those at 1500 \AA for similar B and $\Delta R(\theta_A)/R$. Thus when $\Delta(1500)$ for a mode is as given in Table 4.2, visual P_{MAX} values are a factor of fifteen below the 3×10^{-4} criterion. This rules out

TABLE 4.2: Polarization detectability thresholds for $i > 45^\circ$.

| $\Delta(1500)$ in magnitudes | | | | |
|------------------------------|------|------|------|------|
| l | 0 | 1 | 2 | 3 |
| m | | | | |
| 0 | none | none | 0.07 | 0.02 |
| 1 | | none | 0.14 | 0.03 |
| 2 | | | 0.17 | 0.12 |
| 3 | | | | 0.04 |

the use of visual data in all stars except BW Vul and even then the use is limited to some of the $l = 3$ modes. Observations with a satellite polarimeter are thus recommended. We finally note that if a periodic polarization change is detected in a particular star, the polarization to light range ratio observed may be of some use in assignment of a particular mode if a further constraint on i is available. The Φ dependence of (P, θ) will not be useful in identifying a particular mode because of similarities between modes.

4.5 DISCUSSION OF INDIVIDUAL STARS

Here some of the larger amplitude variables are discussed in the context of recent specific suggested modes for particular stars and the polarization expected in such cases.

4.5.1 *BW Vul*

This has by far the largest amplitude light variations of any β Cephei star. Lesh (1978) gives a $\Delta(1500) = 0.66$. The wavelength dependence of the light range, as shown in Chapter 3 and discussed by Stamford and Watson (1978a), suggests that this star undergoes radial pulsation. The spectral line variability would, in this case, be primarily a shock effect. Models by Stamford and Watson (1978b), which are discussed in detail in Chapter 6, suggest that this is feasible. Evidence for shock effects in other β Cephei stars, as described by Campos and Smith (1980), also encourages this possibility. If this interpretation is correct, no variable polarization should be found. The spectral line variability has, however, led to the suggestion of specific nonradial modes, though these have not been tested by quantitative fitting of accurate profiles over a cycle. Kubiak (1978) proposes that a $(2, -1)$ mode seen near $i = 60^\circ$ might be suitable. Stamford and Watson (1976) had also noted this configuration.

Reference to Figure 4.3 shows that for the observed $\Delta(1500)$ of BW Vul we expect $P_{\text{MAX}} \sim 20 \times 10^{-4}$ at 1500 \AA . This should be readily detectable. The (2,-2) mode, seen at $i = 90^\circ$, as discussed by Smith (1977) for instance, would also produce a readily detectable $P_{\text{MAX}} \sim 12 \times 10^{-4}$. Visual P variability, being a factor of fifteen down on the 1500 \AA values, may not be detected in these two favoured nonradial modes unless extensive observation and accompanying Fourier analysis is undertaken. Modes such as $l = 3, m = 0, \pm 1, \pm 3$, which have not been specifically suggested for BW Vul, would in principle produce visual polarization effects if they were responsible for the observed light changes. However, they would require large nonlinear surface motions to do so.

4.5.2 σ Sco

Beeckmans and Burger (1977) give $\Delta(2110) = 0.176$ for the large amplitude long period oscillation in this star. The steeply increasing amplitude as a function of wavelength would give this star $\Delta(1500) > 0.20$. The wavelength dependence of light range (Stamford and Watson, 1978a) and the line profiles (Campos and Smith, 1980) argue for a radial pulsation for the line-broadening mode. No recent specific nonradial modes have been proposed for this star, but the ultraviolet amplitude is sufficient for the detection of any $l = 2$ or $l = 3$ mode with $i > 45^\circ$.

4.5.3 12 Lac

This star may offer the best chance of detecting variable polarization. A detailed discussion of it is left until Section 4.6.2 after the complications of multimode pulsations have been considered in Section 4.6.1.

4.5.4 β Cep, ξ^1 CMa, HR 6684

Of the remaining β Cephei variables observed in the satellite ultraviolet, these have the largest light ranges. Arguments based on pulsation amplitude spectra indicate all three may be pulsating radially. The line profile studies of β Cep by Campos and Smith (1980) support the radial pulsation concept for that particular star. Kubiak (1978) on the other hand argues that $l = 1, 2$ modes with $m = 0$ must still be considered as possible. The $\Delta(1550)$ data of Hutchings and Hill (1977) and Beeckmans and Burger (1977) imply $P_{\text{MAX}} \sim 6 \times 10^{-4}$ at 1500 \AA for a high inclination (2,0) mode in these three stars. Thus this hypothesis can be tested. It can now also be seen that Schafgans and Tinbergen's (1979) null result in monitoring polarization of β Cep in the visual does not rule out the presence of any nonradial modes.

4.5.5 53 Per

This star is the prototype of a group of variables identified by Smith (1979a). These variables exhibit changes in line width and symmetry but little in the way of radial velocity change. This is taken as evidence for nonradial surface motions. They also have highly unstable periods, changing frequently from one period to another. Buta and Smith (1979) report six different periods from 3.6 to 45 hours being present in 53 Per on different occasions. During late 1977 and 1978 a pair of close modes with periods near 45 hours was dominant. A variety of arguments led Smith and Buta (1979) to identify these modes as (3,-3) and (3,-2).

Simply as an example of what might be possible with this star, a specific polarization calculation was undertaken using the (16000,4.0) atmosphere and a (3,-2) mode seen at $i = 60^\circ$ with a 45-hour period.

These parameters were taken from Smith and Buta (1979), and, under adiabatic conditions, correspond to $B \sim -60$. For a $\Delta R(90^\circ)/R = 0.01$ one obtains, using Equation 2.20, $2K \sim 12 \text{ kms}^{-1}$ and $\Delta V \sim 0.03$.

These are not unreasonable values for this star. With this configuration we obtain a $P_{\text{MAX}} \sim 12 \times 10^{-4}$ at 1500 \AA , which would be readily seen. However, Buta and Smith argued that temperature effects contributed little to the light amplitude when the 45-hour period was present. Repeating the calculations with $B = 0$ shows a negligible polarization in this extreme. Thus the actual polarization effects in 53 Per are highly uncertain due to nonadiabatic effects as well as the different pulsation modes possible with time. However, some polarization monitoring may be worthwhile since it is possible that, under some conditions, the variations may be detectable.

4.6 POLARIZATION OF MULTIMODE PULSATORS

4.6.1 *Relation to Separate Modes*

Because they are directly related to the extent of stellar surface distortion, the Stokes parameters of a pulsation mode increase in proportion to the pulsation amplitude within the linear regime. Trial calculations with the numerical polarization model confirm that this linearity holds for superimposed modes. Thus the Stokes parameters of the combined modes are simply the sum of the total Stokes parameters of the individual modes. That is

$$\left. \begin{aligned} I &= I_0 + \sum_{i=1}^n \Delta I_i ; & Q &= \sum_{i=1}^n Q_i \\ U &= \sum_{i=1}^n U_i ; & V &= \sum_{i=1}^n V_i = 0 \end{aligned} \right\} \quad (4.8)$$

where the subscripts $i = 1, \dots, n$ refer to the integrated Stokes parameters for the n modes, $I_i = I_0 + \Delta I_i$, and I_0 is the integrated mean

intensity (i.e. mean observed flux). The observables are the degree of polarization, $P = (Q^2 + U^2)^{1/2}/I$ and the polarization angle θ given by $\tan(2\theta) = U/Q$. These are related to the (P, θ) values for the individual modes by

$$\left. \begin{aligned} P^2 &= \sum_{i=1}^n \sum_{j=1}^n P_i P_j \cos 2(\theta_i - \theta_j) \\ \tan(2\theta) &= \left(\sum_{i=1}^n I_i P_i \sin(2\theta_i) \right) / \left(\sum_{i=1}^n I_i P_i \cos(2\theta_i) \right) \end{aligned} \right\} (4.9)$$

providing $\Delta I_1, \dots, \Delta I_n \ll I_0$.

Considering, for simplicity, two interfering modes, there is a beat cycle in polarization associated with that observed in light and radial velocity. The degree of polarization is

$$P = P_1^2 + P_2^2 + 2P_1 P_2 \cos 2(\theta_2 - \theta_1).$$

The value of $(\theta_2 - \theta_1)$ will vary over this cycle causing the polarization amplitude to range between $|P_1 - P_2|$ at beat minimum and $|P_1 + P_2|$ at beat maximum.

4.6.2 Application to 12 Lacertae

This star may be the best candidate for obtaining a positive detection of variable polarization because the pulsation amplitude spectrum, frequency spectrum and line profiles all indicate that the largest amplitude mode is nonradial. Smith (1980a) has acquired high signal to noise Reticon spectra of this star and concludes from these that the frequency triplet found by Jerzykiewicz (1978) corresponds to the (2,0), (2,-1) and (2,-2) modes. The other mode in the closely spaced group of four in the frequency spectrum is identified by Smith as a radial pulsation. The polarization expected from 12 Lac is calculated here by assuming Smith's mode identifications and his

inferred axial inclination of $i = 15^\circ \pm 5^\circ$. According to Smith the spectral data is consistent with nonradial surface velocity ranges of 80 km s^{-1} for each of the quadrupole modes. Using these parameters the degree of polarization and polarization angle for each of the $(2,0)$, $(2,-1)$, $(2,-2)$ modes may be calculated separately and then combined using Equation 4.9. The polarization corresponding to each mode may be evaluated by two methods. The resulting polarization maxima at 1500 \AA , P_{MAX} , are summarized in Table 4.3.

Method 1 employs the light ranges given by Jerzykiewicz (1978) for each of the components. These were converted to satellite ultraviolet ranges $\Delta(1500)$, by use of the quadrupole models of Figure 3.3c. For a $B \sim 2$ to 4 , which brackets the values determined observationally in Section 3.4 for radial pulsations, the resulting $\Delta(1500)$ are insensitive to the exact B value. The $\Delta(1500)$, because they define $\Delta R(\theta_A)/R$ for a specified i and B , enable the direct prediction of (P, θ) for each mode. These predictions are also insensitive to the exact B value because it affects light and polarization similarly. They demonstrate that the polarization should be dominated by the $(2,-2)$ mode. The inferred P values of the $(2,0)$ and $(2,-2)$ modes are sensitive to the particular inclination angle

TABLE 4.3: Polarization maxima for 12 Lac.

$P_{\text{MAX}}(1500 \text{ \AA}) \times 10^4$

| (ℓ, m) | Method 1 | Method 2 | |
|-------------|----------|----------|---------|
| | | $B = 4$ | $B = 2$ |
| $(2,0)$ | 0.3 | 0.7 | 0.5 |
| $(2,-1)$ | 0.5 | 2 | 1.3 |
| $(2,-2)$ | 12 | 7 | 4.5 |

assumed here. A change of $\pm 5^\circ$ in i can cause up to a 50 percent change in the corresponding P_{MAX} values in Table 4.3.

Method 2 uses the quadrupole surface velocity ranges of 80 km s^{-1} given by Smith (1980a). For a pulsation period of 4.6h and an assumed stellar radius of $8.5 R_\odot$ (Lesh and Aizenman, 1978), nonradial surface displacements of ~ 3.5 percent are required at the antinode of each mode. (P, θ) results were obtained for these values of $\Delta R(\theta_A)/R$ in the two cases $B = 2$ and $B = 4$. From the P_{MAX} values in Table 4.3 it is again apparent that the $(2, -2)$ mode dominates. The result for the $(2, -2)$ mode is insensitive to the assumed i in this method.

The results of Method 2 differ substantially from those of Method 1. This is essentially a reflection of the fact that the inferred $(2, -1)$ and $(2, -2)$ mode amplitudes relative to that of the radial mode are different depending on whether they are obtained from observed light amplitudes or the profile fitting of Smith. The relative mode amplitudes implied by the light and radial velocity frequency analysis of Jerzykiewicz (1978) do not differ greatly, but Smith notes that, when multiple modes are present, radial velocity amplitudes are not always additive as periodogram analyses assume. So the relative amplitudes obtained from nonradial profile fitting can differ considerably from those expected from the radial velocity spectrum. Clearly a further refinement of the model geometry is needed to resolve this discrepancy between the relative light and velocity amplitudes of the $(2, -1)$ and $(2, -2)$ modes.

The significant conclusion here is that, according to both methods the $(2, -2)$ mode should dominate the observations, with only a relatively small beat modulation expected from the other modes. A value of P in the range 4.5×10^{-4} to 12×10^{-4} (depending on the exact model geometry) is predicted. The magnitude of P should remain

relatively constant over the 4.6h pulsation period of 12 Lac but the corresponding θ variation is almost linear with time. With the predicted magnitude of P this should enable the variability in the polarization to be detected by a suitable satellite polarimeter.

4.7 CONCLUSION

It has been shown that realistic atmospheres applicable to B type variables have a polarization which is quite small in the visual range, as is to be expected from the work of Collins (1970) and Haisch and Cassinelli (1976). However, polarization effects comparable to the pure-scattering results of Chandrasekhar (1946) are obtained for wavelengths longer than the Lyman limit. Calculations at 1500 Å showed nonradial surface oscillations would produce sufficiently large variable polarization effects at these wavelengths to be detectable. A consideration of existing periodicity, light and line profile arguments for mode identification suggested that in 12 Lac and 53 Per nonradial modes may be present with an amplitude such that satellite ultraviolet polarization monitoring would show a detectable variation. Similarly, several instances were cited for which the monitoring may produce a significant null result confirming the presence of a radial oscillation.

C H A P T E R F I V E

THE LINE PROFILES

5.1 INTRODUCTION

High resolution spectroscopy of pulsating stars can provide a valuable key to understanding the velocity fields which affect stellar atmospheres. Most importantly, the profile shapes contain information on such stellar properties as the mode index of pulsation m , the rotational velocity and the inclination angle which cannot, at present, be deduced by any other technique. Technological advances in data acquisition have considerably improved the signal-to-noise ratio and the time resolution attained in observing line profiles to the extent that synthetic line profiles constructed theoretically assuming a particular velocity pattern in the stellar atmosphere can now be meaningfully compared with observational data.

Ledoux (1951) first investigated the broadening characteristics of profiles originating from stars undergoing quadrupole oscillations. He showed that a sectoral quadrupole travelling wave can exhibit periodic variations in line profile broadening which are qualitatively similar to the changes observed for some β Cephei stars. Christy (1966) also considered quadrupole oscillations in this context and Osaki (1971) made extensive line profile calculations for this model. This was the state of the 'art' when the work described in this chapter was initiated, however since then interest in nonradial line profile modelling has burgeoned with investigations by Stamford and Watson (1976, 1977), Kubiak (1978), Smith (1977, 1978, 1979b, 1980a,c), Smith and McCall (1979a,b), Smith and Buta (1979) and Campos and Smith (1980). Kubiak (1978) has calculated line profiles and radial velocity curves for modes up to and including $l = 4$. The other works have involved the detailed modelling of observed profile data for individual stars.

This chapter proceeds in the following way. The results of the method of line profile synthesis discussed in Section 2.3 are examined in Section 5.2 where the profile signatures of individual modes are briefly surveyed. In Section 5.3 BW Vul is discussed briefly and the results of the initial attempt to model the profile variations of 12 Lac (as reported in Stamford and Watson (1977)) are described. Then the more recent published work on this star is discussed and the line profile studies of other β Cephei variables and 53 Persei stars by Smith and his co-workers are considered. A discussion of different radial velocity measures and the corresponding correction factors is undertaken in Section 5.4. This is particularly relevant to any attempt to apply the Baade-Wesselink method discussed in Section 2.7' in a nonradial context. Finally in Section 5.5 the assumptions which are embodied in the conventional method of nonradial profile synthesis are examined in detail. Radial and nonradial profiles are compared with accurate flux profiles obtained by solving the transfer equation for a moving and rotating atmosphere in this section.

5.2 NONRADIAL PROFILE CHARACTERISTICS

5.2.1 *A Grid of Profiles*

Nonradial line profiles are sensitive to amplitude, rotational speed and the observer's axial inclination. To investigate the interplay of these contributing influences on the detected profiles for various nonradial orders l and indices m a grid of profiles was calculated in which these parameters were varied. Line profiles were formed according to the technique described in Section 2.3 at v_p/v_e values of 0.1, 0.2, 0.5, 1.0, 2.0 and 5.0 and at inclination angles i of 90° , 67.5° , 45° and 22.5° for $l \leq 3$. Calculations were performed for the $l = 3$ modes at additional angles chosen to coincide with the

oscillation nodes and antinodes. Here v_e denotes the equational rotational speed. v_p is the nonradial velocity amplitude, which is defined here as the velocity semi-amplitude of the dominant surface antinode. This definition is a consistent extension of Osaki's (1971) notation but differs from that used by Kubiak (1978). Time sequences of profiles with identical v_p/v_e (and v_b/v_e) ratios are, of course, identical in shape except for an appropriate expansion or contraction of the wavelength scale to account for the actual magnitudes of the surface velocities. For convenience the v_p/v_e ratio will be referred to as the 'velocity ratio'. Values of the velocity ratio which are much less than unity correspond to a rotation-dominated velocity configuration, whereas a large velocity ratio indicates pulsation dominance.

The grid of profiles generated is displayed in Appendix 6. The phase convention of Osaki (1971) was adopted. In this convention phase $\Phi = 0$ corresponds to a meridian displacement of zero and the meridian velocity having its maximum value towards the observer. The profiles are only plotted for phases between 0.25 and 0.75 because of the mirror symmetry of the velocity curve. Only prograde modes were modelled since the retrograde modes follow simply by time inversion of the prograde mode results about phase 0.5. Prograde modes are in any case indicated by the majority of the observations since line broadening, if it is present, occurs on the descending branch of the velocity curve ($\Phi \sim 0.75$). Radial velocity curves have not been obtained here since, as will be demonstrated in Section 5.4, the velocity characteristics depend strongly on which part of the profile is chosen as the radial velocity measure.

5.2.2 Morphology of Radial and Nonradial Profiles

The general morphology of the line profiles as a function of velocity ratio, inclination and nonradial l and m will now be briefly examined for $l \leq 3$.

1. $l = 0, m = 0$ (radial)

As the velocity ratio is increased, the line profile at maximum expansion velocity changes from a rounded form (rotation dominated) to a quasi-triangular shape (pulsation dominated). If the rotational velocity is increased with the pulsation amplitude held constant, the profile asymmetry increases and the line core displacement also increases. The dependence on i is such that conserving $v_p/v_e \sin i$ preserves the profile shape.

2. $l = 1, m = 0$

The profiles for this mode are similar to the radial profiles for $v_p/v_e < 2$ at all inclinations. At larger velocity ratios the $\Phi = 0.5$ profiles assume a shallow, rectangular shape betraying the nonradial character of the oscillation. The aspect dependence is weak.

3. $l = 1, m = -1$

The line profiles for the (1,-1) mode are very similar to the (2,-2) and (3,-3) sectoral modes for $v_p/v_e < 2$. For larger velocity ratios the $\Phi = 0.5$ profiles become rectangular, in contrast with the higher order sectoral modes which are sharply-cored at this phase. Like the (1,0) profiles, the (1,-1) profiles are also insensitive to aspect.

4. $l = 2, m = 0$

These profiles are similar to those for $l = 0$ only for inclination angles $i < 45^\circ$ and small velocity ratios $v_p/v_e < 1$. At larger i the profiles undergo little variation through the cycle and become

increasingly rectangular near $\Phi = 0.5$ as the velocity ratio is increased.

5. $l = 2, m = -1$

The character of the (2,-1) profile variations is very sensitive to i . For $i > 55^\circ$ the lines are sharply-cored at $\Phi = 0.25$ and 0.75 and doubly-cored at $\Phi = 0$ and 0.50 . However at near-polar inclinations, $i < 30^\circ$, the profiles are deep and narrow at $\Phi = 0.25$, changing to a broad and weakly-doubled line at $\Phi = 0.75$. At intermediate inclinations ($30^\circ < i < 55^\circ$) the profiles exhibit a complex behaviour which depends strongly on the actual velocity ratio. The variations are similar to those for $i < 30^\circ$ when $v_p/v_e < 1.5$ but follows those for $i > 50^\circ$ when $v_p/v_e > 1.5$. Thus for $i \sim 45^\circ$ the lines undergo doubling only once per cycle ($\Phi = 0.75$) at low velocity ratios but are doubled twice each cycle ($\Phi = 0, 0.50$) at larger velocity ratios.

6. $l = 2, m = -2$

The profile variations for this mode are the best studied of all the nonradial modes. For $i > 35^\circ$ the profiles are sharp and deep at $\Phi = 0.25$ and broad and shallow near $\Phi = 0.75$, becoming double-cored at this phase for $v_p/v_e > 0.5$. For polar inclination angles the line profiles are more diffuse except for a pronounced central core which is present at all phases and strengthens with increasing velocity ratio.

7. $l = 3, m = 0$

At small velocity ratios the profiles for this mode are similar to those for $l = 0$, however increasing the velocity ratio causes the profile to become rectangular and ultimately weakly-doubled at large velocity ratios. For inclinations $i > 55^\circ$ the variations are small.

8. $l = 3, m = -1$

This mode displays broad lines at $\Phi = 0.25$ and narrow lines at

$\Phi = 0.75$, an effect which becomes more pronounced with diminishing inclination angle. This phase reversal of the normal broadening sequence occurs because at θ less than the node angle of 63.4° the travelling wave motion is retrograde rather than prograde. For $v_p/v_e > 1$ the profiles are double-cored twice per cycle ($\Phi = 0.0$ and 0.5) at all inclination angles.

9. $l = 3, m = -2$

The profiles generated by the (3,-2) mode display a particularly complex dependence on inclination angle and velocity ratio. For $i > 80^\circ$ the profiles are sharp at $\Phi = 0.25$ and 0.75 and broad at $\Phi = 0$ and 0.5 , becoming strongly-doubled at the latter phases for $v_p/v_e > 0.5$. For $i < 45^\circ$ the amplitude and aspect dependence is very similar to that of the (2,-2) mode. This can be readily understood since

$$\xi_p(3, -2) \propto \sin^2 \theta \cos \theta \sin(\sigma t - 2\phi) \propto \xi_p(2, -2) \cos \theta .$$

In the transition region, at inclination angles $45^\circ < i < 80^\circ$, the behaviour of the profiles is extremely complex. For $v_p/v_e < 0.5$ the profile variations are similar to those for $i < 45^\circ$, while for larger amplitude ratios the variations are similar to those for $i > 80^\circ$.

10. $l = 3, m = -3$

The inclination angle and velocity ratio dependence of the (3,-3) mode is also *very* similar to that exhibited by the (2,-2) mode.

11. *Summary*

There are strong generic similarities amongst the profiles resulting from the stationary modes and from the sectoral modes, however the tesseral modes generate a considerable variety of line profile forms. Because of only subtle differences between the profiles for some parameter combinations, it follows, as noted by Kubiak (1978),

that simple criteria for mode identification using line profile data are difficult to establish. Two types of line doubling phenomena were found to occur in the theoretical profiles. The first is that commonly associated with the (2,-2) mode, exemplified by narrow lines at $\Phi = 0.25$ and doubled lines at $\Phi = 0.75$. The second type of line splitting occurs twice during the cycle, at phase $\Phi = 0$ and 0.5. The (2,-1) mode seen at $i > 55^\circ$ typifies this class. Only the first line-doubling scenario appears consistent with the spectral variations reported for members of the β Cephei group. In the next section the origins of these two different mechanisms of line doubling are investigated.

5.2.3 *Nonradial Broadening Mechanisms*

The first and most effective of the two broadening mechanisms mentioned in Section 5.2.2 is referred to here as the 'field-interaction' mechanism. This mechanism is due to the interaction of the pulsational travelling wave with the rotational velocity field. For example, in the case of the (2,-2) mode seen at $i \sim 90^\circ$, at $\Phi = 0.25$ the pulsational and rotational velocity fields in both left and right hand hemispheres cancel, causing a reduction in the overall velocity and generating a deep, narrow line centred at zero velocity. At $\Phi = 0.75$, however, the pulsational and rotational velocities reinforce in both hemispheres causing a broad, shallow profile which becomes distinctly double-cored at velocity ratios comparable to unity.

However, since variations in line broadening and even line doubling can occur for the stationary modes, a second broadening mechanism must be operative. This is referred to here as the 'adjacent-antinode' mechanism. It results from the presence of two or more antinodes within the field-of-view of the observer. For adjacent antinodes the senses of particle motion are reversed and

the two oppositely directed streams of matter will generate a broadened profile at the phase when velocities are maximised. This occurs below the observer twice each cycle, at $\phi = 0$ and 0.5 .

Clearly, only the field-interaction mechanism can be operative in the sectoral modes since for these modes only one antinode in polar angle (at the equator) exists. Conversely, only the adjacent-antinode mechanism can be operative in the stationary modes since there is no azimuthal velocity dependence. This is the origin of the generic similarities amongst these two classes of modes. However, for the tesseral modes, either or both mechanisms can be present, depending on the observer's angle of inclination. At many angles the two mechanisms interact to produce line doubling which is considerably stronger than that achieved by either mechanism independently.

As an example consider the $(3,-2)$ mode which has nodes at the equator and the poles, and antinodes at $\theta_A = 54.7^\circ$ and 144.7° . Because of the equatorial node, the motions in the upper and lower hemispheres are oppositely directed, with the direction of travel prograde in the upper hemisphere and retrograde in the lower. For this reason, when viewed from equator-on, the observed spectral variations occur with twice the oscillation frequency. For $i \sim 90^\circ$, both antinodes are in view and their opposed motions interact with rotation to produce strongly double-cored lines at $\phi = 0$ and 0.50 and broad lines with a sharp central peak at $\phi = 0.25$ and 0.75 . This is shown in Figure 5.1(a). Figure 5.2(a) illustrates the projected velocity fields across the disc at constant polar angle as a function of the longitude ϕ at $\phi = 0.25$. The extremes of $\phi = \pm 90^\circ$ correspond to the limb while $\phi = 0$ lies on the observer's meridian. Values at three polar angles are shown - at the two antinodes and the equatorial node. The individual projected velocity fields corresponding to

$$(3, -2) \quad V_p/V_e = 1$$

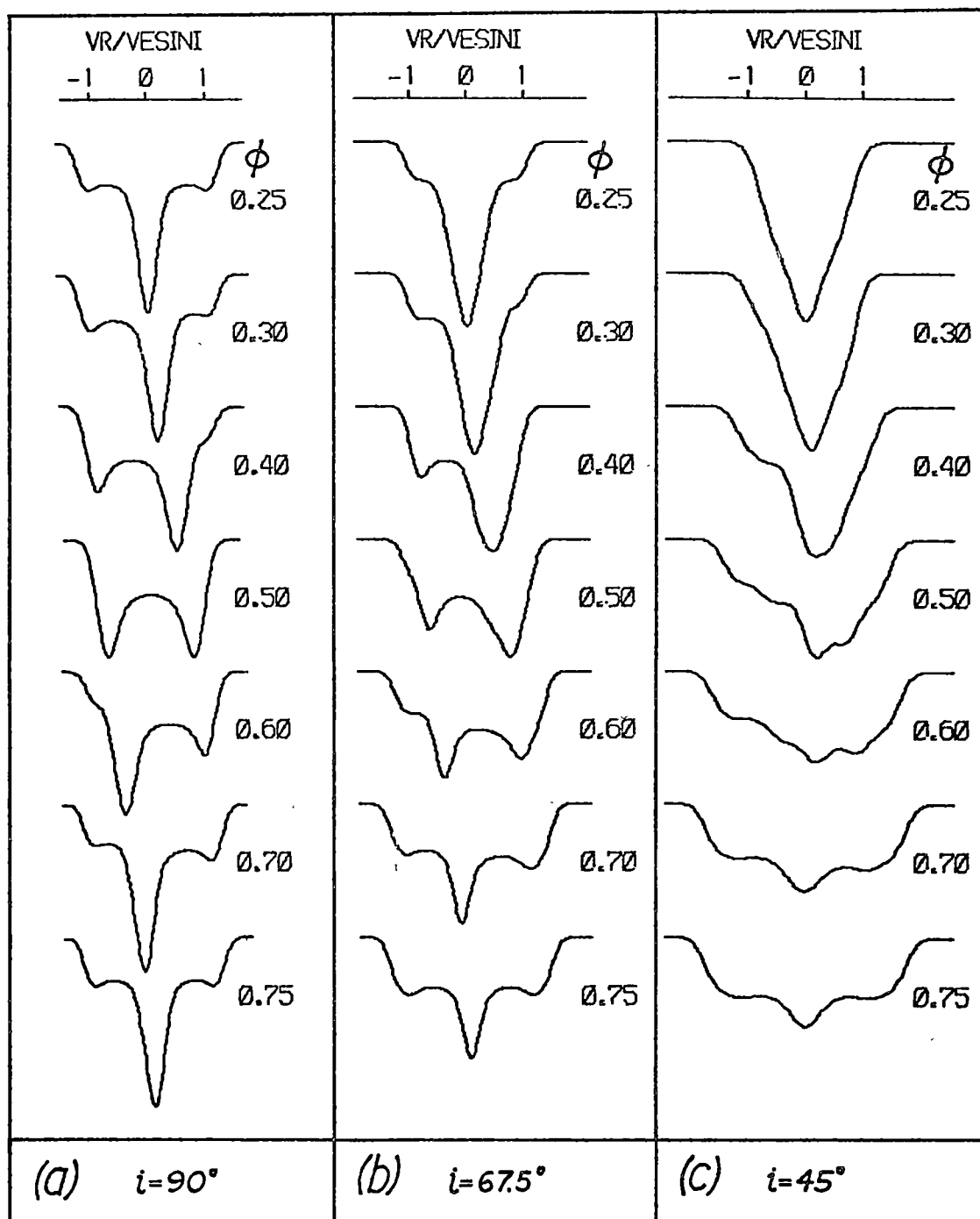


Figure 5.1 Time sequences of line profiles for the (3,-2) mode with $v_p/v_e = 1$ viewed at inclination angles of 90° , 67.5° and 45° .

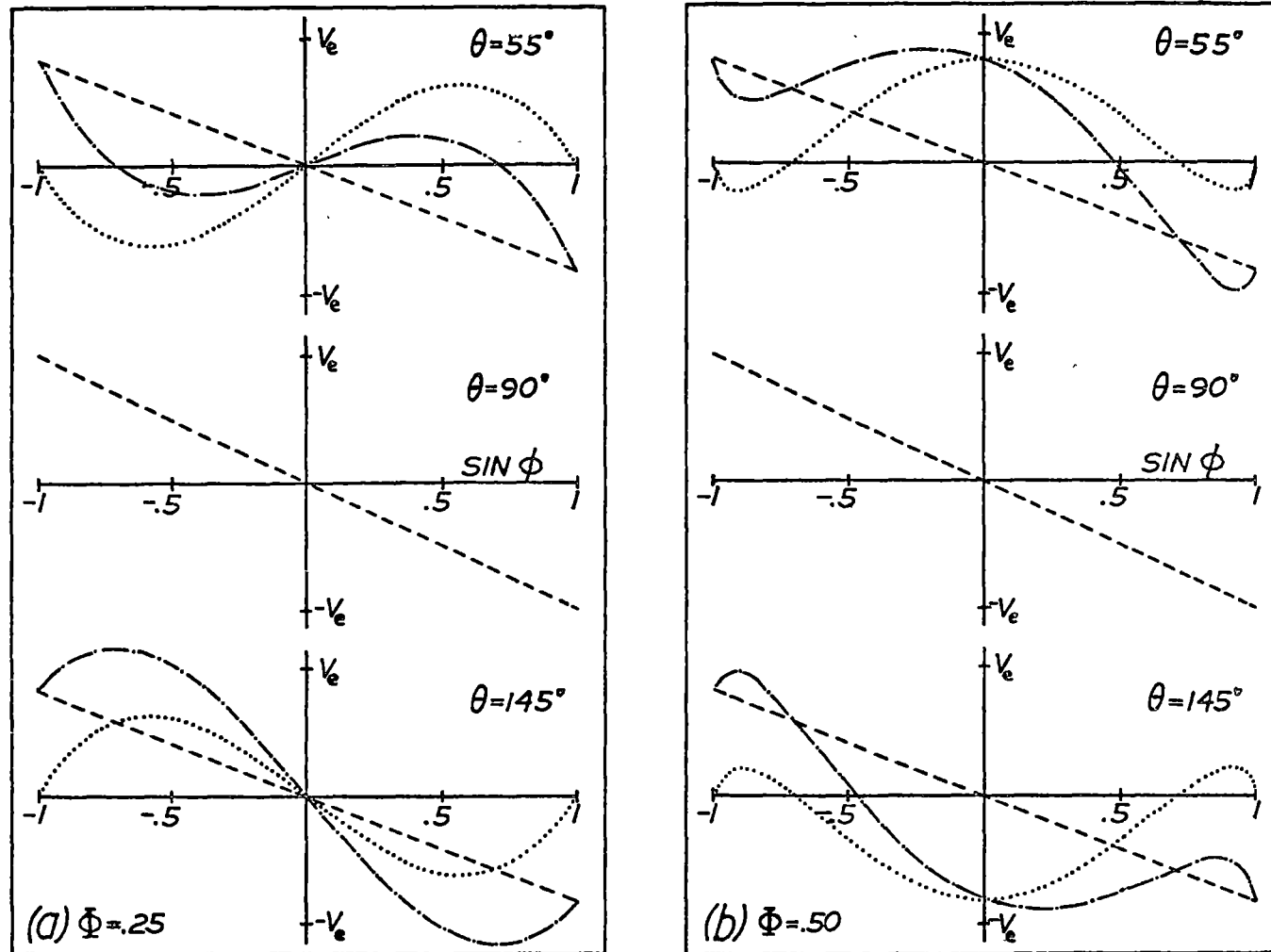


Figure 5.2 Projected velocities at constant polar angle θ as a function of azimuthal angle ϕ for the (3,-2) mode ($v_p/v_e = 1$) seen at $i = 90^\circ$. Dashed lines correspond to projected rotational velocities while dotted lines represent projected pulsation velocities. Dot-dash lines indicate the total resultant projected velocity.

rotation and pulsation are shown separately, together with the resultant velocity for $v_p/v_e = 1$, assuming $i = 90^\circ$. It can easily be seen that in the northern hemisphere at $\phi = 0.25$ the rotational and pulsational velocity fields cancel causing the sharp central peak observed at this phase, while the velocity fields in the southern hemisphere augment to produce the wide shallow base of the observed profile. At $\phi = 0.75$ the upper and lower hemisphere velocities reverse, producing an identical profile to that at $\phi = 0.25$. If the inclination angle is reduced to $i < 45^\circ$, so that the retrograde field of the southern hemisphere cannot contribute, then a single sharp line results at $\phi = 0.25$ and a broad, shallow profile is produced at $\phi = 0.75$. For this configuration the field-interaction mechanism dominates. The resulting line profiles are shown in Figures 5.1(b) and (c). Figure 5.2(b) shows the disposition of the velocity fields at $\phi = 0.50$ for the equator-on configuration of Figure 5.2(a). It can be seen that rotation and pulsation reinforce in the upper left and lower right hemispheres, but oppose in the upper right and lower left hemispheres. This channels the velocities into $\pm v_e$ velocity extremes over half the apparent disc producing a prominently doubled line.

5.3 COMPARISON WITH OBSERVATIONS OF PARTICULAR STARS

5.3.1 *BW Vulpeculae*

BW Vul has been observed recently by Goldberg *et al.* (1976) and Young, Furenlid and Snowden (1979) have formed a time lapse movie of its spectral variations. Stamford and Watson (1976) showed that the stillstand effect displayed by BW Vul can be crudely approximated by a (2,-1) mode seen at an inclination $i \sim 65^\circ$ for a velocity ratio of between 0.5 and 1.5. This possibility has also been investigated by Kubiak (1978) who showed that this particular configuration was capable

of satisfactorily reproducing the large and small amplitude velocity curves of BW Vul obtained by Odgers (1956). Figure 5.3(a) shows a comparison of the velocity curve derived from the line cores of the spectra obtained by Goldberg *et al.* (1976) with the (2,-1) predictions for the same velocity amplitude. The corresponding nonradial line profiles are also presented in Figure 5.3(b). These become doubled near $\Phi = 0.6$. The evolution of the line doublet involves the steady transfer of intensity from the redshifted to the central component of the doublet, in qualitative agreement with the high quality observations of Goldberg *et al.*

However, in spite of this qualitative similarity, it is clear that this identification is very unsatisfactory in many respects. One objection is that the velocity gradient on the rising branch is considerably steeper than that observed. Another objection is that the model predicts an upturned stillstand, contrary to the observations. A further problem is that the data of Goldberg *et al.* reveals that at $\Phi \sim 0.70-0.75$, as the redshifted component of the doubled line decays, it becomes almost totally separated from the stillstand component. The nonradial models do not exhibit such *extreme* splitting. Perhaps the most severe difficulty of a simple nonradial model is its inability to reproduce the pronounced asymmetry of the observed velocity about the axis of zero velocity and about phase 0.75. This could certainly be due, as many authors have suggested, to the influence of hydrodynamic effects on the large amplitude variations of this star. However, BW Vul has a single periodicity only, and since the pulsation amplitude spectra considered in Section 3.4 argued for *radial* pulsations in this star, it is natural to first investigate hydrodynamic effects in the case of radial pulsations. It will be argued in Chapter 6 that the observed line variations in the case of BW Vul are more readily described by a radial shock model without having to resort to nonradial motions to produce line doubling.

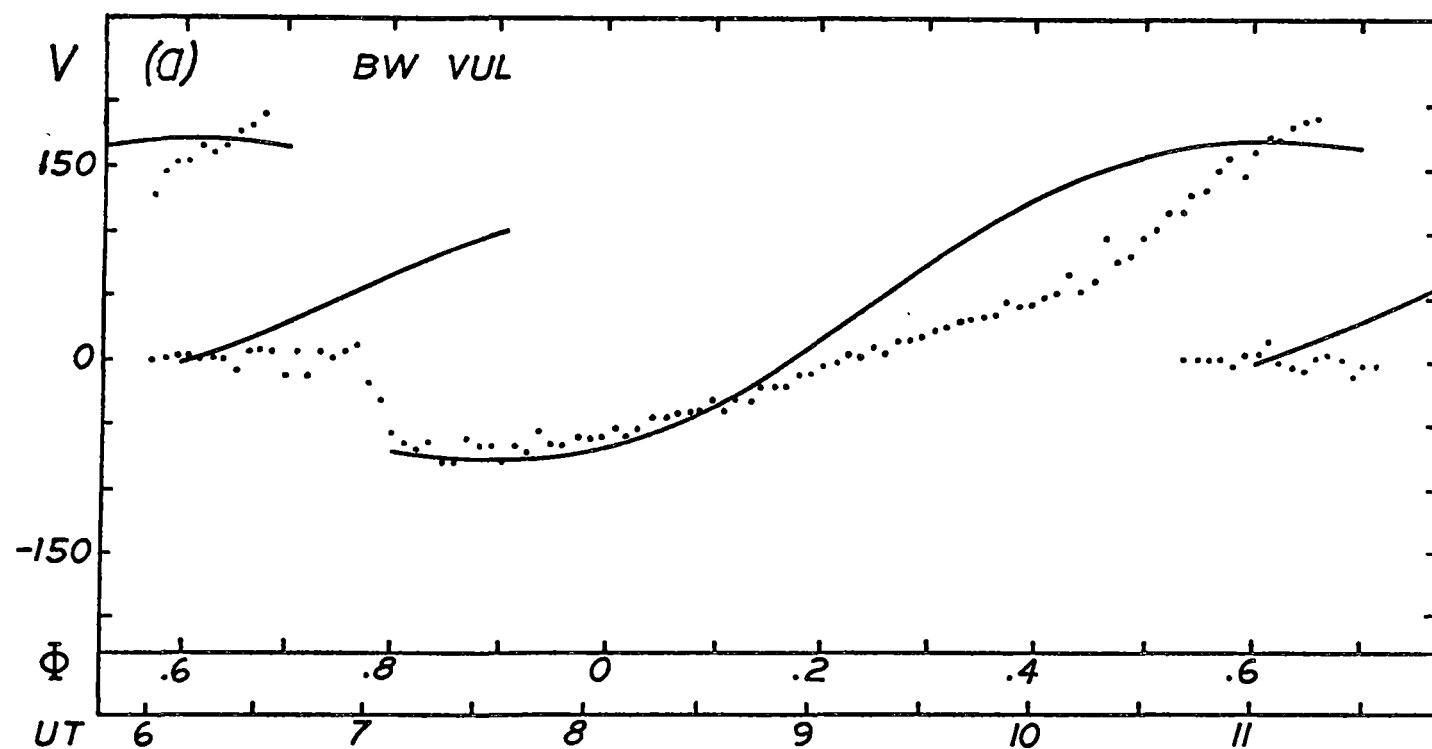
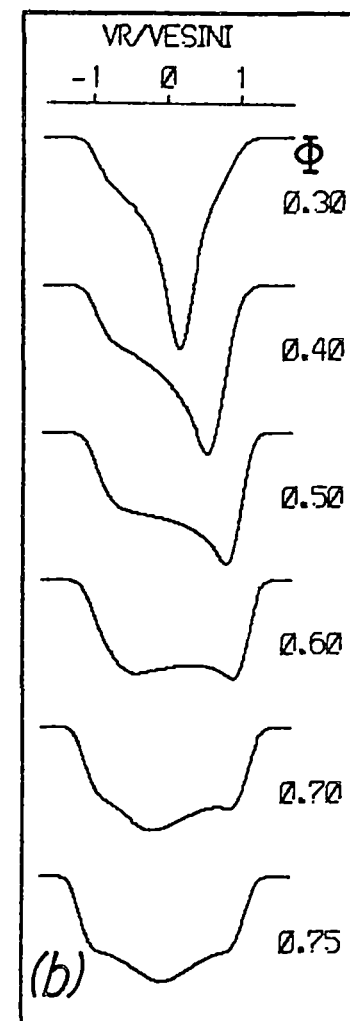


Figure 5.3

- (a) Comparison of observed line core data points for BW Vul obtained by Goldberg *et al.* (1976) with the model line core values for the (2,-1) case of (b). Model values are represented by a solid line. Velocities units are km s^{-1} .
- (b) The time sequence of line profiles for the (2,-1) mode with $i = 67.5^\circ$ and $v_p/v_e = 0.7$.



5.3.2 *Initial Profile Modelling of 12 Lacertae*

The fact that 12 Lac has a smaller ΔV and thus probably smaller pulsation amplitudes than BW Vul, together with the fact that the colour to light ratio of its principal oscillation is consistent with quadrupole oscillations and the knowledge that more than one oscillation is present, encouraged an examination of this star in terms of a simple nonradial model. The following discussion was presented by Stamford and Watson (1977). It represents the first published attempt to model the detailed profile changes of a pulsating star using interfering nonradial modes. The more recent works of Jerzykiewicz (1978) and Smith (1980a), which observationally supercede this work, are then discussed in Section 5.3.3.

It was first necessary to select appropriate spectral lines for comparison with predictions of the nonradial models. This was limited by the requirements that the lines should not be too weak or they would be poorly defined by the observations, and that they should not be too strong with cores arising from very small optical depths. In the latter case, the neglect of progressive wave motion in the models would be of increased significance. The moderate strength Si III lines $\lambda\lambda$ 4552, 4567, and 4574 provide a good compromise in this context. Further, an accurate continuum level could be established in the neighbourhood of these lines. A final desirable point was that lines used should have low pressure and temperature sensitivity so that profile changes reflected the velocity and geometry changes only. In 12 Lac the Si III lines lie near the maximum of line strength as a function of stellar effective temperature according to the data of Watson (1971a). Thus they were at least moderately satisfactory in this regard. Through the courtesy of the staff at David Dunlap Observatory, spectroscopic plate material of Heard *et al.* (1976) were made available

for analysis. These photographic spectra were converted to digital form by Dr. Robert Watson from tracings produced by the PDS microdensitometer of the David Dunlap Observatory. From the numerical data for the Si III lines on each plate a mean profile was formed. The instrumental convolved into these final observational profiles was approximately a Gaussian with a full width at half maximum of 0.35 \AA .

To quantify the line variations the approach of Heard *et al.* (1976) was followed in using $W(0.5)/\bar{W}(0.5)$, the line width at half-depth normalized by the mean width over a complete cycle. To define the changes near the core the quantity $W(0.85)/\bar{W}(0.85)$ was used, and a further characterization of changes was given by the normalized line depth D/\bar{D} . The changes in these parameters are shown in Figure 5.4 for the two complete cycles covered by the data. Radial velocity measures based both on line core and midpoint at half depth values are given in Figure 5.5. The variations over the two cycles differ principally in the fact that on 1971 November 8-9 the lines show a clear tendency for doubling at the phase of maximum broadening. This is not apparent in the cycle on 1971 November 1-2. The complete set of profiles for the cycle on 1979 November 8-9 is shown in Figure 5.6.

The fitting of a nonradial $(l,m) = (2,-2)$ and $(2,0)$ model proceeded as follows. The two primary periods in the data of 12 Lac were taken from the analysis of Sato (1973). The main oscillation with $P \approx 0.19308$ day was hypothesized to correspond to $(l,m) = (2,-2)$. The oscillation with $P \approx 0.19738$ day was, following Osaki (1971), assumed to correspond to the $(l,m) = (2,0)$ form. The results were, in any case, not sensitive to the exact form of the secondary oscillation used, the main requirement being that it have small line broadening effects. At that time it was believed (Sato, 1973) that there were

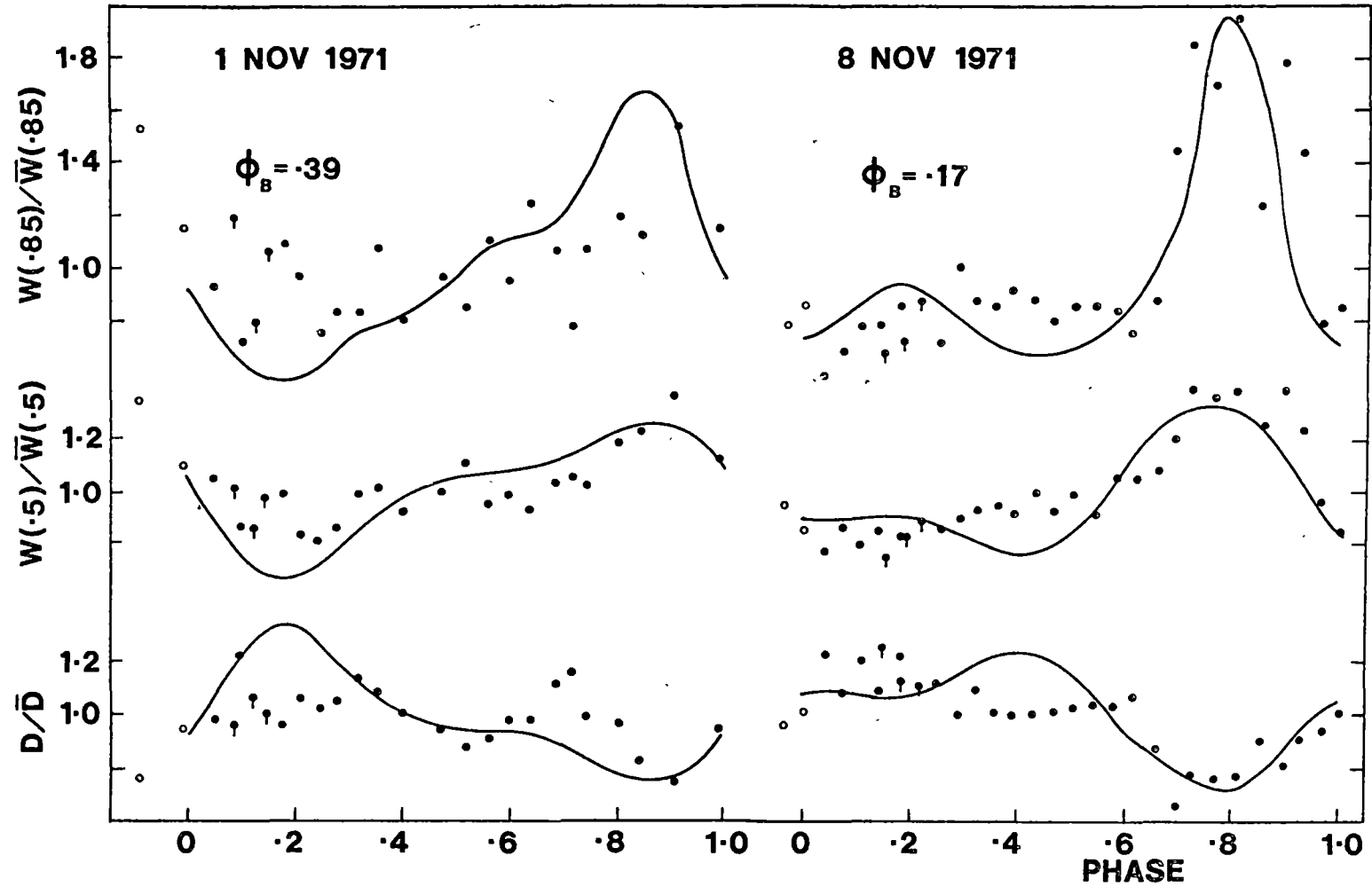


Figure 5.4 Comparison of Si III nonradial model predictions with the 12 Lac observations of Heard *et al.* (1976). The time sequence of observations is folded to cover the corresponding cycle. Observations at the beginning of the time sequence are distinguished with tails until there is no confusion due to overlapping data. ϕ_B is phase in the beat cycle of Sato (1973).

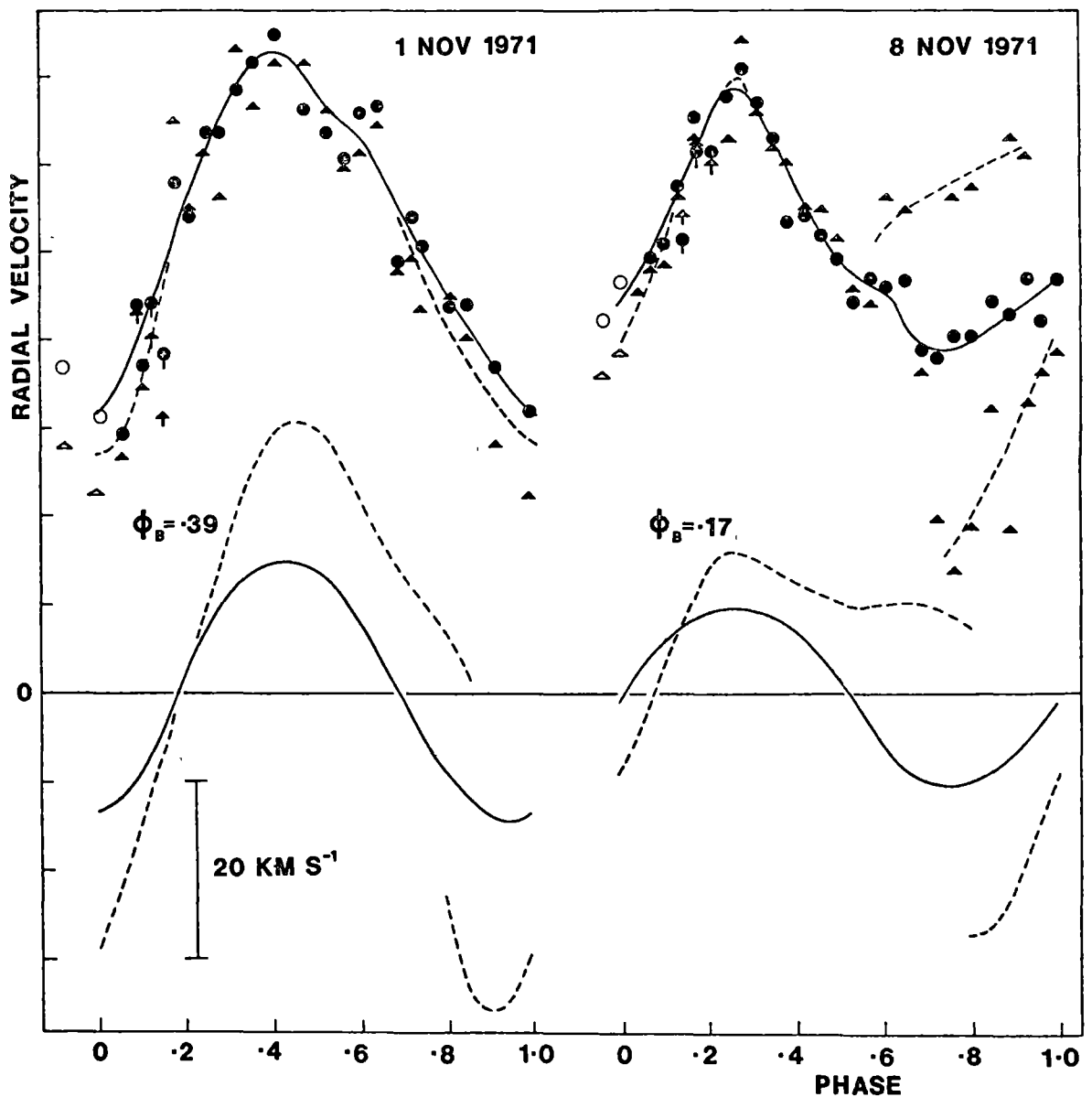


Figure 5.5 Comparison of nonradial model velocity curves with the observed Si III data derived from the material of Heard *et al.* (1976). The zero point of the observed velocity data is arbitrary. The upper panel gives the observations of the midpoints at line half depth (filled circles) and of the line cores (filled triangles), with trend lines sketched in as full and dashed lines respectively. The lower panel gives the corresponding curves from the adopted nonradial model.

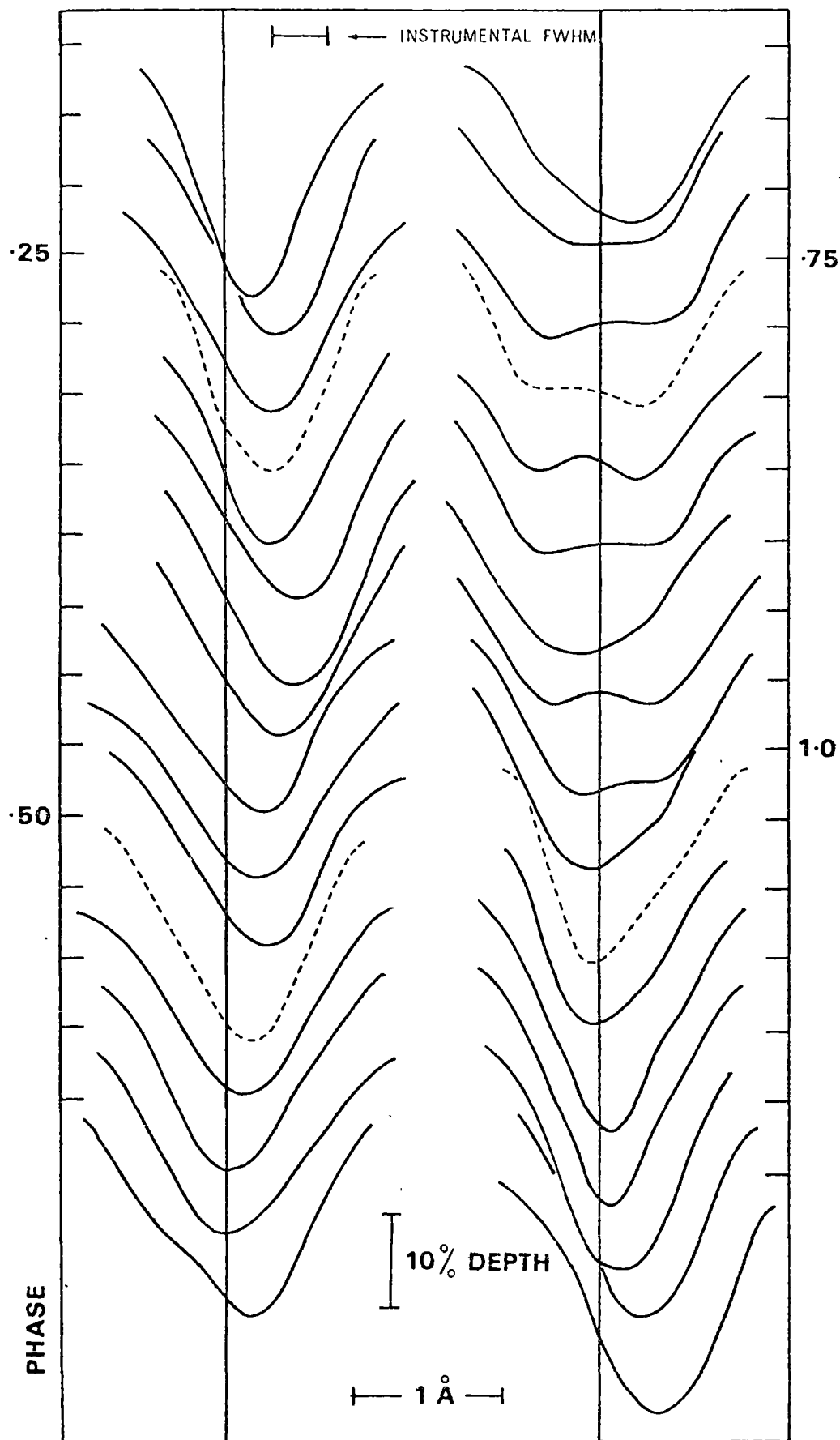


Figure 5.6 The time sequence of Si III profiles (mean of $\lambda\lambda$ 4552, 4567, 4574) in the 12 Lac observations of Heard *et al.* (1976) for the night of 1971 November 8-9. Continuum levels are marked. Profiles of the adopted nonradial model (dashed curves) convolved with the instrumental, are shown for each 0.25 phase and placed in the appropriate location of the time sequence.

two other short periods, each shorter than 4 hours, in the 12 Lac data. No attempt was made to account for these. The 2K values listed in Table 3.1 were assumed to be the core radial velocity ranges of the two oscillations. For the assumed 2K of the $m = -2$ mode, the equatorial velocity amplitude $v_p^{(2)}$ was constrained to be a function of v_e . Hence the amplitudes of the variational parameters $W(0.5)/\bar{W}(0.5)$, $W(0.85)/\bar{W}(0.85)$ and D/\bar{D} were calculated from the models as functions of v_e alone. The instrumental profile associated with the data was convolved with all the calculated models. Reading in the observed amplitudes of the three variational parameters gave an estimate of v_e and hence $v_p^{(2)}$. Further, for the assumed 2K of the $m = 0$ mode, the v_e value which had been already determined enabled a unique $v_p^{(0)}$ to be selected. The determination of the velocity set $(v_p^{(2)}, v_p^{(0)}, v_e)$ of the model was done using one cycle of data, that of 1971 November 8-9, under the assumption that $i = 90^\circ$. Due to the insensitivity of the line structure to the value of i , at least down to $i = 45^\circ$, a successful fitting of the model is not contingent on the $i = 90^\circ$ assumption. A smaller i simply requires larger velocity values for the mode. Amplitudes of $(v_p^{(2)}, v_p^{(0)}, v_e) = (12, 29, 40)$ were found where units are km s^{-1} . This compares with Smith's (1977) values for $(v_p^{(2)}, v_e)$ of (24, 55) and (12, 45), which were obtained by examining the broad line phases of the observations of Allison *et al.* (1977) using an $(l, m) = (2, -2)$ oscillation alone.

Using the derived $(v_p^{(2)}, v_p^{(0)}, v_e)$, a set of model profiles for comparison with the observations was then generated. The beat phase of the two modes in the model was determined from the ephemerides of Sato (1973). For the 1971 November 1-2 cycle $\Phi_B = 0.39$, and for the 1971 November 8-9 cycle $\Phi_B = 0.17$, where $\Phi_B = 0$ is the phase of minimum beat amplitude. The theoretical line variation parameters for the appropriate beat phases are shown in Figure 5.4. Model phase

zero in this figure was taken to be the time of commencement of the outward expansion of the sub-observer point due to the $(l,m) = (2,-2)$ oscillation for the appropriate cycle in the beat. The time sequences of observational data were folded to cover the corresponding cycle for ease of comparison between different nights' observations. Within a particular cycle, the observational data were shifted in phase with respect to the models until the times of maximum and minimum in the observed and model radial velocity curves coincided. This procedure gave a phase uncertainty of approximately ± 0.05 in the location of the model with respect to the observations. Observations of Si III $\lambda\lambda 4552$ and 4567 on 1972 October 15 and 16, as studied by Allison *et al.* (1977), provided a further comparison with the model. These observations are of higher time and wavelength resolution. The $W(0.5)/\overline{W}(0.5)$ and D/\overline{D} expected for these observations were calculated at the appropriate beat phase, using again the model parameters determined from the 1971 November 8-9 data. They are shown in Figure 5.7 plotted against the mean of the $\lambda\lambda 4552$ and 4567 observations.

Consideration of Figures 5.4 and 5.7 shows that, despite some real departures in detail, the nonradial model has considerable success in describing the general character of the line variations. In particular, the duration of the broad lined phase is in reasonable accord with the observations, though the large observational scatter in the 1971 November 1-2 data makes evaluation of that cycle difficult. Amplitudes of the variational parameters in the cycles, other than the cycle on 1971 November 8-9 which was used to establish the model, are also in reasonable accord with the observations. The time of occurrence of the broad-lined phase with respect to the positions of maximum or minimum radial velocity is also reasonably consistent with the model predictions. Thus the fact that the broad line phase occurs

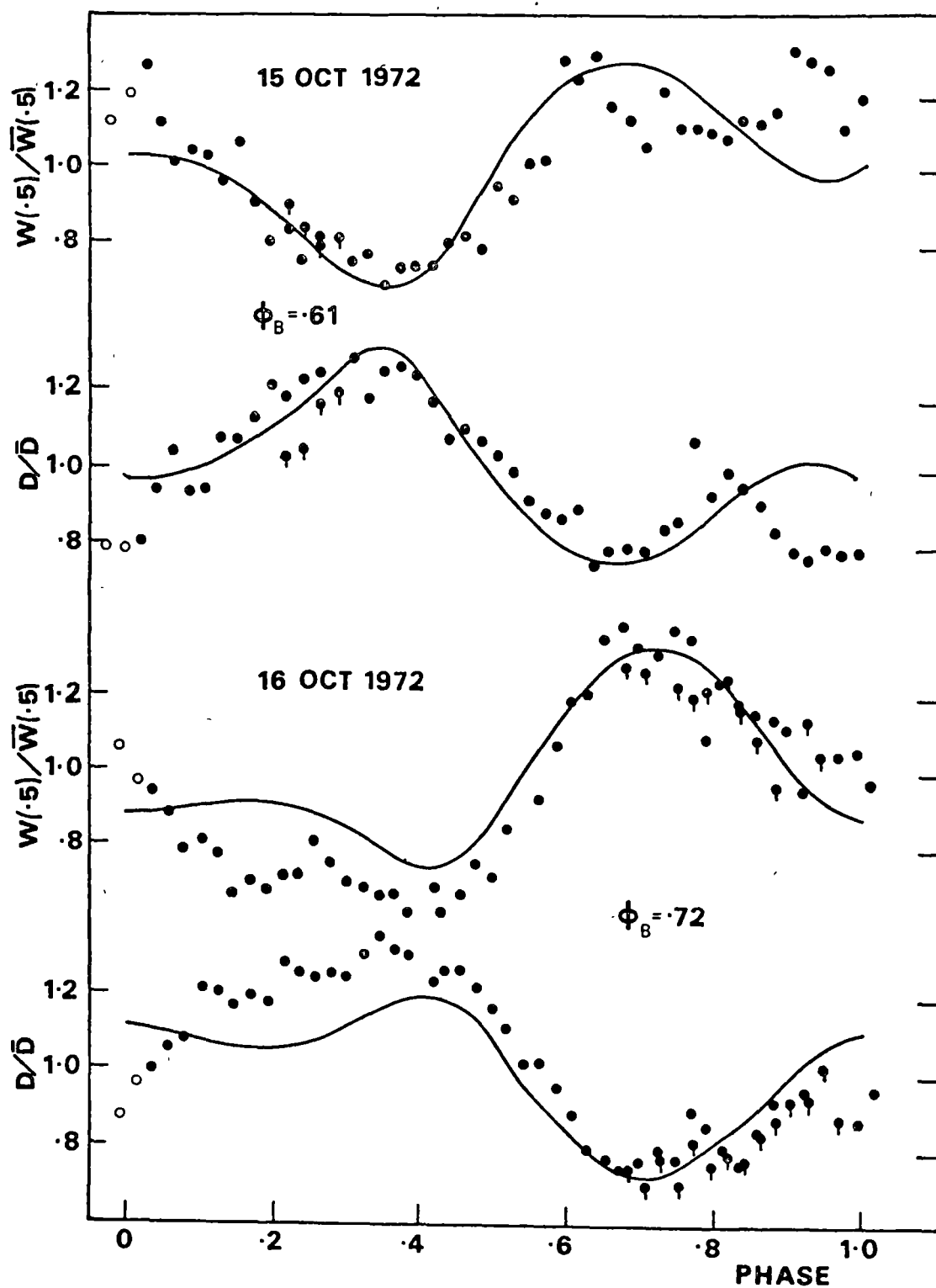


Figure 5.7 Comparison of Si III nonradial model predictions with the 12 Lac observations of Allison *et al.* (1977).

near the bottom of the descending branch of the radial velocity curve in the observations of Heard *et al.* (1976) and nearer the top of the descending branch in the data presented by Allison *et al.* (1977) is simply an artifact of the beating of the two modes.

Model radial velocity curves are plotted in Figure 5.5 for comparison with the observations. There is a clear morphological similarity between the observed and theoretical curves in the existence of a double-branched structure in the core velocities on 1971 November 8-9. There is, however, considerable disagreement in velocity amplitudes, which must be due, in part at least, to the neglect of hydrodynamic effects in the simple models used here. In particular, the model radial velocity curves gave a smaller amplitude for the location of the midpoint of line half depth. This was not reflected in the observations. The applicability of the assumed $2K$ values may also be a contributing factor to the disagreement. The calculated profiles for 1971 November 1-2 had an essentially flat-cored structure at the phase of maximum broadening whereas the calculations for 1971 November 8-9 showed a weak double-humped structure. This is consistent with the fact that the observations show no sign of splitting on the former night but do on the latter night. The presence of detectable line doubling in 12 Lac presumably then depends on the beat phase. Some sample model profiles are shown in Figure 5.6 for comparison with the observed profiles of 1971 November 8-9. Here model profiles were scaled in depth by equating the mean core depth of the model profiles over the cycle to the mean observed depth. Relative wavelength positions were fixed by equating the mean model and observational radial velocities over the cycle. As was indicated by the variational parameters, the model gives a satisfactory representation of the form of the line profiles during this cycle.

In summary, it appeared at that stage that an equator-on (2,-2) oscillation together with another low-broadening mode could adequately represent the photographic spectra.

5.3.3 *Recent 12 Lacertae Models*

Following the publication of the work described in Section 5.3.2, two important contributions to the debate on the modes of pulsation present in 12 Lac have appeared. The frequency analysis performed by Jerzykiewicz (1978) revealed the presence of six sinusoidal components in the light and velocity curves of 12 Lac, three of which form an equidistant triplet. This frequency triplet can be most readily explained by the rotational splitting of three nonradial m -states. Since the primary oscillation (P_2 in the Struve notation) is the lowest frequency member of the triplet, and since the P_1 oscillation is not a member of the triplet, the mode assignments suggested by Osaki (1971) and assumed in the previous section must be incorrect. Jerzykiewicz argued that the triplet members correspond to the $\ell = 3$ prograde modes. However this identification contradicts the evidence of the pulsation amplitude spectrum of this star, discussed in Section 3.4, which strongly suggests that the P_2 mode is quadrupole. Smith (1980a) has used line profile fitting techniques to convincingly demonstrate that the triplet frequencies correspond to prograde quadrupole modes pulsating at equal amplitudes. The P_2 oscillation therefore corresponds to the $(\ell, m) = (2, 0)$ mode, while the P_1 oscillation has been identified by Smith as radial. The P_1 identification is not surprising as the broadening and depth indices used in the investigation of Section 5.3.2 implied the presence of a stationary mode, though discrimination between the various alternatives was not possible. Initially it *does* seem surprising that the line broadening oscillation could correspond to the $(2, 0)$ mode since for many combinations of inclination and velocity ratio this mode displays little variation in broadening. However, examination of the profiles of Appendix 6 for this mode at the appropriate amplitude ($v_p/v_e \approx 1$) and inclination ($i = 15^\circ \pm 5^\circ$) determined by

Smith reveals that they undergo a factor of two variation in width at half-depth. In addition, Smith plausibly argues that the interaction between interfering modes produces profiles which do not resemble those expected from individual modes because of the complex pattern of velocity reinforcements and interferences across the stellar disc.

Experience gained in the attempts to model 12 Lac over the last few years leads to a number of conclusions. The initial reasonably successful attempts of Smith (1977) and Stamford and Watson (1977) in modelling the gross profile characteristics with an apparently incorrect configuration indicates that stringent profile-fitting criteria must be applied before a unique mode identification can be confidently assigned. Otherwise, because of the large number of free parameters (l, m, i, v_p, v_b, v_e) which are capable of adjustment, more than one solution may exist. It seems likely that only exact fitting of long sequences of high dispersion, high quality profiles, as has been achieved by Campos and Smith (1980) and Smith (1980a), can satisfy this requirement. The experience with photographic spectra suggests that these are not sufficiently accurate for this purpose because of signal-to-noise considerations. Further, it is not sufficient to match only a few profiles over the cycle because of the similarity of profiles amongst the different modes, particularly the sectoral modes. Finally it appears that the Struve designation of the line-broadening mode is at best an imprecise guide for mode identification which can be particularly misleading when several modes are present.

5.3.4 *Other β Cephei and Related Stars*

Smith and McCall (1978a) have studied the β Cephei star γ Peg and found that the line profiles could be modelled in detail by assuming radial pulsations, although the possibility of a nonradial stationary mode viewed from near pole-on could not be completely

eliminated. Smith and McCall's investigation revealed the presence of a moving spectral absorption feature, previously reported by Le Contel (1968), which was interpreted as originating from one or more ejected shells. This absorption feature was present in the spectrum of the star over almost the entire pulsation cycle. High dispersion Reticon observations of three other β Cephei stars β Cep, δ Cet and σ Sco were obtained by Campos and Smith (1980) who found similar absorption features in the visual spectrum of σ Sco and the ultraviolet (but not visual) spectrum of β Cep. In all four cases the detailed spectral variations were found to be consistent with radial pulsations. Once again, the possibility of a nonradial stationary wave observed at a pole-on inclination could not be totally rejected. However, on statistical grounds, this must be considered very implausible. Three of these four stars (γ Peg, δ Cet, β Cep) are singly periodic. The fourth, σ Sco, is multiply periodic, but the large amplitude mode which dominates the profile changes is the only one effectively studied by Campos and Smith (1980). The conclusions of Campos and Smith that these four stars are primarily radial pulsators is in full agreement with the mode identifications obtained in Chapter 3 for these stars. These recent successes of the profile fitting method indicate that the technique is finally realising its potential as a powerful mode identification diagnostic.

The line profile fitting techniques used by Smith and his co-workers in their results on line-profile-variable B stars may be summarized as follows. For a suitable equilibrium atmosphere, intensity profiles were generated at different μ -points across the stellar disc. These were then numerically integrated taking account of the projected Doppler motions due to pulsation, rotation and radial-tangential macroturbulence. This process, of course, ignores any differential velocities lying

along an optical path length. Smith then extracted the rotational velocity and macroturbulence from the symmetric profiles, while the observed profile asymmetries and radial velocity range determined the pulsation amplitude. The rotational velocity was then held constant throughout the cycle, while the macroturbulence was adjusted to obtain the best-fit for each profile. The constancy of the latter parameter over the cycle provided Smith with an estimate of the "goodness-of-fit" of the resulting solution. Because of its use of actual LTE profiles over the disc, Smith's method of profile synthesis is more general than the methods of Osaki (1971), Stamford and Watson (1976, 1977) and Kubiak (1978) which assumed a limb darkened profile of fixed shape. The difference between the two approaches is in fact small, as will be seen in Section 5.5.

In a number of recent papers Smith and McCall (1978b) and Smith (1978, 1979a, c, 1980b) have obtained evidence that surrounding the β Cephei strip in the H-R diagram there is a broad region of instability extending in spectral class from O8 to B5. This region is occupied by a class of irregular variables named after the mid-B star 53 Persei. These stars are characterized by periodic changes in the width and asymmetry of line profiles. However they exhibit little change in radial velocity. Unlike the β Cephei stars, the 53 Persei variables possess highly unstable periods, ranging from 3 to 50 hours, which can change abruptly on timescales of only a few days. Smith (1980b) has concluded from line profile fitting that these stars are nonradial pulsators. This view is supported by the long periods which have been observed and the colour-to-light arguments of Buta and Smith (1979) and Smith and Buta (1979). The 53 Persei stars, however, are apparently not the only variables close to the β Cephei region. Between the β Cephei group and the zero-age main sequence Jakate (1979) has discovered a number of early-type ('ultra-short-period') variables with periods of an hour

or less and light ranges of typically ~ 0.02 mag.

The discovery of an apparent widespread instability in the neighbourhood of the β Cephei group may be relevant to the problem of the evolutionary state of the β Cephei stars. Lesh and Aizenman (1978) have argued against the hypothesis that the β Cephei stars are in the core hydrogen burning phase because of the apparent absence of a continuous distribution of variables between the main sequence and the point of hydrogen exhaustion. However, as Jakate has noted, the 'ultra-short-period' variables and the 53 Persei stars may well form part of such a distribution. The extent of stellar instability is also pertinent to the question of the location of the β Cephei instability mechanism within the stars. Osaki (1978) has pointed out that if the instability zone is confined to a narrow strip of the H-R diagram then the deep stellar interior is likely to be responsible for driving the pulsations. This is because the structure of stellar envelopes changes slowly with evolution in this region. Conversely, if the instability zone is widespread, then an envelope excitation mechanism is implied. In this context the envelope opacity mechanism, resulting from the He^+ ionization edge, which has been suggested by Stellingwerf (1978), appears to be the most promising candidate. Related to this is the question of whether the β Cephei, 53 Persei and 'ultra-short-period' variables have similar excitation mechanisms even though the modes excited in these groups are probably quite different. Searches for additional early-type variables may help to resolve this question by delineating the boundaries between these groups, if indeed there are any.

One may attempt to summarize the proliferation of new data into a coherent scenario as follows. Firstly there is now overwhelming evidence that 12 Lac is a *nonradial* pulsator. Three lines of independent evidence - the frequency spectrum, the line profiles and the light amplitude spectrum - concur on this identification. The occurrence of

close periods in other β Cephei stars strongly suggests that many or all of the multiperiodic β Cephei variables support nonradial modes. Secondly, all the evidence is consistent with the fact that the singly-periodic β Cephei variables are *radial* pulsators. Since 12 Lac also supports a radial pulsation, it may be conjectured that *all* the β Cephei stars possess a radial mode which in some cases may drive a nonradial mode or modes of nearly the same frequency. This scenario has been previously suggested by Campos and Smith (1980). Thirdly, there appears to be widespread instability in the general β Cephei neighbourhood of the H-R diagram. Smith (1980b) has interpreted this as indicating an underlying instability of the region to *nonradial* pulsations. However it is difficult to reconcile this assumption with the fact that the singly-periodic β Cephei pulsators exhibit only a *radial* mode. Perhaps the simplest conjecture is that a common instability mechanism, such as that proposed by Stellingwerf (1978), drives the oscillations in these different groups of B-type variables, but that different modes are manifested according to the physical structure, evolutionary state and the effectiveness of mode-coupling.

5.4 RADIAL VELOCITY MEASURES

Radial velocity observations of pulsating stars provide important information on the displacement and acceleration of the pulsating atmosphere, particularly in the case of radial oscillations for which the radial velocity curve can be readily interpreted. However the radial velocity measured from the line profile must be corrected for the centre-of-mass velocity and for foreshortening effects which reduce the true atmospheric velocity. In the nonradial case the local velocity will vary from point to point in the atmosphere and the radial velocity can only be meaningfully interpreted as some average velocity across the apparent stellar disc. A rotational velocity field also

complicates the interpretation even in the radial pulsation case.

Ideally, that part of the profile which is used as a radial velocity indicator should be insensitive both to noise and to the spectroscopic resolution employed. A brief survey of the literature on the β Cephei stars published during the last decade reveals that a considerable variety of indicators have been chosen for these stars. For example, Goldberg, Walker and Odgers (1974, 1976) and Stamford and Watson (1977) used the line core, Kubiak (1972) chose the centre at 75% of the line's depth, Hutchings and Hill (1977) used the mean of values measured from the line centres at 50% and 75% depth, and Stamford and Watson (1977) and Campos and Smith (1980) adopted the centre at 50% depth as a measure. Many authors used a Grant spectro-comparator to determine radial velocities. According to Parsons (1972), this device measures the line centre at $60 \pm 10\%$ of the total central depth. Clearly the conversion factor from the measured radial velocity to the atmospheric velocity depends on precisely which measurement criterion has been utilised.

Using the $60 \pm 10\%$ criterion, Parsons (1972) constructed synthetic profiles for a uniformly moving cepheid model atmosphere and showed that a factor of $p \sim 1.31$ is applicable in converting from measured radial velocities to atmospheric velocities. This compares with the previously used factor $p \sim 24/17 \sim 1.41$ obtained by Getting (1935) in forming the mean line-of-sight velocity over the stellar disc with a limb-darkening coefficient of $u = 0.60$. However Parsons' correction factor suffers from two restrictions. Firstly it cannot be applied when a radial velocity index other than the line centre at 50%-70% has been used. Secondly rotational effects were not included in Parson's analysis. In fact, for radial oscillations, the line core displacement is quite sensitive to rotational fields. Consequently,

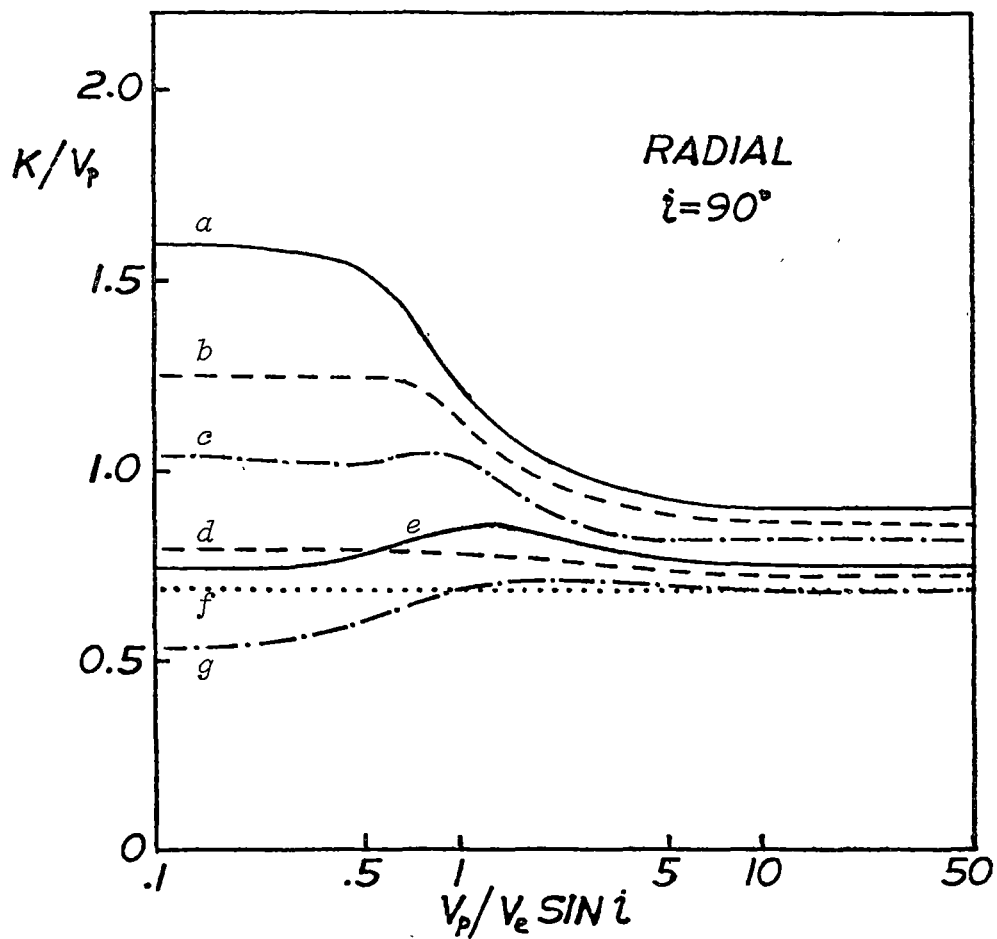
any radial velocity measure which uses the line centre at a depth greater than about 60% of the maximum depth is strongly contaminated by rotation.

5.4.1 *Radial Pulsation with Rotation*

The effect of rotational fields in the radial case is illustrated in Figure 5.8 where the factor $K/v_p = p^{-1}$ is plotted as a function of $v_p/v_e \sin i$ for seven different radial velocity indicators : $v(100\%)$, $v(85\%)$, $v(70\%)$, $v(50\%)$, $v(33\%)$, the median velocity and the mean profile velocity. Here $v(d\%)$ refers to the velocity measured from the centre at $d\%$ total depth - thus $v(100\%)$ refers to the line core. The median velocity is that velocity which divides the line profile into equal areas. The mean profile velocity is defined as

$$\bar{v}(t) = \int_{v_{min}}^{v_{max}} v \left(1 - \frac{F(v, t)}{F_{cont}}\right) dv / \int_{v_{min}}^{v_{max}} \left(1 - \frac{F(v, t)}{F_{cont}}\right) dv \quad (5.1)$$

where v_{max} and v_{min} are respectively the upper and lower velocity limits of the profile. The surface radial velocity amplitude is $v_p = \sigma \Delta R = \sigma R \epsilon$, where $\epsilon = \Delta R/R$. In Figure 5.8 a constant ratio of intrinsic broadening to rotational velocity $v_p/v_e = 0.16$ has been assumed. From this figure it can be seen that the $v(100\%)$ and $v(85\%)$ velocity indicators are particularly sensitive to rotation. This is because the rotation and pulsational fields interact to produce an enhanced profile asymmetry. Increasing the rotational speed at constant pulsation velocity causes an increase of the line core displacement leaving the centre at half depth almost unchanged. Figure 5.9 demonstrates this behaviour. The effect of the interaction of expansion and rotation was previously noted by Thiessen (1957), but largely ignored until the point was raised again by Stamford and Watson (1977) and Duval and Karp (1978). The $v(100\%)$ and $v(85\%)$ indices are also very sensitive to microtubulent

(a) $V(100\%)$ (b) $V(85\%)$ (c) $V(70\%)$

(d) median

(e) $V(50\%)$

(f) mean

(g) $V(33\%)$

Figure 5.8 Velocity correction factor K/v_p as a function of the velocity ratio $v_p/v_e \sin i$ for different radial velocity measures in the case of radial pulsations.

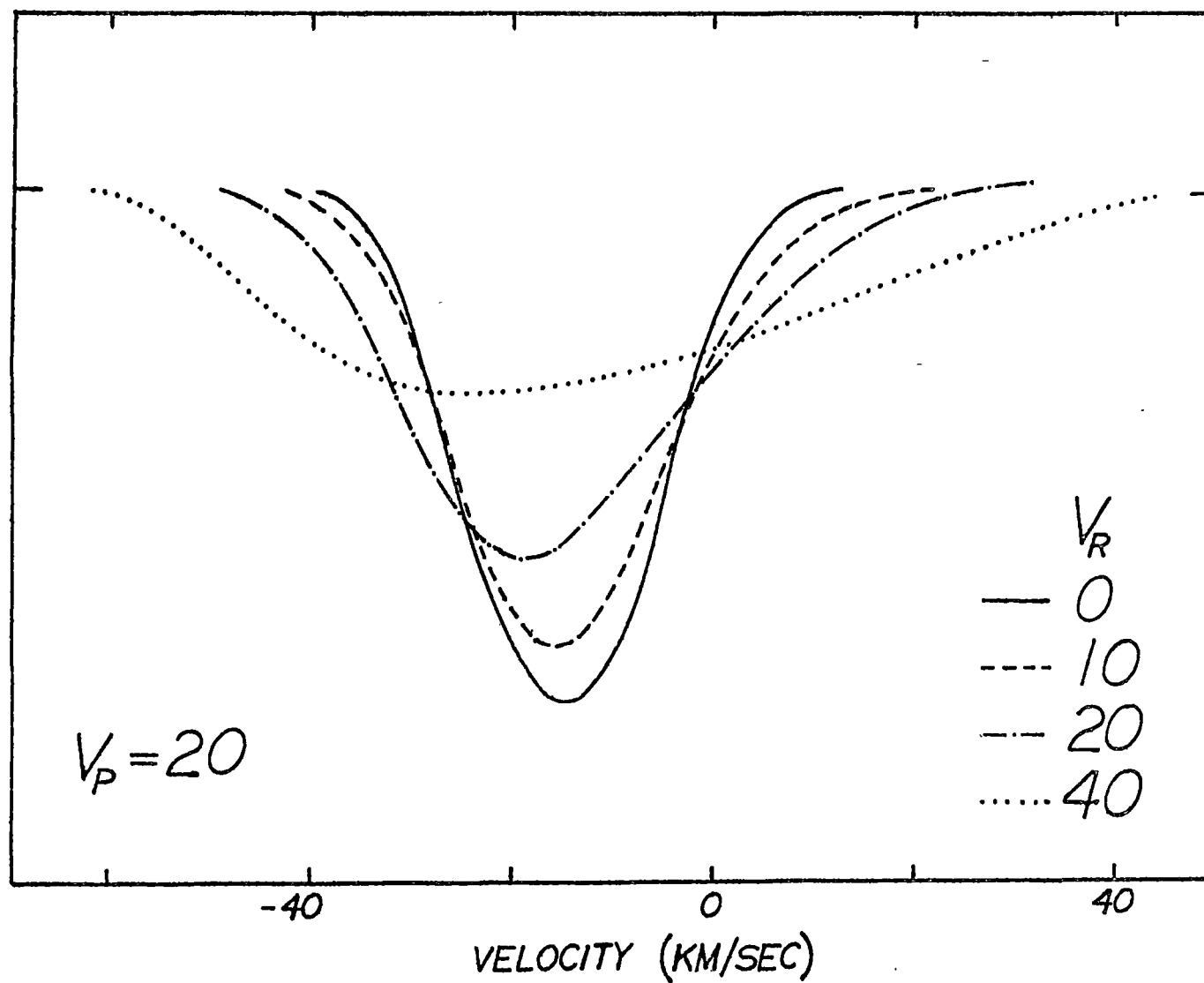


Figure 5.9 Effect of rotation on radial line profiles resulting from an expansion velocity of 20 km s^{-1} . Units of velocity are km s^{-1} .

and instrumental broadening which diminishes the measured velocity by some factor which depends on the v_b/v_e ratio.

It can be seen from Figure 5.8 that the other velocity indices which have been plotted are considerably less affected by rotation. The $V(70\%)$ and $V(33\%)$ indices are the worst of these, varying by about 20 percent over the range of velocity ratio. Campos and Smith (1980) have recommended the use of the $V(50\%)$ measure because of its insensitivity to rotational and broadening effects. For this index the conversion factor K/v_p undergoes a maximum near $v_p/v_e \sin i \sim 1.2$, where it attains a value some 10 percent above the pulsation-dominated and rotation-dominated extremes. At these extremes the conversion factor is very close to the value of $p^{-1} = (1.31)^{-1} = 0.76$ given by Parsons. The median velocity is even less sensitive to rotation and remains within 5 percent of Parsons' conversion factor over the entire range of velocity ratio. The mean profile velocity, which differs only slightly from the old 17/24 value because a limb darkening coefficient different from the Eddington value was assumed, is strictly constant with velocity ratio, independent of rotation. This was noted by Thiessen (1957) and follows because of the cancellation of rotational velocities between left and right hemispheres of the apparent disc. This strict constancy of \bar{v} with v_e holds true irrespective of the form of the surface pulsation. The $V(33\%)$ index converges to this value in the pulsation-dominated limit because of the quasi-triangular shape of the radial line profiles in this extreme. The mean velocity then lies at the profile centroid which is the centre at one-third maximum profile depth in this case. To summarize, it appears that to convert $2K$ to surface pulsation amplitude for radial pulsators in the presence of rotation, and to accurately apply Wesselink's method, an index such as $V(50\%)$, the median velocity or preferably the mean velocity

should be used. The former is, of course, easier to determine in practice than the latter two.

5.4.2 Nonradial Modes

For nonradial pulsations the correction factor p for the mean velocity may be found as follows. Dziembowski (1977) gives the mean velocity amplitude for the mode (l, m) as

$$K_{mean} = \sigma R \epsilon P_{l,m}(\cos i) [I_4 + k I_5], \quad (5.2)$$

where the integrals I_4 and I_5 are defined by Equation 2.19. This gives a correction factor for nonradial oscillations of

$$p^{-1} = K_{mean}/v_{NR} = I_4 + k I_5 \quad (5.3)$$

where $v_{NR} = \sigma R \epsilon P_{l,m}(\cos i)$ is the apparent nonradial surface velocity amplitude (this differs from the quantity v_p defined in Section 5.2.1). Values of p^{-1} determined from this equation are tabulated in Table 5.1 for modes $l \leq 4$ for the Eddington limb darkening law and for the darkening functions appropriate to a β Cephei atmosphere at wavelengths of 3600 Å and 5500 Å assuming $k = 0.05$. It can be seen from this table that with increasing mode order l the conversion factor p^{-1} becomes

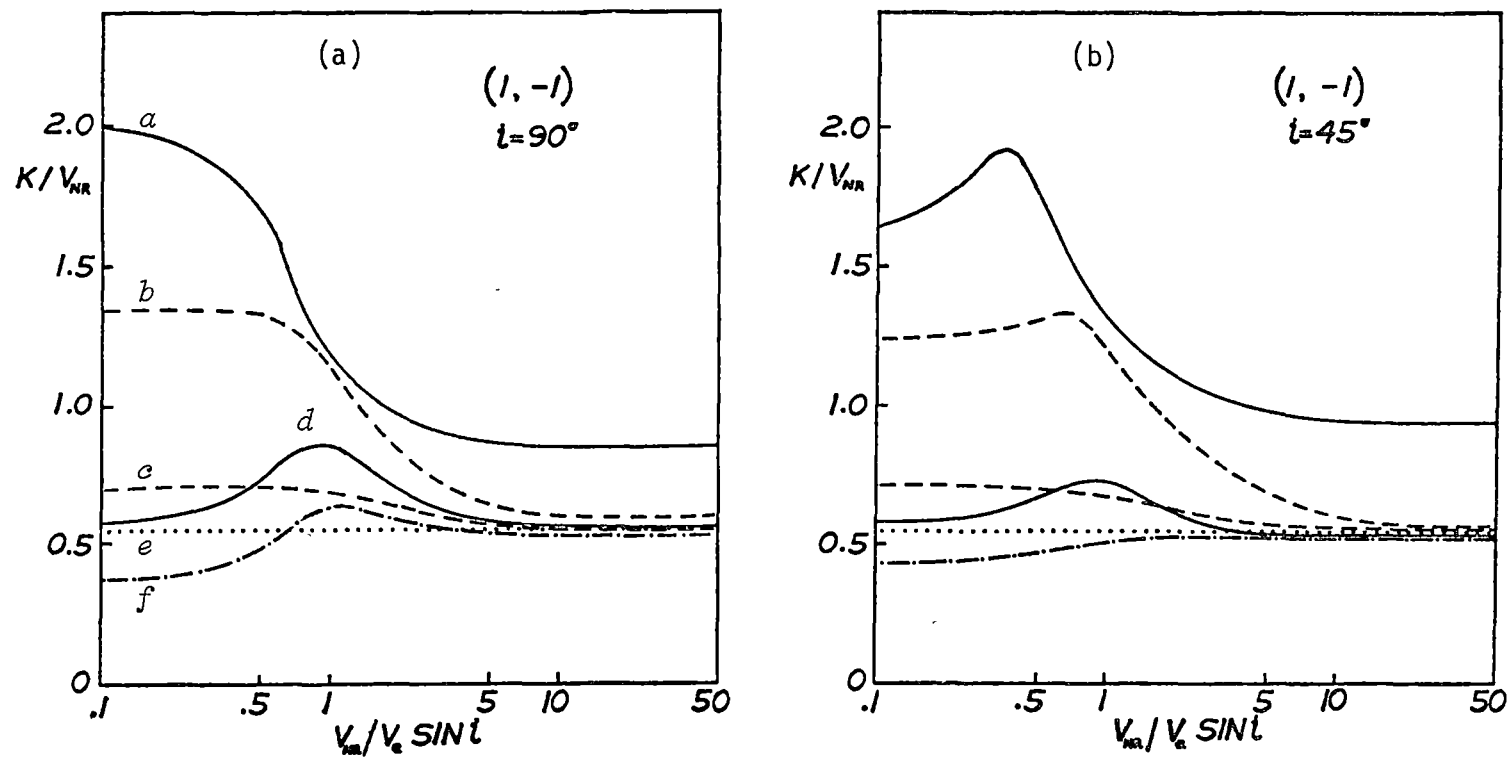
TABLE 5.1: Velocity conversion factors for nonradial modes

| l | $p^{-1}(\text{EDD.})$ | $p^{-1}(3600 \text{ Å})$ | $p^{-1}(5500 \text{ Å})$ |
|-----|-----------------------|--------------------------|--------------------------|
| 0 | 0.708 | 0.689 | 0.685 |
| 1 | 0.573 | 0.549 | 0.545 |
| 2 | 0.360 | 0.333 | 0.328 |
| 3 | 0.157 | 0.132 | 0.127 |
| 4 | 0.031 | 0.014 | 0.011 |

increasingly sensitive to the limb darkening function used to form the integrals I_4 and I_5 . This implies that the choice of the darkening law $h_I(\mu)$ used to weight the individual line intensity profiles, which is generally quite different from the photospheric darkening law, is important for $l > 2$. For a reasonable choice of $h_I(\mu)$ the mean profile velocity determined from observations using Equation 5.1 should correspond to the mean velocity given by Equation 5.2 providing line saturation effects are negligible.

As discussed in Section 2.7, Dziembowski (1978) and Balona and Stobie (1979a) have recently generalised the Baade-Wesselink method to permit its application to nonradial pulsators. Both of these generalisations assume that the mean projected velocity, as given by the Dziembowski formula, can be determined from the line profiles. The velocity curve can then be integrated to give, after multiplication by an appropriate factor, the geometric contribution to the light variations. The question is: can the mean velocity, or a good approximation to it, be easily measured from the observed line profiles? Clearly the mean profile velocity can be calculated explicitly using Equation 5.1 if the detailed line profile structure is available in digital form. Unfortunately this method is not feasible when the spectroscopic data is stored in analogue form, which is often the case. Of course if the profile is quasi-triangular, the centroid may be approximated by the line centre at 33 percent depth.

To investigate the viability of approximating the mean velocity by one of the easily-measured velocity indicators discussed previously in Section 5.4.1, some nonradial profiles were analysed for rotational effects. Figures 5.10(a) and (b) show the dependence of K/v_{NR} with $v_{NR}/v_e \sin i$ for six measures applied to the sectoral dipole mode seen at 90° and 45° inclination. Figures 5.11 (a) and (b) show similar



(a) $V(100\%)$ (b) $V(85\%)$ (c) median (d) $V(50\%)$ (e) mean (f) $V(33\%)$

Figure 5.10 Nonradial velocity correction factor as a function of the velocity ratio for different radial velocity measures in the case of sectoral dipole pulsations.

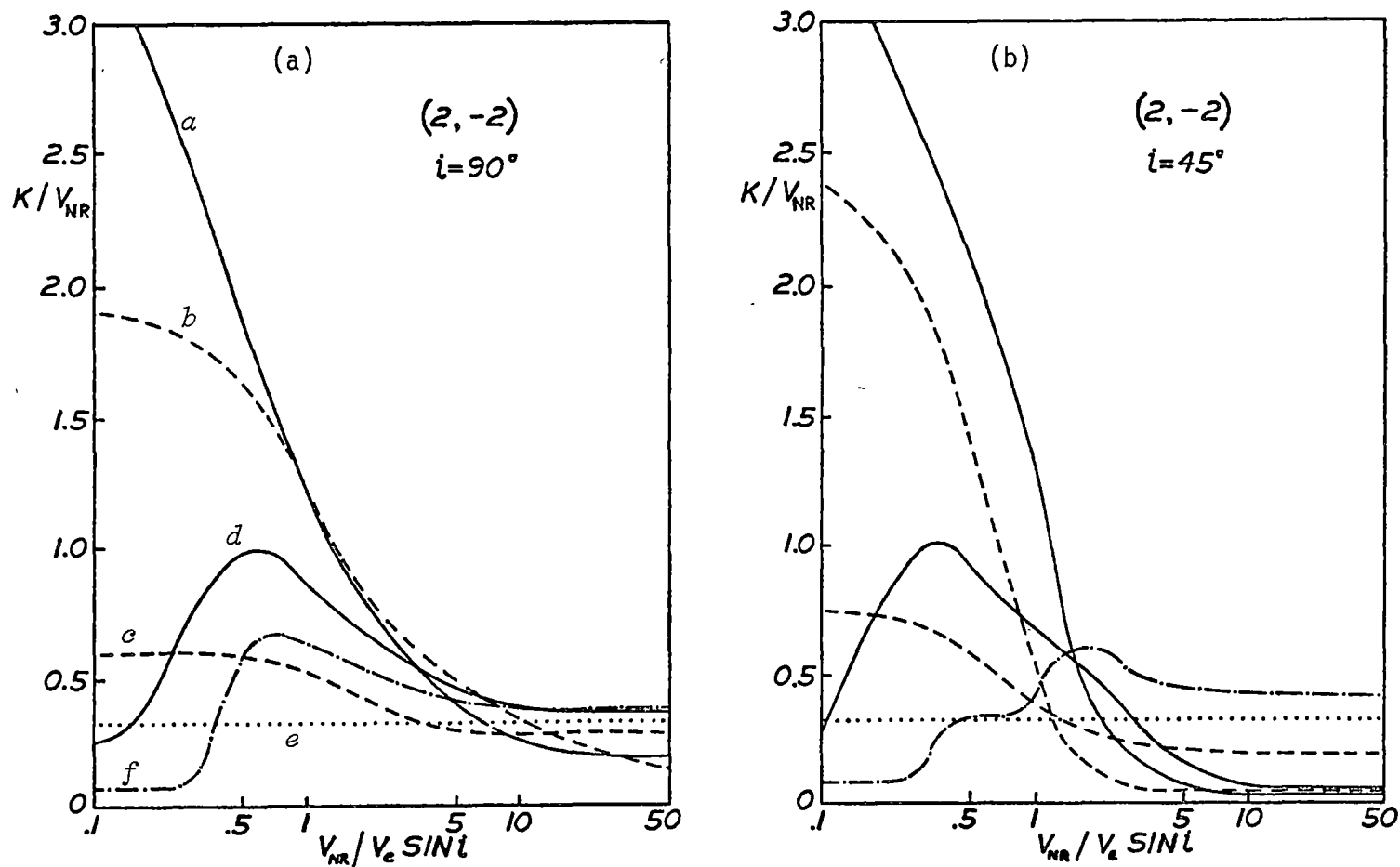


Figure 5.11 Nonradial velocity correction factor as a function of the velocity ratio for different radial velocity measures in the case of sectoral quadrupole pulsations. Labels are the same as in Figure 5.10.

plots for the sectoral quadrupole mode. For the dipole mode, the curves resemble those obtained for the radial case with the $v(85\%)$, $v(50\%)$, $v(33\%)$ and median indicators all converging to the mean velocity when pulsation dominates rotation. However, in the case of the quadrupole mode, the situation is considerably more complicated with *all* the conversion factors (except that for the mean velocity) varying by a factor of *at least two* over the range of possible $v_{NR}/v_e \sin i$ values. In particular the core velocities for this mode display an enormous sensitivity to rotation. A further difficulty is that, for both modes, the conversion factors K/v_{NR} for all but the mean velocity depend on the axial inclination of the observer. One is forced to the conclusion that *only the mean profile velocity* is useful in the context of a nonradial Wesselink analysis in which, a priori, the mode, inclination and velocity ratio are all unknown. Unless the mean profile velocity is calculated explicitly by numerically integrating under the profile flux data, in the general nonradial case the interacting effects of rotation, pulsation and inclination cannot be disentangled.

5.5 LINE MODELS AND THE EFFECT OF ATMOSPHERIC STRUCTURE

In addition to the basic velocities associated with the pulsation mode and the complications of stellar rotation discussed in Section 5.4, atmospheric velocity gradients, stellar winds and varying scales of turbulence may also affect spectral line profiles. Initial modelling of line profiles in variables assumed a constant 'intrinsic profile' which was integrated over the limb-darkened stellar disc. This approach has been used here and in other recent works for nonradial pulsations (Stamford and Watson, 1977; Kubiak, 1978) because of computational ease. Employing an LTE analysis to predict centre-to-limb profile variations, which are then integrated over the disc, represents an improvement on this. This has been done, for example, by Parsons (1972) for radial

pulsations in cepheids and by Smith (1978) for nonradial oscillations in B stars. Mihalas (1979) has recently made an even more detailed examination of profiles in expanding atmospheres which involved consideration of velocity gradients, departures from LTE and rotation.

Mihalas demonstrates that, in addition to the problem of the interaction of the pulsational and rotational velocity fields, a velocity-depth relation, such as might be associated with a stellar wind above the photosphere, can produce dramatically different centre-to-limb profile changes in comparison with those produced by a uniformly expanding atmosphere. He further shows, as is to be expected, that the nature of the centre-to-limb variations depends strongly on non-LTE effects. Because of these problems, Mihalas is justifiably led to doubt the validity of currently used procedures, such as Fourier techniques of line profile analysis and pulsational mode studies which rely on the 'intrinsic profile' assumption. To assess the extent to which these criticisms apply to the particular problem of the diagnosis of pulsational velocity fields in β Cephei variables, a number of computational tests were undertaken. These tests involved the calculation of Si III $\lambda 4552$ profiles for a standard abundance $(T_e, \log g) = (25000, 3.6)$ atmosphere. The techniques used in these computations and the results obtained are discussed in the following two sections (5.5.1, 5.5.2).

5.5.1 *Solution of the Transfer Equation for a Rotating and Expanding Atmosphere.*

The procedure employed for the construction of line profiles originating from a rotating and expanding atmosphere was a generalization of the method described by Karp (1973). This method involves solving the equation of radiative transfer assuming conditions of LTE. The

presence of rotation complicates the integration of specific intensity over the observed disc because the projected velocity no longer depends solely on the angle of emergence. For reasons of computational economy the line absorption was approximated by a Gaussian profile when rotation is present, but in the absence of rotation a full Voigt profile $H(\alpha, u)$ was used, where the damping parameter α was permitted to vary with depth and $u = \Delta\nu/\Delta\nu_D$. The Doppler width $\Delta\nu_D$ was formed from the appropriate value of the thermal velocity at a particular depth and an assumed constant microturbulence of 5 km s^{-1} . The line absorption per gram is $\ell_\nu \propto H(\alpha, u')$ where the frequency shift u must be corrected for the Doppler shift of the gas according to

$$u' = u - v\nu/c\Delta\nu_D, \quad (5.4)$$

where v is the local gas velocity projected onto the line-of-sight. For an equatorial rotational speed of v_e and a pulsation velocity of v_p then

$$v(\tau) = [v_e \sin \phi + v_p(\tau) \cos \phi] \sin \theta \sin i. \quad (5.5)$$

Thus it is evident from Equations 5.4 and 5.5 that the line absorption and line optical depth at a particular frequency at some point on the stellar disc depend implicitly on the polar and azimuthal coordinates of that point.

The emergent specific intensity at polar angle θ and azimuthal angle ϕ is then

$$I_\nu(\theta, \phi) = \int_0^\infty B_\nu(m) e^{-\tau_\nu(m, \theta, \phi)/\sin \theta \cos \phi} \frac{k_\nu(m) + \ell_\nu(m, \theta, \phi)}{\sin \theta \cos \phi} dm. \quad (5.6)$$

Thus the observed flux is

$$F_\nu = \oint I_\nu(\omega) d\omega \propto \int_{-\pi/2}^{\pi/2} \int_0^\pi I_\nu(\theta, \phi) \sin^2 \theta \cos \phi d\theta d\phi. \quad (5.7)$$

The integration over angle was performed using a 32 point Gaussian quadrature in each dimension. It is essential to use a large number of angle points so that the intensity profiles sufficiently overlap, otherwise, as noted by Karp (1975), spurious bumps can appear in the flux profile. The integration over mass was performed using a weighted quadratic interpolation formula, similar to that used by Kurucz (1970). Typically 150 mass points were employed for the mass quadrature.

5.5.2 *Results*

In the first series of tests, spectral lines were calculated both under the simple 'intrinsic profile' assumption and using the full LTE method in order to make comparisons. Calculations were for radially and nonradially pulsating systems in the presence of rotational velocity fields but assuming no atmospheric velocity gradient. The results for the disc-integrated LTE Si III $\lambda 4552$ models are shown as full lines in Figure 5.12. Some examples of similar nonradial calculations for the equator-on $(l, m) = (2, -2)$ mode are given in Figure 5.13. For the 'intrinsic profile' models a Gaussian function, with a total broadening which could be chosen appropriately, was used. For the purposes of this exercise a simple linear limb-darkening law was used to form the integrated intrinsic profile. A value $u = 0.6$ was employed but the results are not sensitive to this choice. Some resultant profiles, normalized in central depth to the corresponding LTE solution, appear in Figures 5.12 and 5.13. These figures illustrate the general result that, with the appropriate choice of the microturbulent velocity parameter v_t , the two methods yield very similar profiles. The most notable difference is that the line cores of the 'intrinsic profile' method are slightly more ($\sim 2 \text{ km s}^{-1}$) displaced. The physical significance of the v_t parameter in this method is, of course, even more obscure

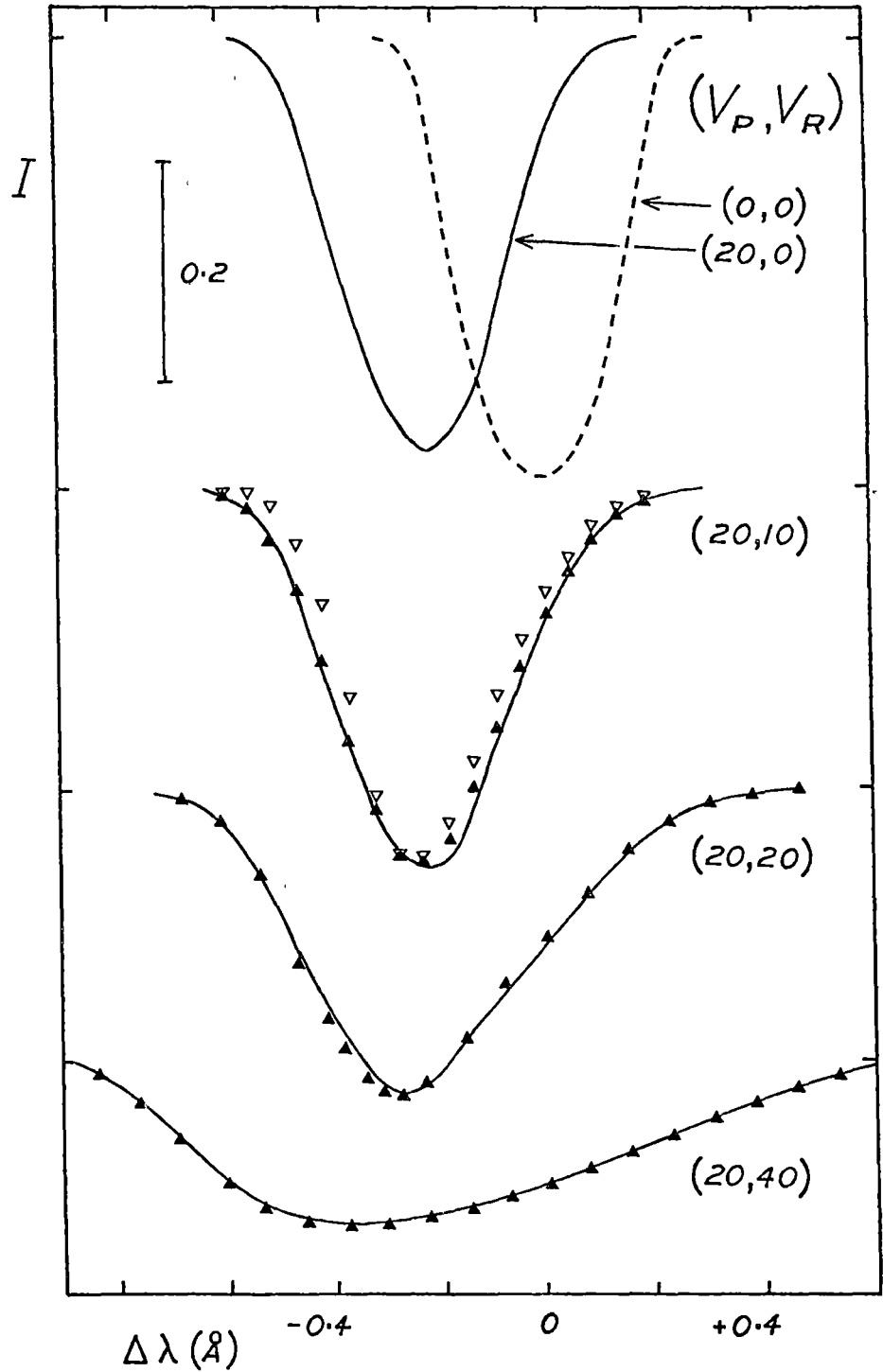


Figure 5.12 The Si III profile for a $(T_e, \log g) = (25000, 3.6)$ star in the presence of some differing equatorial rotational velocities V_R (km s^{-1}) and uniform outward expansion velocities V_P (km s^{-1}). Full lines are the results of LTE profiles integrated over the disk. Triangles outline results for a constant 'intrinsic profile' with a microturbulence parameter $V_T = 7 \text{ km s}^{-1}$ (open triangles) and 10 km s^{-1} (filled triangles).

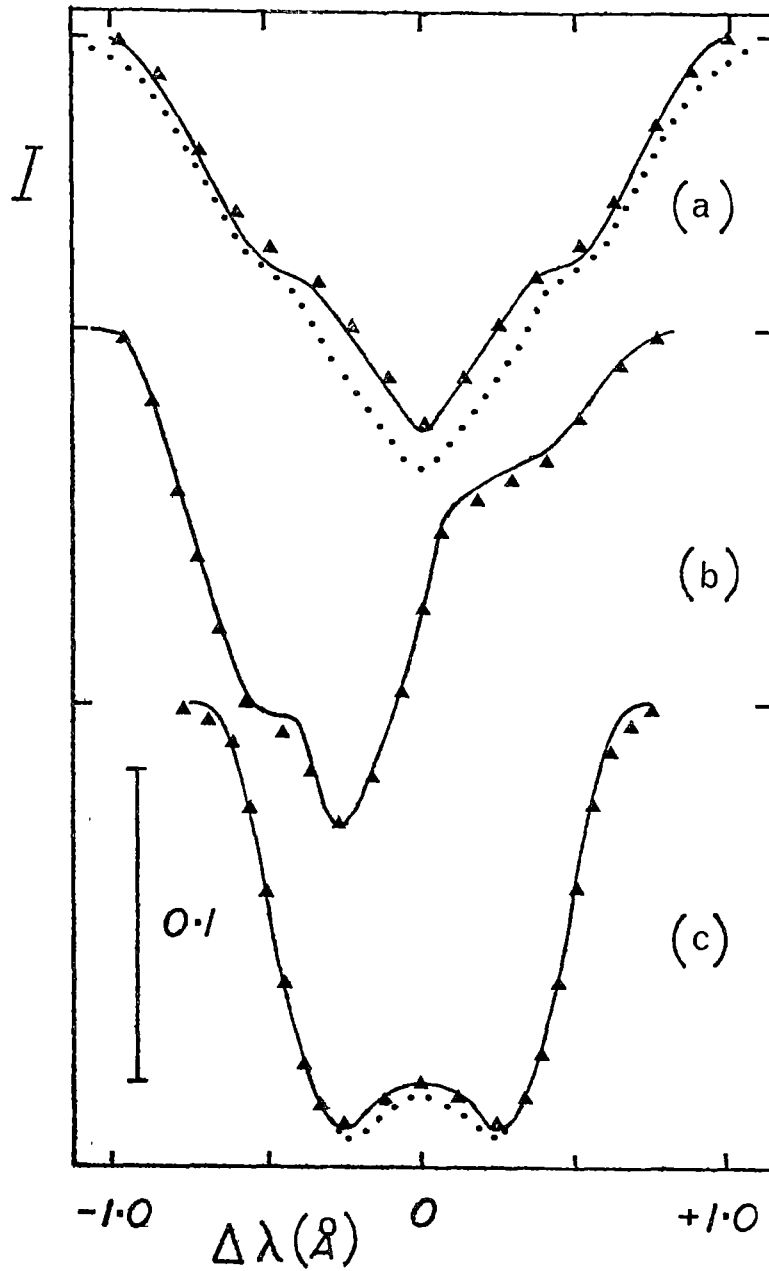


Figure 5.13 Details here are the same as for Figure 5.12 but the pulsation velocity amplitude v_p is modulated over the stellar surface in the manner of an equatorially viewed $(l, m) = (2, -2)$ mode. Filled triangles outline results for a constant 'intrinsic profile' with $v_t = 10 \text{ km s}^{-1}$. The parameters (v_p, v_e, Φ) are $(100, 50, 0.25)$, $(50, 25, 0.5)$ and $(30, 15, 0.75)$ in (a), (b) and (c) respectively. Here Φ is the pulsation phase. Dots give LTE profiles in the presence of a velocity gradient. The velocity gradient is $v(\tau) = v_0(1 - \log \tau/3)$ where $v_0 = 75 \text{ km s}^{-1}$ and 22 km s^{-1} in (a) and (c) respectively. This gives $v(0.1)$ velocities which are the velocities of the corresponding uniform expansion models.

than it is in the full LTE method. However, the inference that can be drawn from these tests is that, over the period of pulsation, a profile fitting exercise for the three parameters v_p (pulsation surface velocity amplitude), v_e (equatorial rotational velocity), and v_t will yield values for v_p and v_e , together with mode identification, which are not appreciably less reliable if the simple 'intrinsic profile' approach is employed instead of the full LTE method.

Since non-LTE effects typically involve centre-to-limb line strength increases, it can also be inferred that the differences between the 'intrinsic profile' and non-LTE models should be of the same order as those found between the 'intrinsic profile' and LTE approach. In the one case the differences are due to an increasing line strength compared with a constant strength and in the other case the differences are due to a line strength decreasing to zero at the limb compared with a constant strength.

A second series of tests involved the calculation of line profiles in radially and nonradially varying atmospheres with a velocity gradient present. Figure 5.14 shows the centre-to-limb and integrated profiles for radial motion in the presence of two different velocity gradients. The form of $v(\tau)$ given in Figure 5.14(c) is that used by Mihalas (1979). It represents an extreme gradient appropriate to a stellar wind. According to this $v(\tau)$, atmospheric velocities increase by an order of magnitude between $\tau = 1$ and $\tau = 10^{-2}$, where the gas flow asymptotically approaches terminal velocity. The dissimilarity of the intensity profiles displayed in Figure 5.14(c) can be readily understood. The nonlinear velocity law causes a bump in the disc-centre profile near the terminal velocity because essentially all mass at $\tau > 10^{-2}$ moves at this speed and line opacity accumulates there. However the bulk of absorption of the normally-emergent radiation occurs deeper in the

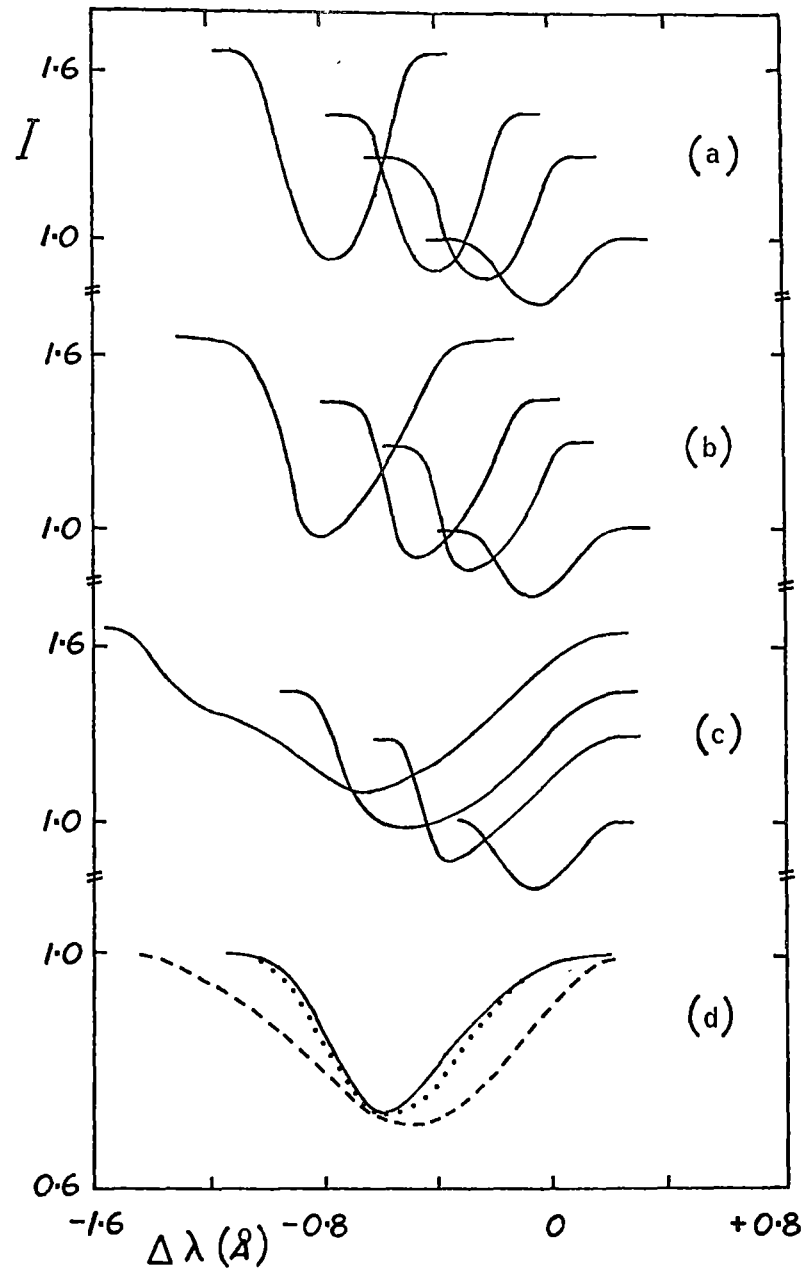


Figure 5.14 Centre-to-limb variations in the Si III $\lambda 4552$ profile of a $(T_e, \log g) = (25000, 3.6)$ atmosphere which is expanding in the presence of the following velocity gradients: - (a) $V(\tau) = 50 \text{ km s}^{-1}$; (b) $V(\tau) = 37(1 - \log \tau/3) \text{ km s}^{-1}$; (c) $V(\tau) = 9(\tau + 0.025)/(\tau + 0.05) \text{ km s}^{-1}$. In each case $V(0.1) = 50 \text{ km s}^{-1}$ and profiles for $\mu = 1.0, 0.5, 0.3$ and 0.05 are shown with continuum intensity decreasing according to the photospheric limb darkening. The disc-integrated flux profiles are illustrated in (d). The solid, dotted and dashed lines correspond to case (a), (b) and (c) respectively.

atmosphere where velocities are lower. Nearer the limb, absorption occurs higher in the atmosphere and only velocities near the terminal velocity are sampled.

The hydrodynamic envelope models discussed in detail in Chapter 6 indicate that the velocity gradient chosen by Mihalas is not of the form expected for the velocity field *associated with a β Cephei pulsation* and that a simple law the form $V(\tau) \propto -\log \tau$ is more appropriate. The hydrodynamic models also provide a rough guide to the magnitude of the velocity gradient applicable to the B star variables. Except for the brief period when any shock is passing through the atmosphere, this model suggests that, even in an extreme variable such as BW Vul, the velocity at most doubles over the interval $\tau = 1$ to $\tau = 10^{-3}$. Another, indirect, line of evidence for this being a valid upper limit to the velocity gradient *associated with the pulsation* is the agreement between spectroscopic and photometric $\Delta R/R$ values obtained in Section 3.4 for radially pulsating variables. To model this upper limit situation a $V(\tau) \propto (1 - \log \tau/3)$ was used. This doubles $V(\tau)$ between $\tau = 1$ and $\tau = 10^{-3}$. The results for this appear in Figure 5.14(b). Figure 5.14(d) clearly shows the previously documented results that a velocity gradient acts to both increase the line equivalent width and to provide asymmetry in the opposite sense (velocity gradient distortion) to that induced by a uniform expansion velocity (geometric distortion). The effect of this logarithmic velocity gradient on nonradial (2,-2) profiles is illustrated in Figure 5.13. Clearly, from both Figure 5.13 and Figure 5.14, the velocity doubling limitation over $\tau = 1$ to $\tau = 10^{-3}$ permits only small changes to the line profiles. The physical meaning of the v_p parameter determined under the assumption of uniform expansion is, of course, made uncertain to the extent of the unknown gradient.

In summary it appears that, while atmospheric velocity gradients will certainly be present in the atmospheres of pulsating B stars,

the effect on spectral lines of moderate strength will be small and will not interfere with mode identification. A simple 'intrinsic profile' approach is adequate for this latter purpose at least for $l < 3$. The exception to this is the brief period of any atmospheric shock passage when substantial profile changes occur, as illustrated by Stamford and Watson (1978b) and discussed in detail in Chapter 6.

5.6 CONCLUSION

The line profile studies discussed in this chapter support the conclusions of Chapter 3, which indicated that radial and nonradial pulsators coexist within the β Cephei group. Smith and his co-workers have further shown that the β Cephei strip is surrounded by a group of irregular variables, the 53 Persei stars, which, on the evidence of line profile analyses, appear to be undergoing nonradial oscillations. The evidence points to the fact that all stable single-periodic pulsators are radial oscillators. However the overwhelming evidence for nonradial pulsation in 12 Lac and the occurrence of close periods in a number of other β Cephei variables suggest that the multiperiodic β Cephei pulsators support both radial and nonradial modes.

Although it has been conclusively demonstrated that nonradial motions can qualitatively produce similar line broadening and line doubling characteristics to those observed in some β Cephei stars, there is firm evidence that the stars which display these features most markedly, BW Vul and σ Sco (the P_2 mode), are in fact radial pulsators. This suggests that *two distinct* line doubling mechanisms are operative in the β Cephei variables. The first is associated with nonradial motions as described in Sections 3.2 and 3.3. These variations are smooth and continuous over the pulsation cycle. The second, and more abrupt, line-doubling mechanism is probably associated with the passage of

shock waves through the atmosphere of radially pulsating variables.
This is the mechanism which is investigated in Chapter 6.

C H A P T E R S I X

SIMPLE NONLINEAR RADIAL MODELS

6.1 INTRODUCTION

The line splitting phenomenon observed in the spectra of the large amplitude β Cephei stars BW Vul, σ Sco and 12 Lac has, in the past, often been regarded as evidence for the nonradial character of the surface motions. Indeed, the successful modelling of the spectral profiles of 12 Lac by Smith (1980a) indicates that a combination of radial and nonradial motions are almost certainly responsible for the doubled lines reported for that star. However, as has been shown in Chapter 3, the light amplitude spectra of BW Vul and the line-broadening mode of σ Sco, which display doubled lines most conspicuously, are strongly indicative of radial motions. Furthermore Campos and Smith (1980) have shown that the line profiles of σ Sco are consistent only with radial oscillations for the line-broadening mode. Hydrodynamic calculations by Hill (1972) for the atmosphere of an RR Lyrae star undergoing radial pulsations suggest that doubled lines might originate from stellar atmospheres during the passage of a strong shock wave. Similar effects have been investigated using a radial shock interpretation by Hillendahl (1970), Skalarfuris (1974) and Karp (1975) for the case of classical cepheids, and Hill and Willson (1979), Willson and Hill (1979) and Wood (1979) for the Mira variables. Radial shock effects may also explain the stillstand observed on the rising branch of the light curve of BW Vul. Hutchinson, Hill and Lillie (1975) have demonstrated, in the case of the classical cepheid β Dor, that light curve bumps may be attributable to such a mechanism.

A radial shock model was first proposed for BW Vul by Odgers (1956) and further investigated by Odgers and Kushwaha (1959), Bhatnagar and Kushwaha (1961a, 1961b, 1963) and Bhatnagar *et al.* (1971).

Odgers pictures an 'atmosphere', or superficial layer of higher density, ejected at a highly supersonic velocity, after which it falls back into the stellar photosphere. The photosphere is visible as the velocity stillstand for a period of time before the next 'atmosphere' is ejected. This model has received observational support from Kubiak (1972) and Goldberg, Walker and Odgers (1976).

In an attempt to elucidate the radial shock proposal further, some simple radial pulsation models have been constructed. The properties of these models have been compared principally with the observations of BW Vul, since this is the star for which hydrodynamic effects are likely to be most important. Extensive isocron spectra discussed by Goldberg, Walker and Odgers (1976) provide a useful observational database for this star.

The structure of this chapter is as follows. In Section 6.2 an exploratory hydrodynamic model is examined which considers an isothermal stellar atmosphere driven by a 'hard', sinusoidally-varying subphotospheric piston. This tentative model is shown to possess many features in common with BW Vul. However the boundary condition which drives the pulsations for this model is clearly inadequate and an improved boundary condition is used in later sections. In Section 6.3 the wave equation for linear adiabatic radial oscillations is solved for a complete β Cephei model near core hydrogen exhaustion to obtain the pulsation eigenfunctions. Using the first harmonic period from this calculation, radial pulsations are then imposed on adiabatic and isothermal envelope models (Section 6.4) and a radiative diffusion model (Section 6.5) by a 'soft' piston located at the first harmonic pulsation node deep within the stellar envelope. Finally, in Section 6.6, arguments for and against the radial and nonradial interpretation of BW Vul are summarized.

6.2 THE HARD-PISTON ATMOSPHERIC MODEL

6.2.1 *Model Assumptions*

For use in the numerical computations an equilibrium model atmosphere appropriate to BW Vul was calculated using the ATLAS model atmosphere program of Kurucz. The parameters characterizing this model are given in Table 6.1. These parameters were derived assuming a pulsational Q of 0.026, which is consistent with the empirical values of Lesh and Aizenman (1974), Balona and Feast (1975) and Shobbrook (1978) and the theoretical values of Davey (1973) and Stothers (1976) for the first radial overtone. Thus the imposed piston period of 4.82 hours is consistent with both observational and theoretical data for the adopted model. Three assumptions were made in the numerical calculations. These were:

A1. Plane-parallel approximation - The plane parallel approximation was used since the region modelled was only about 10% of the stellar radius in extent, with a maximum excursion $\Delta R/R < 8\%$.

A2. Isothermality - For speed of computation, the atmospheric temperature structure and radiation pressure structure were assumed invariant in time.

TABLE 6.1: Parameters defining the model

| | |
|---------------------------|--------------------------------------|
| Period | 4.82 hr |
| Effective temperature | 23,000 K |
| Mass | $11 M_{\odot}$ |
| Radius | $8.7 R_{\odot}$ |
| Surface gravity | $4.0 \times 10^3 \text{ cm/s}^2$ |
| Outer-mass depth | $4.0 \times 10^{-8} \text{ gm/cm}^2$ |
| Inner-mass depth | $2.8 \times 10^1 \text{ gm/cm}^2$ |
| Number of sectors | 100 |
| Mass ratio between shells | 1.226 |

A3. Boundary Conditions

(a) At the upper boundary ($\tau \sim 10^{-6}$) the gas pressure was assumed to fall to zero.

(b) At the lower boundary ($\tau \sim 30$) the atmosphere was dynamically driven by a hard piston which was varied sinusoidally in time.

Assumptions A2 and A3(b) have been discussed at length by Hill and Willson (1979) and Willson and Hill (1979). The isothermal assumption is justified in the case of the thermal pulse travelling with a shock front by the short radiative relaxation time, which is of the order of one second for these stars (Whitney, 1967). The neglect of the slower changes in temperature, which relate to the variations of the intrinsic flux during the cycle, is not likely to radically affect the model dynamics. This is because over a cycle the observed fractional temperature changes for BW Vul ($\Delta T/T \sim 25\%$ according to Kubiak (1972)) are considerably less than the fractional density changes ($\Delta \rho/\rho \sim 1000\%$ across a shock) predicted by the model.

Assumption A3(a), requiring that the gas pressure be zero at the outer boundary amounts to including all the remaining mass of the atmosphere in the outermost layer. The effects of assuming this sharp atmospheric cutoff were minimised by placing the outer boundary at $\tau \sim 10^{-6}$, far above the region of interest. Also, a non-zero total pressure was maintained at the boundary because of the inclusion of radiation pressure in the model.

Assumption A3(b), concerning the motion of the lower boundary, is more difficult to justify. The hydrodynamic equations require the specification of a lower boundary condition and, in any case, it is necessary to artificially introduce a driving region somewhere in the model since β Cephei models are not self-excited. However the depth at which this driving region should be located was not initially obvious,

and it seemed simplest to assume a sinusoidal variation below the photosphere. This seemed plausible because the light curve of BW Vul is almost sinusoidal, except for the short interval of stillstand. Furthermore, in a qualitative sense, the atmospheric dynamics of the final model were not found to be strongly dependent on the positioning of the piston within the subphotospheric region, although some quantitative changes occurred. This assumption, together with the plane-parallel assumption, will be discarded in the following sections, which attempt to improve the physical validity of the model.

6.2.2 *The Difference Equations*

The motion of the atmosphere was followed numerically by solving the equations of mass and momentum using the standard finite-difference method as described by Richtmyer and Morton (1967). The atmosphere was divided into $(N+1)$ interfaces ($N = 100$), with the first and $(N+1)$ th interface corresponding to the outer and inner boundaries respectively. The column mass m , radius r and velocity u are defined at each interface, while the state variables are defined at the centre between two interfaces. The I th interface was located at column mass depth $m_{I+1} = \alpha m_1$, where $m_1 \approx 10^{-8} \text{ gm cm}^{-2}$ and $\alpha = 1.23$. Letting the subscript I denote the interface, and the superscript J denote the time instant, then the differential equations of velocity, mass and momentum become the following difference equations:

VELOCITY:

$$u = \frac{\partial r}{\partial t}$$

$$u_I^{J+\frac{1}{2}} = \frac{r_I^{J+1} - r_I^J}{t^{J+1} - t^J} \quad (6.1)$$

MASS:
$$V = - \frac{\partial r}{\partial m}$$

$$V_{I+\frac{1}{2}}^J = - \frac{r_{I+1}^J - r_I^J}{m_{I+1} - m_I} \quad (6.2)$$

MOMENTUM:
$$\frac{\partial u}{\partial t} = - \frac{GM}{r^2} + \frac{\partial P}{\partial m}$$

$$\frac{u_{I+\frac{1}{2}}^{J+\frac{1}{2}} - u_I^{J-\frac{1}{2}}}{t_{I+\frac{1}{2}}^{J+\frac{1}{2}} - t_I^{J-\frac{1}{2}}} = - \frac{GM}{r_I^2} + \frac{p_{I+\frac{1}{2}}^J + Q_{I+\frac{1}{2}}^{J-\frac{1}{2}} - p_{I-\frac{1}{2}}^J - Q_{I-\frac{1}{2}}^{J-\frac{1}{2}}}{\frac{1}{2}(m_{I+1} - m_{I-1})} \quad (6.3)$$

Here $m(r) = \int_r^\infty \rho(r) dr$, V is the specific volume, t is time, P is the total pressure and Q is the artificial viscosity. An expression for Q ,

$$Q_{I+\frac{1}{2}}^{J+\frac{1}{2}} = \begin{cases} \frac{2}{V_{I+\frac{1}{2}}^{J+\frac{1}{2}} + V_I^J} (u_{I+1}^{J+\frac{1}{2}} - u_I^{J+\frac{1}{2}})^2 & \text{for } u_{I+1} > u_I \\ 0 & \text{for } u_{I+1} \leq u_I \end{cases} \quad (6.4)$$

was used. The boundary conditions are

$$(P_{\text{gas}})_{\frac{1}{2}} = 0 \quad \text{at the outer boundary,}$$

and $u_{N+1}(t) = \Delta u \cos(\sigma t)$ at the inner boundary.

The initial conditions are $u_I^{\frac{1}{2}} = u_0$, $r_I^0 = r(m)$ and $T_{I-\frac{1}{2}}^0$ specified for $I = 1, \dots, N+1$. The time step Δt must be chosen to be less than the Courant time Δt_c , which is the minimum time required for sound to travel between adjacent interfaces,

i.e.
$$\Delta t < \Delta t_c = \min_I \{ (r_{I+1} - r_I) / \sqrt{\gamma P_{I+\frac{1}{2}} V_{I+\frac{1}{2}}} \}.$$

Here γ is the ratio of specific heats. Values for the gas pressure as a function of V and T were determined by interpolating in a grid obtained from the ATLAS model atmosphere program using the population I abundances $(X, Y, Z) = (0.70, 0.27, 0.03)$.

Initially a sequence of models was constructed by varying the velocity amplitude Δu of the driving piston. For small piston amplitudes, variations in the line-forming layers remained sinusoidal. However, at larger amplitudes, non-sinusoidal effects developed, leading to the formation of shock waves on the descending branch of the radial velocity curve. Here the term 'shock' is used to refer to a velocity discontinuity in space which exceeds the local acoustic velocity. In the next subsection a particular model having $\Delta u = 40 \text{ km s}^{-1}$ is discussed in detail. This model was chosen since its velocity amplitude was comparable to that of BW Vul and the morphology of its velocity curve was approximately similar.

6.2.3 *Model Properties*

Velocity variations at Rosseland mean optical depths of 0.7, 0.1 and 0.01 are shown in Figure 6.1 for the isothermal model with $\Delta u = 40 \text{ km s}^{-1}$. Also sketched is the observed radial velocity curve for BW Vul obtained by Goldberg *et al.* (1976) from spectral line cores. It should be noted that the model velocities are simply those of the appropriate mass shell, uncorrected for any such effects as foreshortening or rotation. The large velocity discontinuities near phases 0.7 and 0.9 in the model curves plotted in Figure 6.1 mark the passage of two strong shock waves through the atmosphere. The rapid outward propagation of these shocks through the atmospheric mass zones is evident in Figure 6.2, which shows the displacement curve of every eighth interface. The strongest shock (S1) forms at about phase 0.6 when rapidly infalling material collides with the nearly stationary piston. The second shock (S2) develops at phase 0.9 as the outwardly expanding piston rams the overlying atmospheric layers. In addition there is a third very weak shock (S3) which forms high in the atmosphere and is overtaken by S1 at about phase 0.75.

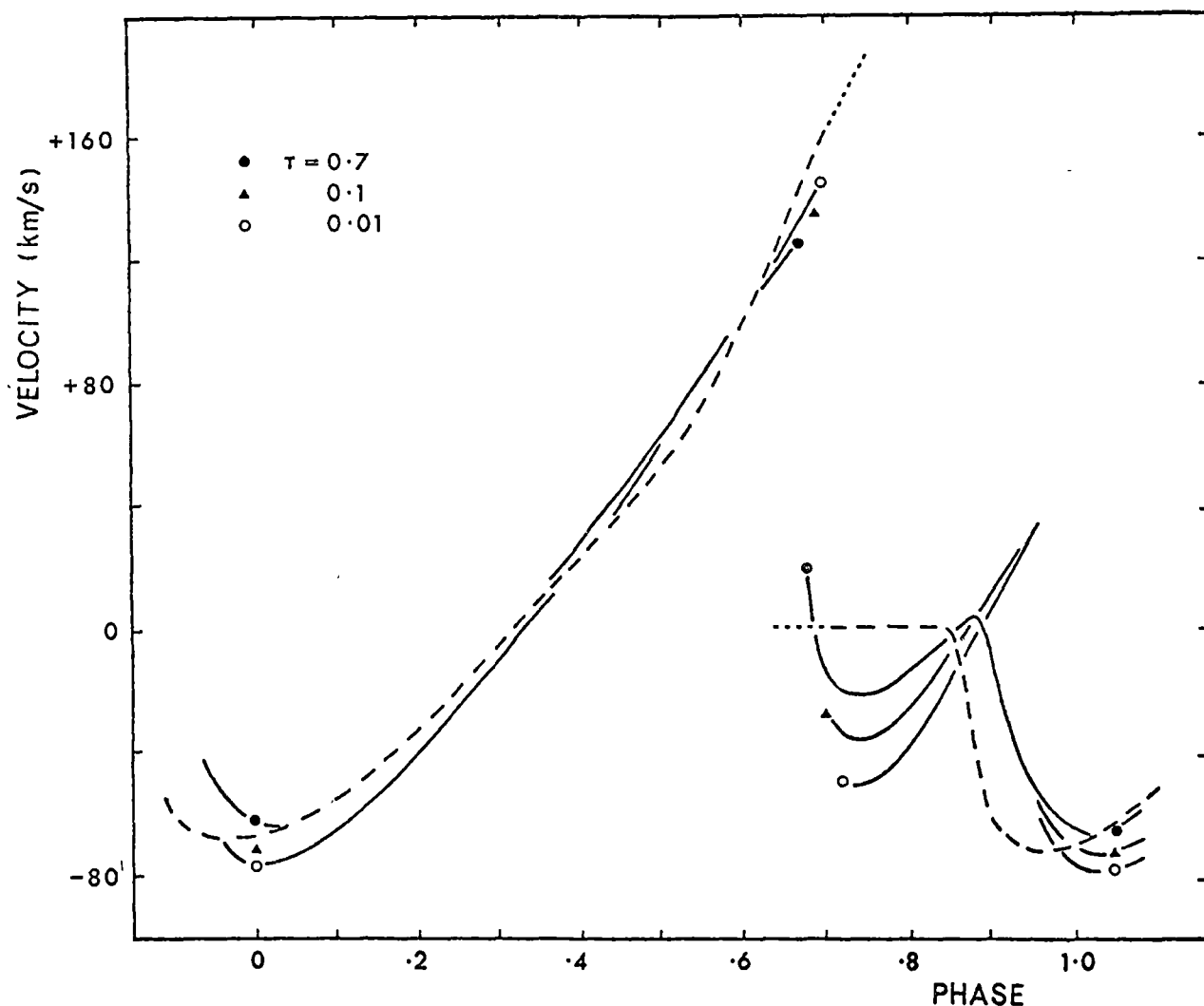


Figure 6.1 Velocity of some mass shells in the isothermal atmospheric model with $\Delta u = 40 \text{ km s}^{-1}$. Mass shells at Rosseland mean optical depths $\tau = 0.7$, 0.1 and 0.01 are denoted by filled circles, filled triangles and open circles respectively. The zero phase point corresponds to the time of passage of the piston outwards through its equilibrium radius. The dashed curve represents the spectral line core radial velocity measurements of Goldberg *et al.* (1976). Dotted segments distinguish the weak component during the line doubling phase.

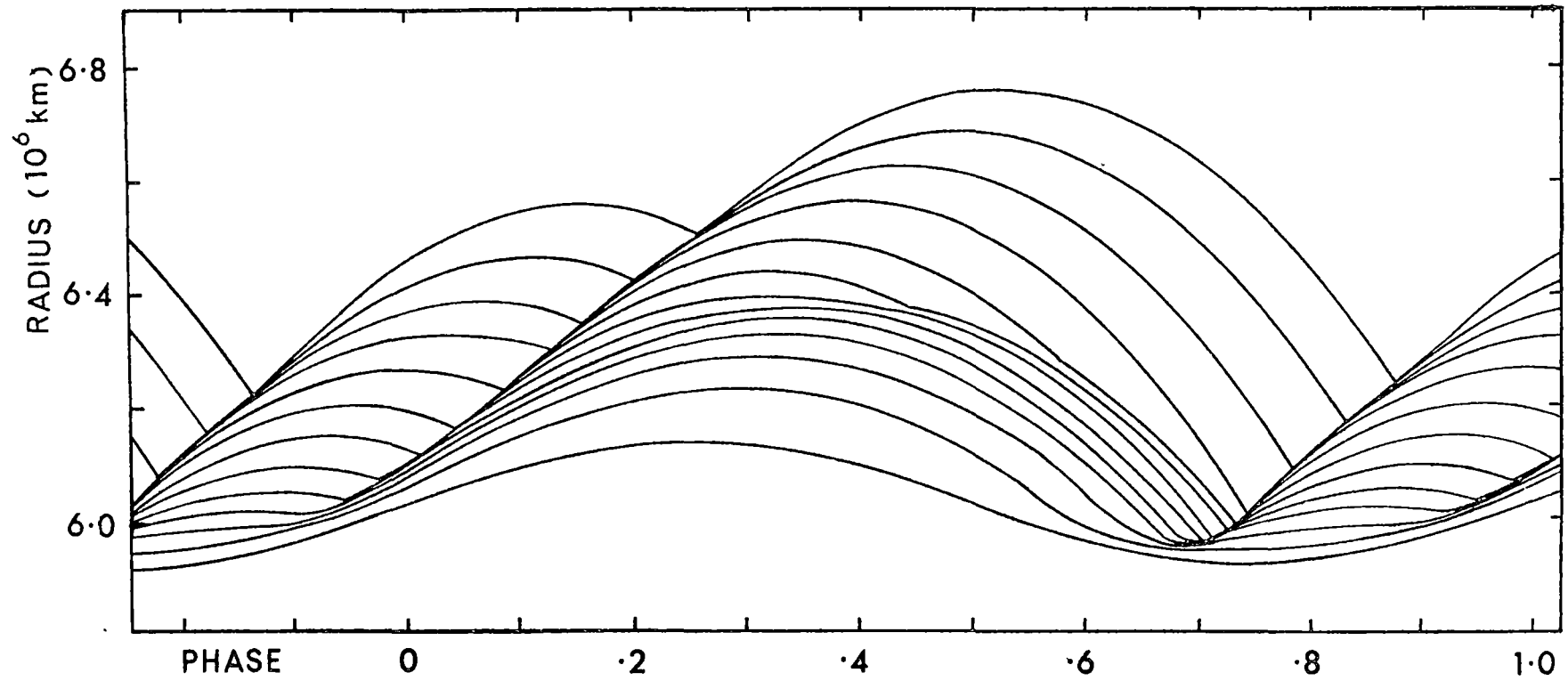


Figure 6.2 Displacement curves of mass shells in the isothermal atmosphere .
The location of each eighth shell is plotted, commencing with the piston.

From Figure 6.1 it is apparent that S1 coincides with the appearance of line doubling in BW Vul. In the context of the model, the line doubling may be interpreted as originating from the passage of the narrow shock front (with a radiative relaxation distance of the order of 10^3 m) through the line-forming layers. In this picture, one might expect that the red-shifted component observed in doubled spectral lines results from the absorption by the infalling pre-shock gas, while the stillstand component is due to the slowly moving post-shock material. The steady shift from one component to the other would correspond to the progressive conversion of pre-shock to post-shock material by the encroaching shock front. To investigate this scenario line profiles of Si III $\lambda 4552$ were calculated for the moving atmosphere using the LTE line synthesis method described in Section 5.5. These are shown in Figure 6.3. It must be emphasized that these profile calculations are only qualitative because of the isothermal assumption. The shock front was approximated by a discontinuity in density and velocity because the rapid radiative relaxation time ensures that it is optically thin. From Figure 6.3 it can be seen that there are indeed brief intervals of line doubling present at $\phi = 0.68$ and $\phi = 0.95$ as the shock fronts pass through the line-forming layers. No splitting has been detected observationally at the end of the stillstand, though Goldberg *et al.* (1976) consider that it may be detectable with higher spectral resolution. In addition, repeating Figure 6.3 calculations to include a rotational speed applicable to BW Vul, reduces the prominence of the line splitting at the latter phase. The duration of the calculated line doubling from the strong shock is $\Delta\phi \sim 0.03$. This is considerably less than the observed $\Delta\phi \sim 0.10$. The isothermal assumption means that the model is not adequate to comment on the observed constancy in equivalent width of lines during splitting. The

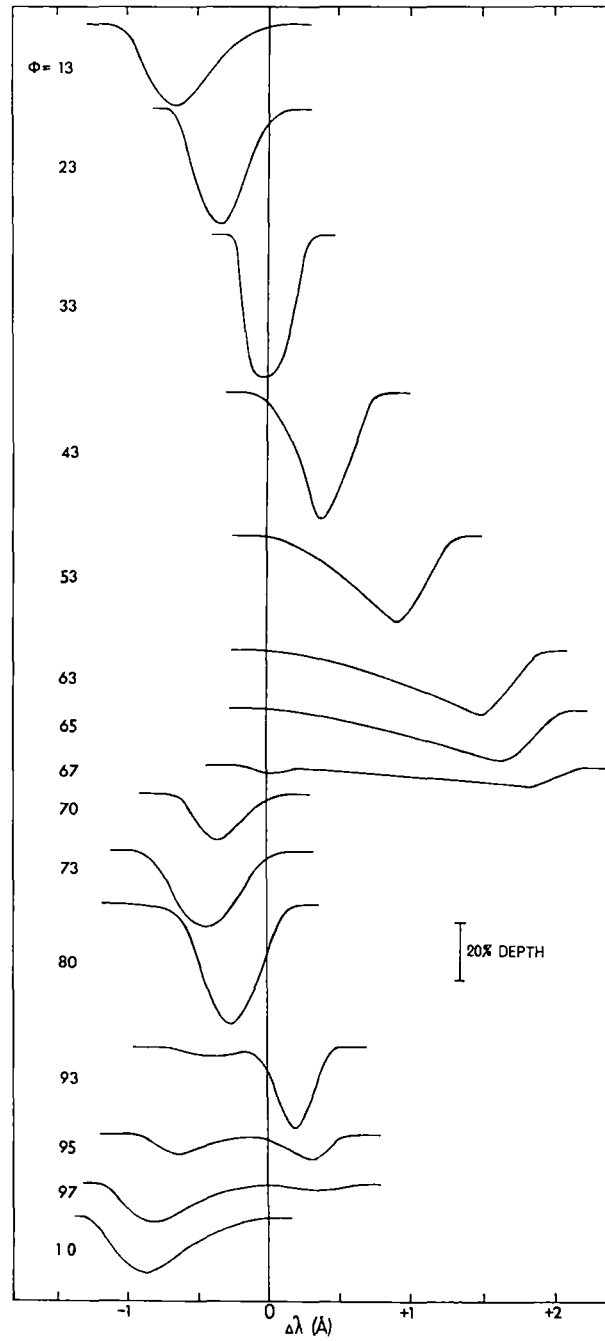


Figure 6.3 . Example Si III λ 4552 profiles calculated for the isothermal atmosphere.

calculations give a large decrease in equivalent widths at this time. This artifact of the isothermal model results from large post-shock densities causing the optical depth scale to move outward in mass to cooler layers, hence diminishing the line depth.

Finally, the simple isothermal model provides a clue to the origin of the stillstand in light which occurs on the ascending branch of the otherwise essentially sinusoidal light curve of BW Vul. This stillstand has been observed in recent years by Kubiak (1972), Cherewick and Young (1975) and Margrave (1979). Kubiak's mean light curve for BW Vul is shown schematically in Figure 6.4, together with the photospheric radius variation in the isothermal model. The light curve has been phase aligned using the points of minimum light and maximum radius. Also illustrated in Figure 6.4 is the radiative flux expected from the shocks in the isothermal model. This was calculated using the relationship given by Hill (1972), $F_S = \rho(\Delta u)^3/2$, where ρ is the pre-shock density and Δu is the velocity discontinuity across the shock. This flux originates from the liberation of the kinetic energy of the infalling pre-shock material. Additional contributions to F_S resulting from the change in specific enthalpy as the shock wave passes through the He II and He I ionization regions are small. It can be seen from Figure 6.4 that the maximum in the shock flux coincides with the stillstand in the observed light, suggesting that S1 may contribute to this feature. The significance of this contribution will depend on the emission spectrum of the shock front, as the maximum value of F_S is only about one percent of the integrated stellar flux per unit surface area. The radiative losses from S2 are an order of magnitude below those from S1.

6.2.4 *Discussion*

The simple isothermal model can qualitatively explain many of the observed properties of BW Vul - the asymmetric, discontinuous velocity

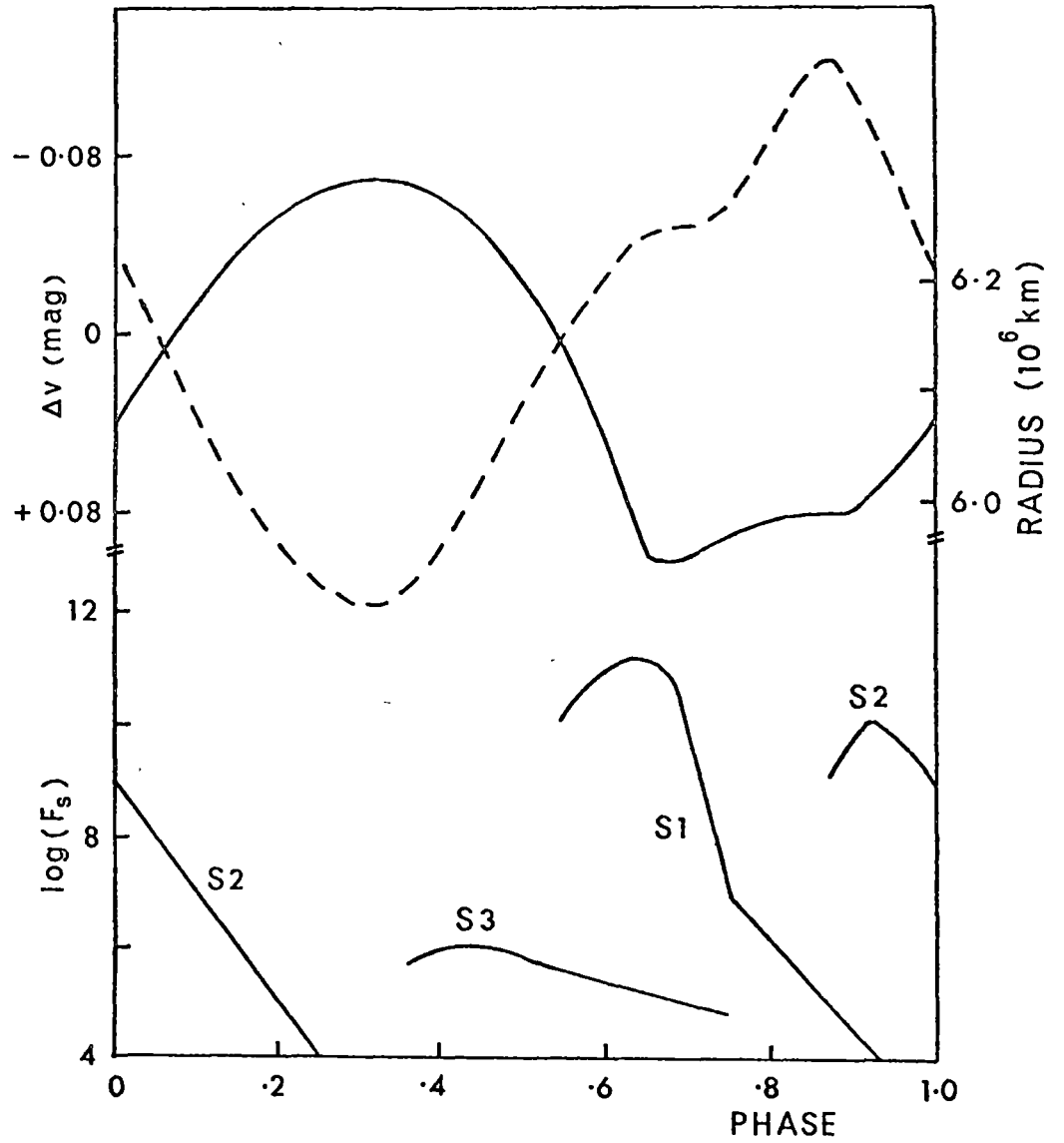


Figure 6.4 Radiative shock fluxes F_s , in $\text{erg}/\text{cm}^2/\text{s}$, obtained from the isothermal model. The photospheric radius variation of the model (full line) and the observed mean light curve of Kubiak (1972) (dashed line) are shown for comparison. The light curve represents Strömgren v observations with an arbitrary zero level.

curve, the line profile doubling and the light stillstand. However the assumptions underpinning this model, particularly the assumption of a hard subphotospheric piston, are unsatisfactory. The piston boundary condition is inadequate for two reasons. Firstly, the placement of the piston was arbitrary. Secondly, a hard piston is dynamically unrealistic, since it prevents any feedback between the atmosphere and the envelope. Clearly a hard piston, being unresponsive to the behaviour of the atmosphere above it, will more readily generate shock waves in the overlying medium.

The problem is that, because the β Cephei excitation mechanism has not been identified, the pulsations must be artificially driven at some interface within the star. However, one would expect that by locating the piston deep enough, in a region where the pulsation eigenfunctions are small, the assumption of a sinusoidal piston variation will become more realistic. The approach finally adopted here was to assume that the star was pulsating in the first radial overtone. This hypothesis is consistent with empirical Q values. Following the suggestion of Dr. Peter Wood (Department of Astronomy, Aust. National University), the inner boundary condition was applied to the *pressure* at the node of the radial eigenfunction $\delta r/r$ for the first harmonic, located deep in the envelope. The boundary condition then becomes $P_{N+1}(t) = \bar{P}_{N+1} - \Delta P \sin(\sigma t)$. The surface amplitude can be controlled through the amplitude ΔP of the nodal pressure variations. To construct a self-consistent model according to this scheme, it is first necessary to ascertain precisely the mass depth of the first harmonic node and the corresponding pulsation period. The determination of these parameters is the subject of the next section.

6.3 THE LINEAR ADIABATIC SOLUTION

A linear adiabatic analysis of the radial oscillations of a realistic β Cephei model was performed using the numerical technique outlined by Davey (1970). Davey has shown that the adiabatic approximation yields pulsation frequencies which are in excellent agreement with the nonadiabatic values. The method involves the direct solution of the linearized adiabatic wave equation using an efficient matrix eigenvalue method.

A late main sequence evolutionary state, near core hydrogen exhaustion, was assumed for the β Cephei model used in these calculations. This is consistent with the conclusions of Jakate (1978) and Shobbrook (1979). A population I interior model appropriate to this epoch, having composition $(X,Y,Z) = (0.74,0.24,0.02)$, was kindly supplied by Dr. Bruce Cogan of the Department of Astronomy, A.N.U. The $12 M_{\odot}$ model had a radius of $8.6 R_{\odot}$ and an effective temperature of 23000 K. An envelope was added to this model and the ATLAS model atmosphere program was used to generate the photospheric region. In this way, by carefully matching the state variables, the flux and the gravity at the boundaries, a complete self-consistent stellar model was constructed. This model was then subdivided into approximately 200 interfaces and for each of these the coefficients of the difference equations were formed. A well-distributed zoning scheme is essential in order that the resultant set of difference equations adequately approximate the stellar structure equations from which they were derived. The interior 50% of the star by radius, containing 95% of the stellar mass, was typically partitioned into one hundred interfaces. The remainder were allocated to the envelope.

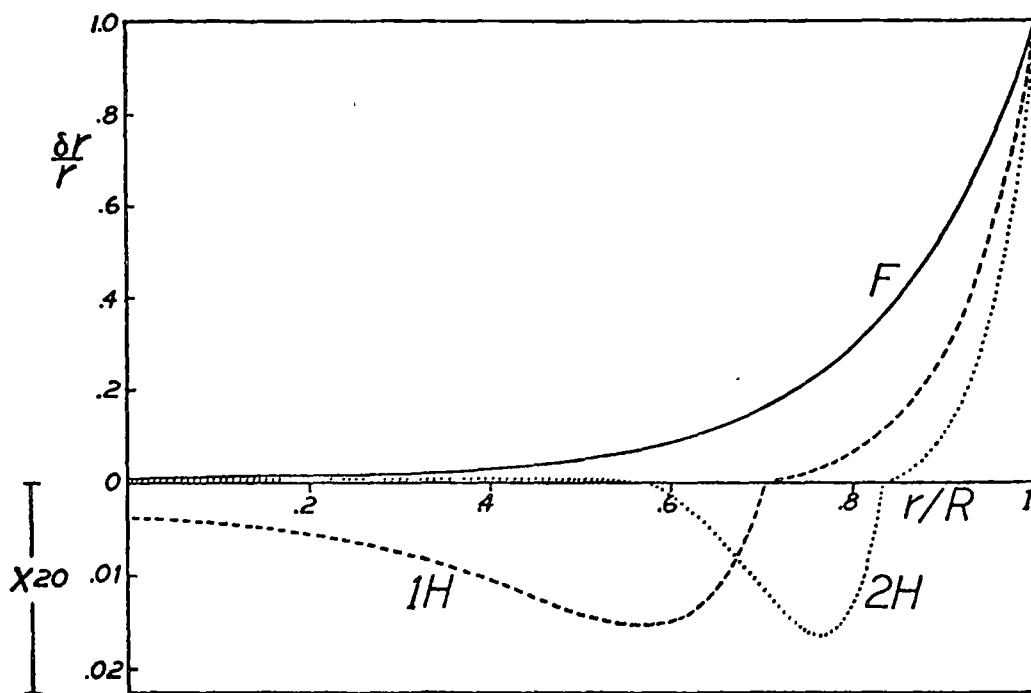


Figure 6.5(a) The linear adiabatic eigenfunctions $\delta r/r$ for the fundamental (F), first (1H) and second harmonic (2H) oscillations of a $12 M_{\odot}$ main sequence star near core hydrogen exhaustion.

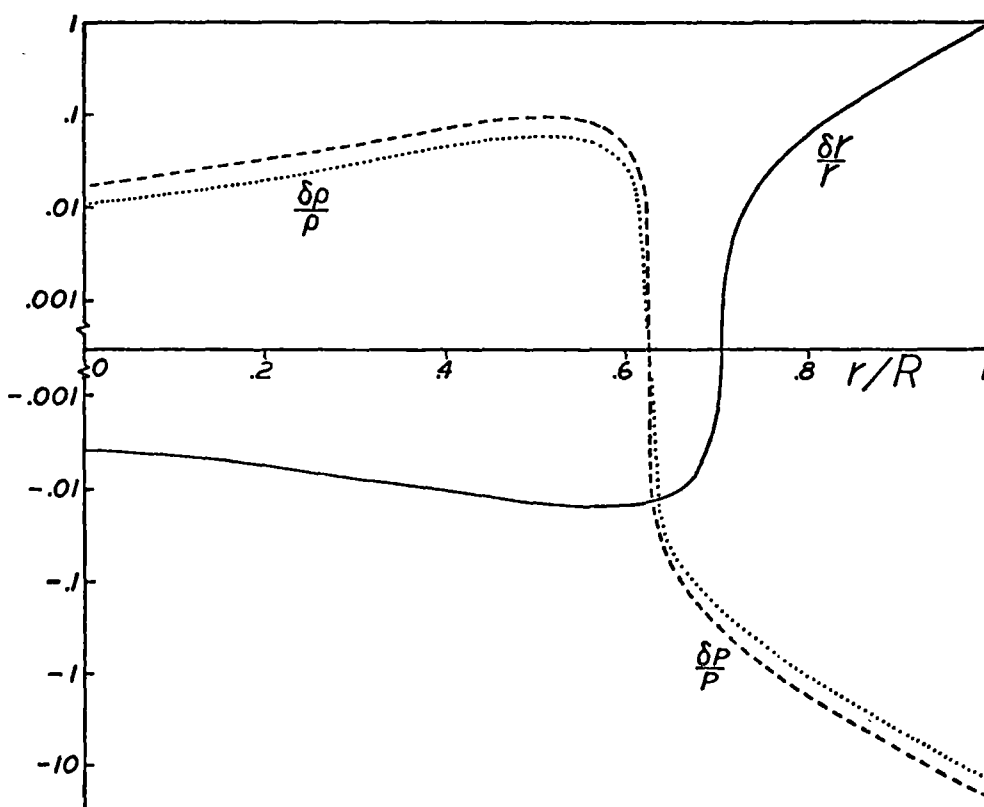


Figure 6.5(b) Radius, density and pressure eigenfunctions for the first harmonic of the $12 M_{\odot}$ model.

TABLE 6.2: Solutions for $12 M_{\odot}$ Model near Core Hydrogen Exhaustion

| Harmonic | Period (hrs) | Q (days) | Period Ratio P_i/P_{i+1} | Outermost Node (r/R) |
|----------|--------------|----------|----------------------------|----------------------|
| 0 | 6.230 | 0.036 | 1.34 | - |
| 1 | 4.664 | 0.027 | 1.24 | 0.707 |
| 2 | 3.766 | 0.022 | 1.20 | 0.830 |
| 3 | 3.129 | 0.018 | 1.17 | 0.895 |
| 4 | 2.666 | 0.015 | 1.15 | 0.928 |
| 5 | 2.314 | 0.013 | 1.13 | 0.953 |
| 6 | 2.050 | 0.012 | 1.12 | 0.966 |

The resulting periods of the fundamental and first six overtones for this model are shown in Table 6.2. Also shown are the Q values, period ratios and the radial locations of the outermost node. These results are in good agreement with the calculations of Davey (1970) and Stothers (1976). Plots of the amplitude eigenfunctions $\delta r/r$ for the three radial oscillations of longest period are shown in Figure 6.5(a), while the radius, pressure and density eigenfunctions for the first harmonic are shown in Figure 6.5(b). Having determined the period and node location for the first radial overtone, it is now possible to proceed to the soft-piston envelope models foreshadowed in Section 6.2.4.

6.4 SIMPLE SOFT-PISTON ENVELOPE MODELS

Throughout most of the stellar mass, gas motions occur adiabatically because luminous energy losses represent only a small fraction of the local thermal energy. Near the surface, however, significant departures from adiabatic conditions will arise. It is of interest to determine the extent to which an adiabatic approximation is applicable to the envelope region.

The location of the transition region which separates the nonadiabatic exterior from the quasi-adiabatic interior can be determined from the order of magnitude relation given by Cox (1974):

$$\frac{(c_V T)_{\text{TR}} (\Delta m)_{\text{TR}}}{L P} \sim 1 . \quad (6.5)$$

Here L is the stellar luminosity, P the pulsation period and $(\Delta m)_{\text{TR}}$ is the total mass above the transition region. Thus the internal energy of the stellar layers above the transition region is of the same order as the energy radiated each period. Values of the left-hand side of 6.5 are given in Table 6.3 as a function of depth within the envelope. These values are comparable to unity in the regime $0.90 < r/R < 0.95$. A calculation similar to that described by Ledoux and Walraven (1958, Section 67) produces results which are roughly consistent with this conclusion. According to the Ledoux and Walraven method, the adiabatic and nonadiabatic variations in temperature become comparable, for an early B star envelope, at a depth where the pressure is of the order of $10^6 - 10^7$ dyne cm^{-2} . In this regime temperatures are in the range 1×10^5 K to 3×10^5 K and the fractional radius is in the interval $0.94 < r/R < 0.97$. Ledoux and Walraven also give expressions for the thermal propagation speeds c' and c'' with which nonadiabatic thermal fluctuations propagate towards the surface. These are

$$\left. \begin{aligned} c' &\approx \left(\frac{16\pi a c T^3}{3\kappa \rho^2 c_V P} \right)^{1/2} \\ \text{and} \quad c'' &\approx \frac{7.5 \sigma T_e^4}{c_V \rho T} \end{aligned} \right\} (6.6)$$

Values of c' and c'' are listed in Table 6.3 as a function of depth. Which one of c' and c'' is relevant depends on the detailed model eigenfunctions. However, since they are of a similar order, they yield

TABLE 6.3: Properties of the 12 M_⊙ Model Envelope

| r/R | Δm (gm) | T(K) | ρ (gm cm ⁻³) | $\frac{c_V T \Delta m}{LP}$ | c' (cm s ⁻¹) | t'/P | c'' (cm s ⁻¹) | t''/P |
|-------|------------------------|-----------|--------------------------|-----------------------------|--------------------------|------|---------------------------|-----------------------|
| 1.000 | 3.8 x 10 ²⁴ | 23,000 | 1.4 x 10 ⁻⁹ | 7.1 x 10 ⁻⁶ | 1.4 x 10 ⁸ | 0 | 3.7 x 10 ¹⁰ | 0 |
| 0.974 | 2.8 x 10 ²⁷ | 124,330 | 1.8 x 10 ⁻⁷ | 2.9 x 10 ⁻² | 9.3 x 10 ⁶ | 0.1 | 5.3 x 10 ⁷ | 0.02 |
| 0.950 | 3.1 x 10 ²⁸ | 223,770 | 1.2 x 10 ⁻⁶ | 5.8 x 10 ⁻¹ | 3.3 x 10 ⁶ | 0.5 | 4.4 x 10 ⁶ | 0.4 |
| 0.927 | 1.5 x 10 ²⁹ | 324,000 | 4.6 x 10 ⁻⁶ | 4.0 | 1.5 x 10 ⁶ | 1.7 | 8.0 x 10 ⁵ | 3.2 |
| 0.887 | 1.1 x 10 ³⁰ | 515,900 | 2.4 x 10 ⁻⁵ | 4.7 x 10 ¹ | 5.8 x 10 ⁵ | 6.7 | 9.5 x 10 ⁴ | 41 |
| 0.841 | 4.8 x 10 ³⁰ | 774,000 | 9.1 x 10 ⁻⁵ | 3.2 x 10 ² | 2.9 x 10 ⁵ | 19 | 1.7 x 10 ⁴ | 320 |
| 0.783 | 2.2 x 10 ³¹ | 1,169,800 | 3.5 x 10 ⁻⁴ | 2.1 x 10 ³ | 1.4 x 10 ⁵ | 54 | 2.9 x 10 ³ | 2.6 x 10 ³ |
| 0.725 | 6.3 x 10 ³¹ | 1,882,000 | 8.2 x 10 ⁻⁴ | 9.9 x 10 ³ | 1.2 x 10 ⁵ | 77 | 9.9 x 10 ³ | 1.2 x 10 ⁴ |

comparable estimates of the characteristic times $\Delta t' = h/c'$ and $\Delta t'' = h/c''$ required for a thermal perturbation to reach the surface from a depth h in the envelope. It can be seen from Table 6.3 that, for h in the region $0.9 < r/R < 0.95$, these times are of the order of a pulsation period. Thus, in this region and above, the oscillations cannot be adiabatic. All of these arguments suggest that the transition region extends from between $\sim 90\%$ and $\sim 95\%$ of the photospheric radius, and that below this the adiabatic approximation will be reasonable.

Since a significant fraction of the envelope, including the region which last scatters the observed light, is located exterior to the adiabatic domain, a nonadiabatic model is necessary for a proper treatment of the outer layers. Such a model will be discussed in Section 6.5. However first it is instructive to consider the elementary isothermal and adiabatic cases. By virtue of their simplicity, it was possible to iteratively follow these models over a considerably larger number of periods than was feasible for the more complex diffusion model of Section 6.5. This was essential since, for the adiabatic model, over three hundred periods were required for the transients arising from the initial conditions to decay to an acceptable value. Only then were periodically repeating solutions obtained. In addition, the adiabatic model was used to provide the initial conditions for the diffusion model.

Including the atmosphere, about forty percent of the stellar radius lies in the region exterior to the first harmonic node. Hence the plane parallel assumption is not valid in modelling this region. Assuming spherical symmetry the equations of velocity, mass and momentum are respectively:

$$u = \frac{\partial r}{\partial t} \quad (6.7)$$

$$V = - 4\pi r^2 \frac{\partial r}{\partial m} \quad (6.8)$$

and
$$\frac{\partial r}{\partial t} = -\frac{GM}{r^2} + 4\pi r^2 \frac{\partial P}{\partial m} \quad (6.9)$$

where $m(r) = \int_r^\infty 4\pi r'^2 \rho dr'$ is the mass exterior to radius r . These equations, together with the boundary conditions

$$\left. \begin{aligned} P_{\text{gas}} &= 0 && \text{at the surface} \\ \text{and } P_{\text{total}} &= \bar{P} - \Delta P \sin(\sigma t) && \text{at the node} \end{aligned} \right\} \quad (6.10)$$

may be solved using the usual differencing scheme with either an adiabatic or isothermal assumption. In these calculations the envelope was partitioned into 51 interfaces. A time-step of half the limiting Courant time was used, requiring about 250 iterations each period.

6.4.1 *The Nonlinear Isothermal Model*

This model was investigated for comparison with the isothermal atmospheric model considered in Section 6.2. Periodic solutions were obtained within forty cycles. The velocity curves at $\tau = 10^{-2}$ are shown in Figure 6.6 for a number of boundary pressure amplitudes. With increasing amplitude the velocity curve becomes progressively non-sinusoidal, developing a gradual ascending branch and a steep descending branch. At large amplitudes a single strong shock develops. This is manifested as a velocity discontinuity at the phase of maximum contraction. The shock forms at optical depths in the region $\tau \sim 10^2 - 10^3$ and propagates rapidly to the outer atmosphere ($\tau \sim 10^{-6}$) within a time $\Delta\Phi \sim 0.05$. A limiting amplitude for the isothermal model of about 350 km s^{-1} is attained for $\Delta P > 1\%$. Increasing the nodal pressure amplitude beyond this value simply displaces the phasing of the velocity curve relative to the nodal pressure changes.

With the change in boundary condition from a 'hard' subphotospheric piston to a 'soft' deep envelope piston, the second shock (S2) predicted

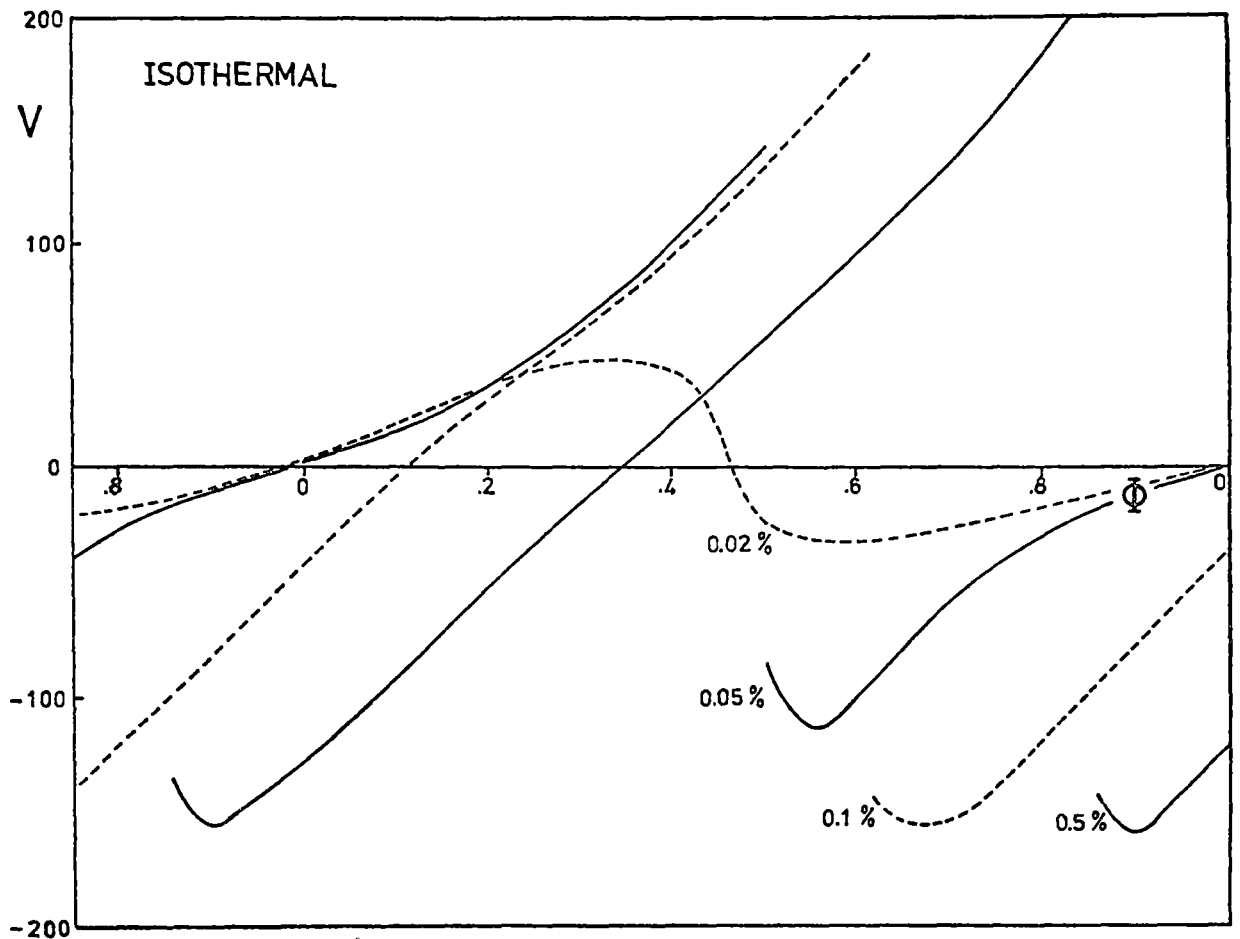


Figure 6.6 Velocity curves for different piston amplitudes at $\tau = 10^{-2}$ within the isothermal model. Fractional piston semi-amplitudes $\Delta P/P$ are indicated. Phase Φ is relative to the nodal pressure variations, which satisfy $P = \bar{P} - \Delta P \sin(2\pi\Phi)$. Velocity units are km s^{-1} .

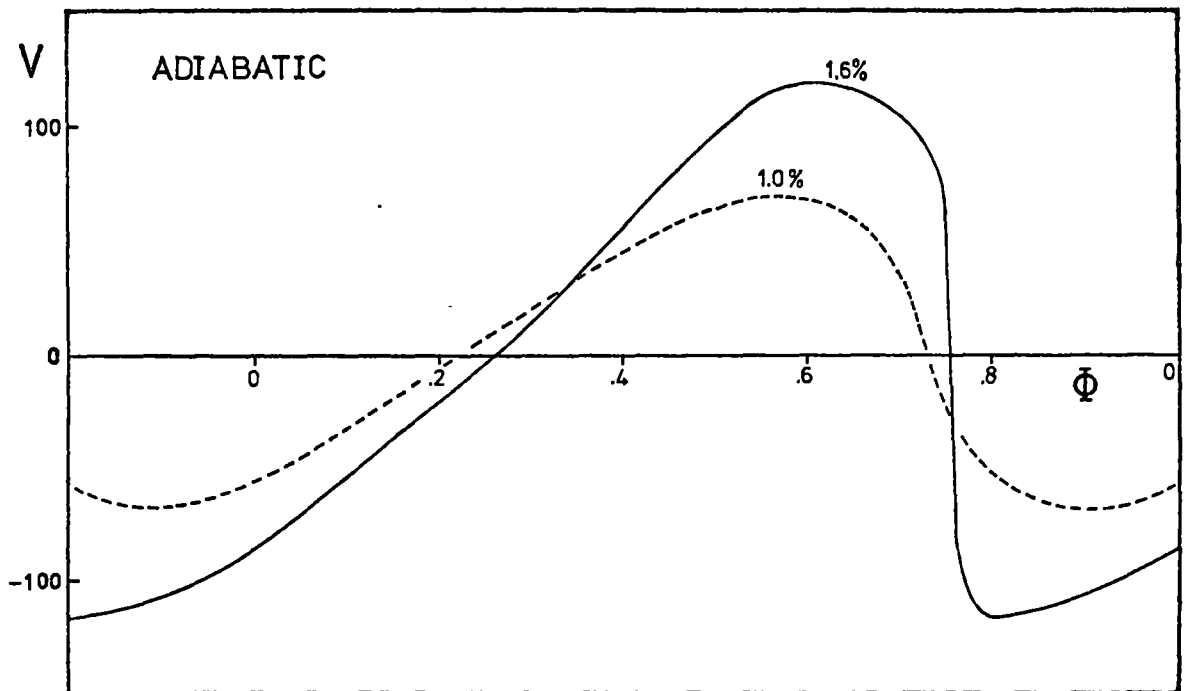


Figure 6.7 Velocity curves for two different piston amplitudes $\Delta P/P$ at $\tau = 10^{-2}$ within the adiabatic model. The phase convention is as for Figure 6.6. Velocity units are km s^{-1} .

by the atmospheric model in Section 6.2 has disappeared, diminishing the correspondance of the model with the observational data. This suggests that the second shock may have simply been an artifact of the 'hard' piston assumption. However, in view of the discussion in the previous subsection concerning the thermodynamics of the envelope, the extension of the isothermal assumption to the deep envelope regions must itself be considered physically unrealistic.

6.4.2 *The Nonlinear Adiabatic Model*

A nonlinear adiabatic model should provide a reasonable description of the stellar thermodynamical behaviour in the 15% to 20% of radius immediately above the first overtone node, although it will not be valid in the outlying transition and nonadiabatic regions. A sequence of adiabatic models was generated primarily to determine the appropriate pulsation amplitude and initial conditions for the diffusion model considered in Section 6.5. Figure 6.7 illustrates the velocity curves at $\tau = 10^{-2}$ for two of these models. At large amplitudes the velocity curve exhibits a steep descending branch. However, this rapid change in velocity is not associated with a shock wave, since the velocity reversal occurs almost simultaneously throughout the envelope, without any large spatial velocity gradient arising. Figure 6.8 shows the displacement curve for every fifth shell of the model with $\Delta P = 1.6\%$. From this it can be seen that the layers move synchronously. The near discontinuity of the velocity curve of this adiabatic model results simply from the nonlinear response of the atmosphere and outer envelope to the underlying sinusoidal variations. This is illustrated in Figure 6.9 which portrays the velocity curves at different depths within the model envelope. Comparing this figure with Figure 6.8 it can be seen that the dramatic steepening of the descending branch of the velocity curve in the outer

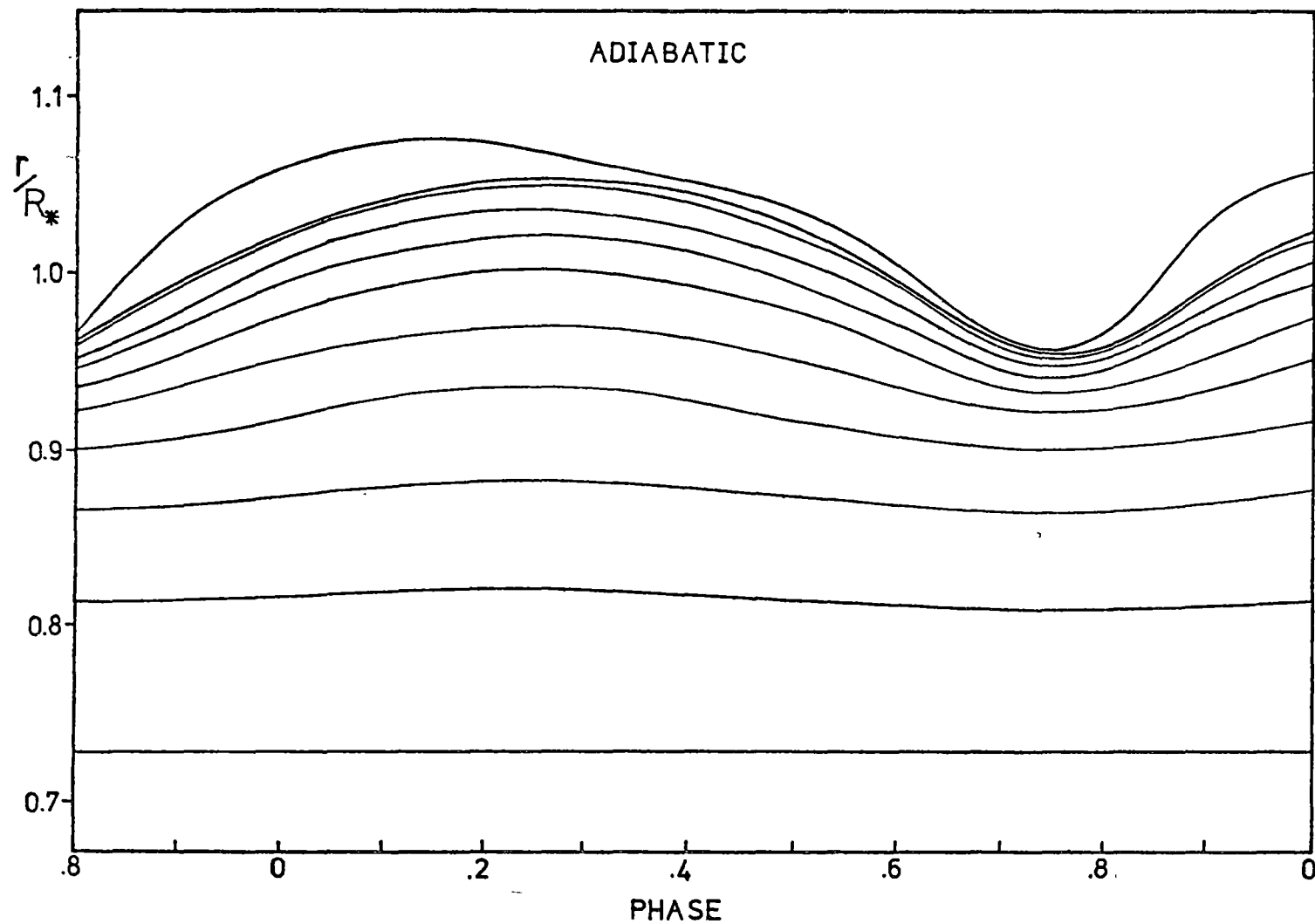


Figure 6.8 Displacement curves for every fifth shell, starting at the node, within the adiabatic envelope having $(\Delta P/P)_{\text{NODE}} = 1.6\%$. The phase convention is the same as in Figure 6.6.

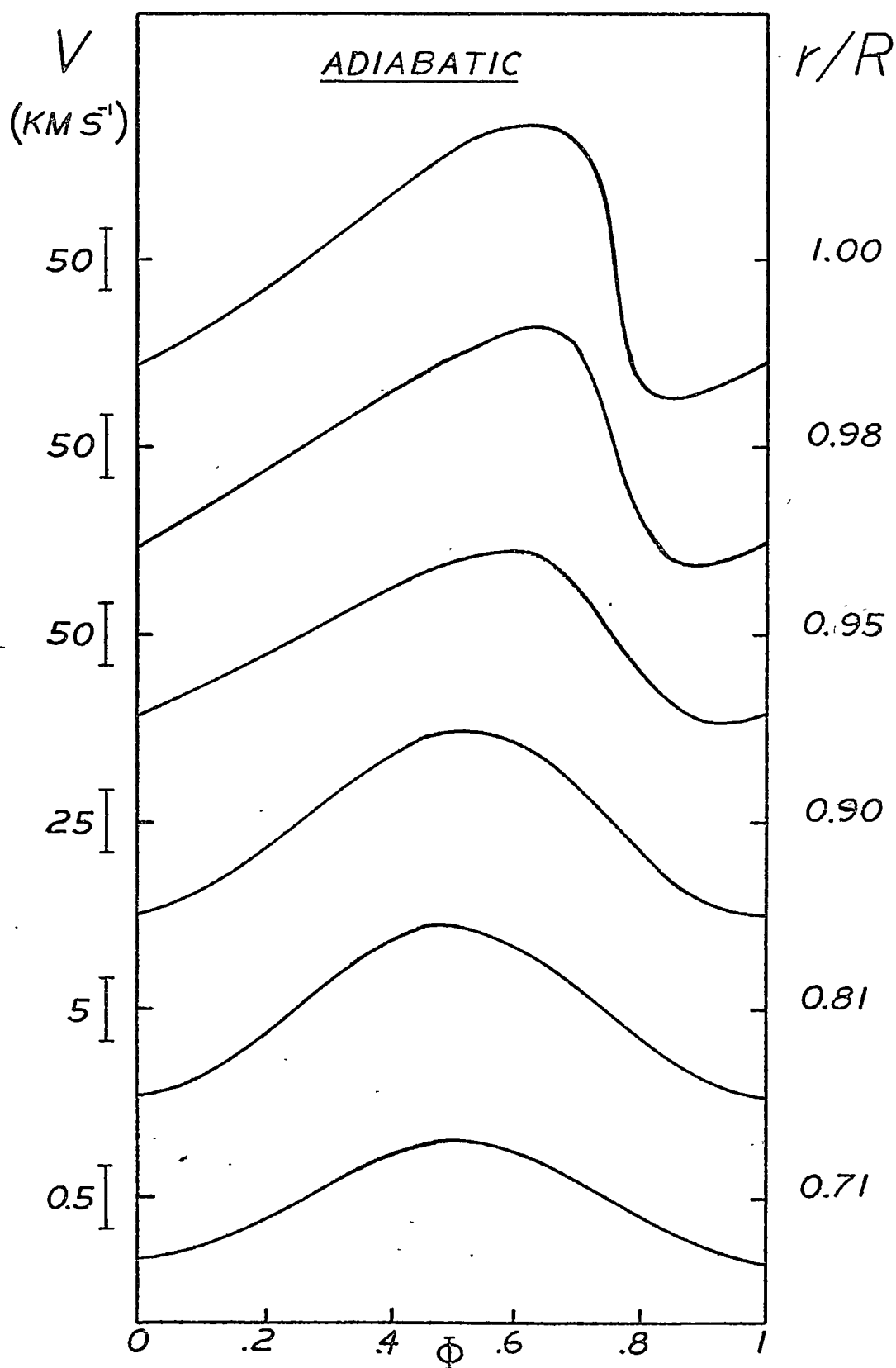


Figure 6.9 Velocity curves at different mass depths within the adiabatic model. Mass shells are labelled according to their location in fractional radius within a static model. Zero velocity levels are marked. The phase convention is the same as in Figure 6.6.

layers is associated with an increase in the time spent by these layers in the expanded phase at the expense of the contraction phase. Qualitatively speaking, this asymmetry between expansion and contraction arises because, on expansion, the dominant restoring force is gravitational, which is limited and diminishes as the mass shell moves out. On contraction, however, the restoring force is the pressure gradient, which, as the gas is compressed, can increase without limit. Consequently, for the nonlinear case, the duration of outward acceleration is considerably shorter than the duration of inward acceleration.

Thus, while the steeply descending branch of the adiabatic velocity curve is reminiscent of the discontinuous velocity curve observed in BW Vul, this similarity is superficial. This is because lack of a spatial velocity gradient means that neither line doubling nor light bump phenomena can occur in the adiabatic model. Also, just as for the isothermal envelope, no feature resembling the velocity stillstand of BW Vul is present in the adiabatic velocity curves.

6.4.3 *Comparison of the Isothermal and Adiabatic Models*

The isothermal and adiabatic models discussed in Sections 6.4.1 and 6.4.2 make very different predictions for the behaviour of the outer envelope. To decide whether or not shock waves are generated a more realistic thermodynamic treatment of the nonadiabatic region is required. Before pursuing this objective, it is useful to document the reason for the difference between the adiabatic and isothermal model predictions.

The cohesive behaviour of the adiabatic envelope compared to the isothermal envelope can be qualitatively understood because pressure changes respond more strongly to changes in density in the former case. Under adiabatic conditions $\Delta P/P = \Gamma \Delta \rho/\rho$, with $\Gamma \approx 5/3$, whereas for isothermal changes $\Gamma = \frac{\partial \ln P}{\partial \ln \rho} = 1$. Thus perturbations in density generate considerably stronger pressure restoring forces in the

adiabatic case. That these differences in the exponent $\Gamma = \frac{\partial \ln P}{\partial \ln \rho}$ are important can be seen from the linearized momentum equation for a mass shell. This equation is (Cox, 1974)

$$r\ddot{\zeta} = -\zeta 4\pi r^2 \frac{d}{dm} [(3\Gamma-4)P] + \frac{1}{r} \frac{\partial}{\partial m} [16\pi^2 \Gamma P \rho r^6 \frac{\partial \zeta}{\partial m}] \quad (6.11)$$

Following the argument of Cox (1974), if homologous motion is assumed (i.e. $\frac{\partial \zeta}{\partial m} = 0$) then Equation 6.11 becomes

$$\ddot{\zeta} = -\zeta 4\pi r (3\Gamma-4) \frac{dP}{dm} = - (3\Gamma-4) \frac{GM}{r^3} \zeta \quad (6.12)$$

Here it has also been assumed that $\frac{d\Gamma}{dm} = 0$ and the equation of hydrostatic equilibrium has been used to specify the equilibrium pressure gradient. From Equation 6.12 it is clear that oscillatory motion can only occur for $\Gamma > 4/3$. The case $\Gamma < 4/3$ corresponds to dynamical instability because the pressure changes accompanying a displacement are insufficient to counteract the geometric changes in gravity and pressure gradient forces. In this case the net restoring force is in the direction of motion, as Equation 6.11 indicates. These conclusions are valid only if $\Gamma < 4/3$ for the entire star because the partial derivatives with respect to mass couple each layer to every other. The isothermal envelope does not disrupt because the inner boundary condition, consistent with adiabatic variations ($\Gamma \sim 5/3$) *below* the node, prevents it from doing so. However, from these considerations, it is understandable that shock discontinuities arise in the isothermal envelope.

Combining the adiabatic and isothermal pictures in a crude way, it is conceivable that the nonlinear steepening of the descending branch of the velocity curve, together with a decrease in the exponent Γ in the nonadiabatic region, may assist in the formation of shock waves in the compression phase. To decide on the validity of this picture a model which incorporates radiation transfer assuming the diffusion approximation will be considered in the next section.

6.5 THE RADIATIVE DIFFUSION MODEL

6.5.1 The Difference Equations

To provide a more accurate treatment of the radiation transfer process, the diffusion approximation was assumed for the calculations described in this section. Although this will not be a realistic approximation for the outer atmospheric layers, it is valid for the large optical depths which pertain to most of the modelled region. The temperature of the upper layer was held constant by the outer boundary condition, so that the atmospheric gas motions were almost isothermal. At the inner boundary, the temperature variations were assumed to be adiabatic. Thus, in addition to the differential equations 6.7, 6.8, 6.9 and the boundary conditions 6.10, the following equations were solved:

$$\text{ENERGY CONSERVATION:} \quad \frac{\partial E}{\partial t} + p \frac{\partial V}{\partial t} = \frac{\partial L}{\partial m} \quad (6.13)$$

$$\text{ENERGY TRANSPORT:} \quad L = \frac{256\sigma\pi^2 r^4 T^3}{3\kappa} \frac{\partial T}{\partial m} \quad (6.14)$$

$$\text{BOUNDARY CONDITIONS:} \quad \left. \begin{aligned} T^4 &= \frac{3}{4} T_e^4 \left(\frac{2}{3} + \tau \right) & (\text{outer boundary}) \\ \frac{\delta T}{T} &= \frac{\Gamma_3^{-1}}{\Gamma_1} \frac{\delta p}{p} & (\text{inner boundary}) \end{aligned} \right\} \quad (6.15)$$

Here E is the internal energy and L is the radiative luminosity.

Convective energy transport was neglected since envelope convection does not carry a significant fraction of the flux in early B stars (Davey, 1970).

Combining Equations 6.13 and 6.14, they can be cast into the difference form:

$$\begin{aligned} & \frac{E_{I+1/2}^{J+1} - E_{I+1/2}^J}{t^{J+1} - t^J} + \frac{\frac{1}{2}(p_{I+1/2}^{J+1} + p_{I+1/2}^J + 2Q_{I+1/2}^{J+1/2})(V_{I+1/2}^{J+1} - V_{I+1/2}^J)}{t^{J+1} - t^J} \\ & - \frac{128\sigma\pi^2}{3(m_{I+1} - m_I)} \left\{ (r_{I+1}^{J+1})^2 (r_I^{J+1})^2 \frac{T_{I+3/2}^{J+1} - T_{I+1/2}^{J+1}}{m_{I+2} - m_I} \left((T_{I+3/2}^{J+1})^3 \kappa_{I+3/2}^{J+1} + (T_{I+1/2}^{J+1})^3 \kappa_{I+1/2}^{J+1} \right) \right. \\ & \quad \left. - \frac{T_{I+1/2}^{J+1} - T_{I-1/2}^{J+1}}{m_{I+1} - m_{I-1}} \left((T_{I+1/2}^{J+1})^3 \kappa_{I+1/2}^{J+1} + (T_{I-1/2}^{J+1})^3 \kappa_{I-1/2}^{J+1} \right) \right\} \end{aligned}$$

$$\begin{aligned}
& + (r_{I+1}^J)^2 (r_I^J)^2 \left[\frac{T_{I+3/2}^J - T_{I+1/2}^J}{m_{I+2} - m_I} \left((T_{I+3/2}^J)^3 \kappa_{I+3/2}^J + (T_{I+1/2}^J)^3 \kappa_{I+1/2}^J \right) \right. \\
& \quad \left. - \frac{T_{I+1/2}^J - T_{I-1/2}^J}{m_{I+1} - m_{I-1}} \left((T_{I+1/2}^J)^3 \kappa_{I+1/2}^J + (T_{I-1/2}^J)^3 \kappa_{I-1/2}^{J+1} \right) \right] = 0 .
\end{aligned} \tag{6.16}$$

The temperatures $\{T_I^{J+1}\}$ for $I = 2, \dots, N$ may be solved simultaneously and iteratively converged using a Newton-Raphson scheme similar to that described by Hill (1972). Rosseland mean opacities and internal energies appropriate to the outer layers were obtained from the ATLAS program. Opacities for the envelope were taken from the KING IVA table of Cox and Tabor (1976).

6.5.2 *Model Properties*

The added complexity of the model due to the incorporation of the diffusion approximation meant that, because of limitations on the available computing time, only ten pulsation cycles could be calculated. The evolution of the displacement of every tenth sector between the node and the photosphere following the changeover from the adiabatic to the diffusion approximation at phase 301.00 is shown in Figure 6.10.

It can be seen that switching to the diffusion code introduces strong transient forces in the mass shells exterior to the adiabatic region. With the adiabatic domain $r/R < 0.9$, however, particle motions are relatively unaffected. Evaluation of the exponent $\Gamma = \frac{\partial \ln P}{\partial \ln \rho}$ at various stages throughout the calculation confirmed that, within this region, values deviate negligibly from the adiabatic value. After about five cycles the outer layers have settled into a quasi-periodic state. Although the solution is not strictly periodic because of slight phase-shifts from cycle to cycle, over periods 306 to 310 the general form of the motions of the atmosphere and envelope undergo little change. In each of these cycles a strong shock wave is generated below the photosphere, at

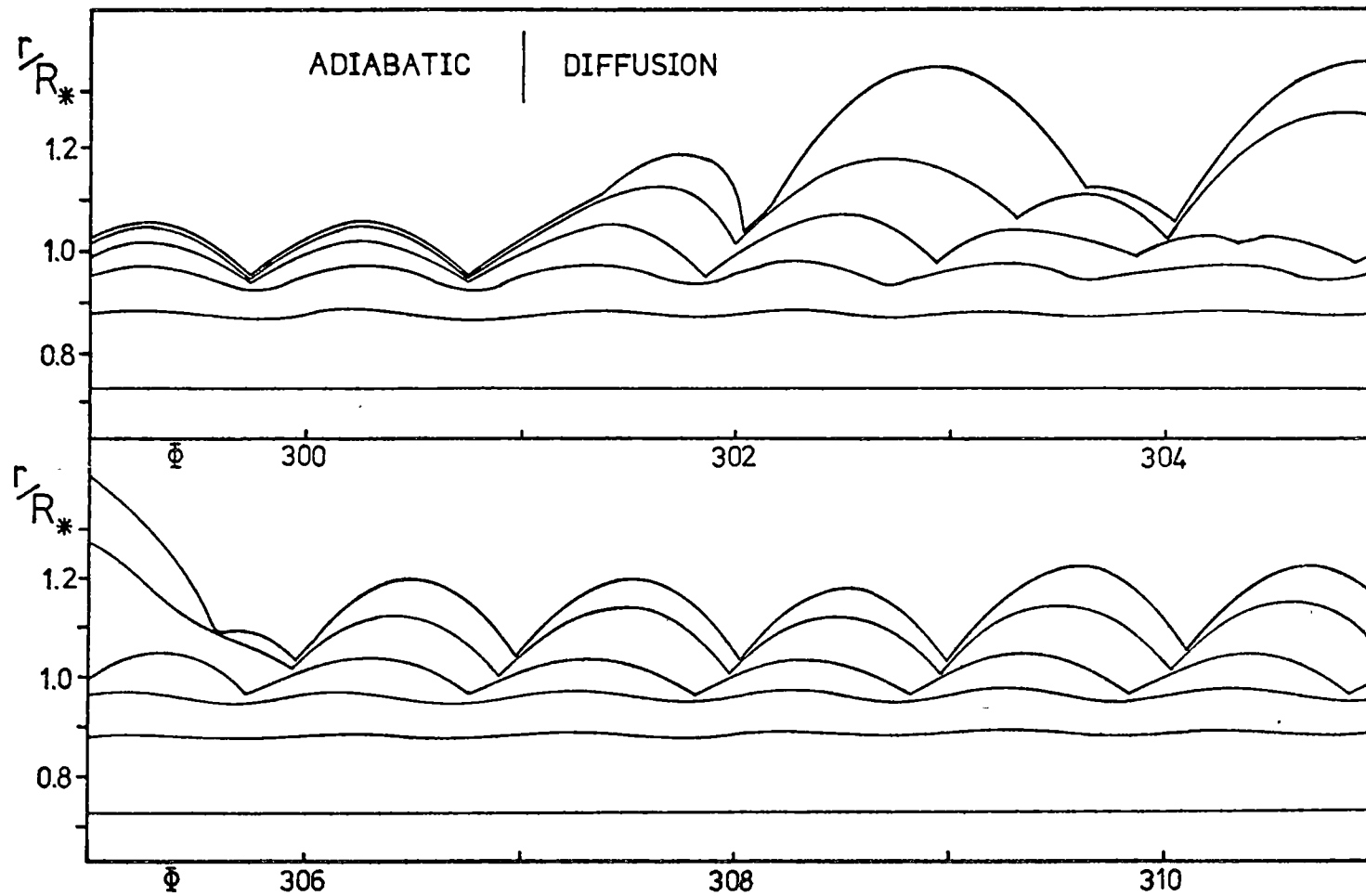


Figure 6.10 Displacement curves from phase 299.0 to 311.0 for sectors 51, 41, 31, 21, 11 and 6 within the adiabatic ($\phi 299 - 301$) and diffusion models ($\phi 301 - 311$). The two outermost sectors correspond to optical depths $\tau \sim 1$ and 10^{-3} . The phase convention is the same as in Figure 6.6.

optical depth $\tau \sim 300$. As was the case for the previous models, the shock coincides with the phase of maximum contraction and corresponds to the collision of infalling material with the expanding, underlying medium. Figure 6.11 illustrates the velocity curves for a number of mass shells. It can be seen from this figure that the formation of the shock wave is associated with the sudden steepening of the descending branch in velocity which occurs in the region $0.95 < r/R < 0.98$. This is also evident from the density and velocity cross-sections shown in Figure 6.12. The velocity curves indicate that the incipient shock forms gradually, steadily increasing in strength from phase 309.45 to 309.90 as the velocity gradient between the inner sinusoidal and outer non-sinusoidal regions intensifies. Near phase 309.75 the velocities within the adiabatic region are almost zero while the lagging upper envelope is still contracting at velocities of about 100 km s^{-1} . As the shock propagates into the outer layers the velocity discontinuity across it increases to become $\sim 300 \text{ km s}^{-1}$ at the photosphere and $\sim 400 \text{ km s}^{-1}$ at $\tau \sim 10^{-3}$. Clearly the model is of a considerably larger amplitude than would be appropriate for BW Vul, although the progenitor adiabatic model was approximately the correct amplitude.

Examination of the density profiles in Figure 6.12 shows that, in comparison with a static model, the outer envelope is in a rarefied state for most of the pulsation cycle. This is also evident from Figure 6.10 which indicates that the atmosphere of the diffusion model is considerably more extended than that for the adiabatic solution. The density profiles reveal that, for a brief period following the shock passage, there is a high density region resulting from post-shock compression. In this compression region, atmospheric densities may be a factor of 50 to 100 up on the corresponding density for a static model. This could explain the large increase in effective gravity during the phase of stillstand

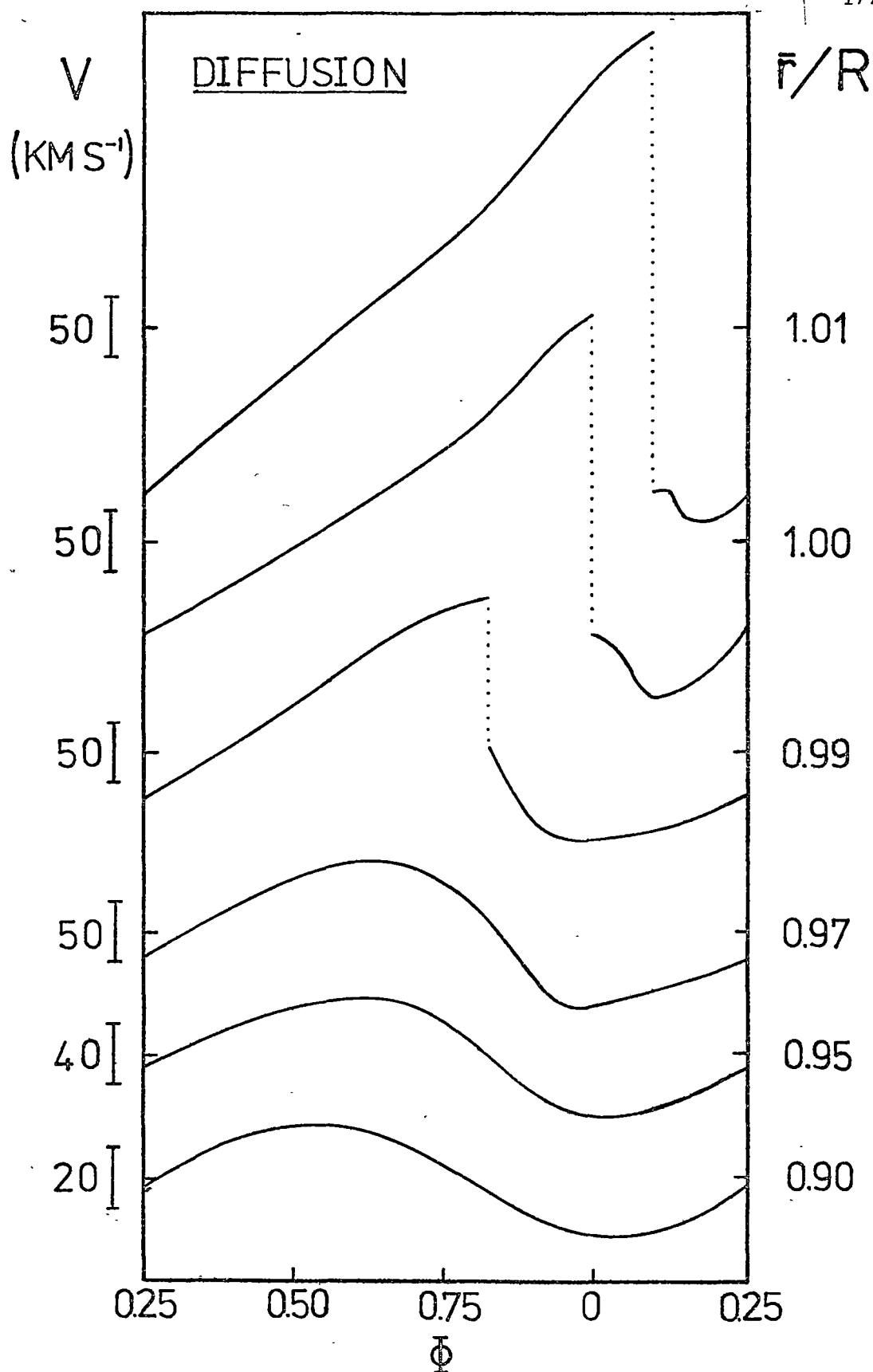


Figure 6.11 Velocity curves at different mass depths within the diffusion model. Details of mass shell labelling, velocity markings and the phase convention used are the same as in Figure 6.9. Shock discontinuities are indicated by dotted lines. The upper three velocity curves correspond to mean optical depths of $\tau = 10^{-3}$, 0.6 and 200.

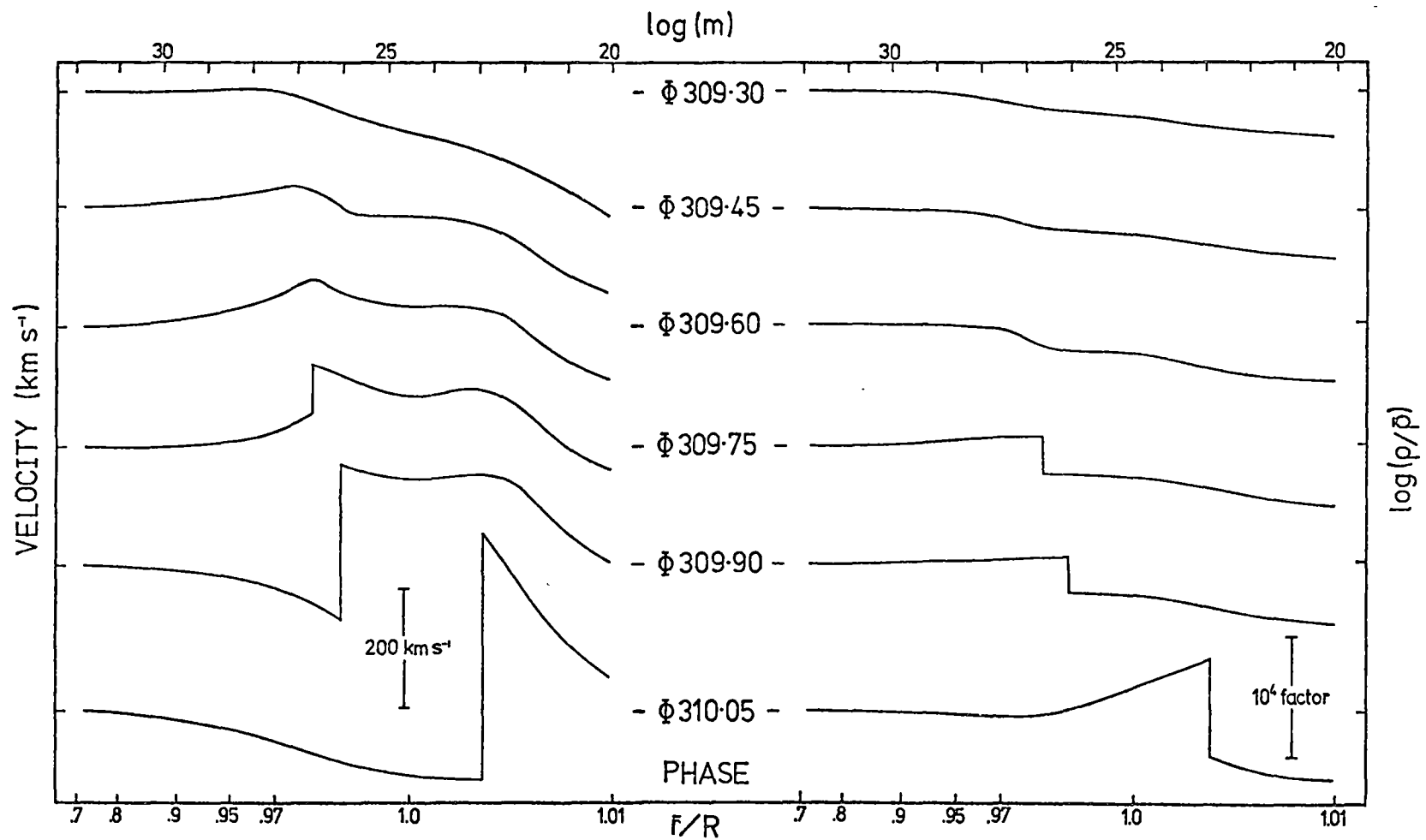


Figure 6.12 Velocity and density cross-sections for the diffusion model at some sample phases. Ordinate marks indicate the zero velocity level and HSE-density level for each cross-section.

determined by Kubiak (1972) from H gamma equivalent widths. Although this density enhancement is reminiscent of the 'ejected shell' postulated by Odgers (1956), this resemblance is only superficial since the post-shock high density region completely dissipates within an interval $\Delta\Phi \sim 0.2$ after the emergence of the shock into the photosphere at phase 310.0. The extended state of the atmosphere, together with the progressive lag in the gas motions throughout the extent of the atmosphere, means that the shock front remains in the line forming region for an appreciable time. For the lastshock calculated (phase ~ 310.0), the shock propagation time from depth $\tau = 1$ to $\tau = 10^{-3}$ was about $\Delta\Phi \sim 0.10$, which is comparable to the duration of line doubling observed by Goldberg *et al.* The phase delay resulting from the propagation time of the shock can be seen in the upper two velocity curves of Figure 6.11. Although the velocity curves do not exhibit a stillstand, there is a suggestion that there may be a brief interval of rapid outward post-shock acceleration similar to that which is present in the velocity curve of BW Vul following the stillstand. However, because of the smoothing of velocities in the neighbourhood of the shock by the artificial viscosity, the state of the post-shock region must be regarded as particularly uncertain. In addition, the coarseness of the model zoning prevents conclusions concerning the detailed velocity structure of the atmosphere being drawn. For this reason, no attempt was made to synthesise line profiles for this model. However, on the basis of the calculations performed in Section 6.2.3, line doubling over a phase interval $\Delta\Phi \sim 0.05 - 0.10$ would be expected. From the pre-shock density and velocity discontinuity an estimate may be obtained for the radiative flux produced by the shock. The maximum flux of about $4 \times 10^{12} \text{ erg cm}^{-2} \text{ sec}^{-1}$ is a factor of about twenty greater than the value predicted in Section 6.2.3 for the shock S1. This difference is primarily due to the larger velocity amplitude of the shock in the diffusion model. Hence the lower value is likely to be

a better estimate of the energy released in the atmosphere of BW Vul.

A final point of comparison of the model with observational data concerns the phase of occurrence of the shock relative to the variations in temperature. Such a comparison is feasible for the subphotosphere where the diffusion approximation remains valid. In this region the maximum in temperature appears to closely follow the passage of the shock front through the region. This is reasonably consistent with the observed phasing of the colour and radial velocity reported by Kubiak (1972).

6.6 LINE DOUBLING MECHANISMS FOR BW VUL

Observationally there is increasing evidence for shock or ejected shell phenomena in stars of the β Cephei class. Le Contel (1968) and Smith and McCall (1978a) have detected a component absorption feature in the line profiles of γ Peg, which they attribute to an ejected shell or shock wave. Similar but stronger features have been observed in the spectra of σ Sco by Campos and Smith (1980). Campos and Smith have also noted the presence of apparent emission features in the cores of ultraviolet spectral lines of β Cep. Significantly, the light amplitude spectrum method (Chapter 3) and the line profile fitting technique (Campos and Smith) both indicate that the single modes of γ Peg and β Cep and dominant (P_2) mode of σ Sco are *all* radial. The presence of a component absorption feature in the case of γ Peg is puzzling, since violent atmospheric effects are not expected for this star where the surface velocities are considerably less than the sound speed.

For BW Vul, the high dispersion spectroscopic observations of Goldberg *et al.* (1976) have yielded detailed information on the profiles during the epoch of line doubling. They provide a number of observational constraints which any mechanism attempting to explain the doubling

phenomenon in BW Vul must satisfy. The principal observational characteristics of the doubling phenomenon are

- (1) that it occurs on the descending branch of the velocity curve,
- (2) that there is no gross difference between the nature of the two components,
- (3) that there is a steady, progressive shift in intensity from the red-shifted component to the stillstand component,
- (4) that there is no drastic change in equivalent width during the splitting phase,

and (5) that the splitting is almost total in the deconvolved profiles.

To interpret the line doubling phenomenon observed in BW Vul, three mechanisms have been proposed. These may be categorized as

- (1) nonradial motions,
 - (2) an ejected shell,
- and (3) one or more shock waves.

The nonradial interpretation for BW Vul has been argued by Osaki (1971), Smith (1977) and Kubiak (1978). In this mechanism the line doubling would originate from differential velocities across the stellar disc associated with the nonradial motions. A nonradial explanation of the line doubling can satisfy all but the last of the five observational constraints listed above. However, a nonradial hypothesis for this star encounters several serious difficulties, such as an inability to reproduce the observed asymmetry in the velocities of the double components. These problems have been described in Section 5.3.1. At present, the only direct evidence concerning the nature of the surface motions of BW Vul, the pulsation amplitude spectrum discussed in Chapter 3, strongly favours a radial interpretation.

The ejected shell model of Odgers (1956) has been recently discussed in detail by Goldberg (1973) and Goldberg *et al.* (1976). Odgers'

interpretation assumes the ejection of an atmospheric shell, defined as a 'superficial layer of higher density', from the photosphere by a shock wave. The trajectory of this shell, which is assumed to be optically thick in the lines but not the continuum, is taken to be responsible for the observed velocity curve from the time of outward acceleration following stillstand to the onset of line doubling. At this latter time the infalling atmospheric shell is presumed to become transparent, so that the underlying photosphere can also contribute to the line absorption, producing line doubling. The shell then rejoins (or passes through) the photosphere, which is observed as the stillstand in radial velocity until the next shell ejection. One major difficulty with this picture is that none of the hydrodynamic models discussed in this chapter, or reported elsewhere in the literature, have resulted in the ejection of a shell which temporarily separates from the photosphere. A second difficulty is that the success of this model is very dependent on the behaviour of the shell opacity. The shell must be optically thin in the continuum and optically thick in the lines, except near the phase of line doubling, when the shell must become increasingly transparent. No convincing explanation of why the opacity should vary in this manner has been proposed. Although the ejected shell model provides a plausible interpretation of the radial velocity curve, it cannot be said with certainty that this theory will satisfy any of five observational criteria for line doubling listed above.

The results of Section 6.2 suggest that *if* a shock wave is present in the atmosphere of BW Vul, then line doubling and a light curve bump would be expected to occur. The steady conversion of pre-shock to post-shock material as the shock wave propagates through the line formation region provides a natural explanation of the observed intensity changes of the doubled line components. Crude line profile synthesis

calculations suggest that there can be a significant splitting of the line into two similar components in these circumstances. As to the question of whether a shock is generated, the diffusion model investigated in Section 6.5 indicated that there are grounds to suspect that this is indeed the case. Thus a radial single shock model is capable of reproducing, at least qualitatively, many of the salient observational characteristics of BW Vul. However, despite this agreement, there remain a number of inadequacies in this model. For example, it is not clear that shock-induced line doubling will roughly conserve line equivalent width. Much more sophisticated models are required to investigate this point. Another problem is that no explanation of the velocity stillstand is provided by the model. This may be because the coarse zoning and diffusion approximation do not permit reliable modelling of the post-shock atmospheric structure. However, for the present, the description of the post-shock gas flow must be regarded as seriously discrepant. Finally, the diffusion model may be legitimately criticized because the iteration was not followed until a more precise periodicity of the envelope dynamics was attained. Unfortunately available computing resources would not permit this. For a similar reason a more realistic treatment of radiation transfer in the outer layers could not be implemented. However the results of the diffusion model are sufficiently encouraging as to merit further investigation with more refined models by investigators with more powerful computing facilities available.

CHAPTER SEVEN

CONCLUSIONS

In this thesis a variety of mode identification diagnostics have been explored with the ultimate aim of determining the nature of the surface motions in the β Cephei stars. Three methods of discerning these motions were investigated in some detail.

The first of these considered the relative amplitudes and phases of the light, colour and radial velocity variations. It was shown that colour to visual light ratios are mode discriminating for the β Cephei stars providing a sufficiently long wavelength baseline is used to derive the colour index. Phase differences between observational quantities are not useful for these stars because the temperature and radius variations are very close to being π out of phase. This is the converse of the situation for the δ Scuti and cepheid variables where the phase difference between temperature and radius changes is about $\pi/2$ radians. For these variables the phase difference between light and colour (but not light and velocity) is mode discriminating, whereas the amplitude ratios are of no use.

An example of the use of photometric indices for mode typing, the wavelength dependence of the light range was examined for ten β Cephei stars. Seven of these stars, γ Peg, δ Cet, ξ ' CMa, β Cep, HR 6684, α Lup and BW Vul, are singly periodic. All of these were found to be radial pulsators. The line broadening mode of σ Sco was also determined as radial. However the data for the line broadening modes of β CMa and 12 Lac were not found to be consistent with radial pulsations but were strongly indicative of quadrupole modes. These identifications have since been independently confirmed by line profile analyses carried out in the case of δ Cet, β Cep and σ Sco by Campos and Smith (1980), in the case of γ Peg by Smith and McCall (1978a) and Campos and Smith (1980), and in the case of 12 Lac by Smith (1980a).

The assumptions underlying the nonradial Baade-Wesselink method formulated by Balona and Stobie (1979a) were investigated in Sections 2.7 and 5.4. It was established that, for $l > 1$, the relation between surface brightness and colour index is not single-valued, even if the flux is insensitive to gravity changes. A modified Baade-Wesselink expression taking this fact into account was then derived. The new expression differs principally from that obtained by Balona and Stobie in that the coefficient of the radial velocity integral is nonzero for odd values of the mode order l . The second Baade-Wesselink assumption, which allows the evaluation of a surface area term from the radial velocity data, was found to be realizable in the nonradial case only if the mean profile wavelength is used to determine the radial velocity.

The second mode identification technique investigated concerned possible polarization variations due to nonradial pulsations in early B stars. It was found that these variations would probably be too small to be detected at visual wavelengths. However observations in the satellite ultraviolet offer a better prospect for success. Estimates of the likely amplitude of the polarization changes in 12 Lac using the Smith (1980a) model were determined. Several instances were cited for which polarization monitoring may yield a significant null result confirming the presence of radial oscillations.

The third mode diagnostic involved the comparison of observed line profiles with those predicted theoretically. Characteristics of the nonradial line profiles for $l \leq 3$ were examined to evaluate this method and facilitate its application. An attempt was made to model the photographic spectral data of 12 Lac over three complete cycles using two interfering quadrupole modes. BW Vul was also briefly discussed from the nonradial standpoint. It was concluded that, because of the large

number of controlling parameters and similarities amongst profiles corresponding to differing nonradial configurations, only the fitting of long sequences of very high quality spectral data can hope to provide a unique solution.

Two of the cases for which the pulsation amplitude spectrum indicated radial pulsation are ones in which line doubling effects appear. These are BW Vul and the dominant mode of σ Sco. It follows that some *radial* line doubling mechanism must be operative in these stars. Hydrodynamic calculations of an envelope diffusion model suggested that shock waves may be generated by the nonlinear response of the outer layers to underlying sinusoidal variations. Simple atmospheric models indicate that, if such a shock wave is present, it would be expected to produce line doubling and light curve bump phenomena similar to those observed in BW Vul.

Despite the evidence for radial pulsations in many β Cephei stars, there is strong reason to believe that 12 Lac undergoes nonradial pulsations. The light amplitude spectrum discussed in Chapter 3, the line profile evidence of Smith (1980a) and the frequency spectrum of Jerzykiewicz (1978), all concur in a nonradial identification for some of the modes present in this star. In addition, the appreciable number of β Cephei stars which pulsate in two or more modes of only slightly different frequencies suggests that nonradial pulsations occur in other stars in the group. Thus we are presented with the complex situation that both radial and nonradial modes are apparently present in these stars, while theoretical analyses indicate instability in neither case. In view of the identification of a radial mode in 12 Lac by Smith (1980a), it is possible that the β Cephei stars are intrinsically unstable to a radial oscillation, but that, in the multiperiodic stars, coupling occurs to close period nonradial modes.

REFERENCES

- Aizenman, M.L., Cox, J.P. & Lesh, J.R. (1975), *Astrophys.J.*, 197, 399.
- Allison, A.M., Glaspey, J.W. & Fahlman, G.G. (1977), *Astron.J.*, 82, 283.
- Balona, L.A. (1977), *Mon.Not.R.Astr.Soc.*, 178, 231.
- Balona, L.A. & Feast, M.W. (1975), *Mon.Not.R.astr.Soc.*, 172, 191.
- Balona, L.A. & Martin, W.L. (1978), *Mon.Not.R.astr.Soc.*, 184, 1.
- Balona, L.A. & Stobie, R.S. (1979a), *Mon.Not.R.astr.Soc.*, 187, 217.
- _____. (1979b), *Mon.Not.R.astr.Soc.*, 189, 641.
- _____. (1979c), *Mon.Not.R.astr.Soc.*, 189, 649.
- _____. (1979d), *Mon.Not.R.astr.Soc.*, 189, 659.
- _____. (1980), *Mon.Not.R.astr.Soc.*, 190, 931.
- Beeckmans, F. & Burger, M. (1977), *Astron.Astrophys.*, 61, 815.
- Bell, R.A. & Gustafsson, B. (1978), *Astron.Astrophys.Suppl.*, 34, 229.
- Bhatnagar, M.S., Kushrestha, K.P. & Tandon, J.N. (1971), *Astrophys.Lett.*, 9, 135.
- Bhatnagar, M.S. & Kushwaha, R.S. (1961a), *Ann.Astrophys.*, 24, 211.
- _____. (1961b), *Prod.Natl.Inst.Sci.India A*, 27a, 441.
- _____. (1963), *Proc.Natl.Inst.Sci.India A*, 29a, 143.
- Bolton, C.T., Percy, J.R. & Shemilt, R.E. (1975), *Publ.astr.Soc.Pac.*, 87, 595.
- Breger, M. (1967), *Mon.Not.R.astr.Soc.*, 136, 51.
- _____. (1975), *Astrophys.J.*, 201, 653.
- Breger, M. & Bregman, J.N. (1975), *Astrophys.J.*, 200, 343.
- Breger, M., Hutchins, J. & Kuhi, L.V. (1976), *Astrophys.J.*, 210, 163.
- Buta, R.J. & Smith, M.A. (1979), *Astrophys.J.*, 232, 213.
- Campos, A.J. & Smith, M.A. (1980), *Astrophys.J.*, 238, in press.
- Chandrasekhar, S. (1946), *Astrophys.J.*, 103, 351.
- Chandrasekhar, S. & Lebovitz, N.R. (1962), *Astrophys.J.*, 132, 1105.
- Cherewick, T.A. & Young, A. (1975), *Publ.astr.Soc.Pac.*, 87, 311.
- Christy, R.F. (1966), *Astron.J.*, 72, 293.

- Clement, M. (1965), *Astrophys.J.*, 141, 1443.
 _____ (1967), *Astrophys.J.*, 150, 589.
 _____ (1969), *Astrophys.J.*, 156, 1051.
- Code, A.D. (1950), *Astrophys.J.*, 112, 22.
- Collins, G.W. (1970), *Astrophys.J.*, 159, 583.
- Cox, A.N. (1979), *Astrophys.J.*, 229, 212.
- Cox, A.N. & Tabor, J.E. (1976), *Astrophys.J.Supp.*, 31, 271.
- Cox, J.P. (1974), *Rep.Prog.Phys.*, 37, 563.
 _____ (1976), *Proceedings of the Solar and Stellar Pulsation Conference*,
 ed. A.N. Cox, R.G. Deupree, pp. 127-139 (Los Alamos Publ. LA - 6544 - C).
- Cox, J.P. & Guili, R.T. (1968), *Principles of Stellar Structure*
 (New York: Gordon and Breach).
- Davey, W.R. (1970), Unpublished thesis, University of Colorado.
 _____ (1973), *Astrophys.J.*, 179, 235.
- Duval, P. & Karp, A.H. (1978), *Astrophys.J.*, 222, 220.
- Dziembowski, W. (1971), *Acta Astr.*, 21, 289.
 _____ (1977), *Acta Astr.* 27, 203.
- Eddington, A. (1926), *The Internal Constitution of the Stars*, (New York:
 Dover Publications).
- Evans, N.R. (1976), *Astrophys.J.*, 209, 135.
- Fitch, W.S. (1967), *Astrophys.J.*, 148, 481.
 _____ (1969), *Astrophys.J.*, 158, 269.
- Gebbie, K.B. (1967), *Mon.Not.R.astr.Soc.*, 135, 181.
- Getting, I.A. (1935), *Mon.Not.R.astr.Soc.*, 95, 141.
- Goldberg, B.A. (1973), Unpublished thesis, University of British Columbia.
- Goldberg, B.A., Walker, G.A.H. & Odgers, G.J. (1974), *Astron.Astrophys.*,
32, 355.
 _____ (1976), *Astron.J.*, 81, 433.
- Gray, D.F. (1970), *Astron.J.*, 75, 958.

- Haisch, B.M. & Cassinelli, J.P. (1976), *Astrophys.J.*, 208, 253.
- Harrington, J.P. (1969), *Astrophys.Lett.*, 3, 166.
- _____. (1970), *Astrophys.Space Sci.*, 8, 227.
- Heard, J.F., Hurkens, R.J., Porco, M. & Percy, J.R. (1976), *J.R.astr. Soc.Canada.*, 70, 213.
- Hill, S.J. (1972), *Astrophys.J.*, 178, 793.
- Hill, S.J. & Willson, L.A. (1979), *Astrophys.J.*, 229, 1029.
- Hillendahl, R.W. (1970), *Publ.astr.Soc.Pac.*, 82, 1231.
- Hurley, M., Robert, P.H. & Wright, K. (1966), *Astrophys.J.*, 143, 535.
- Hutchings, J.B. & Hill, G. (1977), *Astrophys.J.*, 213, 111.
- Hutchinson, J.L., Hill, S.J. & Lillie, C.F. (1975), *Astron.J.*, 80, 1044.
- Jakate, S.M. (1979), *Astron.J.*, 84, 1042.
- Jerzykiewicz, M. (1970), *Lowell Obs.Bull.*, 18, 199.
- _____. (1978), *Acta Astr.*, 28, 465.
- Jerzykiewicz, M. & Sterken, C. (1978), IAU Colloquium No. 46, ed. F.M. Bateson, University of Waikato, New Zealand.
- Jones, D.H.P. & Shobbrook, R.R. (1974), *Mon.Not.R.astr.Soc.*, 166, 649.
- Karp, A.H. (1973), *Astrophys.J.*, 180, 895.
- _____. (1975), *Astrophys.J.*, 201, 641.
- Kato, S. (1966), *Publ.Astron.Soc.Japan.*, 18, 374.
- Kubiak, M. (1972), *Acta Astr.*, 22, 13.
- _____. (1978), *Acta Astr.*, 28, 153.
- Kurtz, D.W. (1980), *Mon.Not.R.astr.Soc.*, 191, 115.
- Kurucz, R.L. (1969), *Proc. Third Harvard Smithsonian Conference on Stellar Atmospheres*, ed. O. Gingerich, MIT Press.
- _____. (1970), *Smithsonian Astrophys.Obs.Spec.Rep.*, No. 309.
- _____. (1979), *Astrophys.J.Suppl.*, 40, 1.
- Kurucz, R.L., Peytremann, E. & Avrett, E.H. (1974), *Blanketed Model Atmospheres for Early-Type Stars*, (Washington: Smithsonian Institute Press).

- Le Contel, J.-M. (1968), *4th Colloq. Variable Stars*, ed. L. Detre, p. 298 (Budapest: Academic).
- Ledoux, P. (1951), *Astrophys.J.*, 114, 373.
- Ledoux, P. & Walraven, Th. (1958), *Handbuch der Physik*, ed. S. Flügge, 51, pp. 353-604, (Berlin: Springer-Verlag).
- Lesh, J.R. (1976), *Astrophys.J.*, 208, 135.
- _____. (1978), *Astrophys.J.*, 219, 947.
- Lesh, J.R. & Aizenman, M.L. (1974), *Astron.Astrophys.*, 34, 203.
- _____. (1976), *Multiple Periodic Variable Stars*, Part 1, ed. W.S. Fitch, pp. 11-32, (Dordrecht: Reidel).
- _____. (1978), *Ann.Rev.Astron.Astrophys.*, 16, 215.
- Lesh, J.R. & Wesselius, P.R. (1979), *Astron.Astrophys.*, 79, 115.
- Leung, K.C. (1965), *Astron.J.*, 70, 145.
- _____. (1968), *Astrophys.Space Sci.*, 2, 302.
- Lomb, N.R. & Shobbrook, R.R. (1975), *Mon.Not.R.astr.Soc.*, 173, 709.
- Margrave, T.E. (1979), *Publ.astr.Soc.Pac.*, 91, 666.
- McNamara, D.H. (1955), *Astrophys.J.*, 122, 95.
- McNamara, D.H. & Feltz, K.A. (1976), *Publ.astr.Soc.Pac.*, 88, 510.
- Meyer, W.F. (1934), *Publ.astr.Soc.Pac.*, 46, 202.
- Mihalas, D. (1979), *Mon.Not.R.astr.Soc.*, 189, 671.
- Milone, L.A. (1963), *Bol.Inst.Mat.Astr.Fis.Cordoba*, 1, 43.
- Morton, A.E. & Hansen, H.K. (1974), *Publ.astr.Soc.Pac.*, 86, 943.
- Odell, A.P. (1979), *Publ.astr.Soc.Pac.*, 91, 326.
- Odgers, G.J. (1956), *Publ.Dom.Astrophys.Obs.*, 10, 215.
- Odgers, G.J. & Kushwaha, R.S. (1959), *Publ.Dom.Astrophys.Obs.*, 11, 185.
- Osaki, Y. (1971), *Publ.Astron.Soc.Japan*, 23, 485.
- _____. (1974), *Astrophys.J.*, 189, 469.
- _____. (1976), *Publ.Astron.Soc.Japan*, 28, 105.
- _____. (1978), IAU Colloquium No. 46, ed. F.M. Bateson, University of Waikato, New Zealand.

- Pagel, B.E.J. (1956), *Mon.Not.R.astr.Soc.*, 116, 10.
- Parsons, S.B. (1971), *Mon.Not.R.astr.Soc.*, 152, 121.
- _____. (1972), *Astrophys.J.*, 174, 57.
- Plavec, M. (1971), *Publ.astr.Soc.Pac.*, 83, 144.
- Richtmyer, R.D. & Morton, K.W. (1967), *Difference Methods for Initial Value Problems*, (New York: Interscience).
- Saio, H. & Cox, J.P. (1980), *Astrophys.J.*, 236, 549.
- Sareyan, J.-P., Le Contel, J.-M. & Valtier, J.C. (1976), *Astron.Astrophys. Suppl.*, 25, 129.
- Sato, N. (1973), *Astrophys.Space Sci.*, 24, 215.
- Schafgans, J.J. & Tinbergen, J. (1979), *Astron.Astrophys.*, 35, 279.
- Schmalberger, D.C. (1960), *Astrophys.J.*, 132, 591.
- Serkowski, K. (1962), *Adv.Astron.Astrophys.*, 1, 289.
- _____. (1968), *Astrophys.J.*, 154, 115.
- _____. (1970), *Astrophys.J.*, 160, 1083.
- Serkowski, K. & Robertson, J.W. (1969), *Astrophys.J.*, 158, 441.
- Shibahashi, H. & Osaki, Y. (1976), *Publ.Astron.Soc.Japan*, 28, 199.
- Shobbrook, R.R. (1973a), *Mon.Not.R.astr.Soc.*, 161, 257.
- _____. (1973b), *Mon.Not.R.astr.Soc.*, 162, 25.
- _____. (1978), IAU Colloquium No. 46, ed. F.M. Bateson, University of Waikato, New Zealand.
- _____. (1979), *Proc.Astr.Soc.Aust.*, 5, 296.
- Shobbrook, R.R., Lomb, N.R. & Herbison-Evans, D. (1972), *Mon.Not.R.astr. Soc.*, 156, 165.
- Skalafuris, A.J. (1974), *Astrophys.J.*, 190, 91.
- Smith, M.A. (1977), *Astrophys.J.*, 215, 574.
- _____. (1978), *Astrophys.J.*, 224, 927.
- _____. (1979a), *Workshop on Nonradial Pulsation*, ed. H. Hill, University of Arizona.

- _____. (1979b), *Astrophys.J.*, in press.
- _____. (1979c), *Proc. IAU Joint Session on Stellar Instabilities, Montreal*, ed. A. Cox.
- _____. (1980a), *Astrophys.J.*, in press.
- _____. (1980b), *Tucson Conference on Nonradial Pulsations in the Sun and Stars*, ed. R. Kippenhahn, (New York: Springer-Verlag).
- _____. (1980c), preprint.
- Smith, M.A., Africano, J. & Worden, S.P. (1979), private communication.
- Smith, M.A. & Buta, R.J. (1979), *Astrophys.J.Lett.*, 232, 193.
- Smith, M.A. & McCall, M.L. (1978a), *Astrophys.J.*, 221, 861.
- _____. (1978b), *Astrophys.J.*, 223, 221.
- Stamford, P.A. & Watson, R.D. (1976), *Proc.Astr.Soc.Aust.*, 3, 75.
- _____. (1977), *Mon.Not.R.astr.Soc.*, 180, 551.
- _____. (1978a), IAU Colloquium No. 46, ed. F.M. Bateson, University of Waikato, New Zealand.
- _____. (1978b), *Proc.Astr.Soc.Aust.*, 4, 273.
- _____. (1980a), *Acta Astr.*, in press.
- _____. (1980b), *Proc.Astr.Soc.Aust.*, in press.
- Stellingwerf, R.F. (1978), *Astron.J.*, 83, 1184.
- _____. (1979), *Astrophys.J.*, 227, 935.
- Stothers, R. (1976), *Astrophys.J.*, 210, 434.
- Stothers, R. & Simon, N.R. (1969), *Astrophys.J.*, 157, 673.
- _____. (1970a), *Publ.astr.Soc.Pac.*, 82, 707.
- _____. (1970b), *Astrophys.J.*, 160, 1019.
- Struve, O. (1955), *Publ.astr.Soc.Pac.*, 67, 135.
- Struve, O., McNamara, D.H., Kung, S.M. & Beymer, C. (1953), *Astrophys.J.*, 118, 89.
- Struve, O., McNamara, D.H., Kung, S.M., Kraft, R.P. & Williams, A.D. (1952), *Astrophys.J.*, 116, 398.
- Struve, O., McNamara, D.H. & Zeberg, V. (1955), *Astrophys.J.*, 122, 122.

- Struve, O. & Zeberg, V. (1955), *Astrophys.J.*, 122, 134.
- Trodahl, H.J. & Sullivan, D.J. (1977), *Mon.Not.R.astr.Soc.*, 179, 209.
- Thiessen, G. (1957), *Zeitschrift für Astrophysik*, 41, 259.
- Underhill, A. (1966), *The Early-Type Stars*, pp. 246-259, (Dordrecht: Reidel).
- Unno, W., Osaki, Y., Ando, H. & Shibahashi, H. (1979), *Nonradial Oscillations of Stars*, (Tokyo: University of Tokyo Press).
- Van Hoof, A. (1961a), *Z.Astrophys.*, 53, 106.
- _____. (1961b), *Z.Astrophys.*, 53, 124.
- _____. (1962), *Z.Astrophys.*, 54, 244.
- _____. (1963), *Z.Astrophys.*, 57, 278.
- _____. (1964), *Z.Astrophys.*, 60, 184.
- _____. (1965), *Z.Astrophys.*, 62, 174.
- _____. (1966), *Z.Astrophys.*, 64, 165.
- _____. (1970), *Spectroscopic Astrophysics*, ed. G.H. Herbig, pp. 343-363, (Berkeley: University of California Press).
- Van Hoof, A., Pretorius, W.S. & Pikoos, G. (1964), *Inf.Bull.Var.Stars* No. 63.
- Walker, M.F. (1952), *Astrophys.J.*, 116, 106.
- _____. (1954), *Astrophys.J.*, 119, 631.
- Watson, R.D. (1971a), *Astrophys.J.*, 169, 343.
- _____. (1971b), *Astrophys.J.*, 170, 345.
- Whitney, C.A. (1967), IAU Symposium 28, *Aerodynamic Phenomena in Stellar Atmospheres*, ed. R.N. Thomas, (New York: Academic Press).
- Willson, L.A. & Hill, S.J. (1979), *Astrophys.J.*, 228, 854.
- Wood, P.R. (1979), *Astrophys.J.*, 227, 220.
- Young, A., Furenlid, I. & Snowden, M. (1979), *Bull.Am.Astr.Soc.*, 11, 728.

$\underline{\xi}(\theta, \phi, t) = (\xi_r(\theta, \phi, t), \xi_\theta(\theta, \phi, t), \xi_\phi(\theta, \phi, t))$, then the instantaneous position vector of this particle at time t is

$$\underline{R}(\theta, \phi, t) = [R_0(\theta) + \xi_r] \underline{r} \quad (A1.1)$$

where $R_0(\theta)$ describes the equilibrium rotational shape defined by Equation 2.1. Changing co-ordinate systems, the position vector is

$$\underline{R}(\theta, \phi, t) = R(\theta, \phi, t) [\sin \theta \cos \phi \hat{i} + \sin \theta \sin \phi \hat{j} + \cos \theta \hat{k}] \quad (A1.2)$$

where $R(\theta, \phi, t) = R_0(\theta) + \xi_r(\theta, \phi, t)$. The normal to the surface is

$$\begin{aligned} \underline{n} &= \frac{\partial \underline{R}}{\partial \theta} \times \frac{\partial \underline{R}}{\partial \phi} \\ &= R \left\{ \left[\frac{\partial R}{\partial \phi} \sin \phi + \sin \theta \cos \phi \left(R \sin \theta - \frac{\partial R}{\partial \theta} \cos \theta \right) \right] \hat{i} + \right. \\ &\quad \left[-\frac{\partial R}{\partial \phi} \cos \phi + \sin \theta \sin \phi \left(R \sin \theta - \frac{\partial R}{\partial \theta} \cos \theta \right) \right] \hat{j} + \\ &\quad \left. \sin \theta \left[\frac{\partial R}{\partial \theta} \sin \theta + R \cos \theta \right] \hat{k} \right\}. \end{aligned} \quad (A1.3)$$

The magnitude of \underline{n} is

$$|\underline{n}| = R \{ R^2 \sin^2 \theta + \left(\frac{\partial R}{\partial \theta} \right)^2 \sin^2 \theta + \left(\frac{\partial R}{\partial \phi} \right)^2 \}^{1/2}, \quad (A1.4)$$

and the equation to the line-of-sight is

$$\underline{\underline{L}} = \sin i \hat{i} + \cos i \hat{k}. \quad (A1.5)$$

Hence, projecting the surface normal onto the line-of-sight gives

$$\begin{aligned} \cos \gamma &= \underline{\underline{n}} \cdot \underline{\underline{L}} \\ &= \{ R^2 \sin^2 \theta + \left(\frac{\partial R}{\partial \theta} \right)^2 \sin^2 \theta + \left(\frac{\partial R}{\partial \phi} \right)^2 \}^{-1/2} \{ R \sin \theta (\cos \theta \cos i \\ &\quad + \sin \theta \cos \phi \sin i) + \frac{\partial R}{\partial \theta} \sin \theta (\sin \theta \cos i - \cos \theta \cos \phi \sin i) \\ &\quad + \frac{\partial R}{\partial \phi} \sin i \sin \phi \}. \end{aligned} \quad (A1.6)$$

The surface area, $A = \iint_{\theta\phi} |\underline{n}| d\theta d\phi$. (A1.7)

Inserting the value of \underline{n} from Equation (A1.4), gives the differential element of surface area

$$dA = R \{ R^2 \sin^2 \theta + \left(\frac{\partial R}{\partial \theta} \right)^2 \sin^2 \theta + \left(\frac{\partial R}{\partial \phi} \right)^2 \}^{1/2} d\theta d\phi . \quad (\text{A1.8})$$

Equation (A1.8) allows the determination of the area of each sector by inserting the appropriate sector centre co-ordinates.

A P P E N D I X 2

PLOTS OF THE NONRADIAL SURFACE CONFIGURATIONS

Figures A2.1 a-i portray the surface distortions, as seen by a distant observer, resulting from nonradial modes with $l \leq 3$. These have been plotted at four equal intervals of phase ($\Phi = 0, 0.25, 0.50, 0.75$) and at three angles of inclination ranging from an equatorial ($i = 90^\circ$) to a polar ($i = 0^\circ$) aspect. The maximum pulsation amplitude of the dominant antinode has been set at $\pm 10\%$ of the equilibrium radius in these diagrams so that the perturbations may be readily seen. The equilibrium surface is represented by the dotted line and the north pole is identified by a cross.

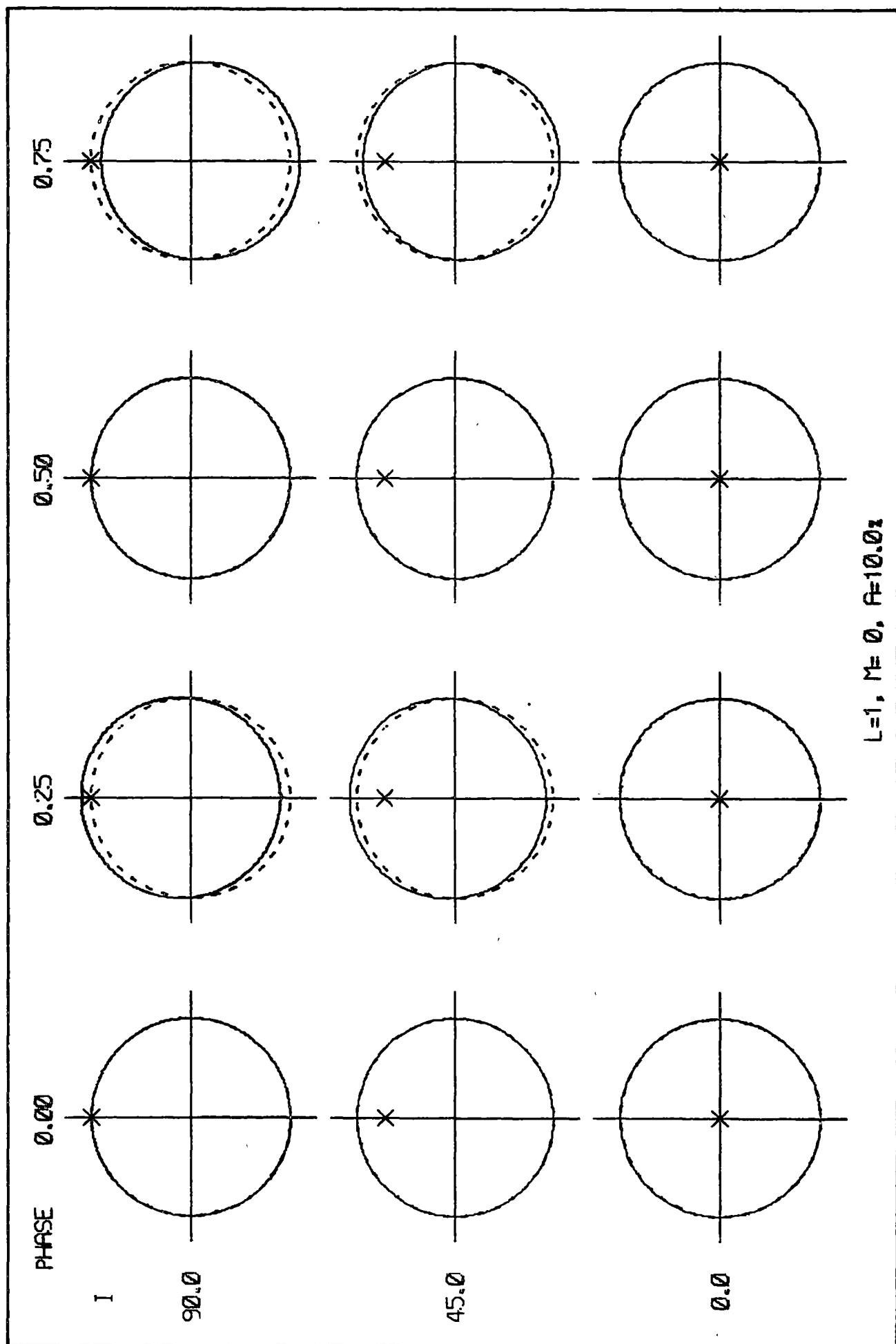


Figure A2.1(a) Surface configuration for (1,0) mode.

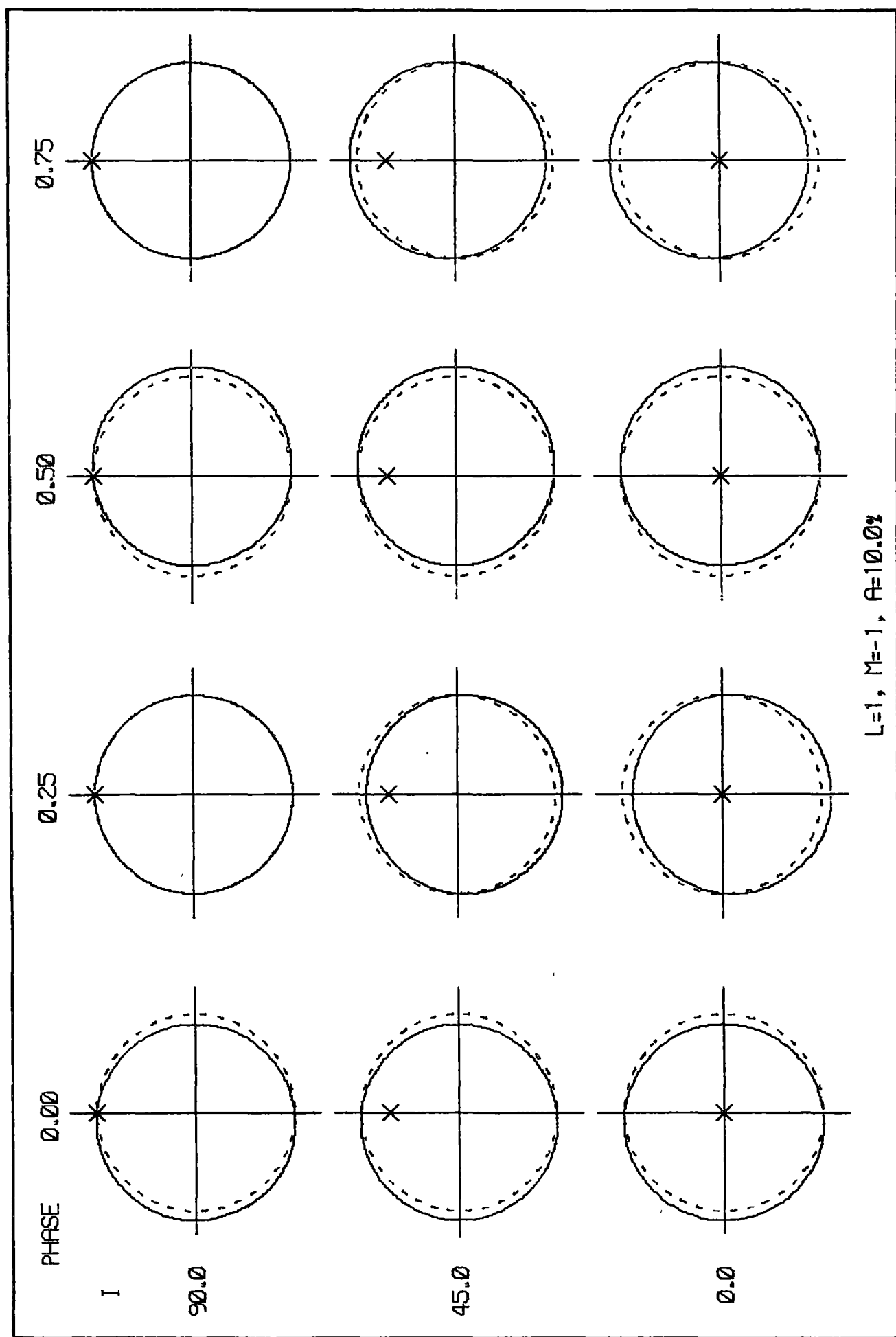


Figure A2.1(b) Surface configuration for (1,-1) mode.

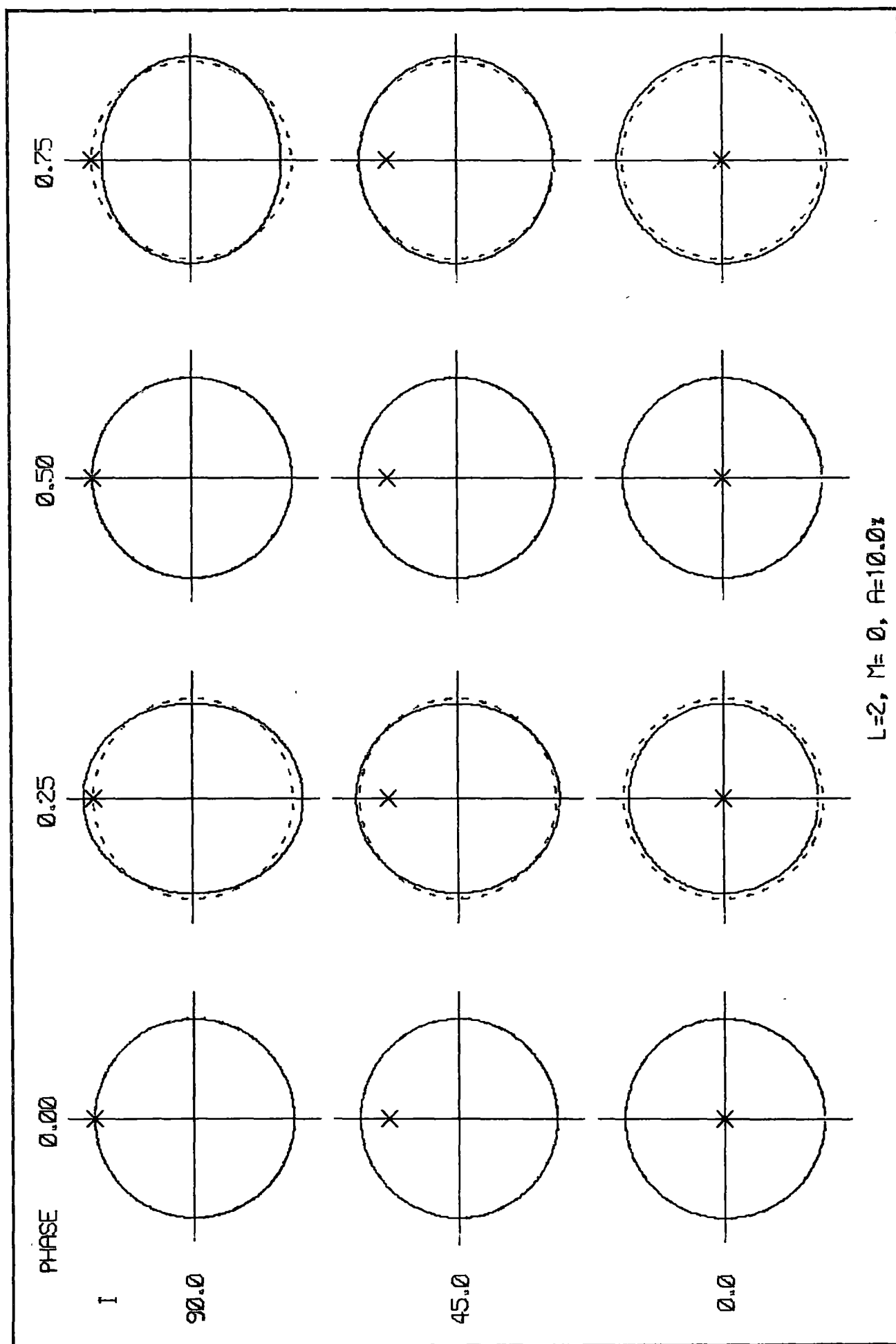


Figure A2.1(c) Surface configuration for (2,0) mode.

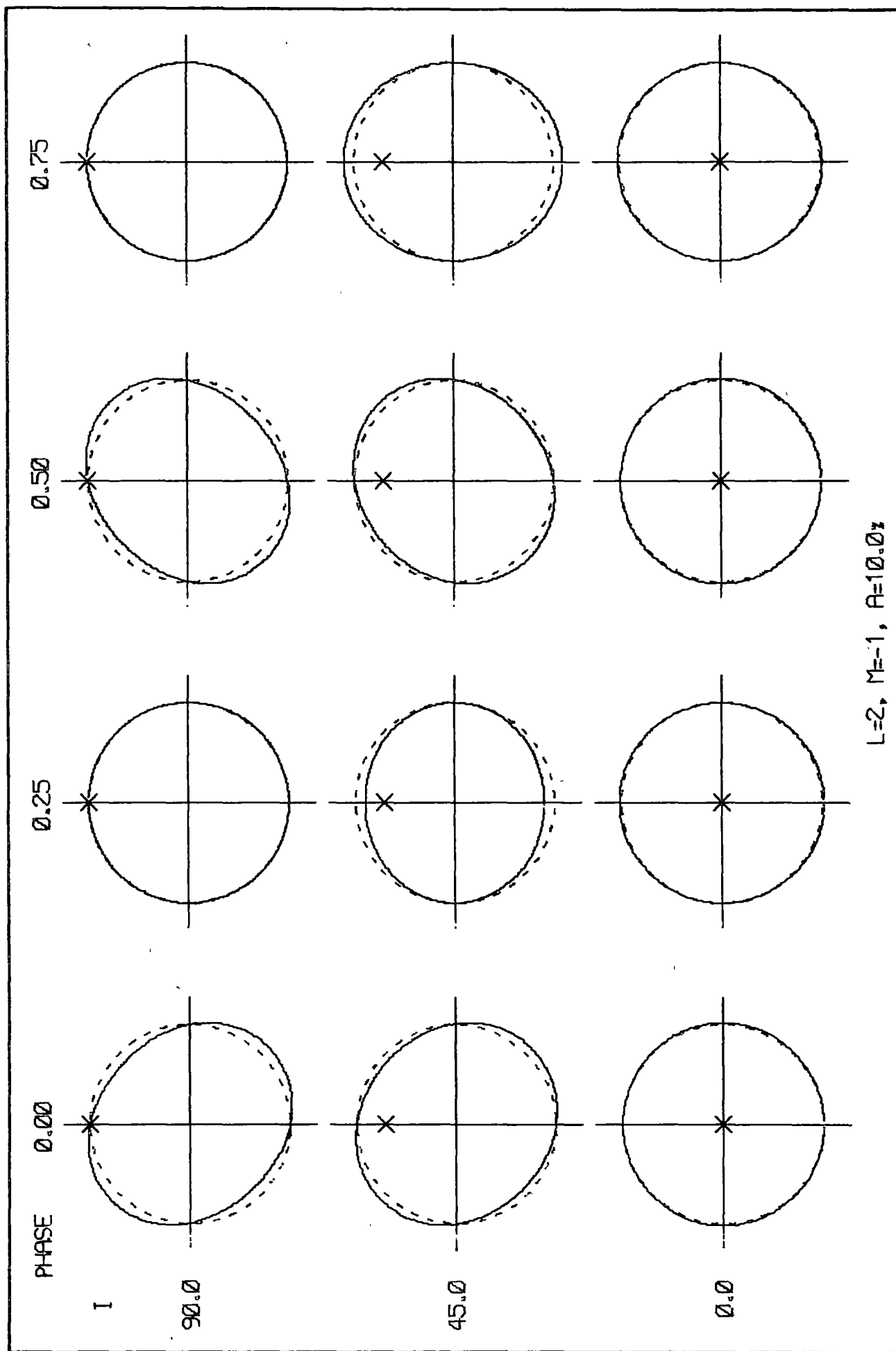


Figure A2.1(d) Surface configuration for (2,-1) mode.

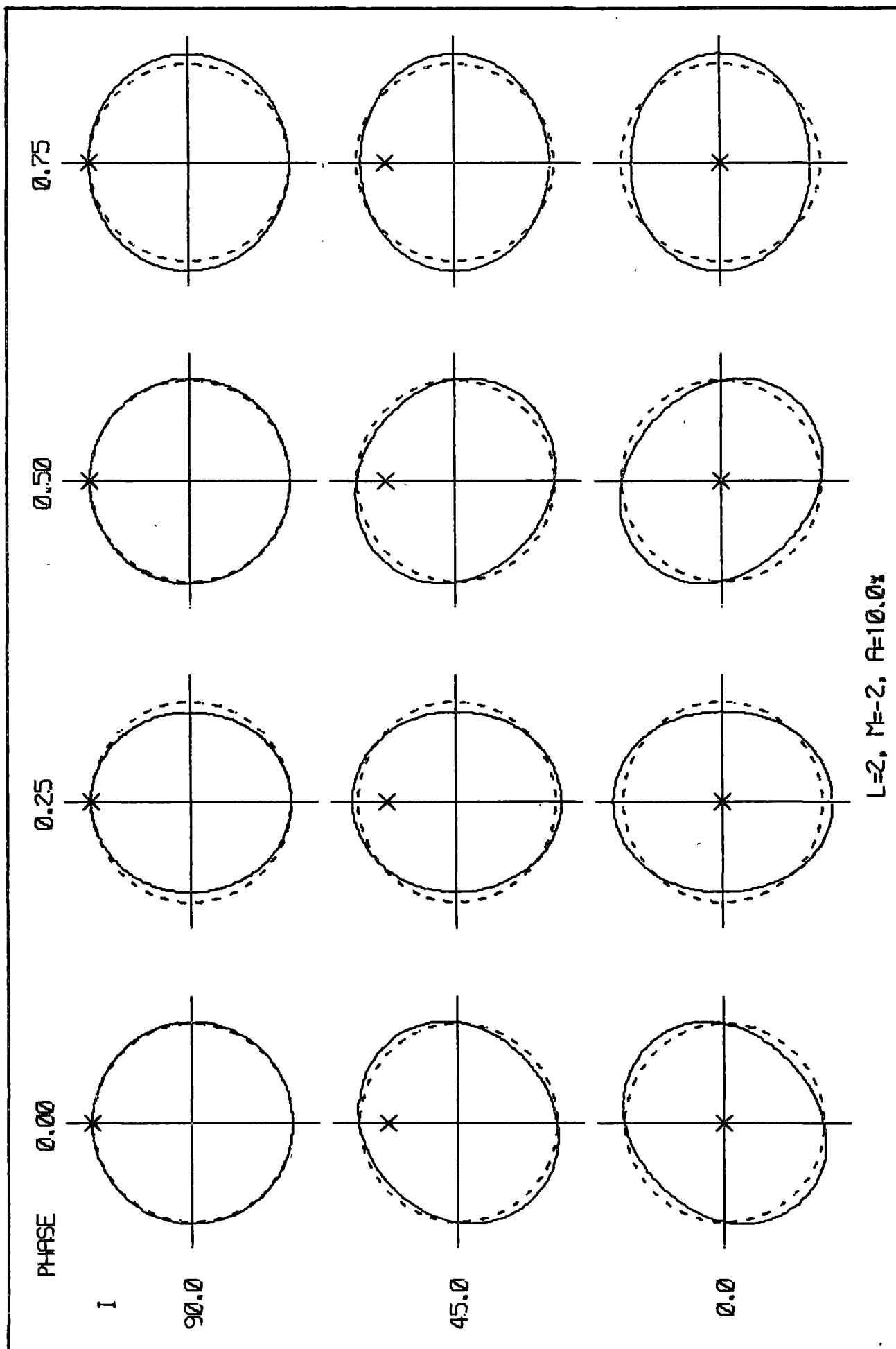


Figure A2.1(e) Surface configuration for (2,-2) mode.

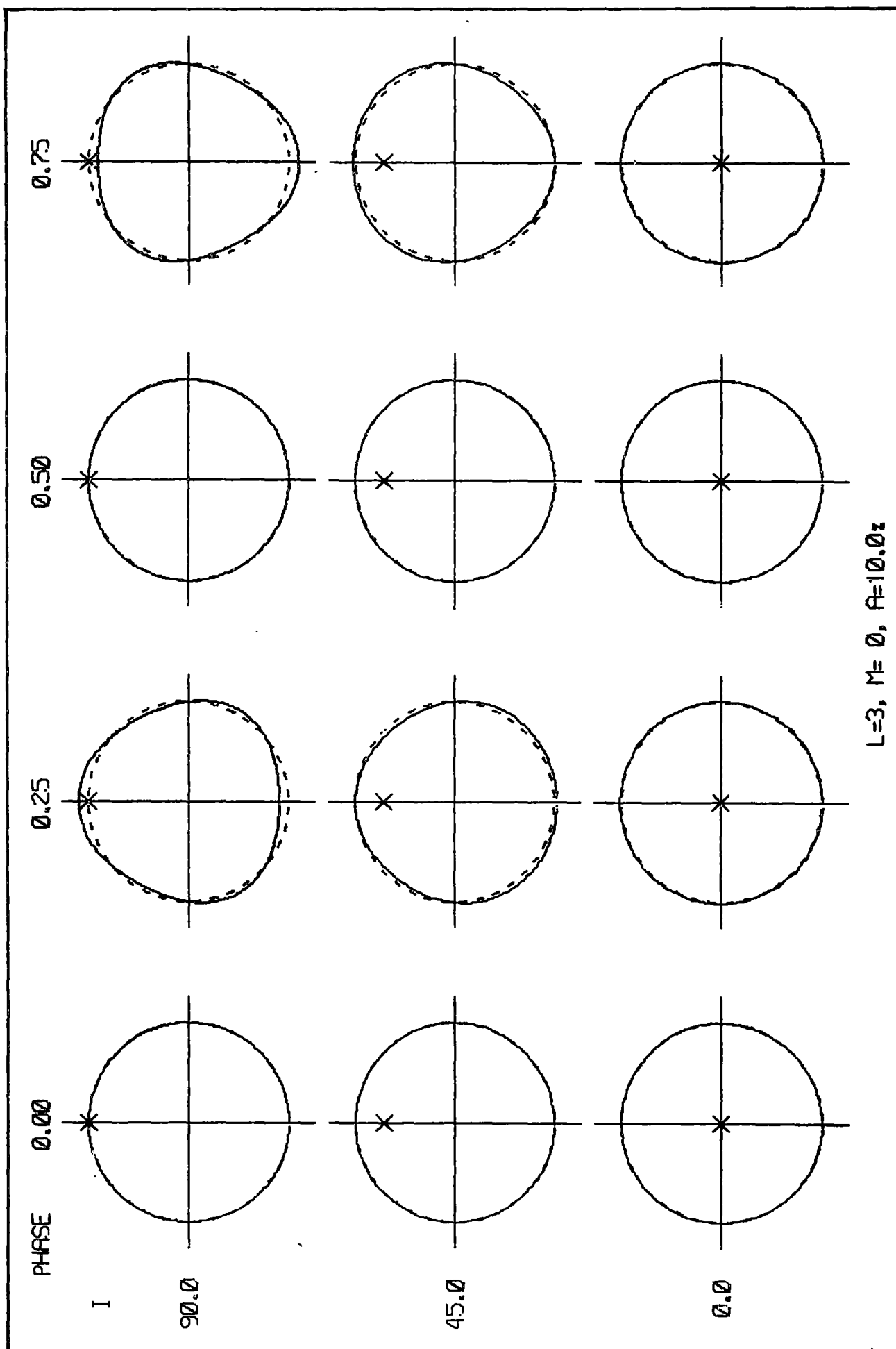


Figure A2.1(f) Surface configuration for (3,0) mode.

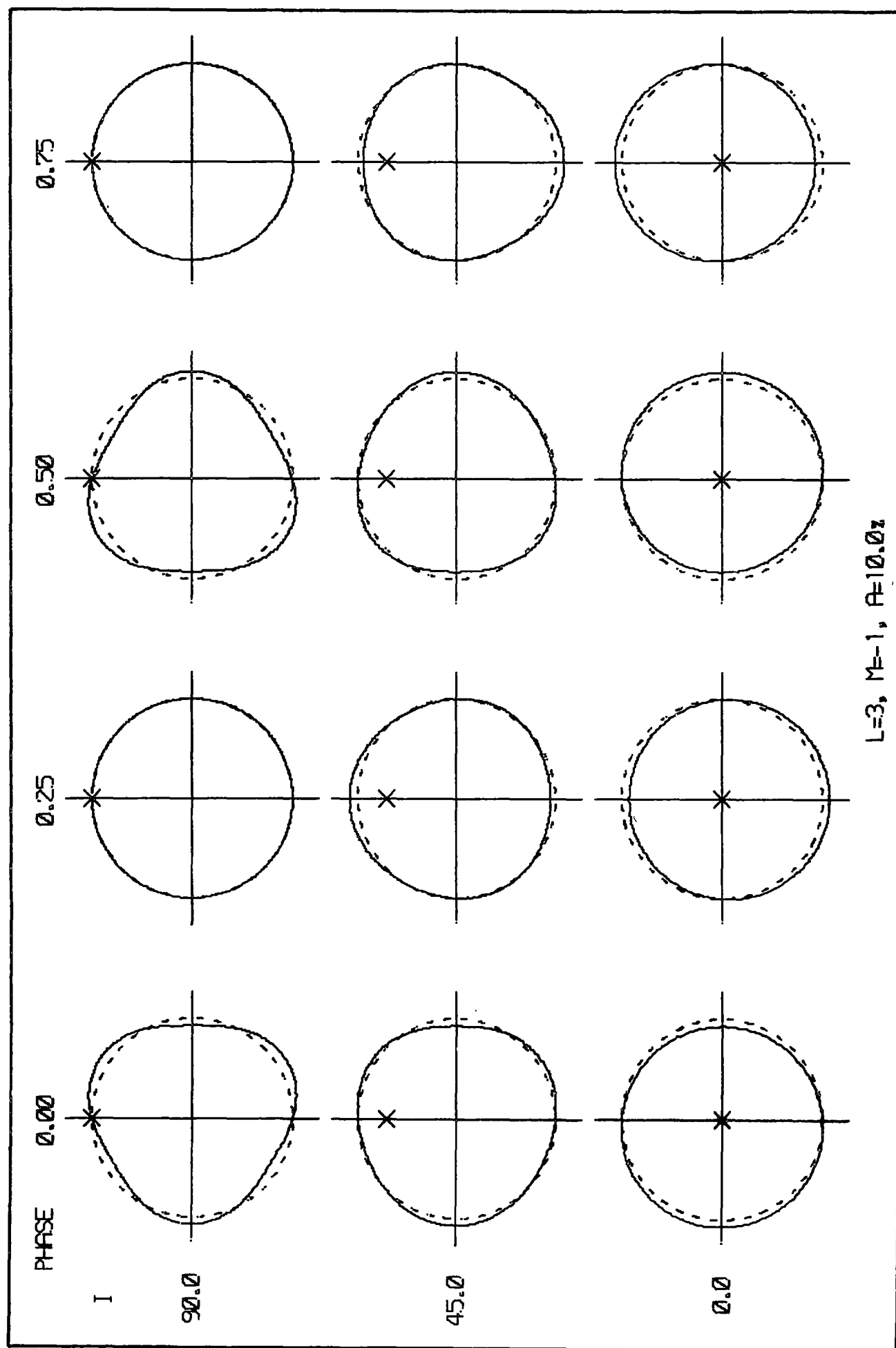


Figure A2.1(g) Surface configuration for (3,-1) mode.

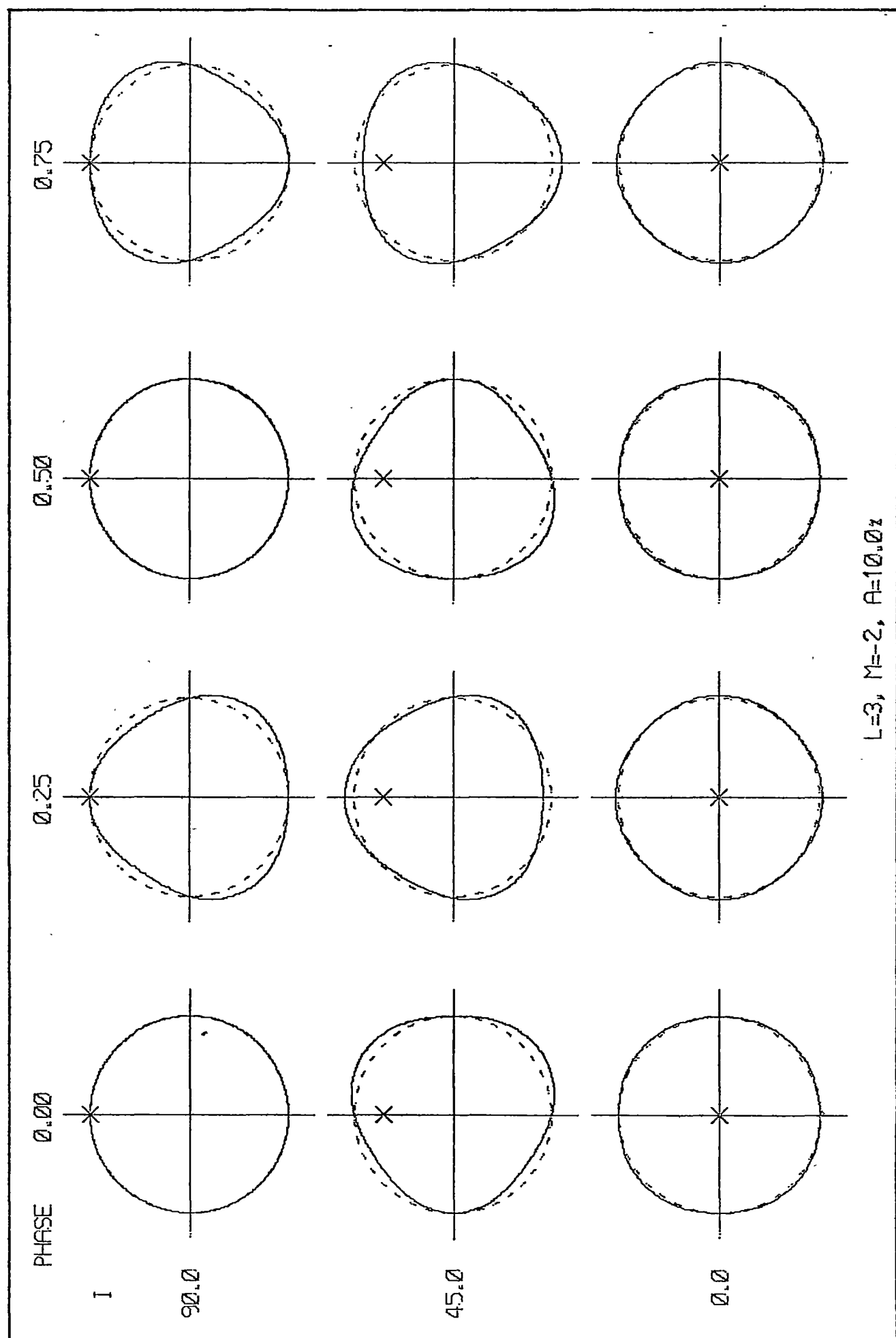


Figure A2.1(h) Surface configuration for (3,-2) mode.

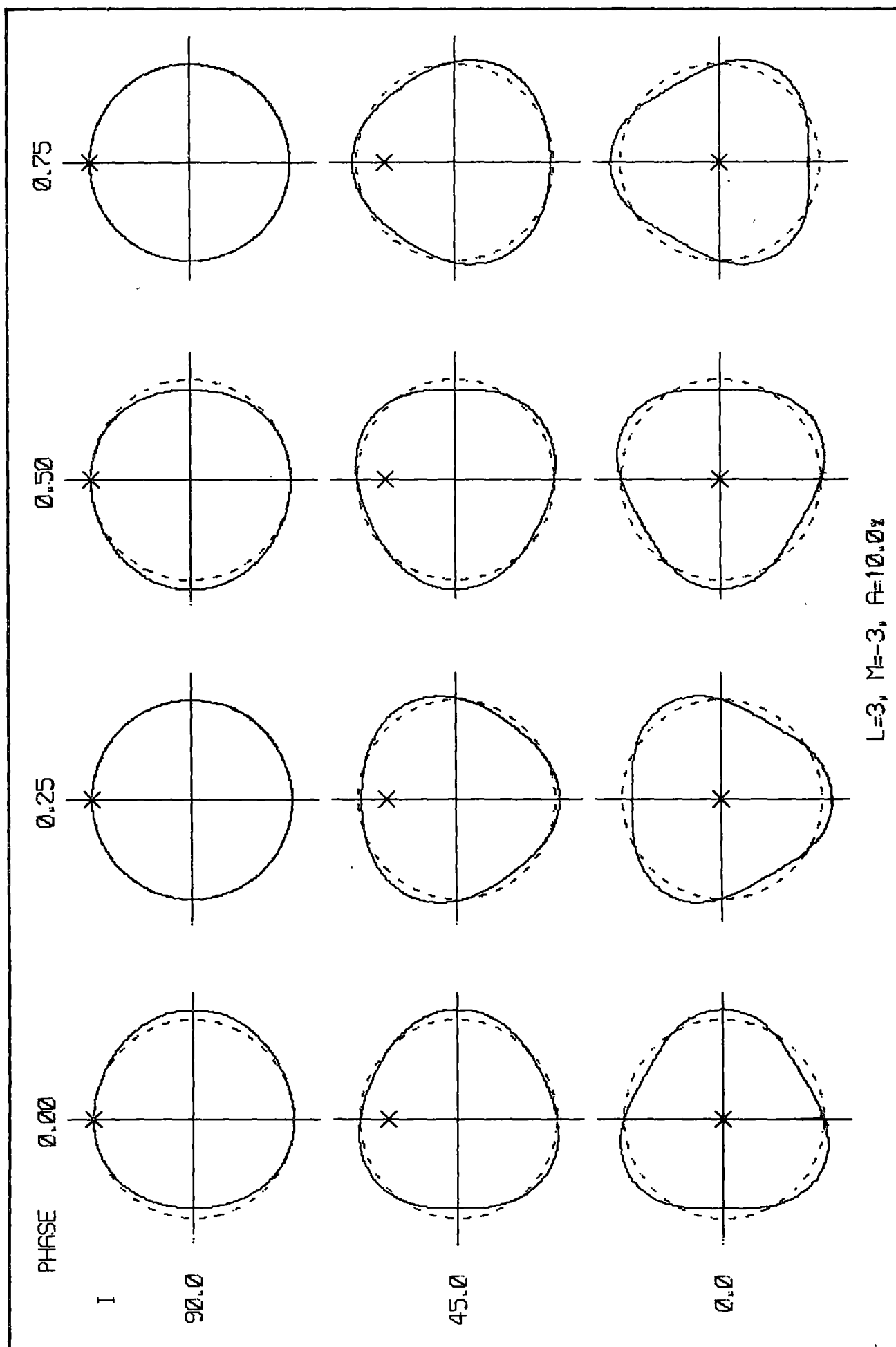


Figure A2.1(i) Surface configuration for (3,-3) mode.

A P P E N D I X 3

THE LINE-OF-SIGHT VELOCITY, v

The velocity of the stellar surface projected along the line-of-sight of the observer determines, through the Doppler effect, the wavelength displacement of the line absorption of that surface element. Differentiating the displacement vector defined by Equation A1.1 with respect to time yields

$$\dot{\underline{R}}(\theta, \phi, t) = \dot{\xi}_r \hat{r} + \dot{\xi}_\theta \hat{\theta} + (\Omega R \sin \theta + \dot{\xi}_\phi) \hat{\phi}. \quad (\text{A3.1})$$

Changing from spherical-polar to rectangular co-ordinates gives

$$\begin{aligned} \dot{\underline{R}}(\theta, \phi, t) = & \{ \xi_r \sin \theta \cos \phi + \dot{\xi}_\theta \cos \theta \cos \phi - \Omega R \sin \theta \sin \phi - \dot{\xi}_\phi \sin \phi \} \hat{i} \\ & + \{ \text{terms} \} \hat{j} + \{ \dot{\xi}_r \cos \theta - \dot{\xi}_\theta \sin \theta \} \hat{k}. \end{aligned} \quad (\text{A3.2})$$

Using the equation to the line-of-sight (A1.5), the component of $\dot{\underline{R}}$ in the observer's direction is, employing the astrophysical sign convention,

$$\underline{v}(\theta, \phi, t) = - \dot{\underline{R}} \cdot \underline{\underline{L}},$$

$$\begin{aligned} \text{i.e. } \underline{v}(\theta, \phi, t) = & \{ [\Omega R \sin \theta + \dot{\xi}_\phi] \sin \phi - \dot{\xi}_r \sin \theta + \dot{\xi}_\theta \cos \theta \} \cos \phi \sin i \\ & + \{ \dot{\xi}_\theta \sin \theta - \dot{\xi}_r \cos \theta \} \cos i. \end{aligned} \quad (\text{A3.3})$$

In the static case (no pulsation) this simplifies to give

$$\underline{v}(\theta, \phi) = v_e \sin \theta \sin \phi \sin i$$

where v_e is the equatorial rotational speed.

A P P E N D I X 4

COS ζ FOR A DISTORTED STAR

In Section 2.4.2 the observed Stokes parameters of the total polarized light from the star were defined with respect to an external co-ordinate system (l_0, r_0) fixed to the apparent disc. Let \hat{l}_0 be the unit vector in the direction of the projection of the stellar rotation axis onto the plane of the sky. Since, in Appendix 1, the line-of-sight was defined to lie in the [Z,X]-plane, it follows that $\hat{r}_0 = \hat{j}$ (refer to Figure A1.1). We wish to determine the angle ζ between the local perpendicular to the meridian plane \hat{r} and the vector \hat{r}_0 .

The former vector is defined by

$$\hat{r} = \frac{\hat{n} \times \hat{L}}{\sin \gamma} \quad (\text{A4.1})$$

where \hat{n} , \hat{L} and γ are defined in Equations A1.3, A1.5 and A1.6 respectively. Defining, for convenience, the quantity

$$s = \{R^2 \sin^2 \theta + \left(\frac{\partial R}{\partial \theta}\right)^2 \sin^2 \theta + \left(\frac{\partial R}{\partial \phi}\right)^2\}^{1/2} \quad (\text{A4.2})$$

then

$$\begin{aligned} \sin \gamma \cos \zeta &= (\hat{n} \times \hat{L}) \cdot \hat{j} \\ &= s^{-1} \left[\left(\frac{\partial R}{\partial \theta} \sin^2 \theta + R \sin \theta \cos \theta \right) \sin i - \right. \\ &\quad \left. \left(\frac{\partial R}{\partial \phi} \sin \phi + R \sin^2 \theta \cos \phi - \frac{\partial R}{\partial \theta} \cos \theta \sin \theta \cos \phi \right) \cos i \right] \end{aligned} \quad (\text{A4.3})$$

From Equation A1.6 it follows that

$$\begin{aligned} \sin \gamma &= s^{-1} \{ s^2 - [R \sin \theta (\cos \theta \cos i + \sin \theta \sin \phi \sin i) + \\ &\quad \frac{\partial R}{\partial \theta} \sin \theta (\sin \theta \cos i - \cos \theta \cos \phi \sin i) + \frac{\partial R}{\partial \phi} \sin i \sin \phi]^2 \}^{1/2}. \end{aligned} \quad (\text{A4.4})$$

Thus

$$\cos \zeta = \{s^2 - [t \sin i + u \cos i]^2\}^{-1/2} \{u \sin i - t \cos i\} \quad (\text{A4.5})$$

where

$$s = \{R^2 \sin^2 \theta + \left(\frac{\partial R}{\partial \theta}\right)^2 \sin^2 \theta + \left(\frac{\partial R}{\partial \phi}\right)^2\}^{1/2}$$

$$t = R \sin^2 \theta \cos \phi - \frac{\partial R}{\partial \theta} \sin \theta \cos \theta \cos \phi + \frac{\partial R}{\partial \phi} \sin \phi$$

and

$$u = R \sin \theta \cos \theta + \frac{\partial R}{\partial \theta} \sin^2 \theta.$$

A P P E N D I X 5

THE NONRADIAL BAADE-WESSELINK METHOD AND RELATED MODE DISCRIMINATION METHODS

This appendix is divided into three sections. Firstly, in Section A5.1, some simple relationships between the various integrals which arise in the nonradial theory are derived. Then Section A5.2 further investigates the nonradial Baade-Wesselink method, particularly the mode discrimination abilities of the Baade-Wesselink coefficients a_l and b_l . The feasibility of mode discrimination using subsets of the observational data required for a full Baade-Wesselink analysis is examined in Section A5.3. Methods utilising the amplitude ratios of the observed light, colour and velocity variations, and the phase differences between these quantities, are considered in this section.

The work described in Sections A5.2 and A5.3 was done in joint collaboration with my supervisor, Dr. Robert Watson. This investigation, which essentially follows on from Section 2.7 but is also interrelated with the technique implemented in Chapter 3, contains work only very recently completed. This accounts for its inclusion as an appendix rather than in the thesis main body.

A5.1 INTEGRAL RELATIONS

A5.1.1 *Equivalence with Dziembowski's Notation*

Dziembowski (1977) defined the following integrals:

$$b_l = \int_0^1 h(\mu) P_l(\mu) \mu d\mu \quad (\text{A5.1})$$

$$\text{and} \quad c_l = l \int_0^1 \left(h + \mu \frac{dh}{d\mu} \right) (P_{l-1} - \mu P_l) d\mu \quad (\text{A5.2})$$

Equation A5.1 corresponds to the integral I_l defined by Equation 2.22. The integral c_l can be recast using a relation satisfied by the Legendre polynomials

viz.
$$(1 - \mu^2) \frac{dP_L}{d\mu} = L(P_{L-1} - \mu P_L) \quad (A5.3)$$

to become

$$e_L = \int_0^1 (1 - \mu^2) \left(h + \mu \frac{dh}{d\mu} \right) \frac{dP_L}{d\mu} d\mu \quad (A5.4)$$

Hence

$$\begin{aligned} 2b_L - e_L &= \int_0^1 [2\mu P_L + (\mu^2 - 1) \frac{dP_L}{d\mu}] h d\mu + \int_0^1 (\mu^2 - 1) \frac{dP_L}{d\mu} \frac{dh}{d\mu} \mu d\mu \\ &= I_2 + I_1 \end{aligned}$$

where I_1 and I_2 were defined by Equations 2.19. Thus the light curve expression given by Equation 2.17 is consistent with Dziembowski's (1977) formula.

A5.1.2 The Surface Area Integrals

In deriving the expression for the photospheric surface area variations, Balona and Stobie (1979a) introduced the integrals p_L and q_L defined by

$$p_L = \int_0^1 \mu P_L d\mu \quad (A5.5)$$

and
$$q_L = L \int_0^1 (P_{L-1} - \mu P_L) d\mu \quad (A5.6)$$

Use of Equation A5.3 transforms A5.6 to

$$\begin{aligned} q_L &= \int_0^1 (1 - \mu^2) \frac{dP_L}{d\mu} d\mu \\ &= [(1 - \mu^2) P_L]_0^1 + \int_0^1 2\mu P_L d\mu \quad (\text{integrating by parts}) \\ &= -P_L(0) + 2p_L \end{aligned}$$

Thus
$$2p_L - q_L = P_L(0) \quad (A5.7)$$

as claimed in Chapter 2.

A5.2 THE NONRADIAL BAADE-WESSELINK EXPRESSION

In Section 2.7.2 a Baade-Wesselink expression was derived which related the light $\Delta m_{\lambda_2}(t)$, colour $\Delta m_{\lambda_1}(t) - \Delta m_{\lambda_2}(t)$ and mean radial velocity $V_{\text{mean}}(t)$ variations of a nonradial pulsator. This expression is

$$\Delta m_{\lambda_2}(t) = a_z(\lambda_1, \lambda_2) [\Delta m_{\lambda_1}(t) - \Delta m_{\lambda_2}(t)] + b_z(\lambda_1, \lambda_2) \int V_{\text{mean}} dt / R. \quad (\text{A5.8})$$

The coefficients a_z and b_z are given by

$$a_z(\lambda_1, \lambda_2) = \alpha(\lambda_2) I_z(\lambda_2) / [\alpha(\lambda_1) I_z(\lambda_1) - \alpha(\lambda_2) I_z(\lambda_2)] \quad (\text{A5.9})$$

$$\text{and } b_z(\lambda_1, \lambda_2) = 1.086 p_{\text{mean}} a_z(\lambda_1, \lambda_2) I_z(\lambda_1) [(2+z)(1-z)(\alpha(\lambda_1)/\alpha(\lambda_2) - 1) - p_* C(\beta(\lambda_2)\alpha(\lambda_1)/\alpha(\lambda_2) - \beta(\lambda_1))], \quad (\text{A5.10})$$

where
$$I_z(\lambda) = \int_0^1 h(\mu) P_z(\mu) \mu d\mu$$

$$\alpha(\lambda) = \frac{\partial \log F_\lambda}{\partial \log T_e}$$

$$\beta(\lambda) = \frac{\partial \log F_\lambda}{\partial \log g}$$

and
$$p_{\text{mean}}(\lambda) = [I_4(\lambda) + k I_5(\lambda)]^{-1}.$$

As noted in Section 5.4.2, the wavelength dependence of p_{mean} becomes significant for $z > 2$. When this dependence is important, it will be assumed for the present discussion that V_{mean} , and hence p_{mean} , are evaluated at λ_2 .

A5.2.1 Example Baade-Wesselink Coefficients

To evaluate $a_z(\lambda_1, \lambda_2)$ and $b_z(\lambda_1, \lambda_2)$ and pursue mode discrimination possibilities, information on $\alpha(\lambda)$, $\beta(\lambda)$, $I_z(\lambda)$ and $p_* C$ is required. Three test models were chosen to do this. A model with $(T_e, \log g) = (25000, 4)$ serves to illustrate the case of β Cephei and other nearby B star variables. A $(8000, 4)$ model applies to the δ Scuti regime and a $(6000, 2)$ model represents the short-period cepheid situation.

The latter case was included, not because there is any current evidence for nonradial pulsations in this regime, but to provide, together with the δ Scuti model, a pair of examples bracketing variables in the lower reaches of this instability region. B and V passbands were selected to illustrate the δ Scuti and short-period cepheid cases. For the β Cephei example a 1500 Å passband was also selected. This wavelength region is covered by satellite ultraviolet data. Both (1500,V) and (B,V) cases were carried through in the β Cephei example to demonstrate their extreme differences.

Data used in the test models are given in Table A5.1. The $\alpha(\lambda)$ and $\beta(\lambda)$ values for the various passbands come from Kurucz (1979). The p_*C numbers are meant as approximate values only. They were derived using p_* values taken from the photospheric regions of the appropriate Kurucz models. These are $p_* \sim 1.3 - 1.5$. The C values come from typical Q. These were taken to be 0.027 in the β Cephei model (Balona and Feast, 1975; Shobbrook, 1978), 0.022 in the δ Scuti model (Breger and Bregman, 1975) and 0.040 in the short-period cepheid model (Cox, 1979). This δ Scuti value corresponds to overtone pulsation, as suggested for $T_e > 7800$ K by Breger and Bregman. For cooler δ Scuti variables a $Q \sim 0.030$ is more appropriate and this reduces p_*C to ~ 25 . The presence of different modes in the regimes of the other test models would affect their p_*C similarly. Equation 2.19 implies that the C values are l dependent. The effect is only appreciable in the short-period cepheid example. The Table A5.1 value is an intermediate one between the $l = 0$ and 5 results in this case.

A limited check on the adopted effective gravity model is possible for the δ Scuti test example, because gravity and radius changes around the pulsation cycle are given directly for AD CMi by Breger (1975) and for RS Gru by McNamara and Feltz (1976). This check shows that

TABLE A5.1 : Data for test models in different variable star regimes

| Regime ($T_e, \log g$) | β Cephei (25000,4) | | | δ Scuti (8000,4) | | Short-Period Cepheid (6000,2) | |
|--|-----------------------------|--------|--------|----------------------------|--------|-------------------------------------|--------|
| Passband | 1500 Å | B | V | B | V | B | V |
| $\alpha(\lambda)$ | 3.85 | 2.00 | 1.85 | 5.05 | 3.75 | 6.40 | 4.90 |
| $\beta(\lambda)$ | +0.002 | -0.027 | -0.024 | -0.043 | -0.018 | -0.013 | -0.014 |
| p_*C | 30 | | | 40 [#] | | 15 | |
| ($B_{\text{observed}}, \psi'$) | (2.5, 180°) | | | (2.5, 90°) | | (1.5, 90°) | |
| $B_{\text{adiabatic}}$ | 5.5 | | | 12.5 [#] | | 4.5 | |
| $\frac{\sigma R}{1.086} \text{ km s}^{-1}$ | 2500 | | | 2000 [#] | | 500 | |

[#]These values are for $Q \sim 0.022$ and reduce to $p_*C \sim 25$,
 $B_{\text{adiabatic}} \sim 7.5$, $\sigma R/1.086 \sim 1500 \text{ km s}^{-1}$ for a $Q \sim .030$ which
approximates a radial fundamental pulsation.

the phase of the effective gravity changes in the model is roughly correct, as is the amplitude, expressed by Equation 2.7, provided the assumption is made that AD CMi and RS Gru have Q appropriate to fundamental pulsations. The Table A5.1 p_*C value may be a little high, but not by more than a factor of two. Observed effective gravity changes in cepheids cannot be validly compared with Equation 2.7 because of their highly nonlinear situation. Clearly only very small radius excursions are permitted by the Table A5.1 p_*C coefficients before nonlinear effects occur. The best that can be said for the short-period cepheid example is that perhaps Equation 2.7 will give a guide to the importance of pressure effects in the low amplitude limit.

Values of the limb-darkening integral $I_z(\lambda)$ for the three test models are given in Table A5.2. These values are derived from the monochromatic limb-darkening laws tabulated by Kurucz (1969) at the equilibrium stellar temperatures and gravities of the test models. Although the tabulated values come from the accurate Kurucz limb-darkening solutions, the basic features of Table 5.2 can be understood in terms of a linearized limb-darkening law $h(\mu) = \chi_0 + \chi_1\mu$. In this case the analytic expressions for $I_z(\lambda)$ are those given in Table A5.3, where it has been assumed that $h(\mu)$ is normalized so $\int_0^1 \mu h(\mu) d\mu = 1$. From these expressions it is clear that the $I_z(\lambda)$ values are much less sensitive to the adopted limb-darkening law for $z \leq 2$ than for $z \geq 3$. For the cases shown in Table A5.2, χ_1 is in the range 0.6 to 2.4. As a consequence of this there must be some doubt for $z \geq 3$ in applying monochromatic $I_z(\lambda)$ to normal filter-based observational data when line-blocking is appreciable in the filter passband. The lines will affect the limb-darkening law. Monochromatic values chosen at appropriate effective wavelengths are adequate in relatively line-free passbands. Values of the limb-darkening integral, $I_z(\text{EDD})$, which result from the Eddington

TABLE A5.2 : Monochromatic $I_z(\lambda) = \int_0^1 \eta_\mu P_z d\mu$

| Regime ($T_e, \log g$) λ | β Cephei (2500,4) 1500 Å 4000 Å 5500 Å | | | δ Scuti (8000,4) 4000 Å 5500 Å | | Short-Period Cepheid (6000,2) 4000 Å 5500 Å | | Eddington value $I_z(\text{EDD})$ |
|--|--|---------|---------|--|---------|--|---------|--------------------------------------|
| $z = 1$ | 0.719 | 0.691 | 0.685 | 0.723 | 0.706 | 0.736 | 0.713 | 0.708 |
| 2 | 0.343 | 0.293 | 0.281 | 0.350 | 0.320 | 0.374 | 0.333 | 0.325 |
| 3 | 0.075 | 0.033 | 0.024 | 0.079 | 0.055 | 0.104 | 0.068 | 0.062 |
| 4 | -0.0200 | -0.0345 | -0.0365 | -0.0205 | -0.0270 | -0.0070 | -0.0205 | -0.0205 |
| 5 | -0.0120 | -0.0070 | -0.0055 | -0.0150 | -0.0105 | -0.0135 | -0.0100 | -0.0080 |

TABLE A5.3: Form of $I_z(\lambda)$ for linearized limb-darkening

$$h(\mu) = \chi_0 + \chi_1 \mu \text{ where } \int_0^1 \mu h(\mu) d\mu = 1 .$$

| z | $I_z(\lambda)$ |
|-----|---------------------|
| 0 | 1 |
| 1 | $2/3 + \chi_1/36$ |
| 2 | $1/4 + \chi_1/20$ |
| 3 | $\chi_1/24$ |
| 4 | $-1/24 + \chi_1/72$ |
| 5 | $-\chi_1/192$ |

limb-darkening law ($\chi_1 = 1.5$), are shown in Table A5.2 for comparison with the monochromatic values.

The Baade-Wesselink coefficients a_z and b_z derived for the test models are given in Table A5.4. The corresponding p_{mean} are also given. The $I_z(\lambda)$ used in deriving Table A5.4 data come from Table A5.2 by interpolating at appropriate effective wavelengths. Values of $b_z(\lambda_1, \lambda_2)$ both with and without effective gravity changes are included in Table A5.4. These show that pressure effects may be substantial in the β Cephei and δ Scuti regimes for low z . The importance of effective gravity changes on Wesselink analyses of δ Scuti stars has been recognised by Breger (1975) who uses gravity-corrected colours in studying radial pulsations.

A5.2.2 Mode Discrimination Ability

The principal mode discrimination ability of the nonradial Baade-Wesselink coefficients comes from the $(2+z)(1-z)$ term in Equation A5.10, though by $z = 3$ the z dependence of $I_z(\lambda)$ is affecting both coefficients strongly. To assess the practical z discrimination possibilities we require, in addition to knowing that

TABLE A5.4 : Example Baade-Wesselink coefficients

| Regime | (1500,V) β Cephei | | | | (B,V) | | | | δ Scuti | | | | (B,V) | | | | Short-Period Cepheid (B,V) | | | |
|----------|-------------------------|-------|------|--|-------|-------|-------------------|------|----------------|-------|-------------------|------|-------|-------|-------------------|------|----------------------------|-------|-------------------|--|
| p_{*C} | a_z | b_z | | | a_z | b_z | p_{mean} | | a_z | b_z | p_{mean} | | a_z | b_z | p_{mean} | | a_z | b_z | p_{mean} | |
| | 0 | 30 | | | 0 | 30 | | | 0 | 40 | | | 0 | 15 | | | 0 | 15 | | |
| $z = 0$ | 0.9 | 3.1 | 5.5 | | 12 | 3.1 | 2.8 | 1.46 | 2.9 | 3.0 | -0.2 | 1.42 | 3.2 | 3.0 | 3.4 | 1.40 | | | | |
| 1 | 0.8 | 0 | 2.0 | | 11 | 0 | -0.3 | 1.84 | 2.8 | 0 | -2.7 | 1.76 | 3.0 | 0 | 0.3 | 1.73 | | | | |
| 2 | 0.6 | -3.1 | -2.1 | | 8 | -2.7 | -2.9 | 3.05 | 2.4 | -3.4 | -5.2 | 2.82 | 2.5 | -3.3 | -3.0 | 2.74 | | | | |
| 3 | 0.2 | -1.3 | -1.1 | | 2.5 | -0.5 | -0.5 | 7.9 | 1.4 | -2.5 | -2.9 | 6.6 | 1.4 | -2.6 | -2.5 | 6.2 | | | | |
| 4 | 7 | 280 | 260 | | 26 | 140 | 140 | 90 | 6.4 | 38 | 42 | 39 | -6.2 | -15 | -15 | 30 | | | | |
| 5 | 0.3 | -5.8 | -5.5 | | 2.5 | -2.5 | -2.5 | -55 | 1.4 | -15 | -16 | -78 | 1.5 | -20 | -20 | -110 | | | | |

Note: The p_{mean} are here evaluated at V.

pressure effects must be included, some idea of the uncertainties related to the $\alpha(\lambda)$ and $I_z(\lambda)$ values used in Equations A5.9 and A5.10. These are difficult to obtain. However, the $a_0(B,V)$ for the short-period cepheid and δ Scuti cases does offer an important point of contact with observation which gives some information on $\alpha(\lambda)$. The $a_0(B,V)$ may be identified with the surface brightness to colour gradient term appearing in maximum likelihood Wesselink analyses. It is well known that observed values of this quantity vary little along the cepheid instability strip and Balona (1977) determines a mean value of 2.15 ± 0.02 . Strictly speaking, we should here make a comparison with values determined from the fundamental sinusoidal components of the cepheid variations as given by Balona and Stobie (1979c). For short-period cepheids Balona and Stobie (1979d) note that $a_0(B,V) = 2.35 \pm 0.04$. The difference between this and the $a_0(B,V) = 3.2$ listed in the Table A5.4 short-period cepheid test model implies an observed $\alpha(B)/\alpha(V)$ some 10 percent larger than given by the Kurucz (1979) models. The Bell and Gustafsson (1978) models, on the other hand, give $a_0(B,V) < 2.5$, which is in closer agreement with the observations. Both sets of models, however, agree in predicting only small changes of $a_0(B,V)$ along the cepheid instability strip. This can be seen in Figure A5.1 where model contours of $a_0(B,V)$ are plotted on the $(T_e, \log g)$ plane. From this figure it is also seen that a range of $a_0(B,V)$ is possible in the δ Scuti regime. Observed values of $a_0(B,V)$ for RS Gru (Balona and Martin, 1978) and the radial mode in 1 Mon (Balona and Stobie, 1980) fall within the hatched δ Scuti region in Figure A5.1, though at somewhat higher T_e than the average T_e observed for these particular stars.

As a result of the preceding considerations it seems prudent to assume that errors of at least ± 0.1 may be present in model $\alpha(\lambda)$, quite apart from any uncertainty introduced when assigning equilibrium

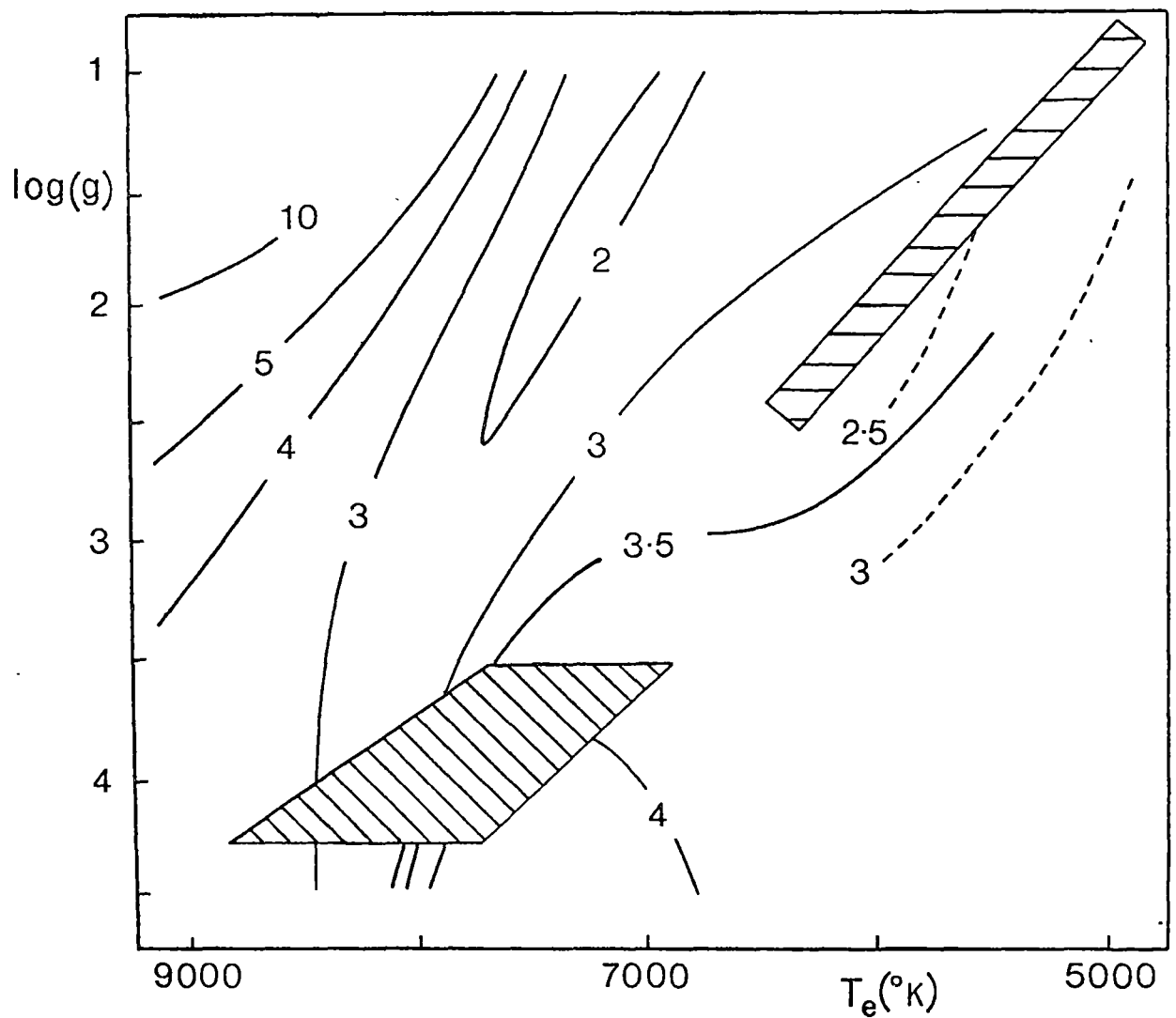


Figure A5.1 Contours of the Baade-Wesselink coefficient $a_0(B,V)$ in the $(T_e, \log g)$ plane. Values derived from Kurucz (1979) model atmosphere data are shown as full lines and those derived from Bell and Gustafsson (1978) are shown as dashed lines. The lower hatched area is the δ Scuti region according to Breger and Bregman's (1975) work. The upper hatched area gives the location of the cepheid instability strip as summarized by Cox (1979).

($T_e, \log g$) values to a particular star. Errors of twice this are necessary to account for the discrepancy in the cepheid region. For $I_z(\lambda)$ we assumed that errors equivalent to a change of χ_1 in Table A5.3 by ± 0.1 represented minimum uncertainties. Such an error in $I_z(\lambda)$ may be introduced by the application of monochromatic $I_z(\lambda)$ to any filter-based data which suffers a relatively small amount of line-blocking. Errors several times this size may result from applying monochromatic $I_z(\lambda)$ to β Cephei 1500 Å and short-period cepheid B passbands, where line-blocking is in the vicinity of 20 percent.

To assess the limitations in mode discrimination ability caused by minimum uncertainties in the Table A5.4 Baade-Wesselink coefficients, we therefore determined the range in both of these coefficients which resulted from independently varying $\alpha(\lambda_1), \alpha(\lambda_2)$, and $\Delta\chi_1$ in each of $I_z(\lambda_1)$ and $I_z(\lambda_2)$, by ± 0.1 . It was clear from this that $a_z(\lambda_1, \lambda_2)$ is not a practical mode discriminant in any test regime. The errors in $\alpha(\lambda)$ present the problem for $z \leq 2$ while for $z \geq 4$ the $I_z(\lambda)$ errors dominate. It was equally clear that $b_z(\lambda_1, \lambda_2)$ is expected to be a successful mode discriminant for $z \leq 2$ provided due attention is paid to pressure effects. This is true in all test regimes except the β Cephei (B,V) case, which is completely unreliable because of its small $[\alpha(\lambda_1) - \alpha(\lambda_2)]$. For higher z the mode discriminating ability of $b_z(\lambda_1, \lambda_2)$ is far less certain. Large positive or negative $b_z(\lambda_1, \lambda_2)$ values would distinguish $z = 4$ or 5 from smaller z . However $z = 3$ is not readily distinguishable from $z = 2$ in any case, and may also be confused with $z = 1$ in the δ Scuti example.

A5.2.3 *Applying the Baade-Wesselink Expression*

Here we consider appropriate means of applying Equation A5.8 to observational data. This is done in general terms and then applied to practical $z \leq 2$ examples in Section A5.2.4.

In the linear regime there are only six observational quantities required to apply a Baade-Wesselink technique for a particular mode. These are the amplitude and phase of the light, colour and radial velocity variations. Writing Equation A5.8 in terms of these gives

$$A_{\lambda_2} \cos(\sigma t + \phi_{\lambda_2}) = a_z(\lambda_1, \lambda_2) A_{\text{col}} \cos(\sigma t + \phi_{\text{col}}) + [b_z(\lambda_1, \lambda_2) / \sigma R] K \sin(\sigma t + \phi_{\text{RV}}) . \quad (\text{A5.11})$$

Here A_{λ_2} , A_{col} and K correspond to the amplitudes of the light, colour and velocity variations, while ϕ_{λ_2} , ϕ_{col} and ϕ_{RV} represent the phases of these quantities relative to the radius perturbations. Hence, in terms of observational quantities, the Baade-Wesselink coefficients (A5.9) and (A5.10) may be expressed as

$$a_z(\lambda_1, \lambda_2) = \frac{A_{\lambda_2}}{A_{\text{col}}} \cdot \frac{\cos(\phi_{\lambda_2} - \phi_{\text{RV}})}{\cos(\phi_{\text{col}} - \phi_{\text{RV}})} \quad (\text{A5.12})$$

and

$$b_z(\lambda_1, \lambda_2) = - \sigma R \cdot \frac{A_{\lambda_2}}{K} \cdot \frac{\sin(\phi_{\lambda_2} - \phi_{\text{col}})}{\cos(\phi_{\text{col}} - \phi_{\text{RV}})} , \quad (\text{A5.13})$$

unless $(\phi_{\text{col}} - \phi_{\text{RV}})$ has values of $\pm \pi/2$.

In the δ Scuti and short-period cepheid cases, observations typically give light and colour changes π out of phase with radial velocity variations. In this circumstance one may certainly obtain independent values of $a_z(\lambda_1, \lambda_2)$ and $b_z(\lambda_1, \lambda_2)$ from the observations in order to compare with model values given by (A5.9) and (A5.10). In principle one could have hoped to solve for both z and R independently from (A5.12) and (A5.13). However, the practical limitations on the mode discrimination ability of $a_z(\lambda_1, \lambda_2)$, noted in Section A5.2.2, preclude the current use of (A5.12). Hence we are limited to using (A5.13) in those circumstances where the mode discrimination ability of $b_z(\lambda_1, \lambda_2)$ is not destroyed by

having only a rough estimate of R . Certainly for $l \leq 2$ one will still be able to mode discriminate.

In the β Cephei case, observations typically give light and colour changes lagging by $\pi/2$ with respect to radial velocity variations. In this situation $a_l(\lambda_1, \lambda_2)$ and $b_l(\lambda_1, \lambda_2)$ are not independently obtainable from the observations via (A5.12) and (A5.13) but a linear relation exists between them. Equation (A5.11) gives this relation as

$$b_l(\lambda_1, \lambda_2) = \sigma R \cdot \frac{A_{\lambda_2}}{K} \cdot [a_l(\lambda_1, \lambda_2) \frac{A_{\text{col}}}{A_{\lambda_2}} - 1] . \quad (\text{A5.14})$$

Thus model values of $a_l(\lambda_1, \lambda_2)$ must be used together with the observations to solve for $b_l(\lambda_1, \lambda_2)$ and hence mode discriminate. Equation A5.14, under another guise, was used for mode discrimination purposes in β Cephei stars in Chapter 3, when plotting K/A_V versus A_{1500}/A_V data for comparison with model predictions. As will be seen in Section A5.3, it is the value of $[a_l(\lambda_1, \lambda_2) A_{\text{col}}/A_{\lambda_2} - 1]$ which is of *prime* observational importance in determining the l dependence of (A5.14) for $l \leq 2$. Here $a_l(\lambda_1, \lambda_2)$ does not change grossly, and the main change is through dependence of $A_{\text{col}}/A_{\lambda_2}$. Contrast this with the δ Scuti and short-period cepheid test cases where it is the value of $(\phi_{\lambda_2} - \phi_{\text{col}})$ which is of *prime* observational importance in determining the $l \leq 2$ dependence of (A5.13). This is also seen in Section A5.3. Finally, it is worth noting that, when using (A5.13) or (A5.14) for mode discrimination purposes, the large scatter of $b_l(\lambda_1, \lambda_2)$ with l means that the method is not as highly demanding of phase matching between light or colour data and radial velocity observations which are not simultaneous, as is a normal radial Wesselink analysis aiming for a precise R determination.

A5.2.4 *Example Applications*

In Figure A5.2 application of the nonradial Baade-Wesselink technique for mode discrimination is illustrated in each of the variable star test regimes. Observations are compared with $b_l(\lambda_1, \lambda_2)$ from either (A5.13) or (A5.14) for $l \leq 2$ and pressure effects are shown.

For examples of the β Cephei regime we firstly examine the four cases, γ Peg, δ Cet, β Cep and the large amplitude mode of σ Sco. All of these cases have been independently identified, from a study of line profile variations by Campos and Smith (1980), as being radial pulsators. Observed $b_l(1500, V)$ were derived from (A5.14) using the data sources quoted in Chapter 3. An $a_l(1500, V) = 0.8 \pm 0.2$, to adequately cover all $l \leq 2$ cases, and an $R = 8 R_\odot$ were initially assumed. The effect of observational errors in light, colour and velocity amplitudes, together with these $a_l(1500, V)$ errors, is shown in Figure A5.2 where the mean value for these four stars is plotted. This clearly agrees with the model $b_0(1500, V)$ value. Each of the four stars individually favours an $l = 0$ identification, though with appropriately larger error ranges. The effect of unknown R values was then assessed by permitting R to vary from $5 R_\odot$ to $11 R_\odot$. The increased range in the observed $b_l(1500, V)$ due to this is also shown in Figure A5.2. Clearly identification with $l = 0$ remains secure and a pressure effect of roughly the same order as given by $p_* C = 30$ is indicated. As a second illustration of the β Cephei regime we examined β CMa, for which Beeckmans and Burger (1977) give satellite ultraviolet data for the two principal pulsation modes. The observed $b_l(1500, V)$ for these modes are identified in Figure A5.2 by the Struve notation P_1 (short period) and P_2 (long period). These $b_l(1500, V)$ values were obtained in the same manner as described in the first example. They suggest that the P_2 mode is an $l = 2$ pulsation while the P_1

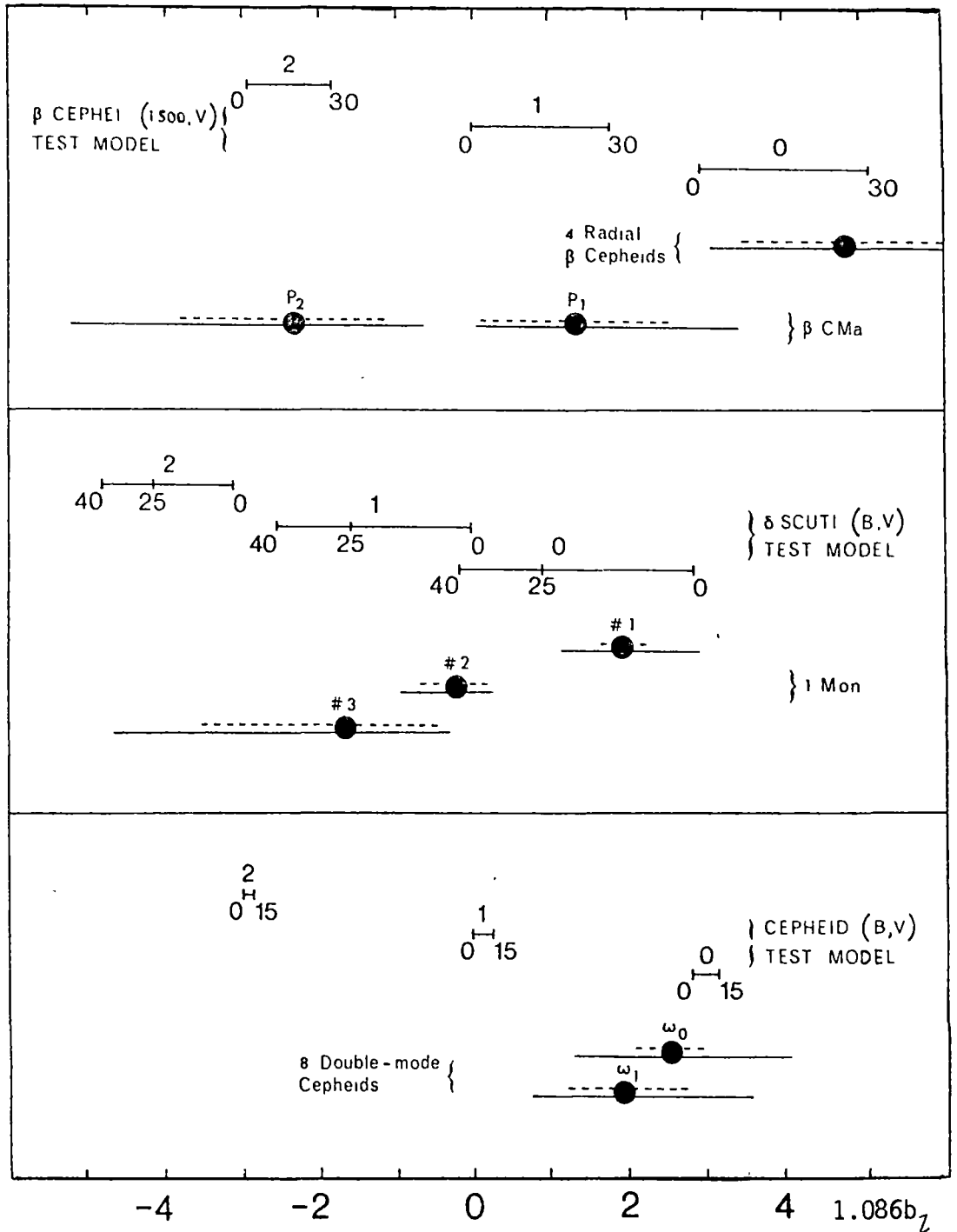


Figure A5.2 Observed and predicted Baade-Wesselink $b_z(\lambda_1, \lambda_2)$ values for $z = 0, 1, 2$. The corresponding p_*C values are shown below fiducial marks on the model lines. Dashed error bars show the range of $b_z(\lambda_1, \lambda_2)$ permitted by the observational errors if radii are specifically taken as $8 R_\odot$, $3 R_\odot$ and $40 R_\odot$ in the β Cephei, δ Scuti and short-period cepheid regimes respectively. Full error bars indicate how these ranges are extended if respective radii are permitted to vary from $5 R_\odot$ to $11 R_\odot$, $2 R_\odot$ to $4 R_\odot$ and $25 R_\odot$ to $55 R_\odot$ in these variable star regimes.

mode may be either $l = 0$ or 1 . The radial velocity uncertainties discussed in Section 5.4 will apply to the P_2 mode if indeed it is an $l = 2$ pulsation. To this must be added the uncertainty, noted by Smith (1980a), that in nonradial multimode pulsations the radial velocity results are not always additive when multiple modes interact, as is assumed in periodogram analyses.

The best illustration of the δ Scuti regime is afforded by the excellent 1 Mon data of Balona and Stobie (1980). Values of $b_l(B,V)$ were obtained from this data using (A5.13) and an R initially assumed to be $3 R_\odot$. Mode #1 was identified by Balona and Stobie as a radial pulsation, while they suggested that the next best observed modes, #2 and #3, were $l = 1$ pulsations. These conclusions were based on an examination of the phase difference between light and colour data, a technique which is discussed in Section A5.3. Figure A5.2 shows that the direct Baade-Wesselink technique is consistent with this interpretation. Mode #1 is certainly radial, even if a liberal range of possible R , $2 R_\odot$ to $4 R_\odot$, is employed. A pressure effect is indicated, though perhaps less than the $p_*C = 25$ value which is applicable in our model if the 1 Mon value of Breger and Bregman (1975) is used. Mode #2 is an $l = 1$ pulsation according to Figure A5.2, but this figure alone does not distinguish between $l = 1$ and 2 for mode #3. Other arguments outlined by Balona and Stobie are necessary to decide in favour of the $l = 1$ choice for mode #3.

To illustrate the short-period cepheid regime, the data for eight double-mode cepheids given by Balona and Stobie (1979b) were used. Balona and Stobie provide information on the fundamental sinusoidal variations of light, colour and radial velocity for both the fundamental period, ω_0 , and the first overtone, ω_1 . Mean $b_l(B,V)$ for these eight stars, calculated using (A5.13), are shown in Figure A5.2. Both ω_0 and ω_1 values identify with radial pulsations even when R is permitted

to vary over a range from $25 R_{\odot}$ to $55 R_{\odot}$ about an initially assumed value of $40 R_{\odot}$. Data for individual stars favour the $l = 0$ identification though with considerably larger error ranges. The Figure A5.2 plot for these eight stars suggests, in agreement with our model, that no large pressure effect exists in this regime.

The general conclusion that may be drawn from Figure A5.2 is that practical mode discrimination between $l = 0, 1$ and 2 is possible in all test regimes. Observational data plotted in this figure would discriminate against $l = 4$ and 5 coefficients listed in Table A5.4 with only one exception. However the $l = 3$ case remains confused, as mentioned in Section A5.2.2.

A5.3 RELATED AMPLITUDE AND PHASE TECHNIQUES

The principal advantage of the Baade-Wesselink technique for l discrimination is that, once the observations of the variations have been acquired, the only extra information needed is an approximate value of R and a knowledge of stellar equilibrium conditions to give the required model atmosphere quantities. Its disadvantage is that observations of light, colour and radial velocity are *all* required. Moreover those observations are generally required in multi-mode situations and situations where the variations are often very small. It is therefore clearly desirable to investigate whether less observationally demanding techniques for l discrimination are possible.

By considering amplitude ratios of, or phase differences between, light colour and radial velocity variations, one can obtain observational quantities which rely on subsets of the Baade-Wesselink observational requirements while remaining free of the unknown amplitude parameter $\epsilon P_{l,m}(\cos i)$. The price paid for this reduced observational requirement is the necessity to know values for the fundamental parameters (B, ψ')

appearing in (2.21) and (2.28). For consistency with the phase notation of Balona and Stobie, the phase shift ψ' between $\Delta T/T$ and $\Delta R/R$ will be used here as the observationally determined quantity. This is, of course, related to the phase shift ψ defined in Section 2.2.2 by $\psi' = \psi + \pi$. In Section A5.3.2 all the possible amplitude ratio and phase difference combinations in each of the test model regimes will be reviewed after justifying the choice of approximate (B, ψ') values for these regimes in Section A5.3.1. The use of $A_{\text{col}}/A_{\lambda_2}$ in the β Cephei regime (Stamford and Watson 1978, Balona and Stobie 1979c) and of $(\phi_{\lambda_2} - \phi_{\text{col}})$ in the δ Scuti regime (Balona and Stobie 1979c, 1980) appear naturally within the context of this review.

A5.3.1 *Test Model (B, ψ') Values*

For radial pulsations it is observationally apparent that $\psi' \sim \pi$ in the β Cephei regime while it is much closer to $\pi/2$ for variables in the cepheid instability strip. The work of Balona and Stobie (1979c) in fact suggests $90^\circ < \psi' < 140^\circ$ for classical cepheids. Similar values are anticipated for the δ Scuti stars (Balona and Stobie 1980).

In the radial pulsation case an approximate observed B value follows from the fact that $\eta \sim 0.1$ in a wide range of variable star regimes (Watson 1971b). Here $\eta = \epsilon/A_{\text{bol}}$, the ratio of fractional radius to bolometric magnitude amplitude. Using a limb-darkening law appropriate to the integrated local emergent flux, then an expression analogous to Equation 2.21 for the bolometric magnitude variations may be written:

$$\Delta m_{\text{bol}}(t) = -1.086 \epsilon P_{\text{lm}}(\cos i) I_{\text{L}}(\text{EDD}) [4B \cos(\sigma t + \psi') + (2+L)(1-L) \cos(\sigma t)] \quad (\text{A5.15})$$

Using the observed η , together with $L = 0$ and $\psi' = \pi$ or $\pi/2$ in (A5.15), it is apparent that a $B \sim 2.5$ applied to our test regimes. The more detailed work documented in Chapter 3 confirms this approximate value, indicating observed B for radially pulsating β Cephei stars ranging from

1.6 to 3.2. A similar range of observed B values results from the work of Breger, Hutchins and Kuhl (1976) on δ Scuti radial pulsators. The classical cepheid work of Balona and Stobie (1979c) implies observed B values which range from 1.2 to 2.0 at a period corresponding to that of the short-period cepheid test model adopted here. The choice of Table A5.1 test model observed B values come from these considerations.

In Table A5.1 adiabatic B estimates are also listed. These were obtained employing by Equation 2.5 with $l = 0$, and using the same Q as yielded the p_*C estimates discussed in Section A5.2.1. Observed B are down by factors of between two and five on their corresponding adiabatic values. A further interesting point is that there is clear evidence in the classical cepheid strip (Balona and Stobie 1979c), and some weak evidence in the case of the β Cephei strip (Chapter 3, Stamford and Watson 1978), that the ratio of observed to adiabatic B decreases in going up the respective instability strips. For the classical cepheids this ratio drops from ~ 0.5 to ~ 0.2 and for the β Cepheids it falls from ~ 0.5 to ~ 0.25 . Thus either the adiabatic assumption or the use of (2.4) is becoming increasingly invalid at higher luminosities. Alternatively, nonlinear effects may contribute to the phenomenon. Available linear nonadiabatic theoretical pulsation models of δ Scuti stars (Stellingwerf, 1979) and β Cephei stars (Davey, 1970; Saio and Cox, 1980) give values of this B ratio which are larger than those observed. In the β Cephei models values of this ratio are ~ 1.0 . This suggests that it may indeed be the use of a boundary condition based on (2.4) which is presenting the problem because of dissipation of mechanical energy in travelling waves.

Effects of the minimum uncertainties in $\alpha(\lambda)$ and $I_Z(\lambda)$, discussed in Section A5.2.2, were examined. This examination confirmed that $A_{\text{col}}/A_{\lambda_2}$ values are not reliable Z discriminants for any $Z < 5$ in the β Cephei (B,V), δ Scuti or short-period cepheid cases, quite apart from any observational errors. It is the $\alpha(\lambda)$ errors which are the problem for $Z \leq 2$ and the $I_Z(\lambda)$ errors which can make colours almost meaningless for $Z \geq 3$. Only in the β Cephei (1500,V) case does the possibility of Z discrimination remain in the face of these $\alpha(\lambda)$ and $I_Z(\lambda)$ uncertainties. Even in this case discrimination is not possible for $Z = 3$ and 5 because of overlap with lower Z values and sensitivity of colours to $I_Z(\lambda)$ errors. The effect on A_{1500-V}/A_V of varying (B, ψ') about the values in Table A5.1 is shown in Figure A5.3 for $Z \leq 2$. This affirms the mode discriminating ability of A_{1500-V}/A_V under wide (B, ψ') uncertainties, particularly if pressure effects are accounted for. The success of this A_{1500-V}/A_V as a mode discriminator has resulted from a combination of a large $(\alpha(\lambda_1) - \alpha(\lambda_2))$ value, which enables reliable colours to be obtained theoretically and observationally, together with a small $\alpha(\lambda_2)$ value, which enables the geometric term in Equation 2.21 to affect A_V in a low Z and $\psi' = \pi$ situation. It is interesting to note that, had B values in the β Cephei test case been close to adiabatic ones, such discrimination would not have been possible.

The K/A_{λ_2} values in Table A5.5 show an Z dependence which is most marked in the β Cephei test case. As for $A_{\text{col}}/A_{\lambda_2}$ the reason for this is the effect of the geometric contributions to A_V when $\psi' = \pi$. Errors in $\alpha(\lambda)$ and $I_Z(\lambda)$ values alone do not destroy the mode discrimination possibilities of K/A_V . However its usefulness is severely limited by the effects of uncertainties in R and B, and by the Section 5.4 problems related to the means by which radial velocity measurements are made.

TABLE A5.5 : Example amplitude ratios and phase differences for test models

| Regime (B, ψ') $p_* C$ | $A_{\text{col}}/A_{\lambda_2}$ | | | | | | | | $K/A_{\lambda_2} \text{ km s}^{-1} \text{ mag}^{-1}$ | | | | | | | |
|--|---|------|-------------------------|------|-------------------------|------|-------------------------------|------|--|-----|-----------------------|------|-----------------------------|------|--|--|
| | β Cephei (1500,V) | | β Cephei (B,V) | | δ Scuti (B,V) | | Short-Period Cepheid (B,V) | | β Cephei (V) | | δ Scuti (V) | | Short-Period Cepheid (V) | | | |
| | (2.5,180°) 0 30 | | (2.5,180°) 0 30 | | (2.5,90°) 0 40 | | (1.5,90°) 0 15 | | (2.5,180°) 0 30 | | (2.5,90°) 0 40 | | (1.5,90°) 0 15 | | | |
| $l = 0$ | 1.9 | 3.0 | 0.15 | 0.16 | 0.33 | 0.34 | 0.30 | 0.30 | 650 | 890 | 145 | 145 | 45 | 45 | | |
| 1 | 1.2 | 1.6 | 0.09 | 0.09 | 0.36 | 0.37 | 0.33 | 0.33 | 430 | 510 | 170 | 170 | 55 | 55 | | |
| 2 | 0.9 | 1.1 | 0.08 | 0.07 | 0.38 | 0.40 | 0.36 | 0.36 | 340 | 370 | 215 | 225 | 65 | 65 | | |
| 3 | 3.2 | 3.4 | 0.33 | 0.32 | 0.51 | 0.50 | 0.49 | 0.49 | 900 | 950 | 400 | 415 | 95 | 95 | | |
| 4 | 0.33 | 0.31 | 0.03 | 0.03 | 0.14 | 0.18 | 0.34 | 0.34 | 35 | 35 | 95 | 95 | 40 | 40 | | |
| 5 | 1.6 | 1.7 | 0.31 | 0.30 | 0.36 | 0.33 | 0.33 | 0.33 | 260 | 270 | 80 | 85 | 15 | 15 | | |
| | $(\phi_{\lambda_2} - \phi_{\text{col}})$ in degrees | | | | | | | | $(\phi_{\lambda_2} - \phi_{\text{RV}})$ in degrees | | | | | | | |
| $l = 0$ | 0 | 0 | 0 | 0 | -12 | 1 | -15 | -17 | 90 | 90 | -12 | -16 | -15 | -17 | | |
| 1 | 0 | 0 | 0 | 0 | 0 | 12 | 0 | -2 | 90 | 90 | 0 | -4 | 0 | -2 | | |
| 2 | 0 | 0 | 0 | 0 | 20 | 31 | 23 | 22 | 90 | 90 | 23 | 19 | 29 | 27 | | |
| 3 | 0 | 0 | 0 | 0 | 25 | 34 | 23 | 23 | 90 | 90 | 47 | 45 | 54 | 53 | | |
| 4 | 180 | 180 | 180 | 180 | 121 | 127 | 168 | 168 | -90 | -90 | -118 | -119 | -112 | -112 | | |
| 5 | 0 | 0 | 0 | 0 | 21 | 27 | 17 | 17 | 90 | 90 | 71 | 71 | 75 | 75 | | |

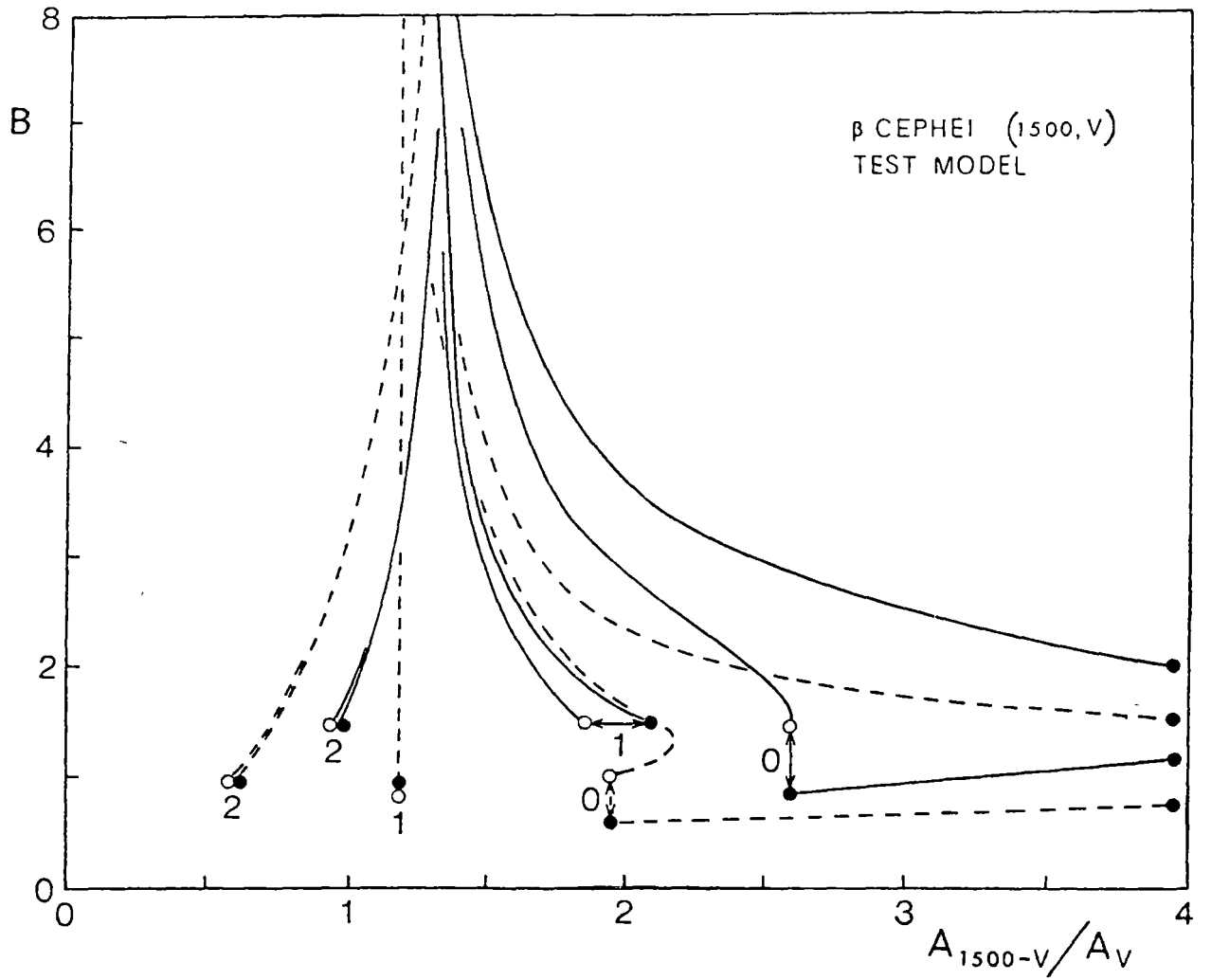


Figure A5.3 A_{1500-V}/A_V versus (B, ψ') for the β Cephei test model with $l = 0, 1, 2$. Full lines are for $p_*C = 30$ and dashed lines are for $p_*C = 0$. Filled circles indicate $\psi' = 180^\circ$ and open circles indicate $\psi' = 150^\circ$ or 210° .

The $(\phi_{\lambda_2} - \phi_{\text{col}})$ values for the δ Scuti and short-period cepheid test cases in Table A5.5 show a variation with l which, when minimum uncertainties in $\alpha(\lambda)$ and $I_l(\lambda)$ are allowed for, suggests that $l \leq 2$ and $l = 4$ modes may be identified by careful observation. The $l = 3$ and 5 modes are confused with small l . For $l \leq 2$, the effect of varying (B, ψ') about Table A5.1 values is illustrated in Figure A5.4. This demonstrates that, provided pressure effects are allowed for, $(\phi_V - \phi_{B-V})$ remains a useful discriminator in spite of substantial (B, ψ') uncertainties. However $l \leq 2$ discrimination would not be possible if observed B were close to adiabatic values. In Table A5.6 the values of $(\phi_V - \phi_{B-V})$ for the δ Scuti model are given for a range of $(\alpha(V)B, \psi')$ to enable direct comparison with Balona and Stobie (1980). Values for both $p_*C = 0$ and $p_*C = 40$ are tabulated. There was an indication from the Baade-Wesselink method of a pressure effect in the 1 Mon radial mode data. The $(\phi_V - \phi_{B-V})$ value for the principal mode in HD101065 also favours the existence of such an effect. Its identification by Kurtz (1980) with an $l = 2$ pulsation is achieved without the need for a very low B value if pressure effects are present.

For $l \leq 2$ the source of the discriminating ability in $(\phi_V - \phi_{B-V})$ is the geometric term in the light variations, as given by Equation 2.21. In the absence of pressure effects the phase of these light variations varies through ψ' as l changes from 0 through to 2. The phase of the colour variations, on the other hand, is closely locked to ψ' in the absence of pressure effects, because the geometric term in (2.28) is either small or zero for $l \leq 2$. As in the case of a successful $A_{\text{col}}/A_{\lambda_2}$ discriminator, a desirable observational system here is one in which a large $(\alpha(\lambda_1) - \alpha(\lambda_2))$ for accurate theoretical and observational colours is combined with a small $\alpha(\lambda_2)$ value to provide large phase changes from (2.21) as l varies from 0 to 2. For $l \geq 3$ the geometric

TABLE A5.6 : $(\phi_V - \phi_{B-V})$, in degrees, for the δ Scuti test model

| $\alpha(V)B$ | | 5.0 | | 10.0 | | 15.0 | | 20.0 | | 25.0 | | 30.0 | |
|-------------------|-----|-----|-----|------|-----|------|-----|------|----|------|----|------|----|
| $p_{\star}C$ | | 0 | 40 | 0 | 40 | 0 | 40 | 0 | 40 | 0 | 40 | 0 | 40 |
| $l = 0 \ \psi' =$ | 90 | -22 | 1 | -11 | 1 | -8 | 0 | -5 | 0 | -5 | 0 | -4 | 0 |
| | 100 | -23 | 1 | -12 | 1 | -8 | 0 | -5 | 0 | -5 | 0 | -4 | 0 |
| | 120 | -23 | 2 | -11 | 1 | -7 | 0 | -5 | 0 | -4 | 0 | -3 | 0 |
| | 140 | -20 | 2 | -9 | 1 | -6 | 0 | -4 | 0 | -3 | 0 | -3 | 0 |
| 1 | 90 | 0 | 21 | 0 | 11 | 0 | 8 | 0 | 6 | 0 | 5 | 0 | 4 |
| | 100 | 0 | 23 | 0 | 12 | 0 | 8 | 0 | 6 | 0 | 5 | 0 | 4 |
| | 120 | 0 | 26 | 0 | 12 | 0 | 7 | 0 | 5 | 0 | 4 | 0 | 4 |
| | 140 | 0 | 26 | 0 | 10 | 0 | 6 | 0 | 4 | 0 | 3 | 0 | 3 |
| 2 | 90 | 32 | 55 | 19 | 30 | 13 | 20 | 10 | 15 | 8 | 12 | 7 | 10 |
| | 100 | 29 | 53 | 17 | 29 | 12 | 19 | 9 | 15 | 7 | 12 | 6 | 10 |
| | 120 | 21 | 47 | 13 | 25 | 10 | 17 | 8 | 13 | 6 | 10 | 5 | 9 |
| | 140 | 14 | 36 | 9 | 18 | 7 | 12 | 5 | 9 | 4 | 7 | 4 | 6 |
| 3 | 90 | 26 | 42 | 24 | 33 | 19 | 25 | 16 | 20 | 13 | 16 | 11 | 14 |
| | 100 | 22 | 36 | 31 | 29 | 17 | 22 | 14 | 18 | 12 | 15 | 10 | 13 |
| | 120 | 15 | 25 | 15 | 21 | 12 | 17 | 11 | 14 | 9 | 12 | 8 | 10 |
| | 140 | 10 | 16 | 9 | 14 | 8 | 11 | 7 | 9 | 6 | 8 | 5 | 7 |
| 4 | 90 | 147 | 150 | 118 | 124 | 96 | 103 | 80 | 86 | 68 | 75 | 58 | 64 |
| | 100 | 147 | 151 | 118 | 125 | 96 | 103 | 79 | 87 | 67 | 74 | 57 | 64 |
| | 120 | 150 | 154 | 120 | 129 | 95 | 107 | 76 | 88 | 63 | 74 | 53 | 63 |
| | 140 | 156 | 160 | 127 | 139 | 95 | 114 | 70 | 90 | 54 | 70 | 44 | 57 |
| 5 | 90 | 14 | 18 | 22 | 27 | 25 | 30 | 25 | 29 | 24 | 27 | 23 | 25 |
| | 100 | 13 | 16 | 19 | 23 | 21 | 25 | 21 | 25 | 20 | 23 | 19 | 22 |
| | 120 | 9 | 12 | 13 | 16 | 15 | 17 | 15 | 17 | 14 | 16 | 14 | 15 |
| | 140 | 6 | 8 | 9 | 10 | 9 | 11 | 9 | 11 | 9 | 10 | 9 | 10 |

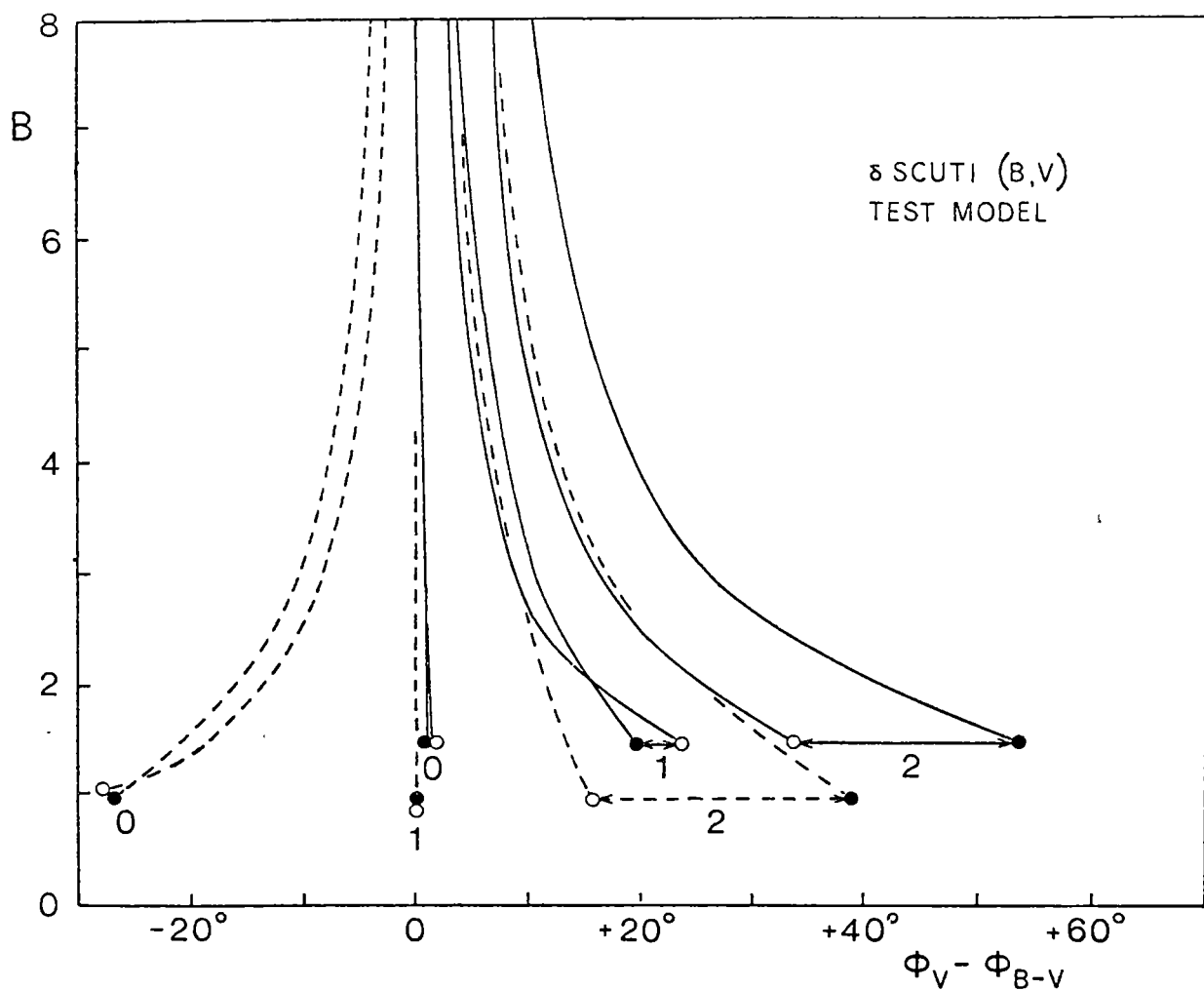


Figure A5.4 $(\phi_V - \phi_{B-V})$ versus (B, ψ') for the δ Scuti test model with $l = 0$. Full lines are for $p_*C = 40$ and dashed lines are for $p_*C = 0$. Filled circles indicate $\psi' = 90^\circ$ and open circles indicate $\psi' = 140^\circ$.

term in (2.28) and the associated limb-darkening uncertainties in $I_z(\lambda)$ begin to affect $(\phi_{\lambda_2} - \phi_{\text{col}})$ values.

Values of $(\phi_{\lambda_2} - \phi_{\text{RV}})$ in Table A5.5 at first sight suggest a mode discriminating ability similar to $(\phi_{\lambda_2} - \phi_{\text{col}})$, particularly in view of the fact that they are independent of errors in $I_z(\lambda)$ and insensitive to $\alpha(\lambda)$ errors. However the discriminating ability is completely removed by uncertainties in ψ' . The difference between the $(\phi_{\lambda_2} - \phi_{\text{RV}})$ case and that for $(\phi_{\lambda_2} - \phi_{\text{col}})$ is simply that, for $z \leq 2$, ϕ_{col} remains tied to ψ' whereas ϕ_{RV} does not.

The general conclusion drawn from all the preceding discussion is that $A_{\text{col}}/A_{\lambda_2}$ or $(\phi_{\lambda_2} - \phi_{\text{col}})$ are useful z discriminators depending on whether $\psi' \sim \pi$ or $\sim \pi/2$. A similar conclusion is implicit in the work of Balona and Stobie (1979c). To this conclusion must be added the provisos that pressure effects be included and that, while discrimination between modes with $z \leq 2$ is feasible, other arguments are required to rule out overlapping higher modes. Use of these discriminators has the obvious advantage of not requiring radial velocity data, particularly in view of the difficulties discussed in Section 5.4 and those discussed by Smith (1980a) for multimode pulsators.

A5.4 CONCLUSION

Abandoning the assumption of a single-valued relation between observed surface brightness and colour variations enables the determination of a Baade-Wesselink formula which will work, in principle, for all z values. Examples from different variable star types suggest that practical use of this formula for $z \leq 2$ is possible, provided that pressure effects are included. Complications arise in the application of the nonradial Baade-Wesselink formula because of the need to evaluate mean wavelengths to determine radial velocity and the fact

that, for $z > 2$, the conversion factor p_{mean} between the mean profile velocity and the nonradial surface velocity amplitude becomes strongly dependent on the assumed profile darkening law. Overlap of discriminants, particularly for $z = 3$, is a further problem.

Radial velocity difficulties are avoided by use of techniques relying on amplitudes and phases of light and colour data. The ratio of colour to light amplitudes is a useful z diagnostic if $\psi' \sim \pi$, while the phase difference between colour and light variations is useful if $\psi' \sim \pi/2$. These techniques should also successfully discriminate for $z \leq 2$. Improvements in model atmosphere limb-darkening, possibly combined with availability of data at many wavelengths to permit analysis similar to that undertaken in Chapter 3, may extend this discrimination ability to higher z .

A P P E N D I X 6

NONRADIAL LINE PROFILES FOR $l \leq 3$

Osaki (1971), Kubiak (1978) and Smith (1980a) have extensively investigated the nonradial line profiles resulting from many combinations of amplitude, rotational speed and inclination angle. However, presumably because of the limitations of space, relatively few sequences of the modelled line profiles have been published. To illustrate the variety of profile shapes resulting from nonradial motions, line profiles up to $l = 3$, covering a coarse grid of velocity ratios (v_p/v_e) and inclination angles i , were generated. These profile sequences are presented in Figures A6.1-A6.10.

In constructing the line profiles, values of the parameters $v_b = 8 \text{ km s}^{-1}$ and $v_e = 50 \text{ km s}^{-1}$ for broadening and rotational velocity respectively were assumed. A value of $k = 0.05$ was chosen for the constant controlling the horizontal surface components to be consistent with the observed ω^2 of the β Cephei stars. To describe the limb darkening of the intrinsic profiles, a formula $I = I_0(1-u+u \cos \gamma)$ with $u = 0.3$, was used. This is comparable to the value of $u = 0.36$ (i.e. $\beta = \frac{u}{1-u} = 0.56$) used by Osaki (1971) and Kubiak (1978). The profiles are, in any case, insensitive to the exact value of u chosen.

Table A6.1 summarizes the range of inclination angles for which line profiles were modelled. In each figure the vertical sequence of profiles shows the evolution of the line profile in phase from $\phi = 0.25$ to $\phi = 0.75$, using Osaki's (1971) phase convention. Each separate panel corresponds to the particular velocity ratio ($A = v_p/v_e$) which is indicated at the base of the panel. Here v_e is the equatorial rotational speed, while v_p is the semiamplitude of pulsational velocity in the radial

direction at the dominant surface antinode. This is a consistent extension of Osaki's (1971) notation[†]. A velocity scale, in units of $v_e \sin i$, is provided at the top of each panel. Although absolute line depths are arbitrary, the relative changes in line depth throughout the cycle have been preserved.

[†] Unno, Osaki and Shibahashi (1979) have suggested that this notation, used by Stamford and Watson (1976), is not consistent with the notation defined by Osaki (1971). However tests indicate that this is *not* the case. The discrepancy noted by Unno *et al.* is the result of a k value which has been misquoted for the (2,-1) case illustrated in the Stamford and Watson (1976) paper. A value for k of 0.05, rather than the quoted value of 0.15, was used for that example. The effect on the (2,-1) line profiles of *decreasing* the k value is similar to that which results from *increasing* the velocity ratio.

TABLE A6.1: Index to Nonradial Profile Figures

| Figure | l | m | i | | | |
|--------|-----|-----|----------------|----------------|----------------|----------------|
| A6.1 | 0 | 0 | (a) 90° | | | |
| A6.2 | 1 | 0 | (a) 23° | (b) 45° | (c) 68° | |
| A6.3 | | -1 | (a) 23° | (b) 45° | (c) 68° | (d) 90° |
| A6.4 | 2 | 0 | (a) 23° | (b) 45° | (c) 68° | (d) 90° |
| A6.5 | | -1 | (a) 23° | (b) 45° | (c) 68° | |
| A6.6 | | -2 | (a) 23° | (b) 45° | (c) 68° | (d) 90° |
| A6.7 | 3 | 0 | (a) 20° | (b) 39° | (c) 63° | |
| A6.8 | | -1 | (a) 31° | (b) 45° | (c) 90° | |
| A6.9 | | -2 | (a) 45° | (b) 68° | (c) 90° | |
| A6.10 | | -3 | (a) 23° | (b) 45° | (c) 90° | |

Figure A6.1(a)
 Line Profiles for $(0,0)$ $i = 90^\circ$
 $l = 0$
 $m = 0$
 $(i = 90^\circ)$

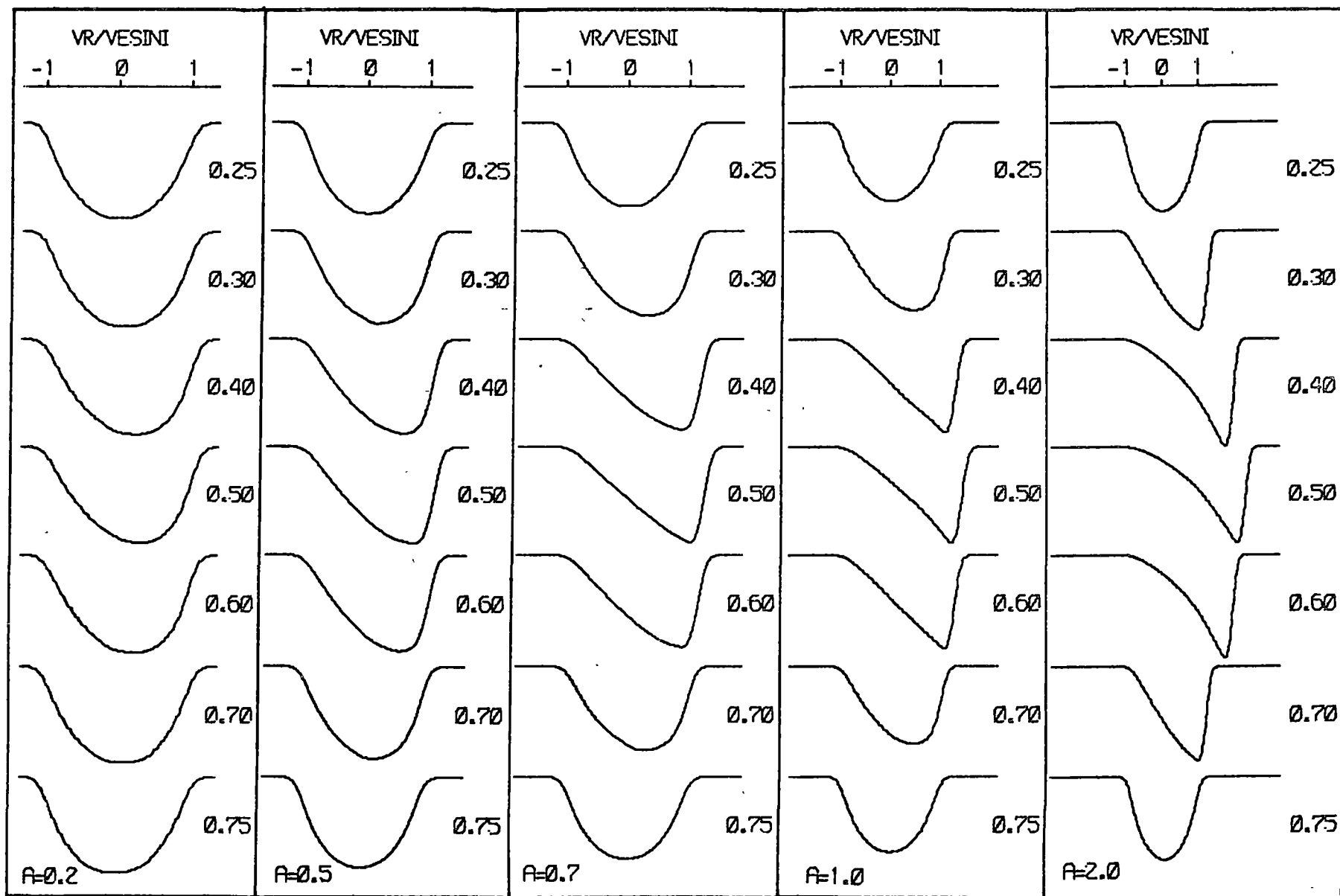


Figure A6.2(a)

Line Profiles for $(1,0)$ $i = 23^\circ$

$l = 1$
 $m = 0$
 $(i = 23^\circ)$

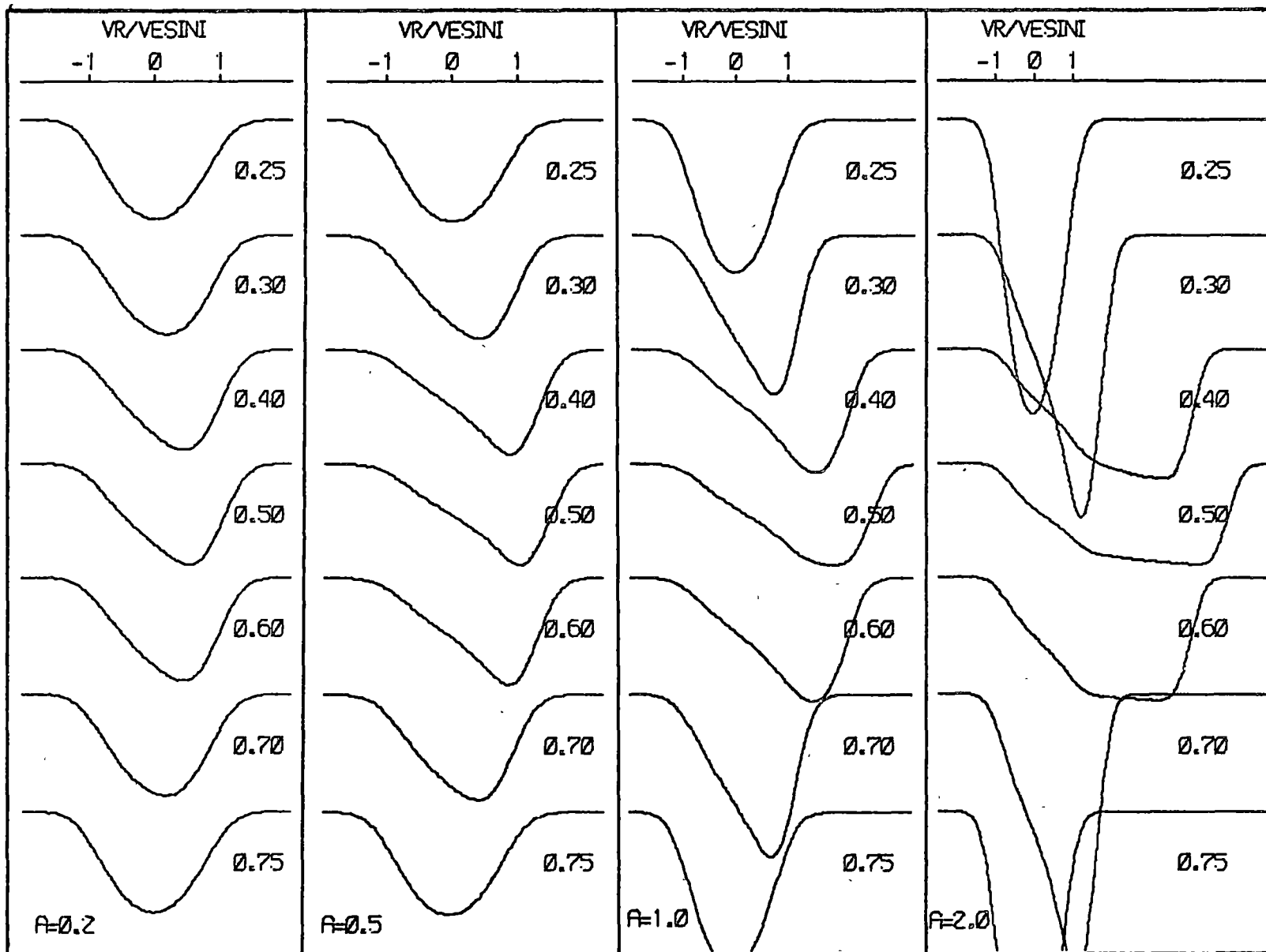
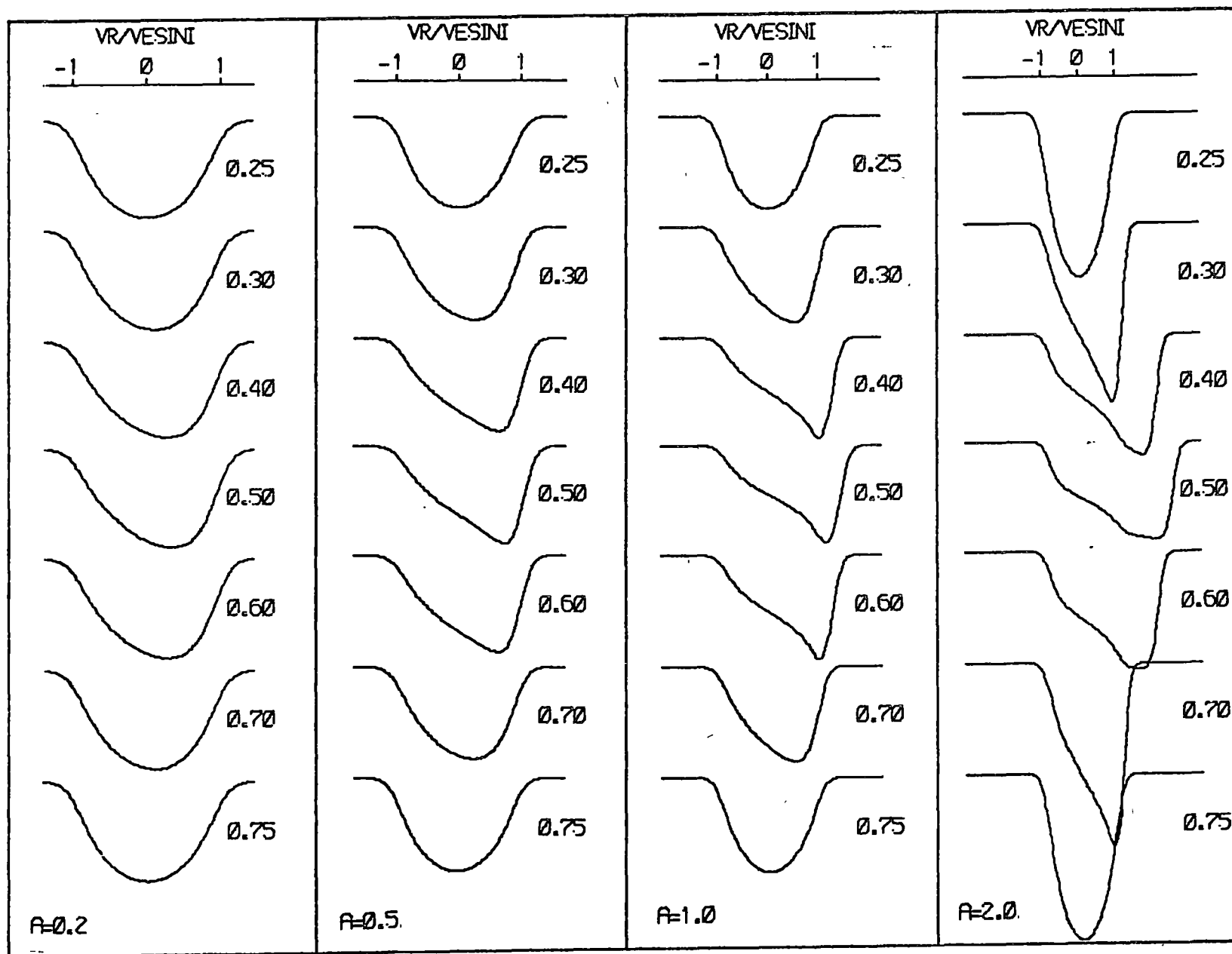


Figure A6.2(b)

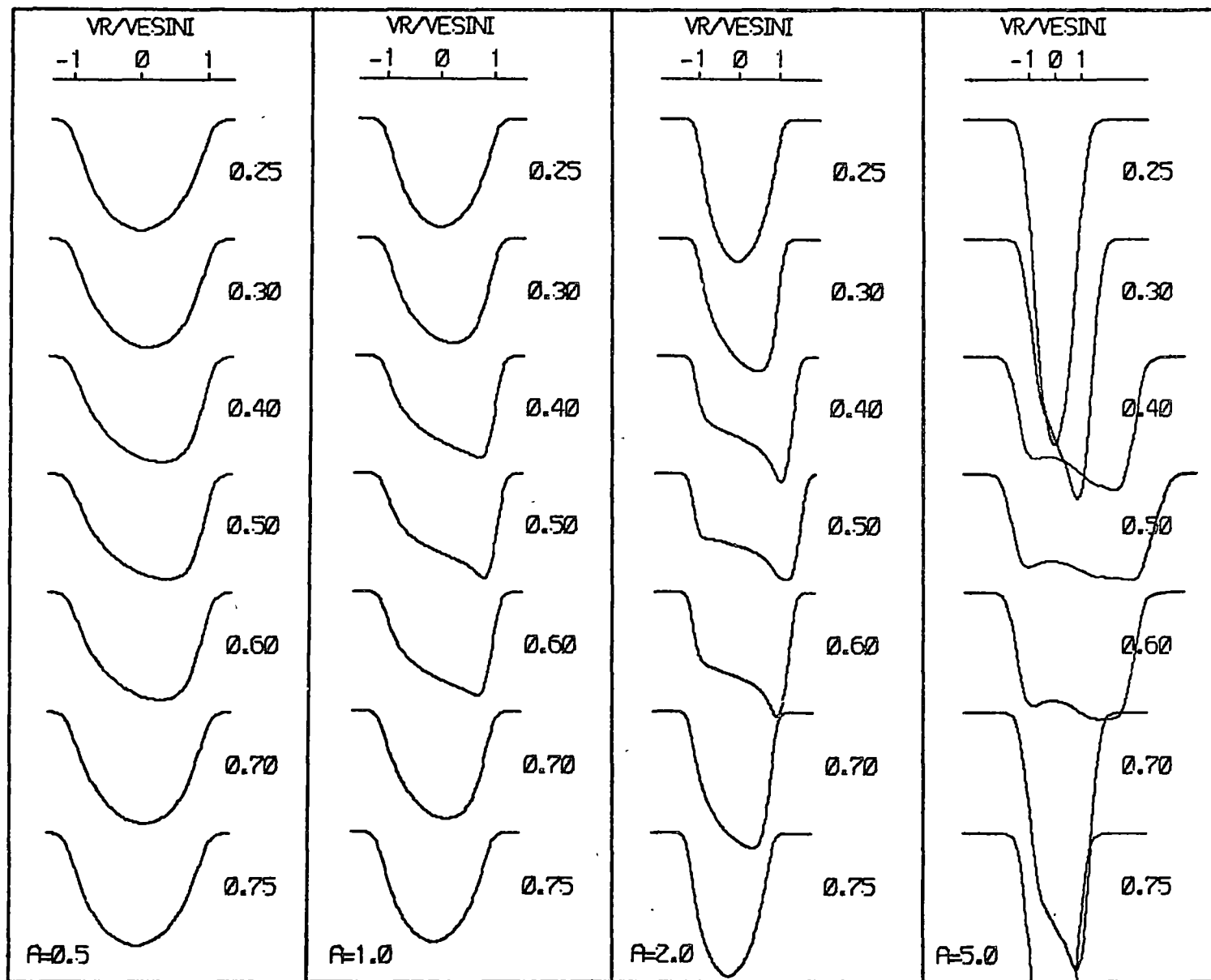
Line Profiles for (1,0) $i = 45^\circ$

$l = 1$
 $m = 0$
 $(i = 45^\circ)$



$l = 1$
 $m = 0$
 $(i = 68^\circ)$

Figure A6.2(c)
Line Profiles for $(1,0)$ $i = 68^\circ$



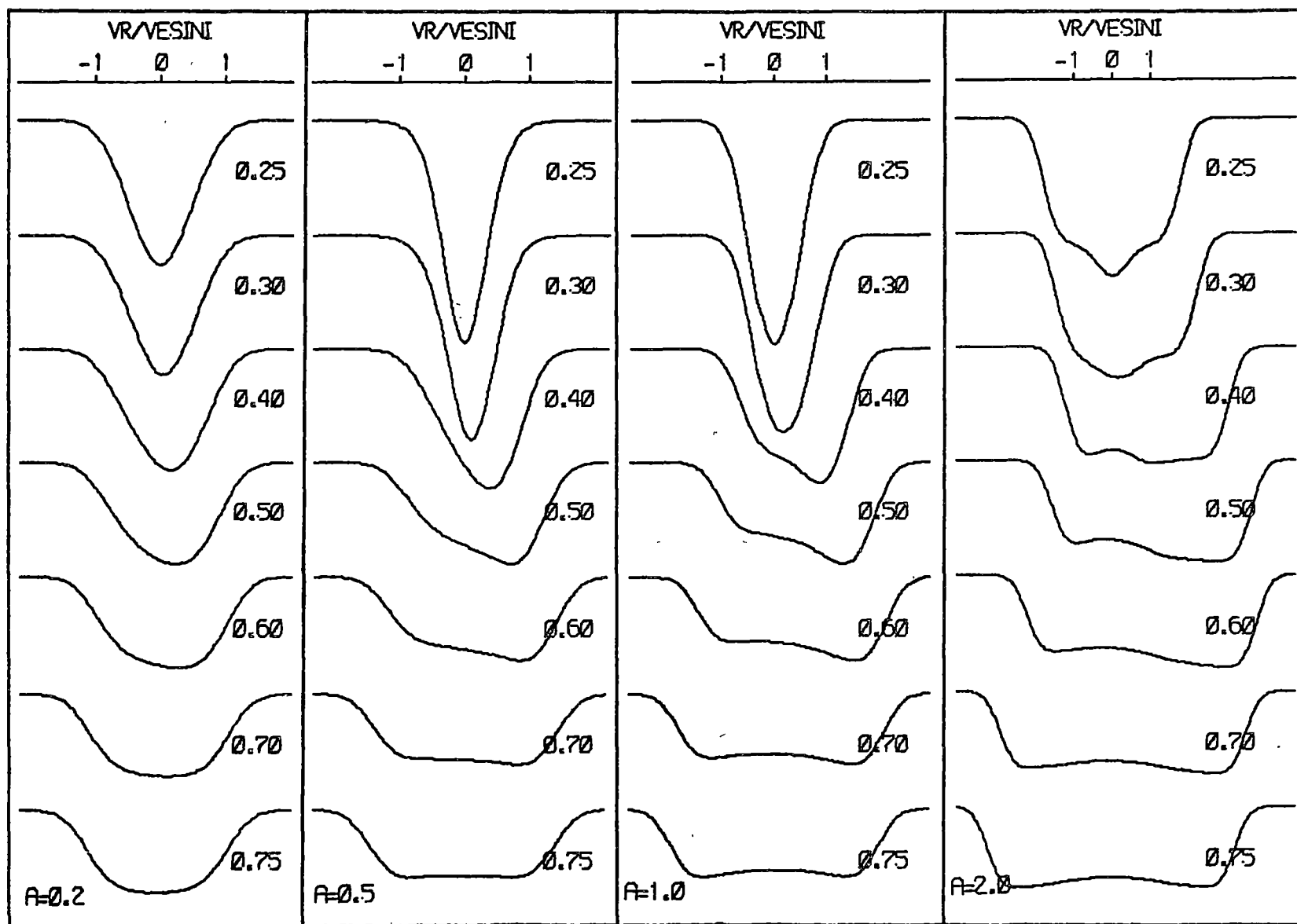


Figure A6.3(a)

Line Profiles for $(1, -1)$ $i = 23^\circ$

$l = 1$
 $m = -1$
 $(i = 23^\circ)$

Figure A6.3(b)

Line Profiles for $(1, -1)$ $i = 45^\circ$

$l = 1$
 $m = -1$
 $(i = 45^\circ)$

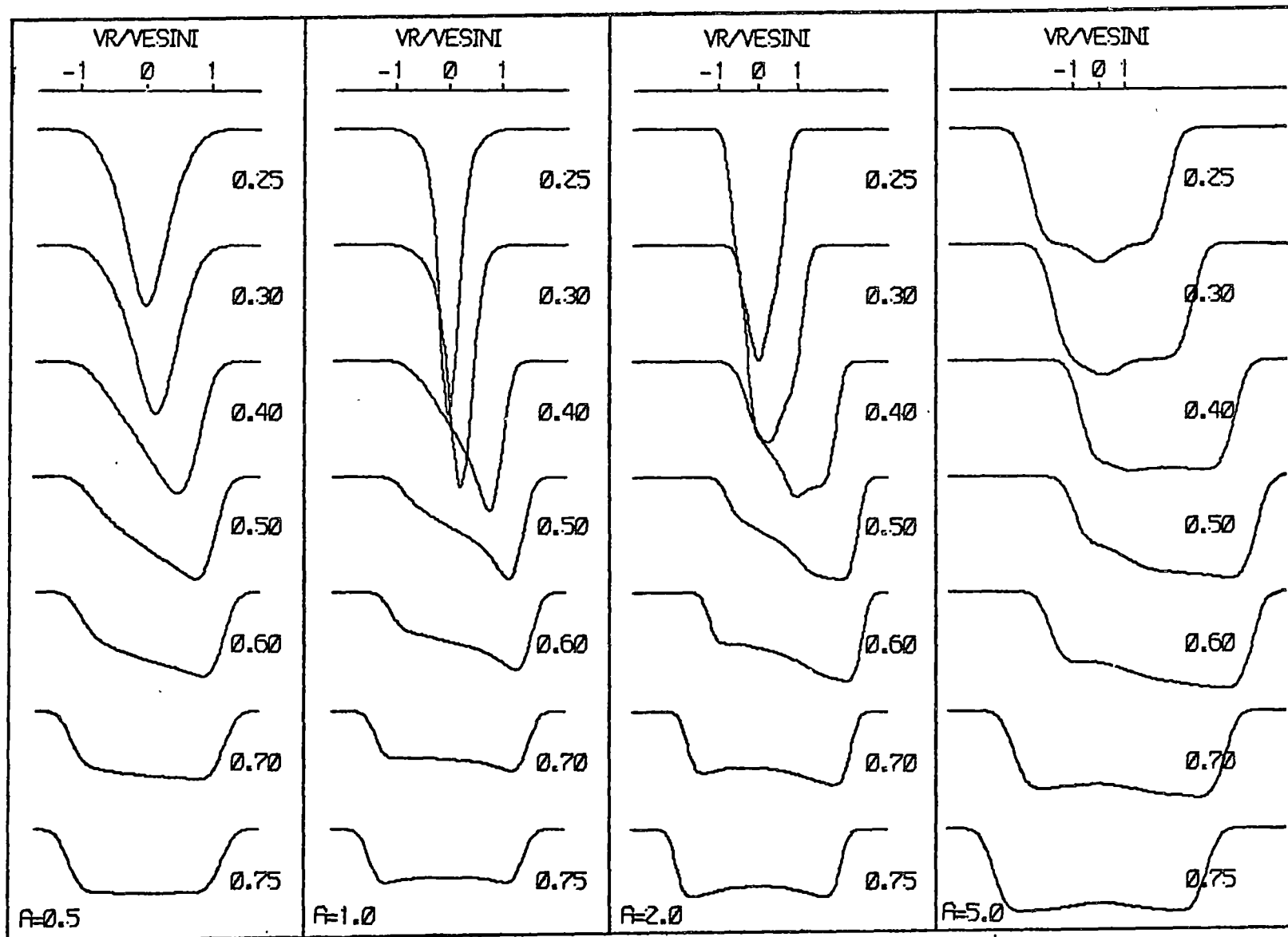


Figure A6.3(c)

Line Profiles for $(1, -1)$ $i = 68^\circ$

$l = 1$
 $m = -1$
 $(i = 68^\circ)$

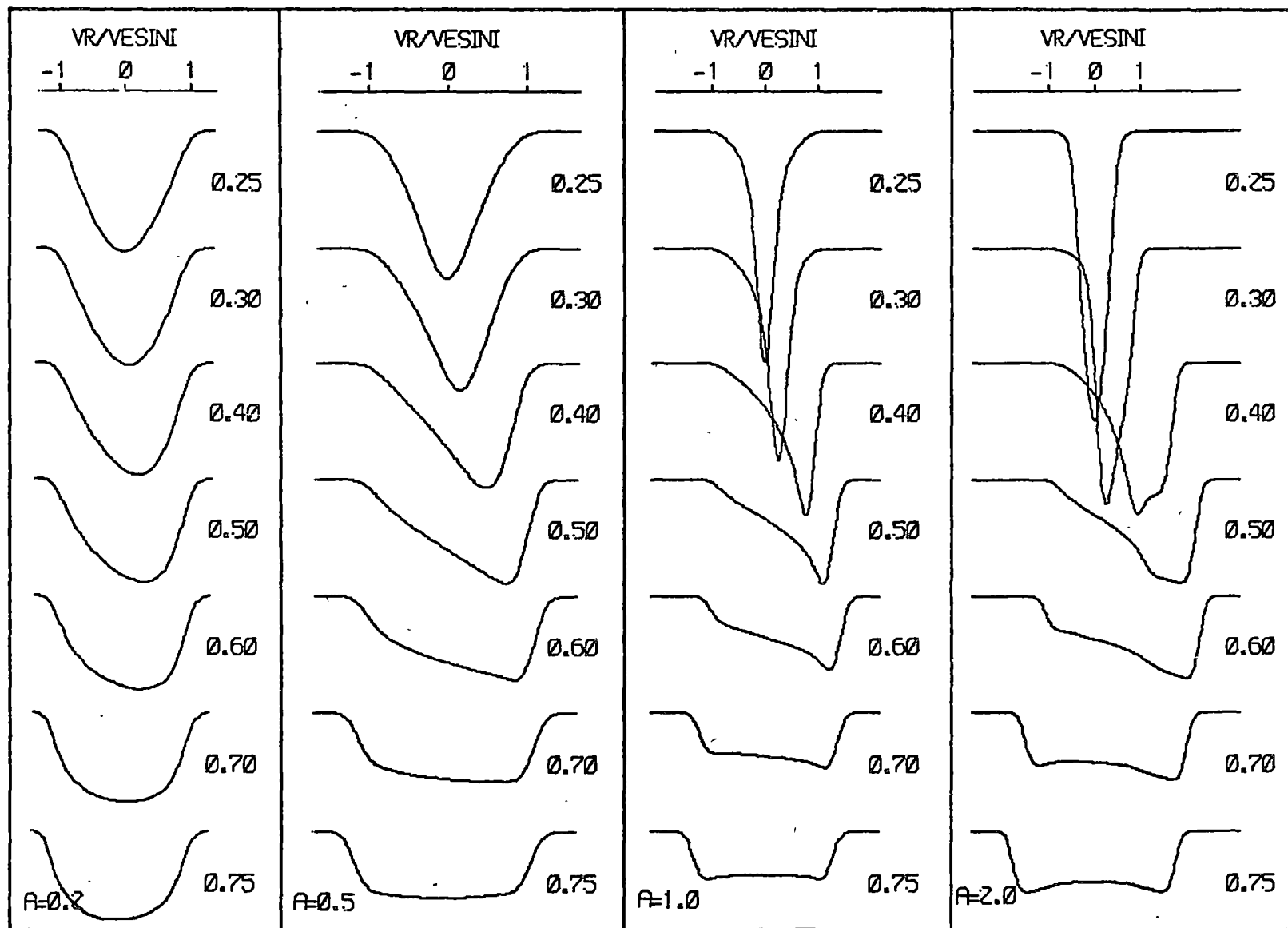
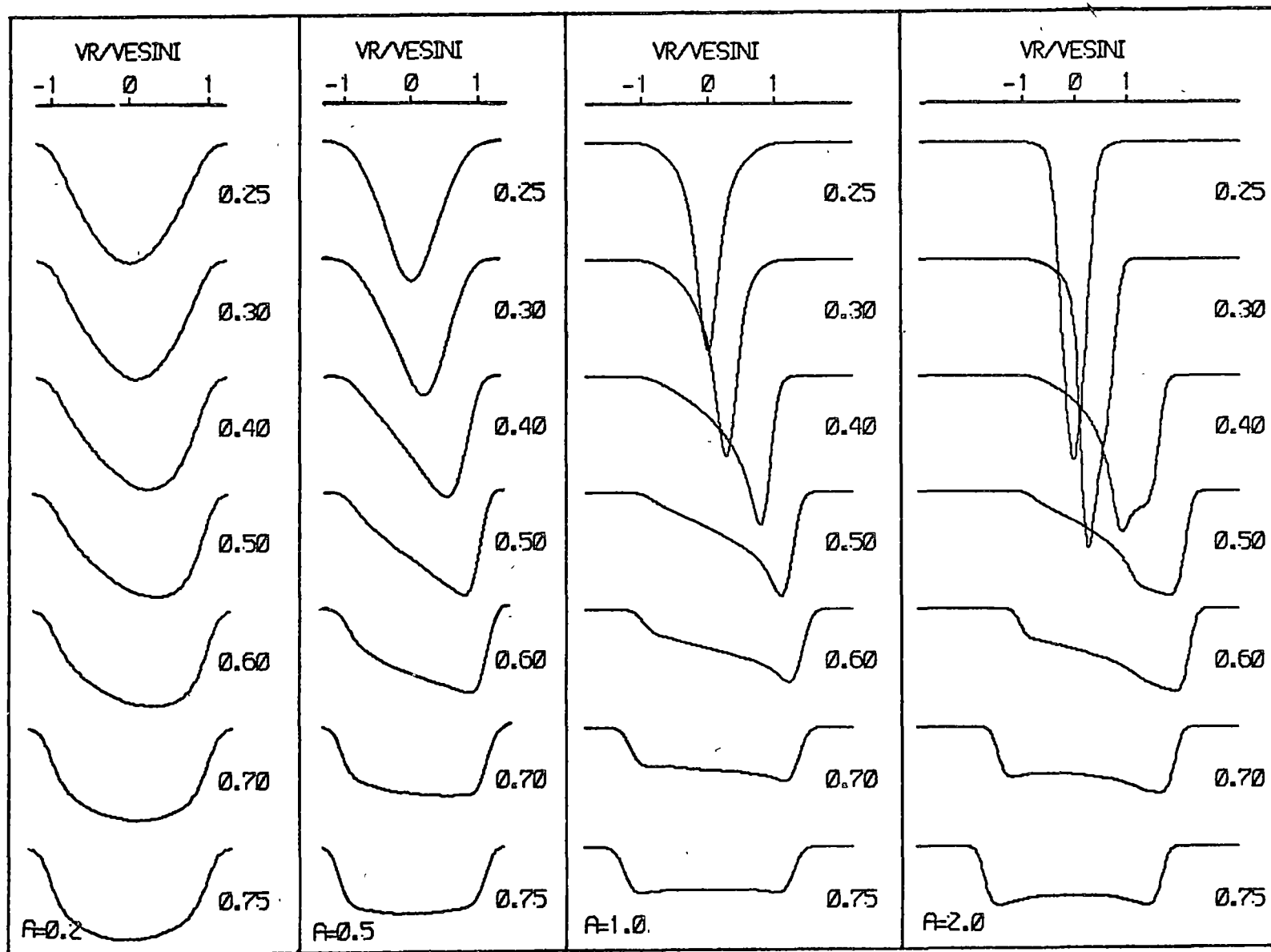


Figure A6.3(d)

Line Profiles for $(1, -1)$ $i = 90^\circ$

$l = 1$
 $m = -1$
 $(i = 90^\circ)$



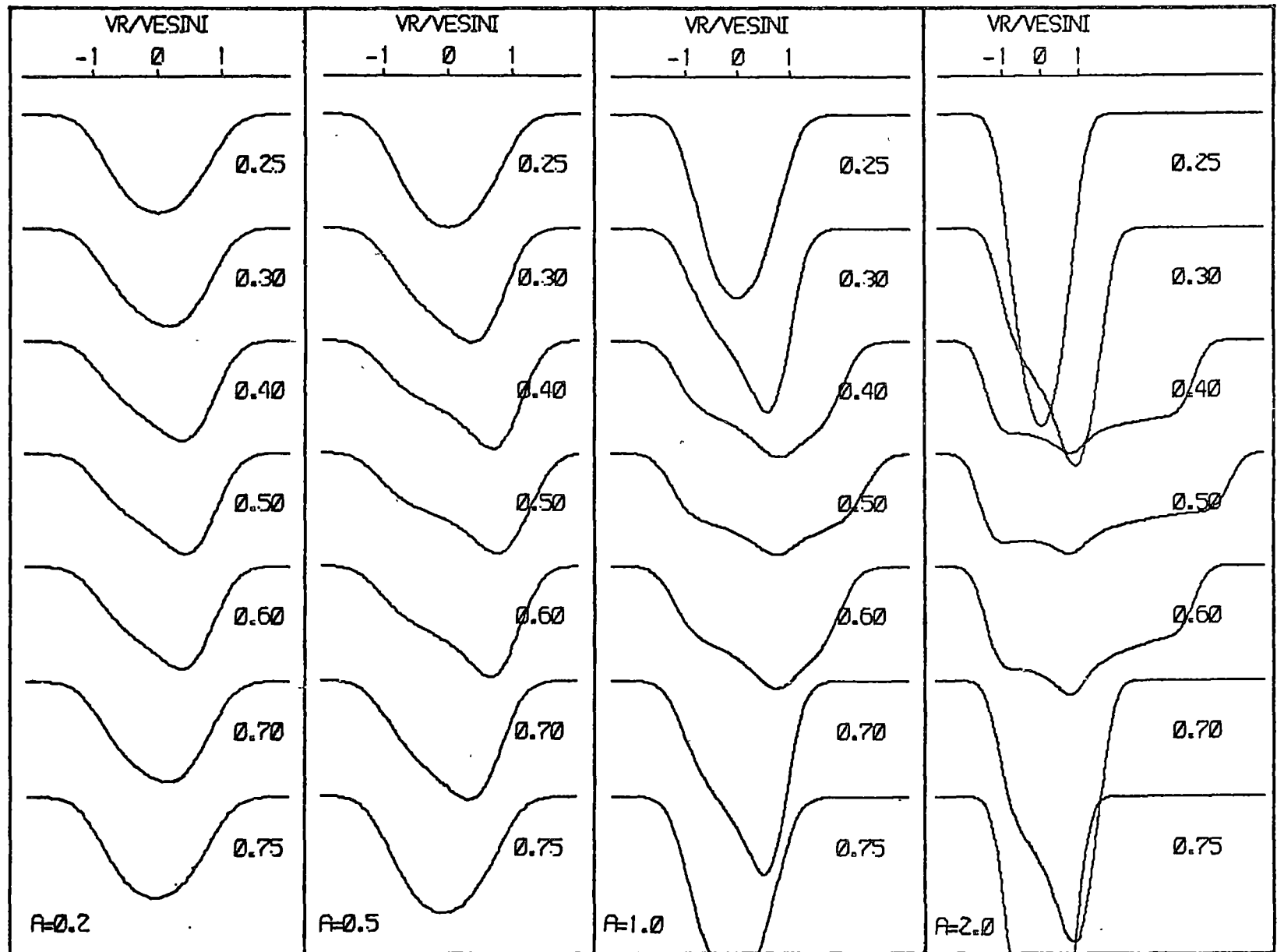


Figure A6.4(a)

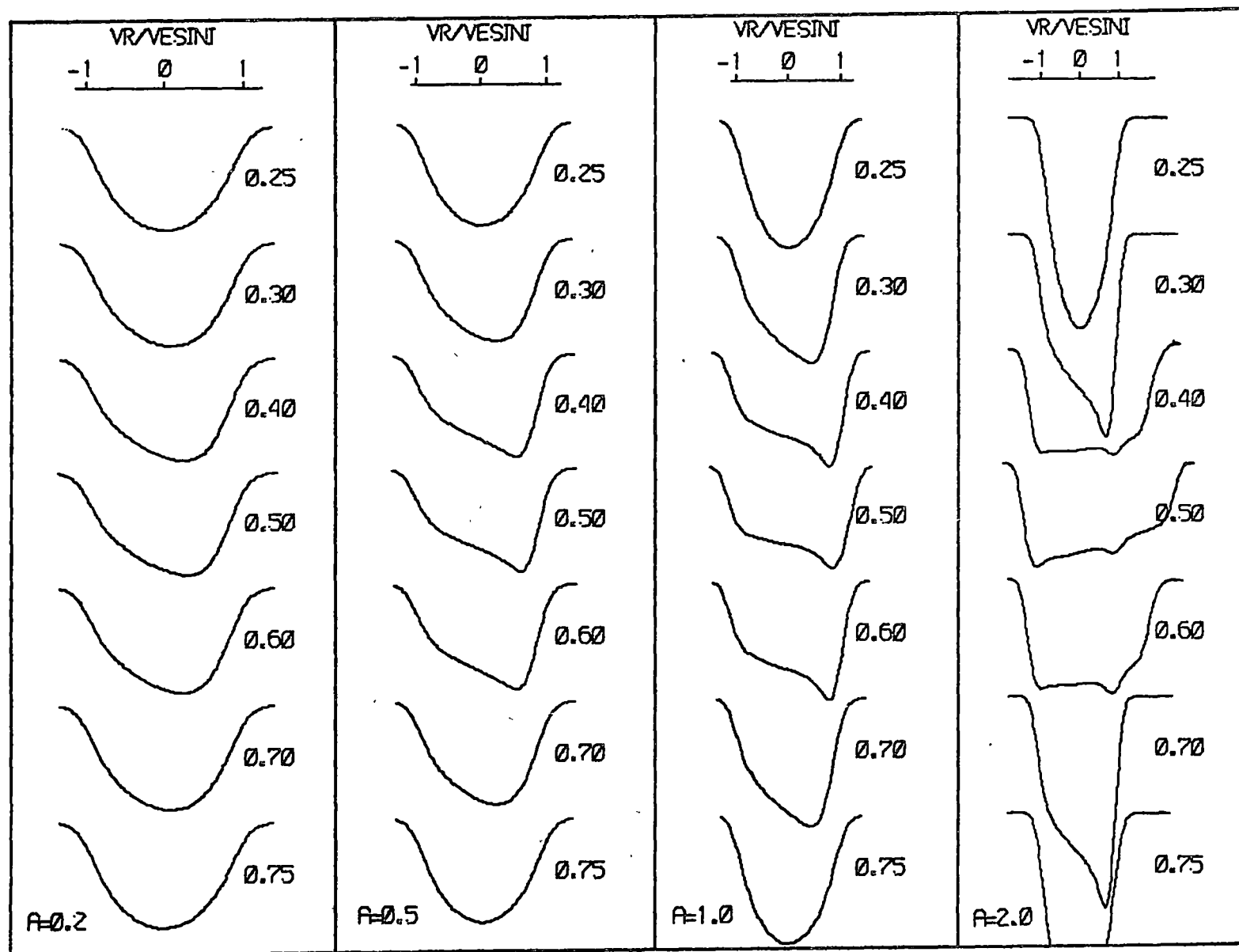
Line Profiles for $(2,0)$ $i = 23^\circ$

$l = 2$
 $m = 0$
 $(i = 23^\circ)$

Figure A6.4(b)

Line Profiles for $(2,0)$ $i = 45^\circ$

$l=2$
 $m=0$
 $(i=45^\circ)$



$$l = 2$$

$$m = 0$$

$$(i = 68^\circ)$$

Line Profiles for $(2,0)$ $i = 68^\circ$

Figure A6.4(c)

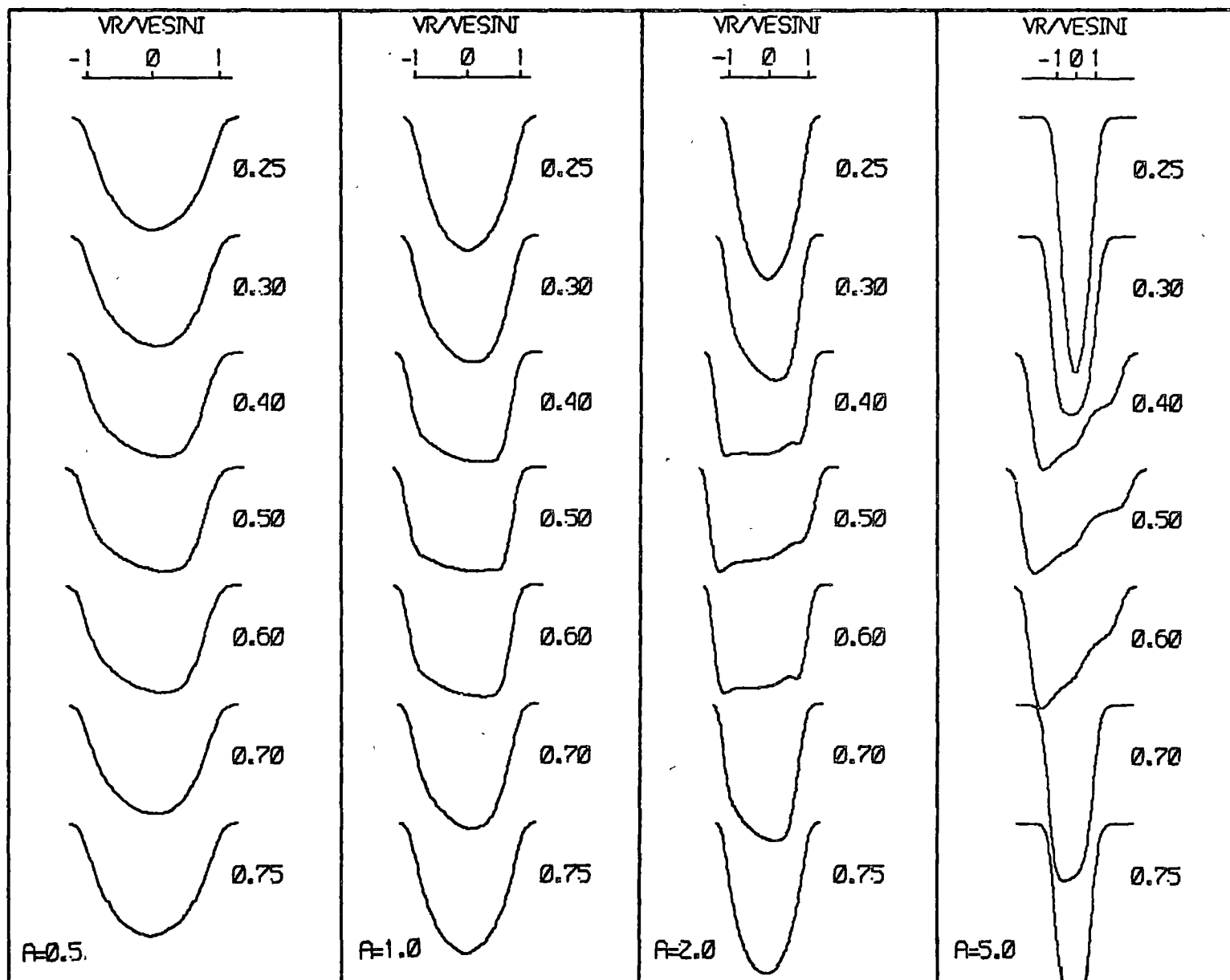


Figure A6.4(d)

Line Profiles for $(2,0)$ $i = 90^\circ$

$l = 2$
 $m = 0$
 $(i = 90^\circ)$

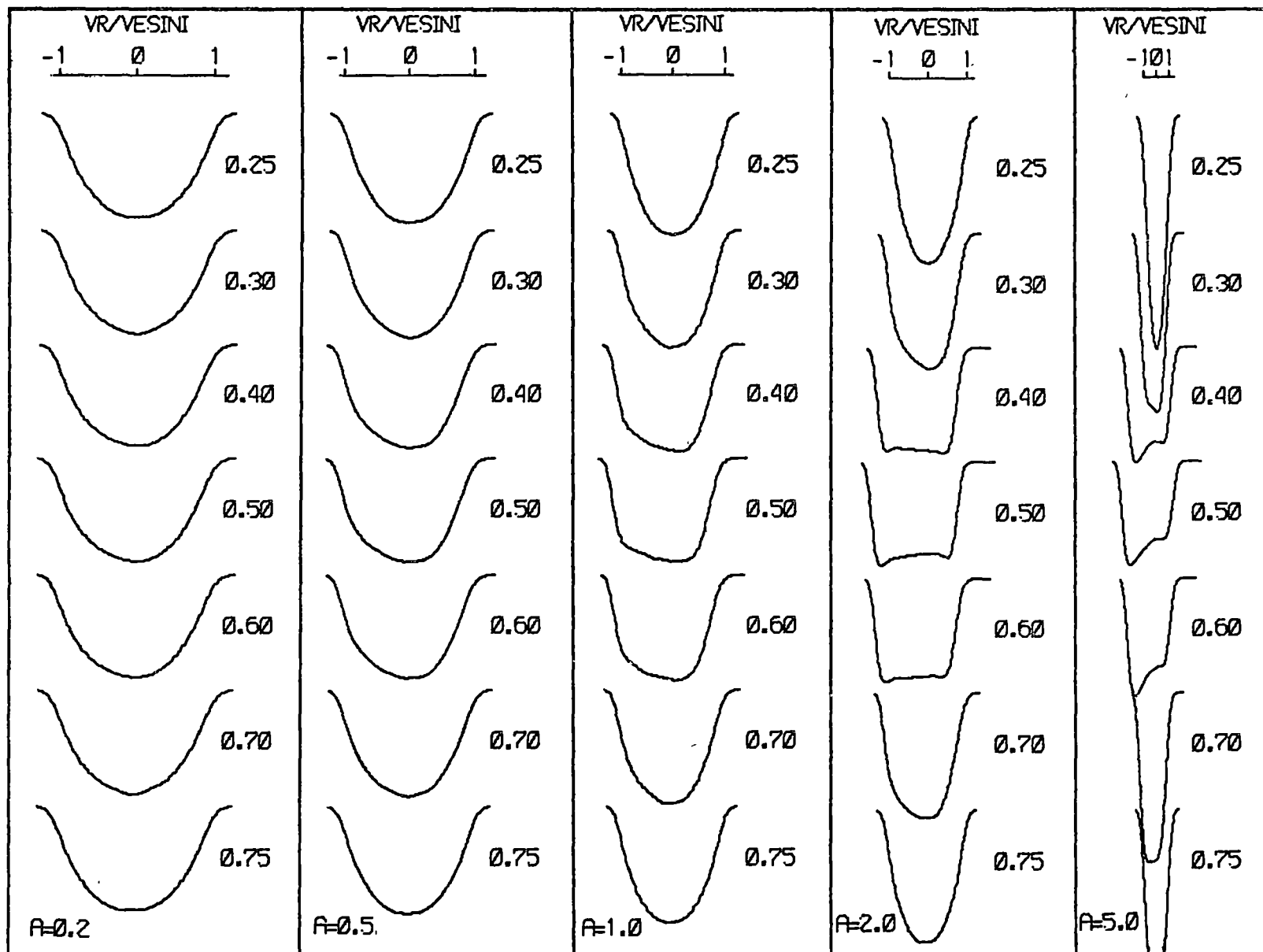


Figure A6.5(a)

Line Profiles for $(2, -1)$ $i = 23^\circ$

$l=2$
 $m=-1$
($i=23^\circ$)

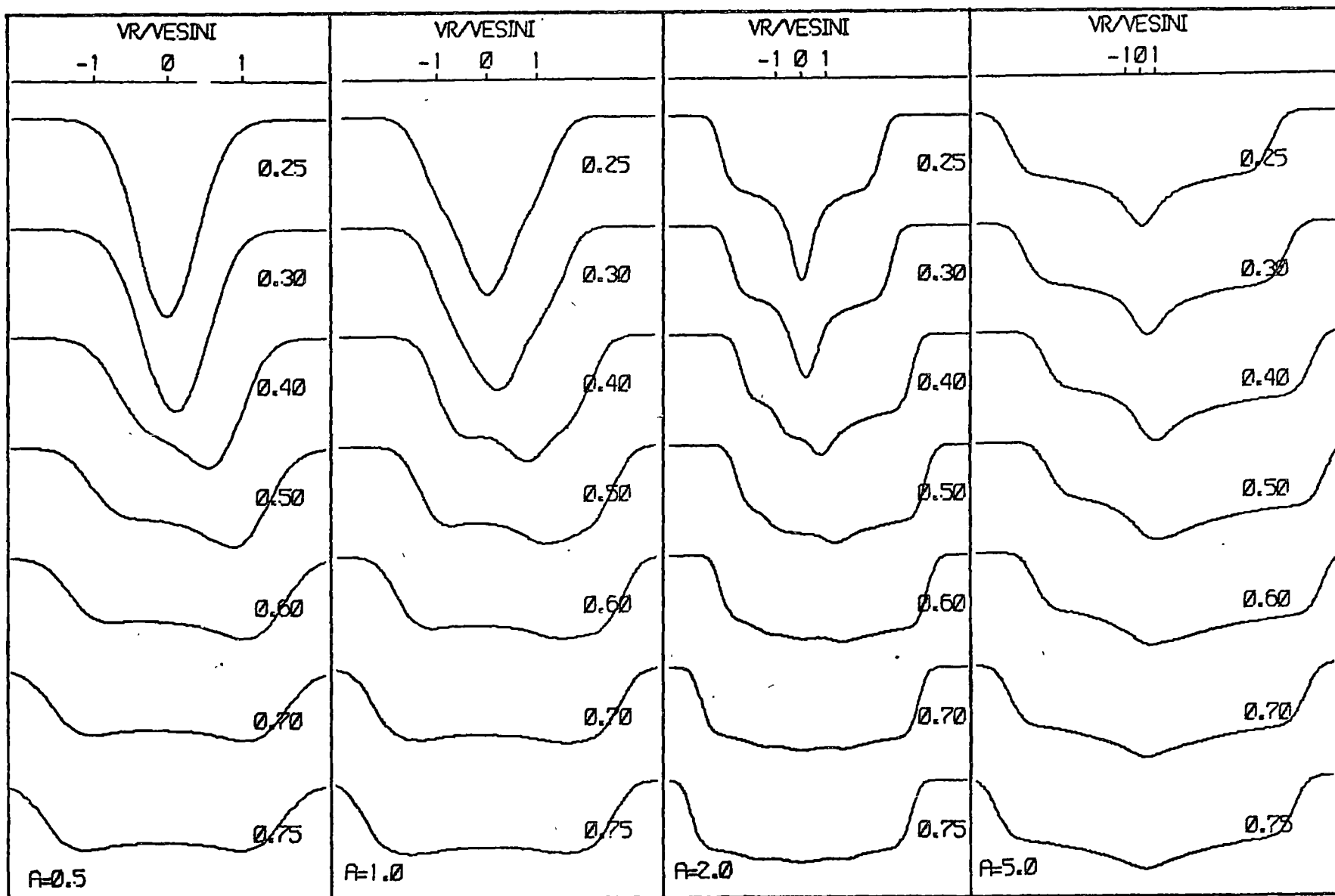
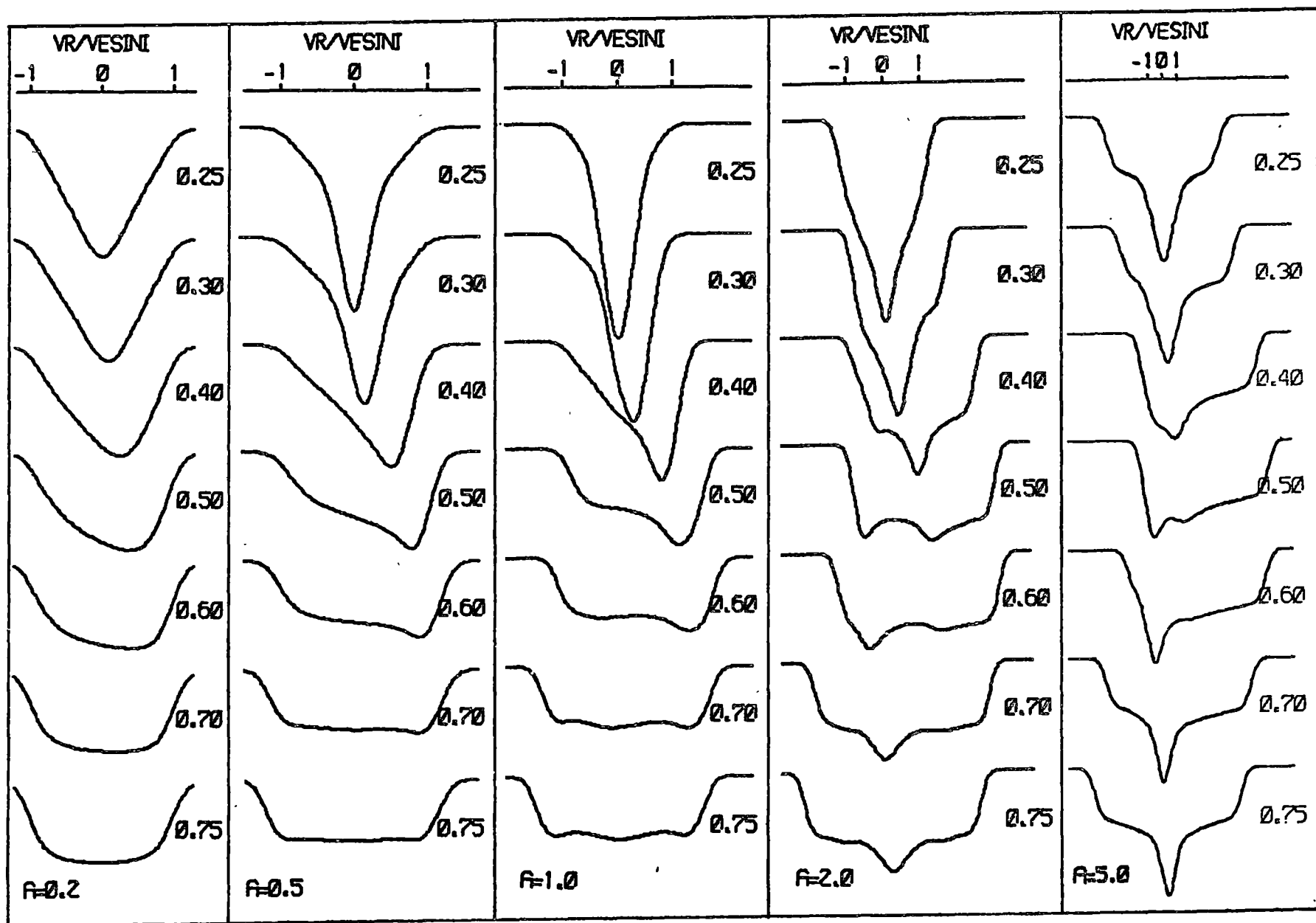


Figure A6.5(b)
 Line Profiles for $(2, -1)$ $i = 45^\circ$
 $l = 2$
 $m = -1$
 $(i = 45^\circ)$



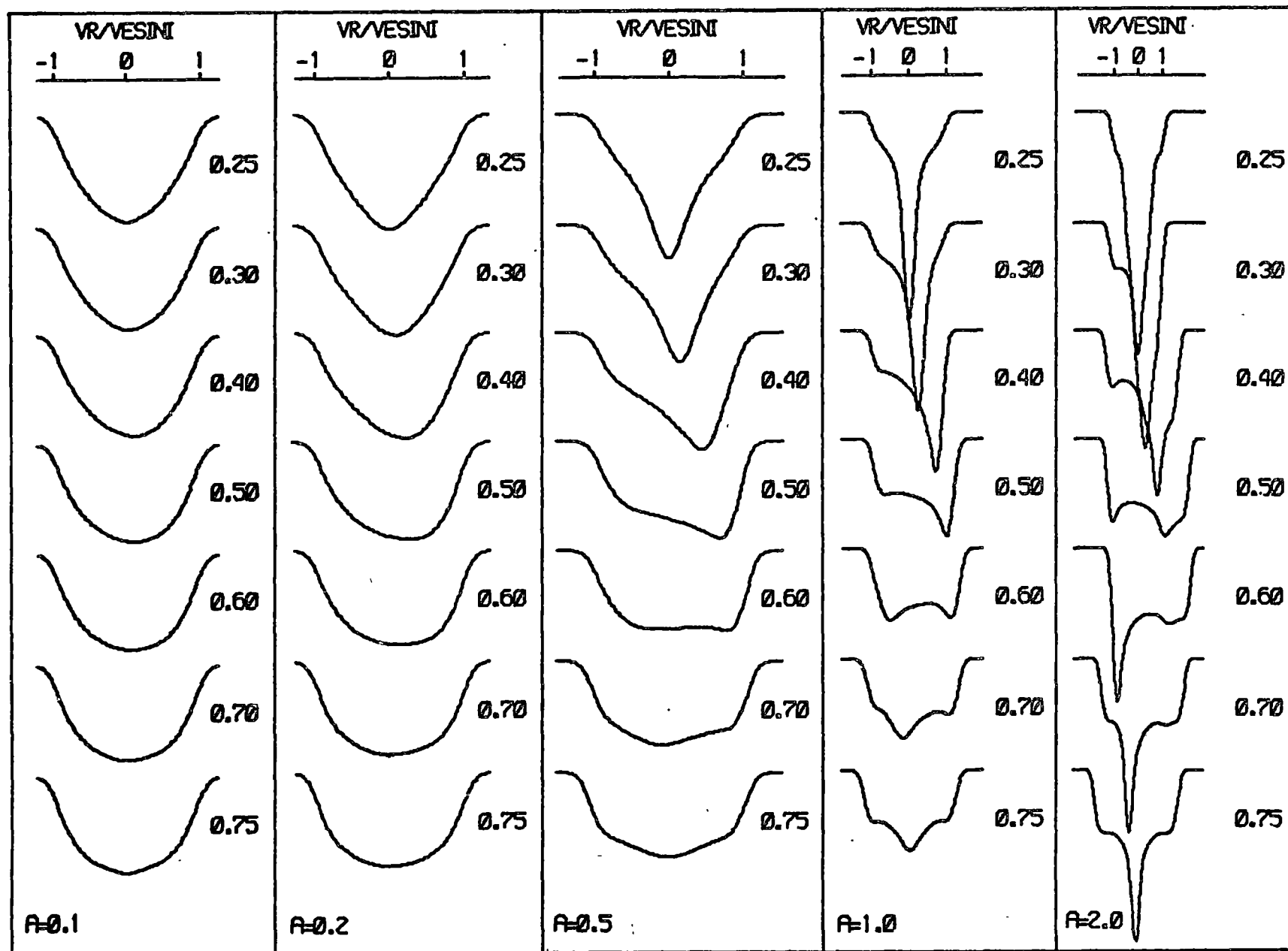


Figure A6.5(c)

Line Profiles for $(2, -1)$ $i = 68^\circ$

$l = 2$
 $m = -1$
 $(i = 68^\circ)$

Figure A6.6(a)

Line Profiles for $(2, -2)$ $i = 23^\circ$

$l = 2$
 $m = -2$
 $(i = 23^\circ)$

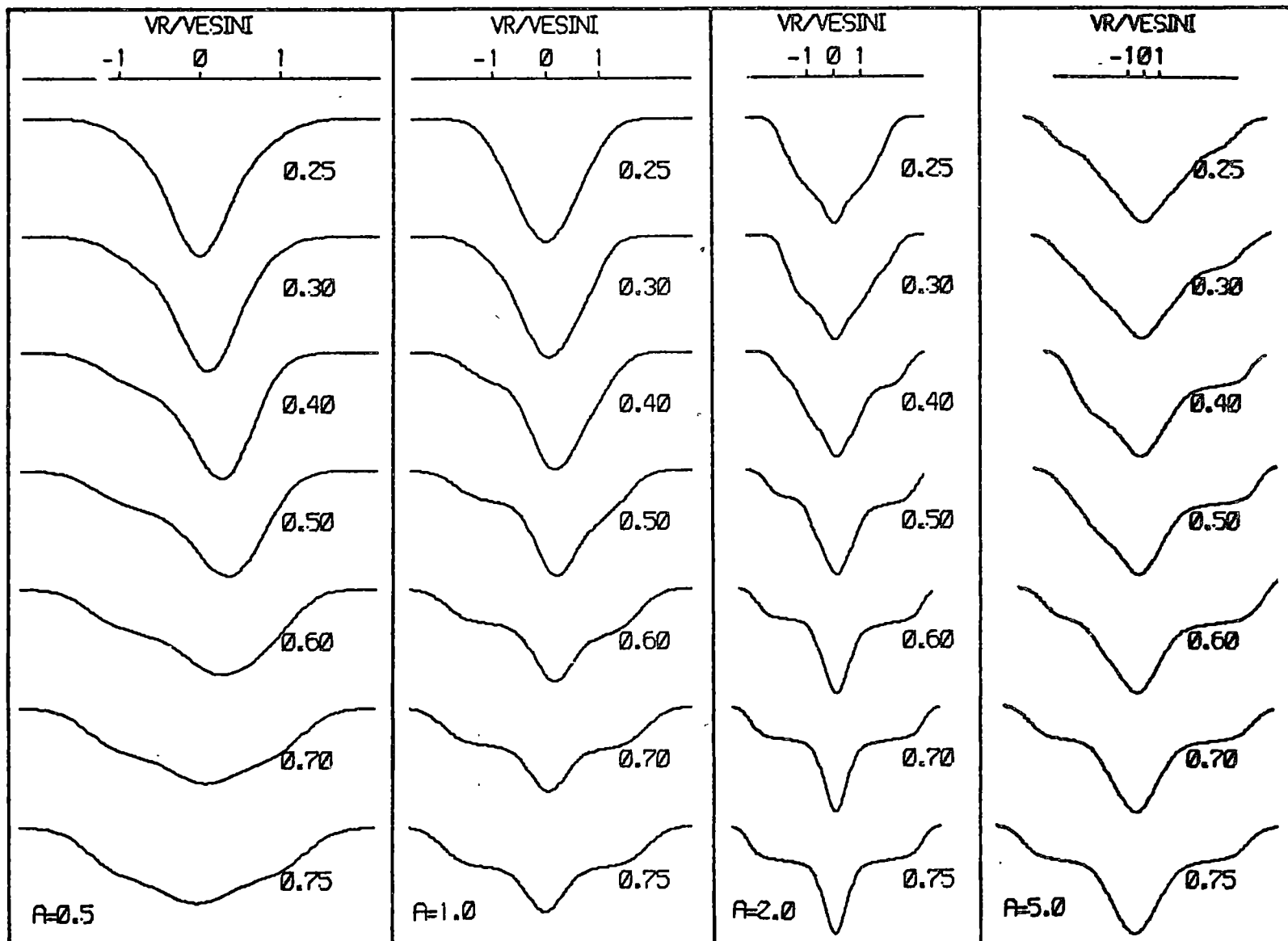


Figure A6.6(b)

Line Profiles for $(2, -2)$ $i = 45^\circ$

$l = 2$
 $m = -2$
 $(i = 45^\circ)$

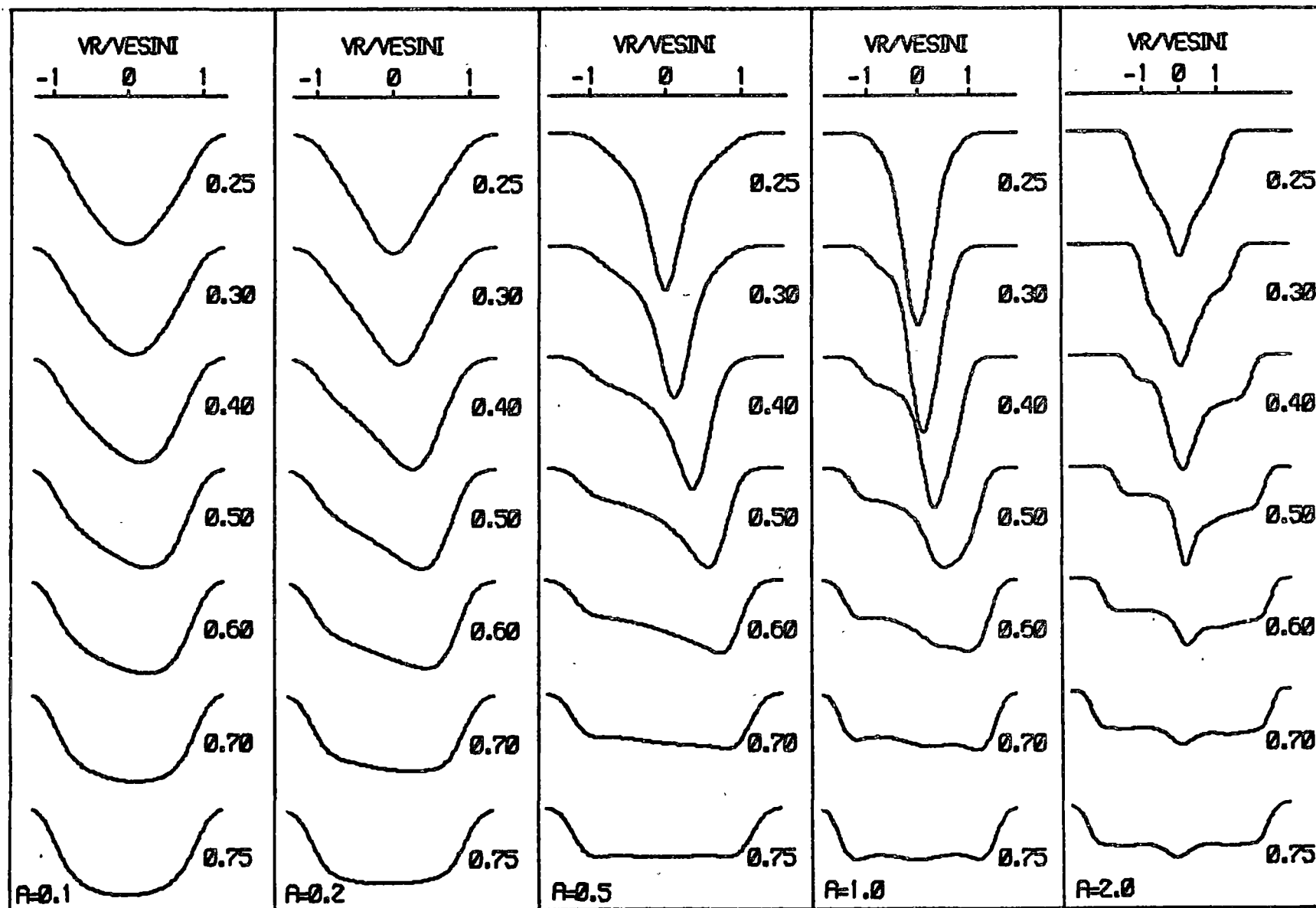


Figure A6.6(c)

Line Profiles for $(2, -2)$ $i = 68^\circ$

$l = 2$
 $m = -2$
 $(i = 68^\circ)$

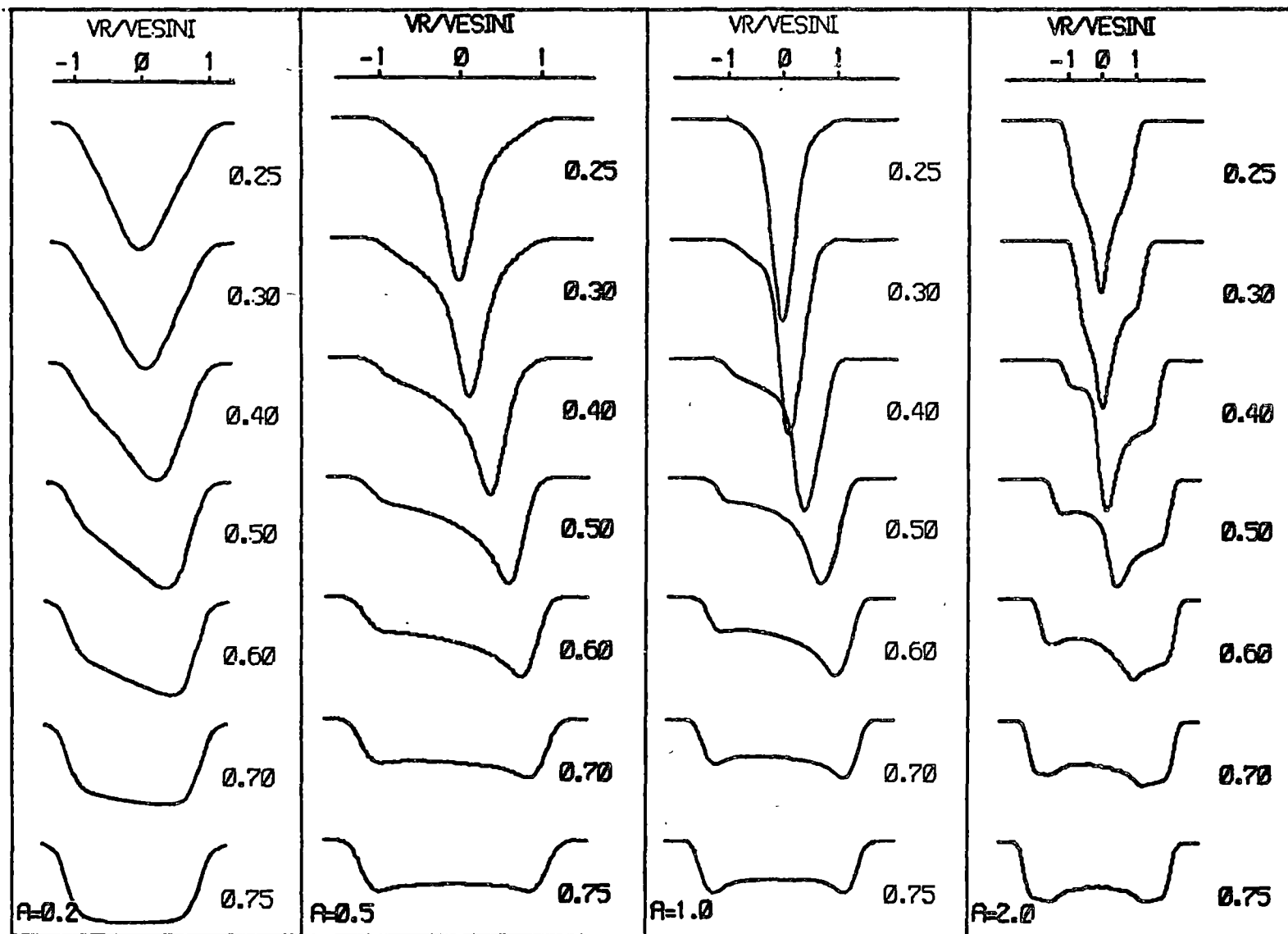


Figure A6.6(d)

Line Profiles for $(2, -2)$ $i = 90^\circ$

$l = 2$
 $m = -2$
 $(i = 90^\circ)$

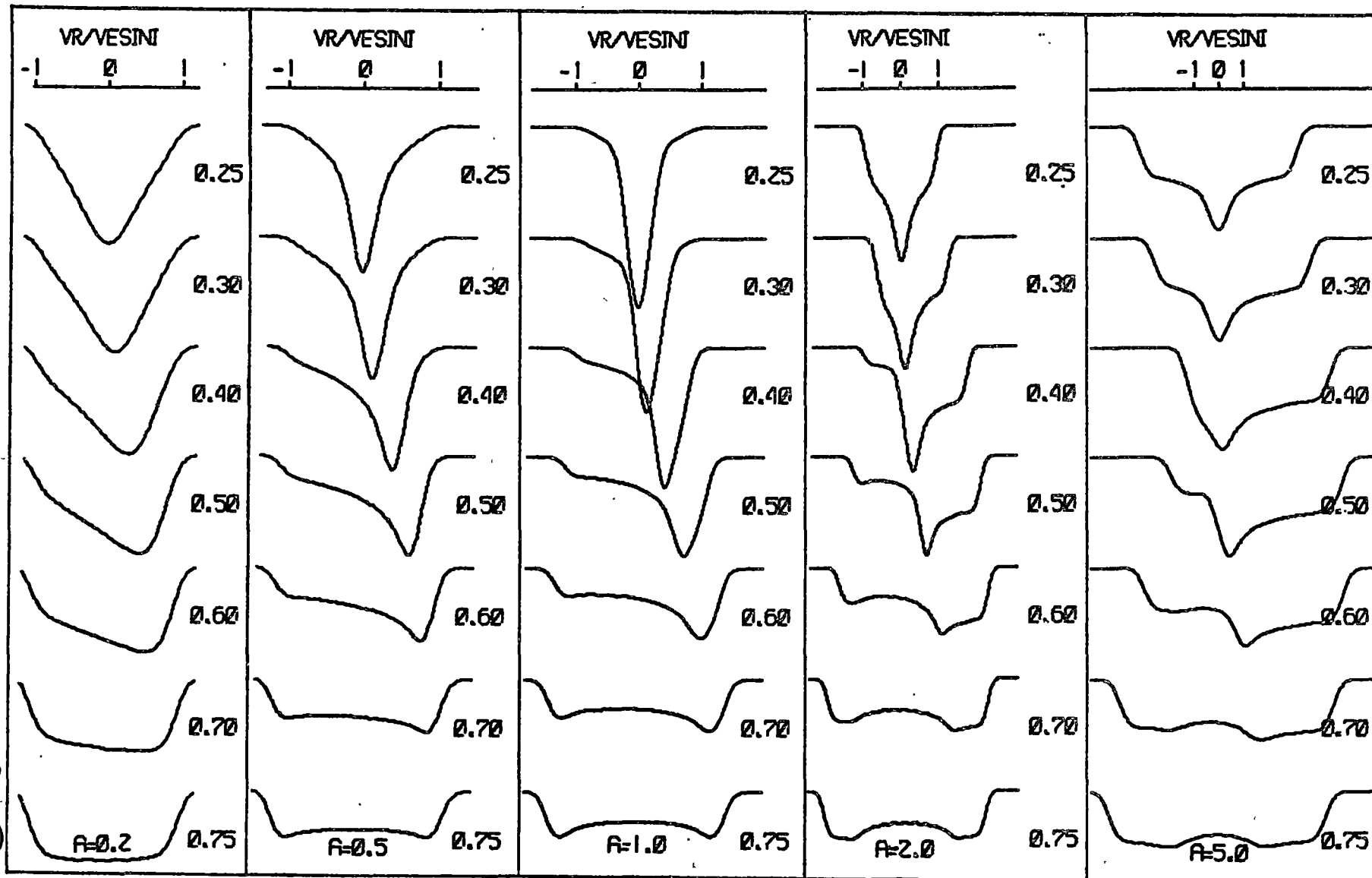
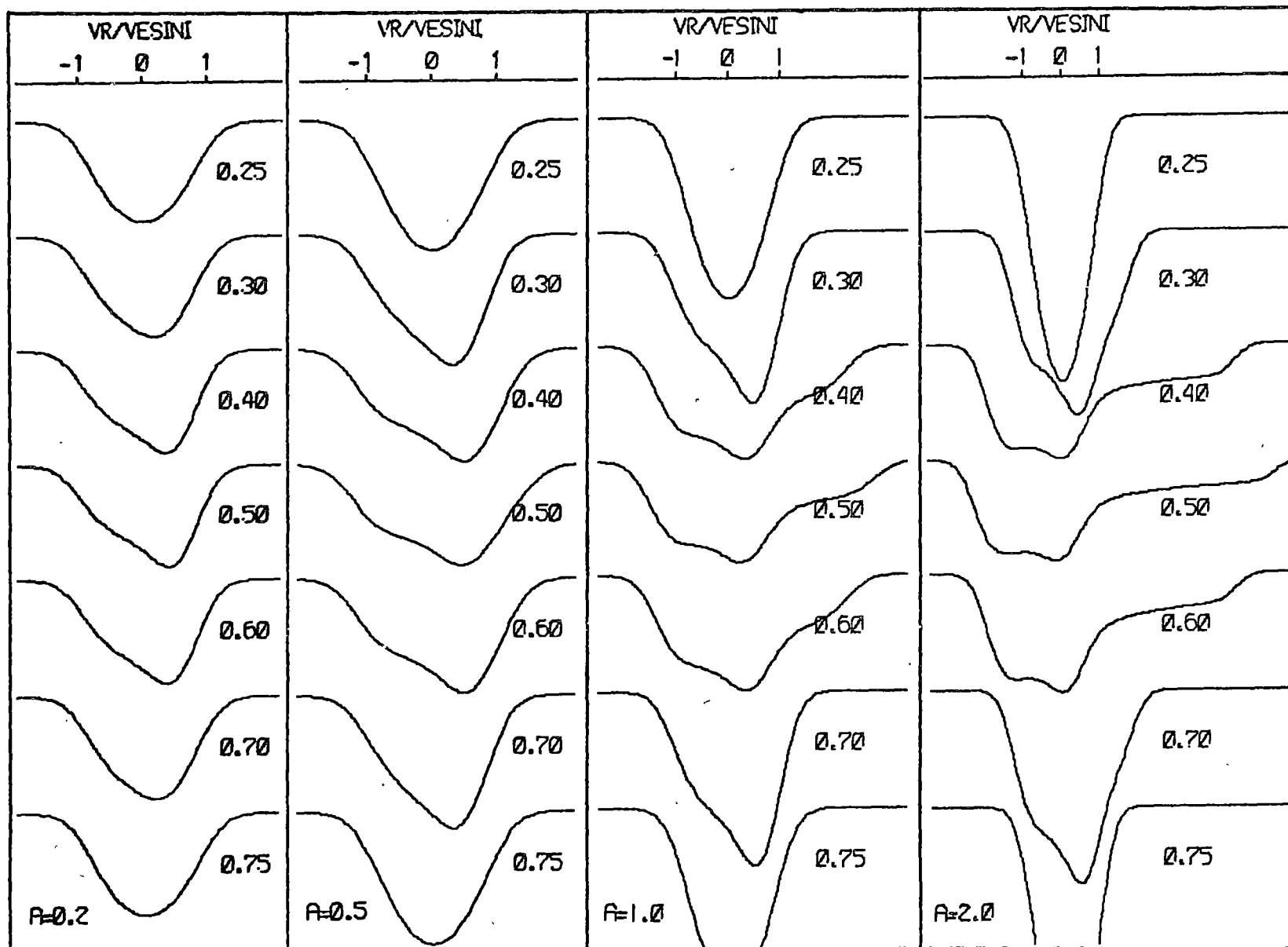


Figure A6.7(a)

Line Profiles for $(3,0)$ $i = 20^\circ$

$l = 3$
 $m = 0$
 $(i = 20^\circ)$



$l = 3$
 $m = 0$
 $(i = 39^\circ)$

Figure A6.7(b)
Line Profiles for $(3,0)$ $i = 39^\circ$

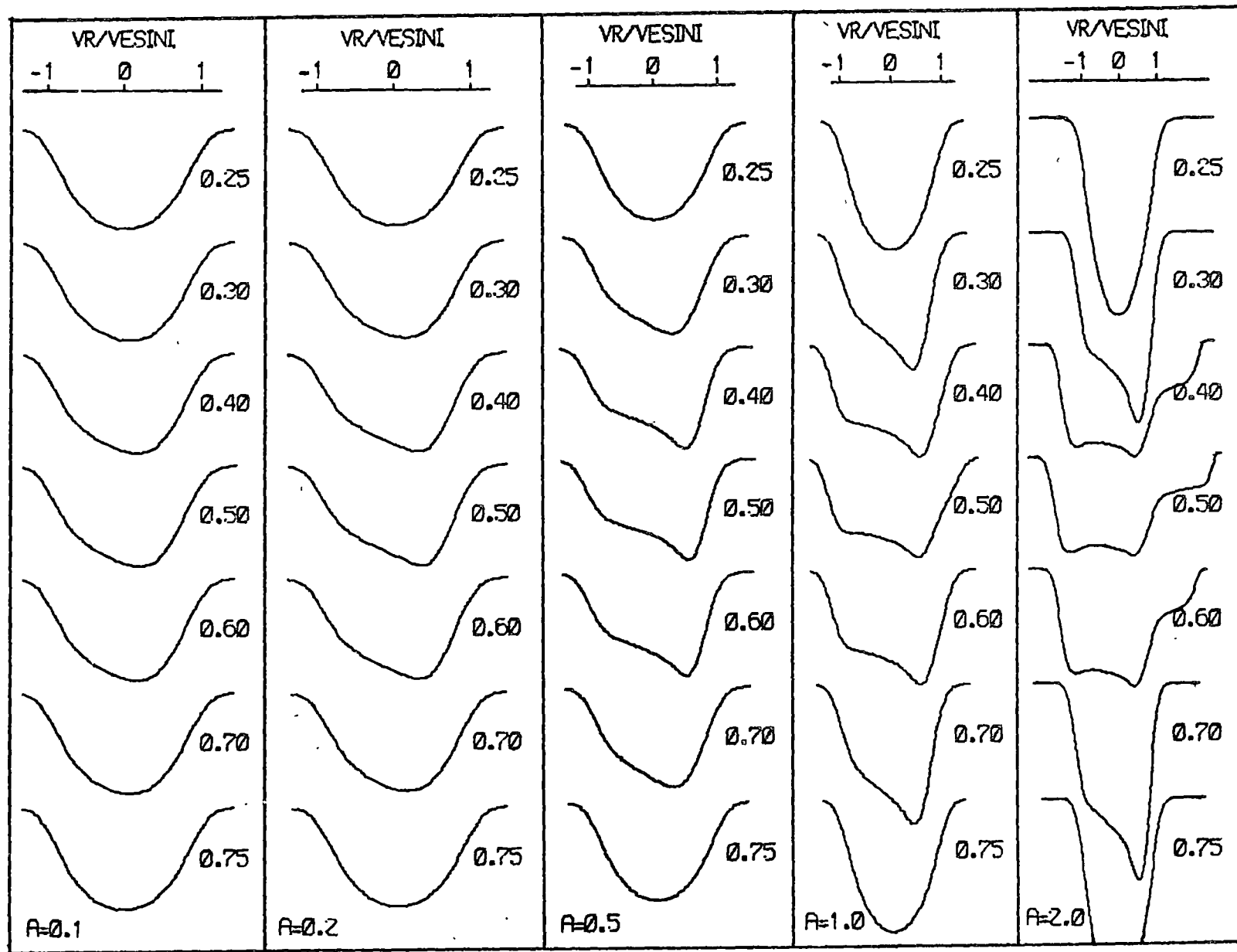
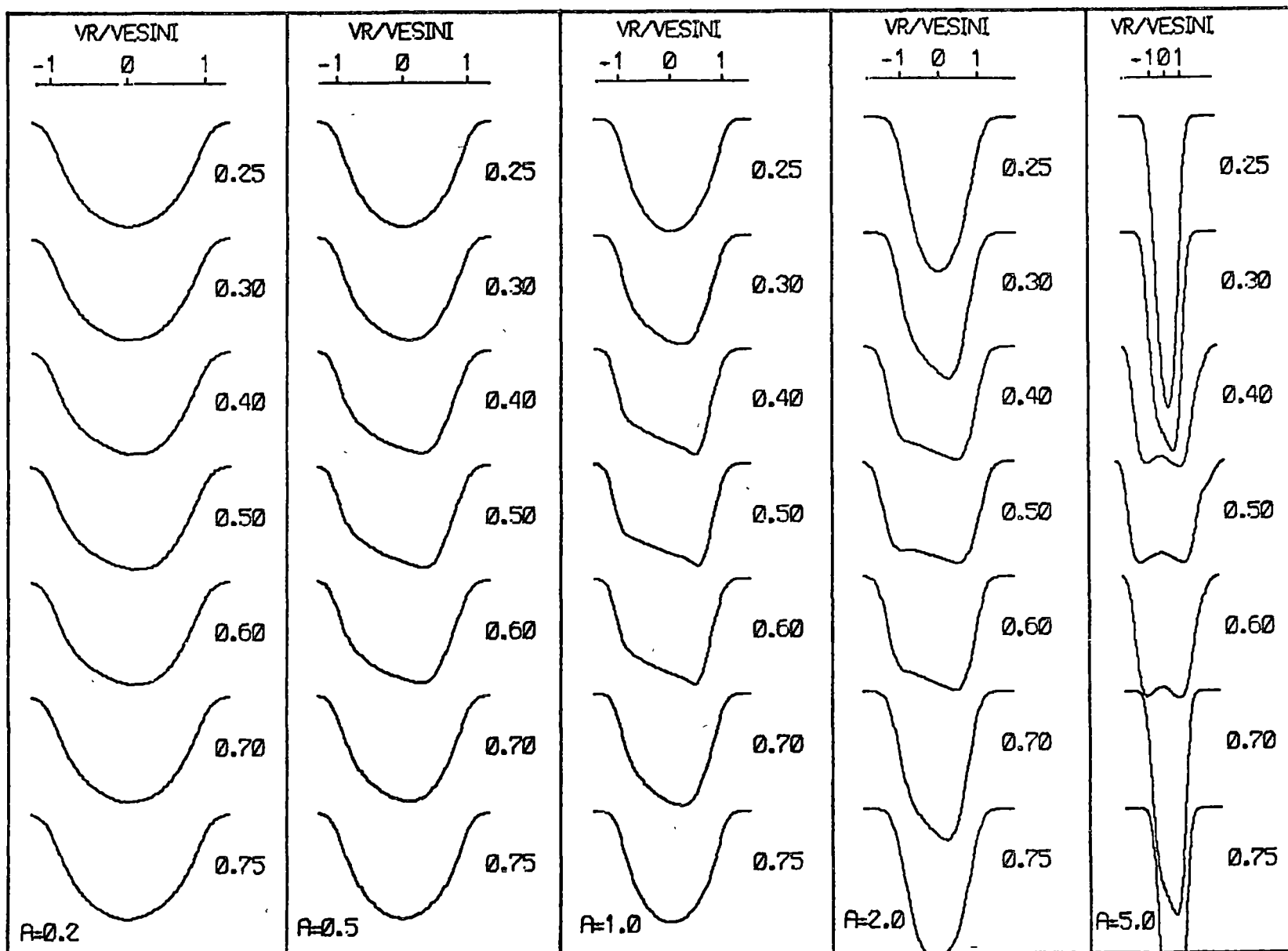


Figure A6.7(c)

Line Profiles for (3,0) $i = 63^\circ$

$l=3$
 $m=0$
 $(i=63^\circ)$



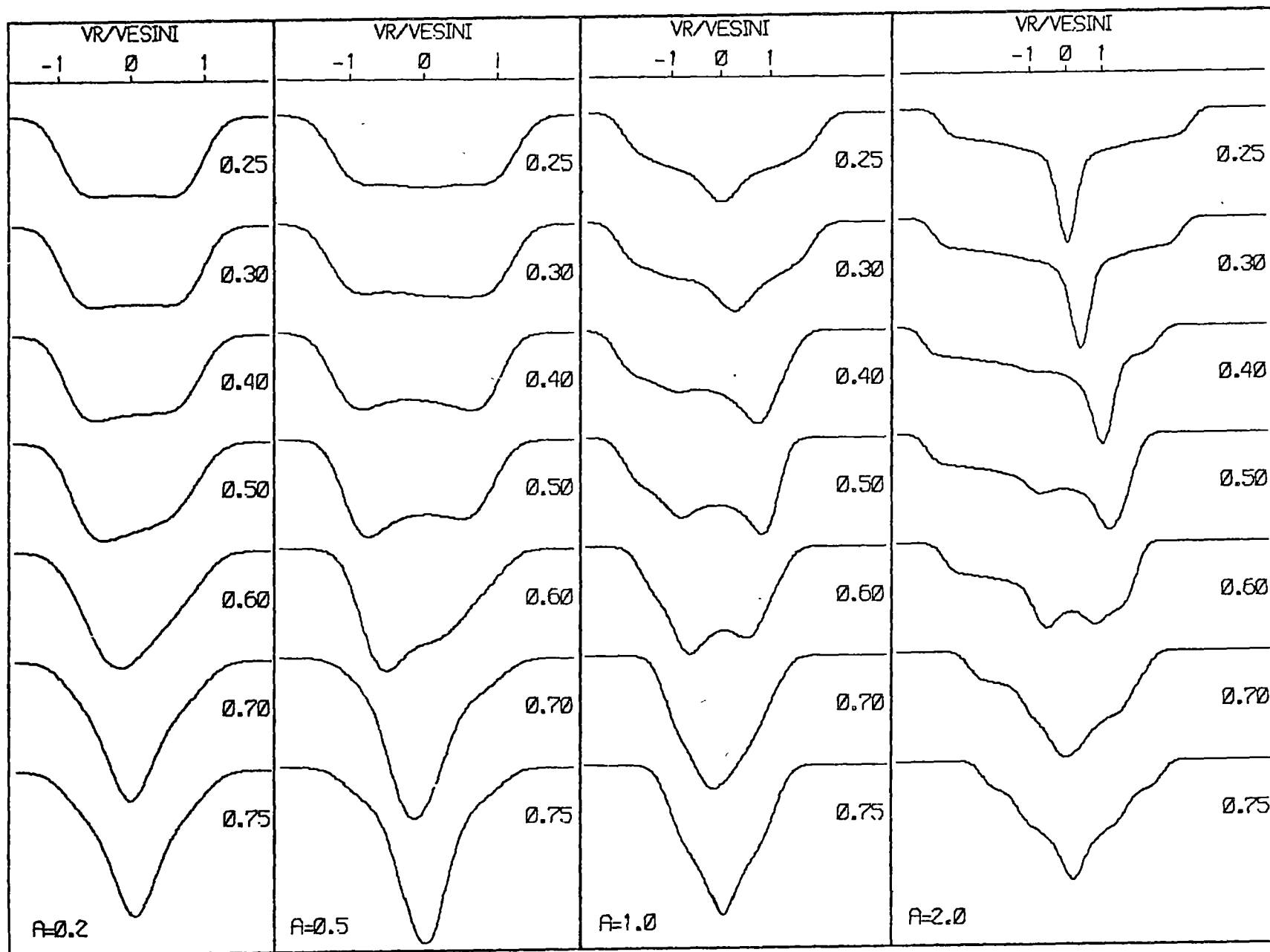


Figure A6.8(a)

Line Profiles for $(3, -1)$ $i = 31^\circ$

$l = 3$
 $m = -1$
 $(i = 31^\circ)$

Figure A6.8(b)

Line Profiles for $(3, -1)$ $i = 45^\circ$

$l=3$
 $m=-1$
 $(i=45^\circ)$

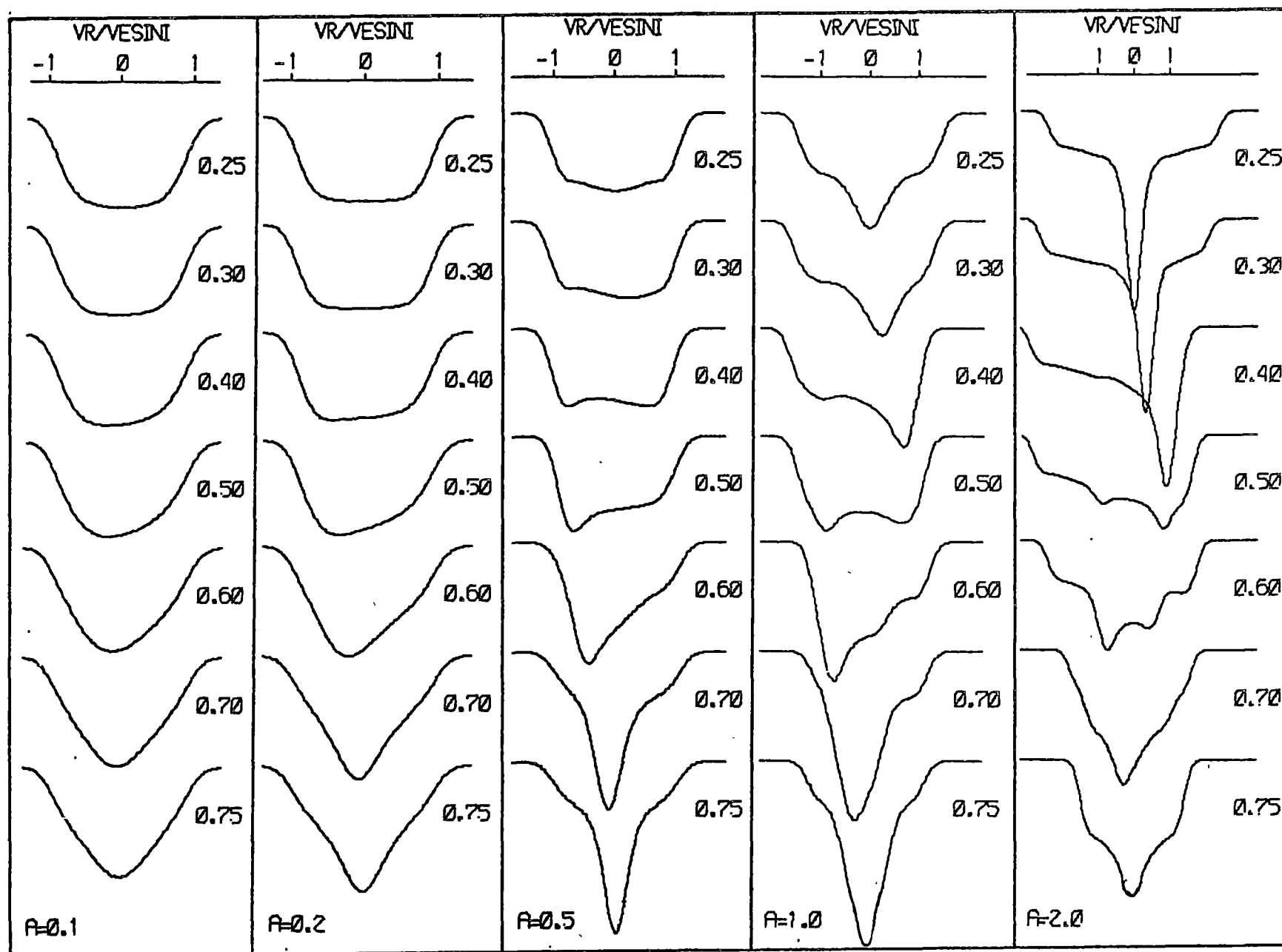


Figure A6.8(c)

Line Profiles for $(3, -1)$ $i = 90^\circ$

$l=3$
 $m=-1$
 $(i=90^\circ)$

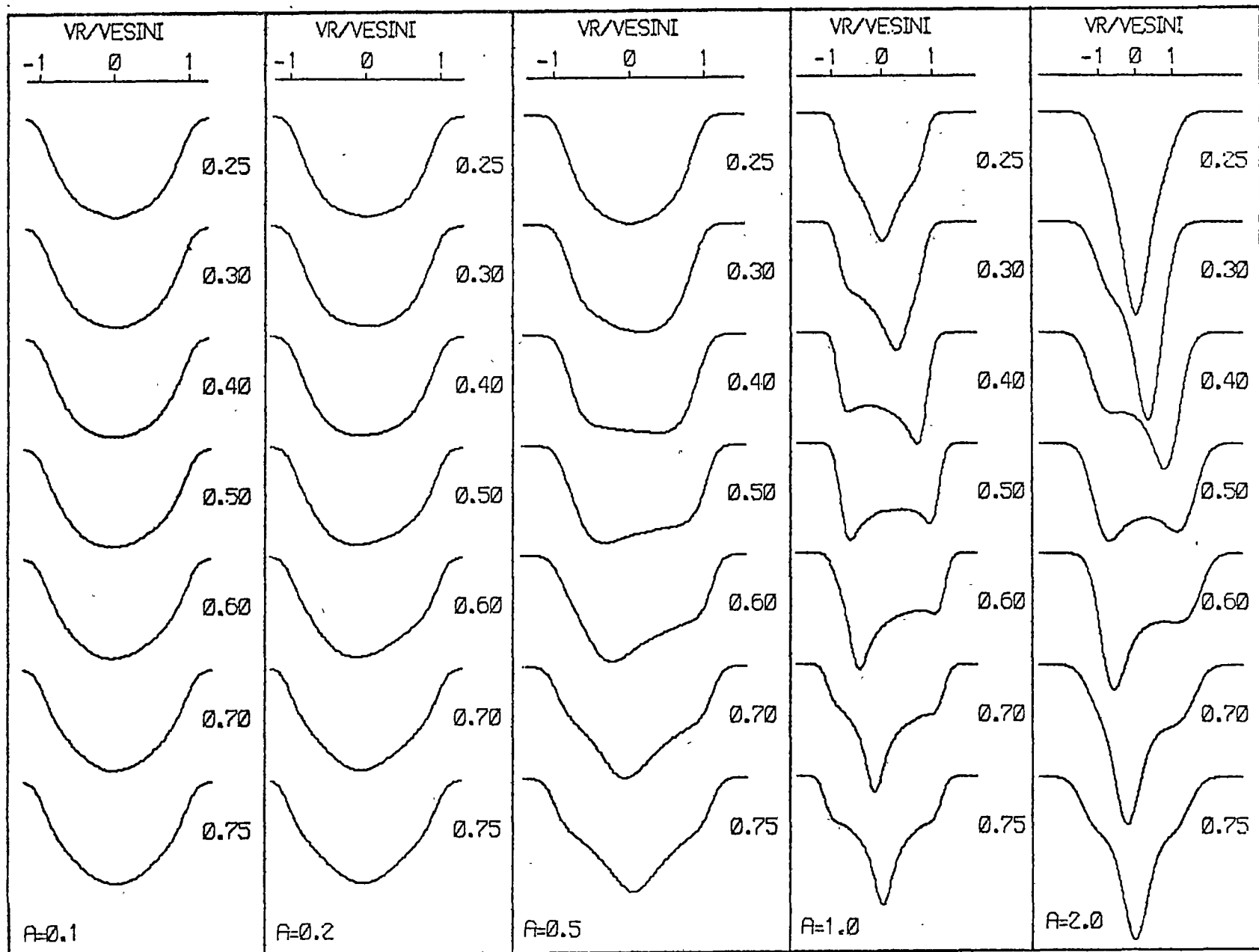
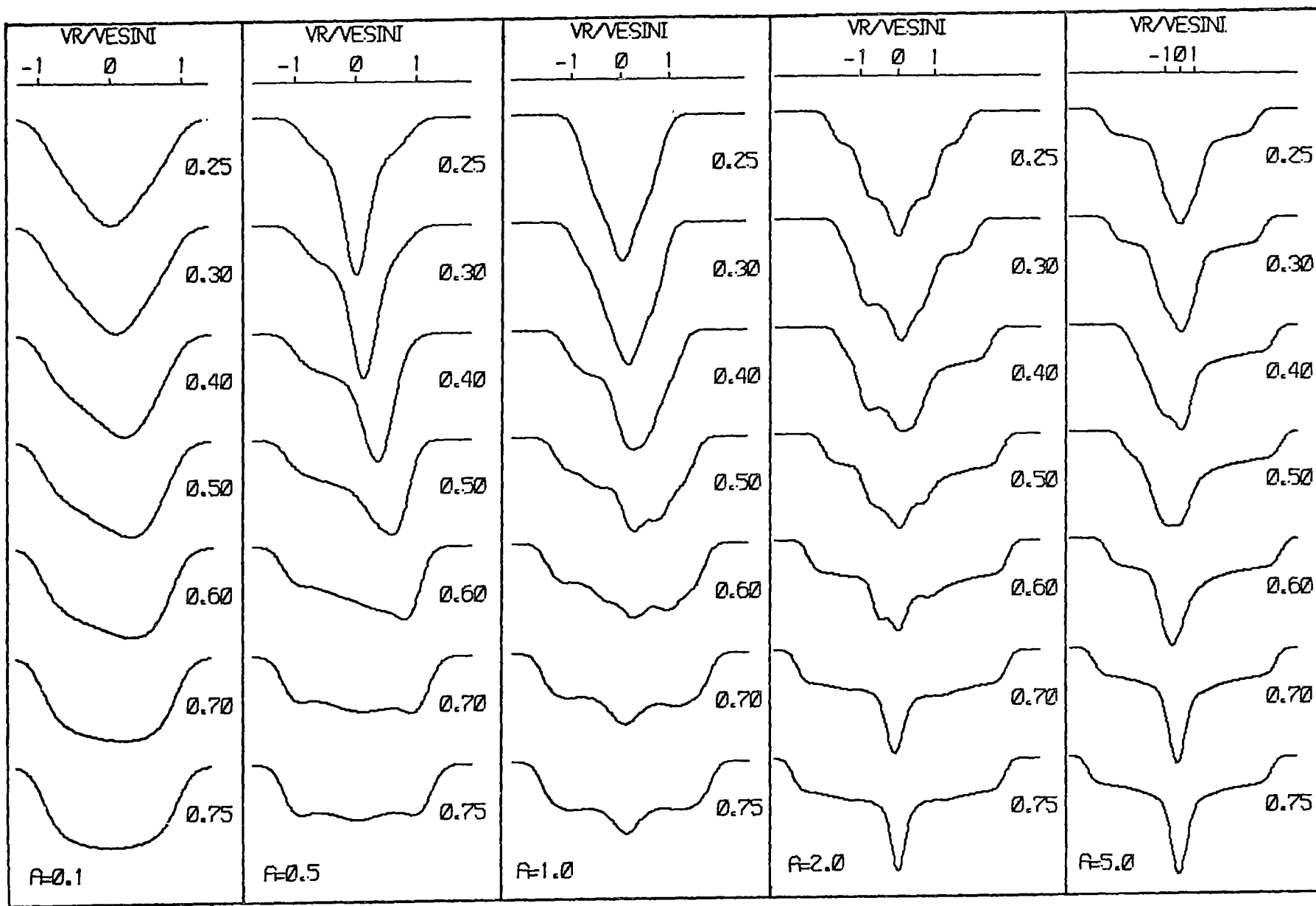


Figure A6.9(a)

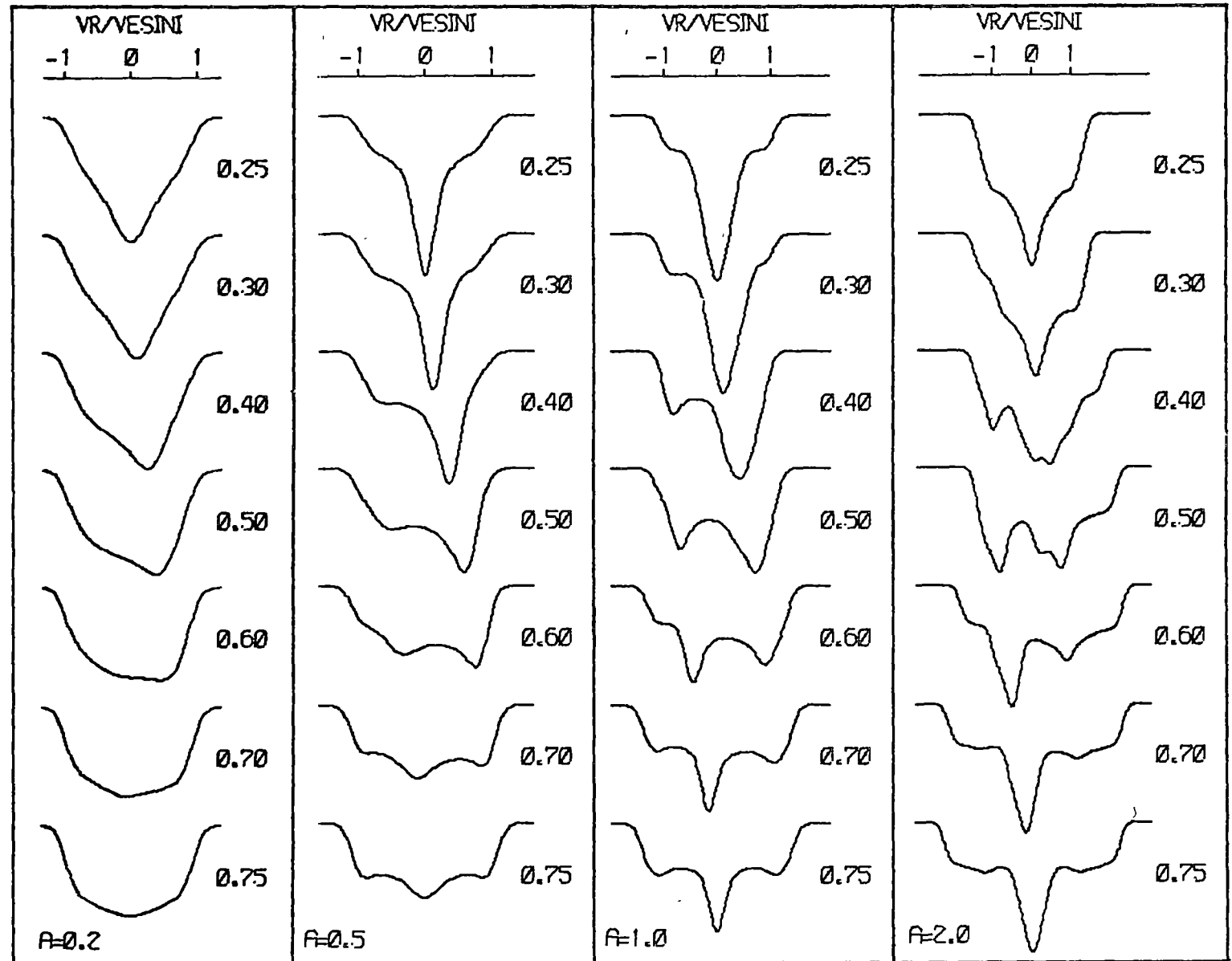
Line Profiles for $(3, -2)$ $i = 45^\circ$

$l=3$
 $m=-2$
($i=45^\circ$)



$l = 3$
 $m = -2$
 $(i = 68^\circ)$

Figure A6.9(b)
Line Profiles for $(3, -2)$ $i = 68^\circ$



$l=3$
 $m=-2$
 $(i=90^\circ)$

Figure A6.9(c)
Line Profiles for $(3,-2) \quad i = 90^\circ$

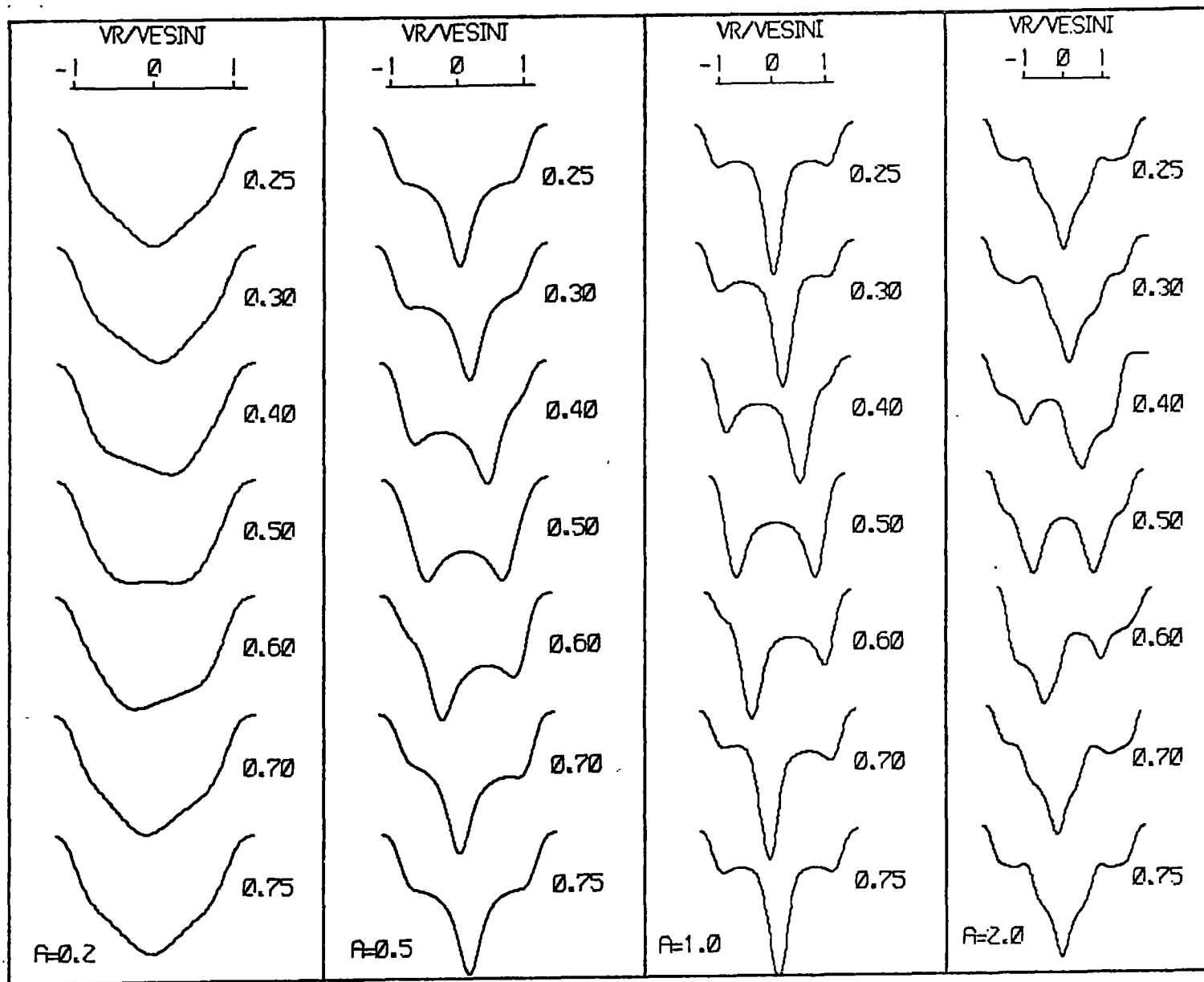
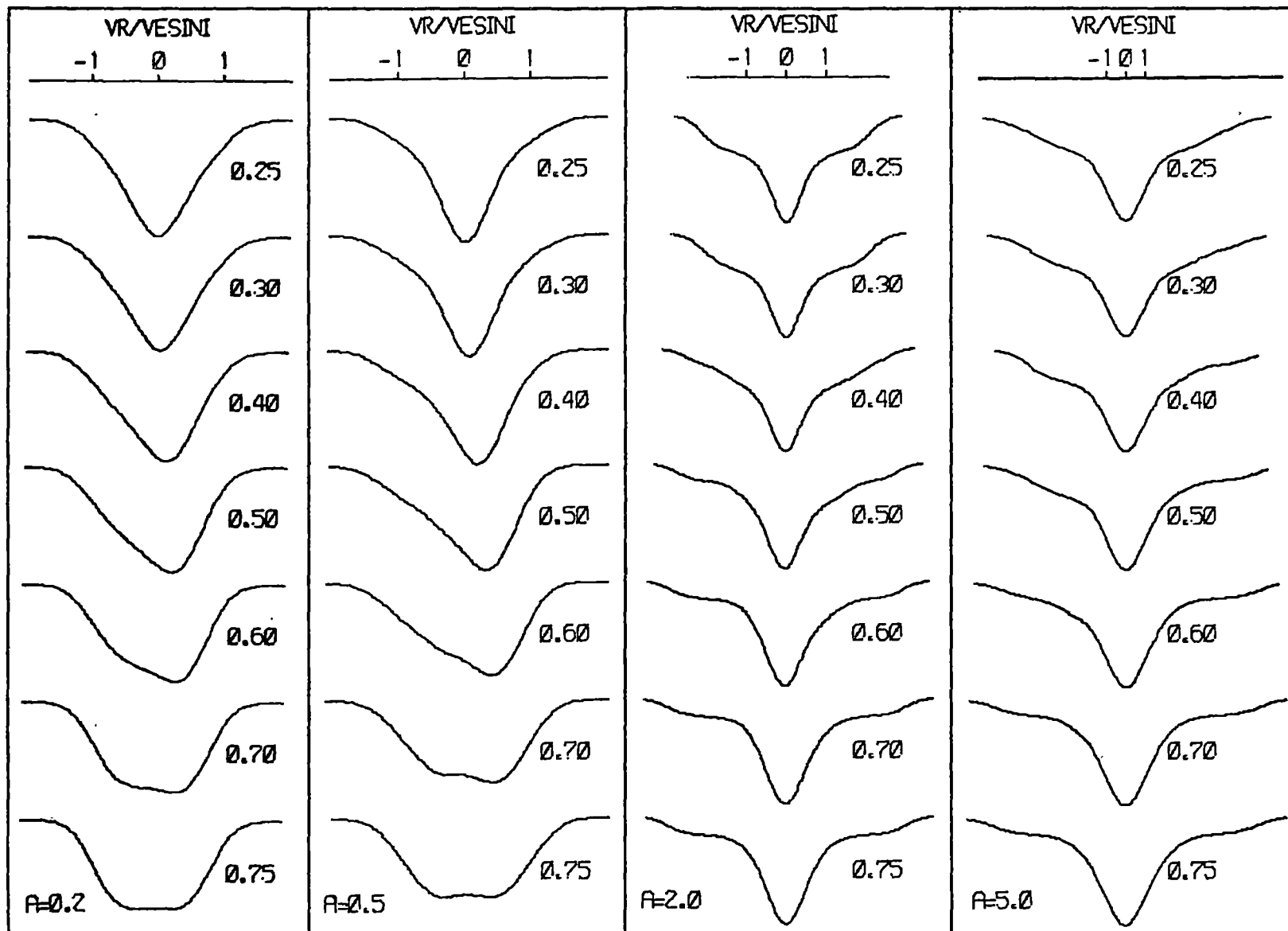


Figure A6.10(a)

Line Profiles for $(3, -3)$ $i = 23^\circ$

$l = 3$
 $m = -3$
 $(i = 23^\circ)$



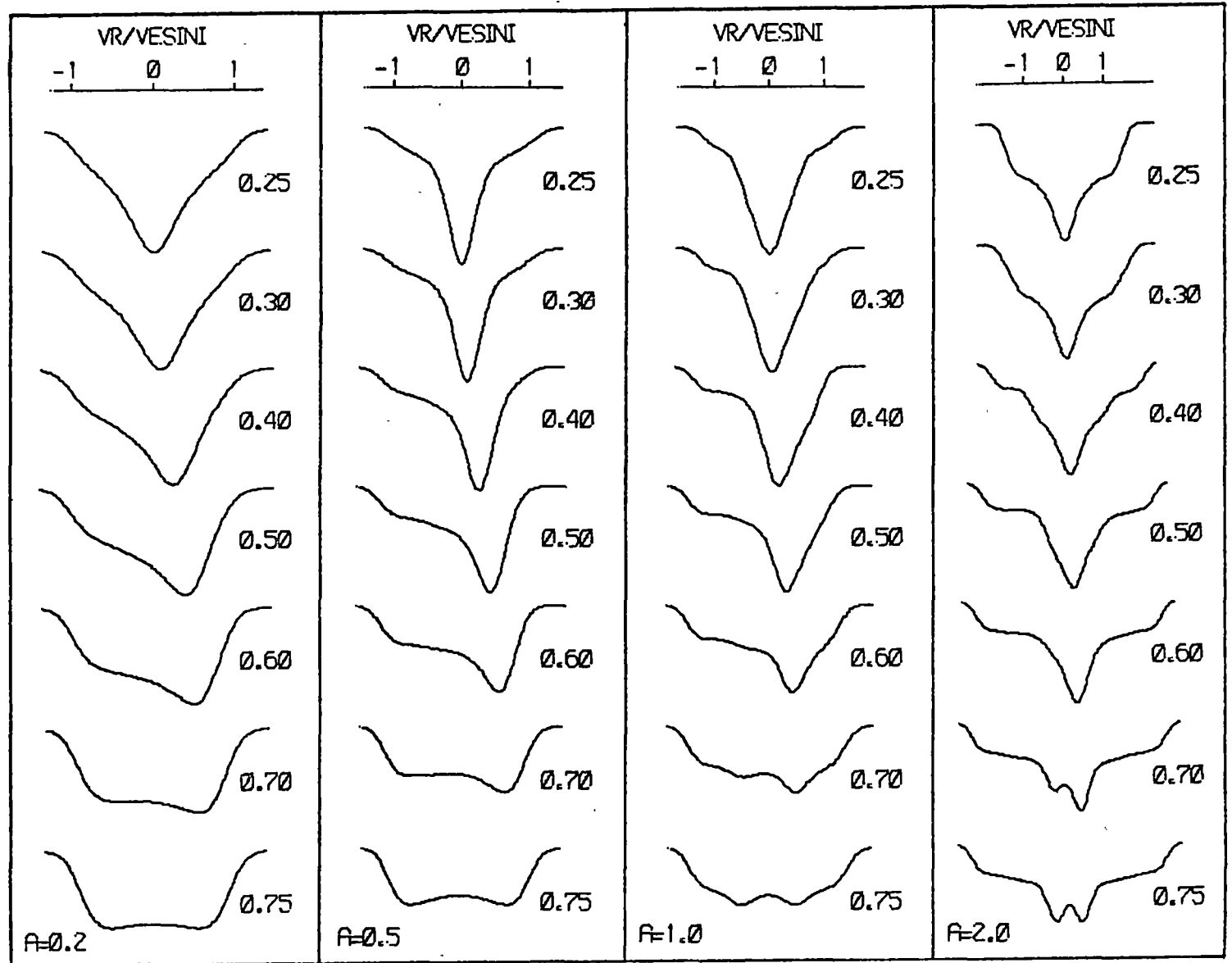


Figure A6.10(b)

Line Profiles for $(3, -3)$ $i = 45^\circ$

$l = 3$
 $m = -3$
 $(i = 45^\circ)$

Figure A6.10(c)

Line Profiles for $(3, -3)$ $i = 90^\circ$

$l = 3$
 $m = -3$
 $(i = 90^\circ)$

